Spectral evolution of the high energy emission from TeV BL Lac Objects

Francesco Massaro

Universitá degli Studi di Roma "Tor Vergata"
Facoltá di Scienze Matematiche Fisiche Naturali
Dipartimento di Fisica
Via della Ricerca scientifica, 1, I-00133, Rome (Italy)

PhD THESIS

Supervisor: Prof. A. Cavaliere

Coordinator: Prof. R. Buonanno

PhD in Astronomy XX Cycle

INTRODUCTION:

Blazars are the most enigmatic class of active galactic nuclei (AGNs) characterized by an extreme variability, that was explained by Blandford & Rees (1978) in terms of highly relativistic motions of emitting particles. Subsequently, with the introduction of the unification scenario of AGNs, Blazars were interpreted as radio-loud sources with a relativistic jet that points toward us (see Urry & Padovani, 1995 for a review). They are divided in two main classes: the first is constituted by BL Lac objects, with featurelss optical spectra; the other, the Flat Spectrum Radio Quasars (FSRQs) in which, typically, there are prominent spectral lines. Both classes show high time variability over the whole electromagnetic spectrum, from radio waves to TeV energies, coupled with high polarization detected in the radio and optical bands. Another difference among these two classes is that BL Lacs do not exhibit apparent cosmological evolution and are observed at redshifts $z < 1$, while FSRQs are observed up to $z \simeq 5$.

The spectral energy distribution (SED) is characterised by two broad bumps, interpreted as two emission components. The former component tipically peaks from the IR to the X-ray band, and the second one in the γ-rays up to TeV energies. A possible classification criterium for BL Lacs is in terms of the SED peak energy position of the first component was proposed by Giommi & Padovani (1995). They named high-frequency peaked BL Lac (HBLs) objects those in which the synchrotron peak is between the UV band and the X-rays, and low-frequency peaked BL Lacs (LBLs), those that show the first bump in the IR-optical range. Another BL Lac subclass was introduced subsequently to distinguish the so called intermediate BL Lac (IBLs) objects with the transition between the first and the second component in the keV range.

The discovery of intense medium-energy γ radiation from over 60 Blazars with the EGRET instrument on board the *Compton Observatory* (Hartman et al. 2001) showed that non-thermal γ-ray production is an important dissipation mechanism of their jets. This scenario was enriched by the discovery of the TeV emission of Mrk 421 that was the first extragalactic source detected at these energies in the range by the Whipple telescopes (Punch et al. 1992, Petry et al. 1996). Subsequently, with the advent of other Atmospheric Cerenkov telescopes: CAT, HESS and Magic, about twenty BL Lacs have been detected, and recently one FSRQ was also discovered as TeV emitter. Finally, the most recent results of the *Auger* seem to indicate Blazars as the sources of the highest energy cosmic rays.

Usually, BL Lac SEDs are interpreted in terms of Synchrotron Self-Compton (SSC) models in which synchrotron photons, emitted by a population of electrons accelerated in the relativistic jets, are scattered into the second component via inverse Compton (IC) scattering by the same electrons. The SEDs of FSRQs, tipically, require other spectral components, as for example soft seed photons produced in regions external to their jets, in order account for their high energy emission. These emission models are generally named as External Compton (EC) radiation.

An important issue that raised new investigations on Blazars in the recent years concerns their spectral shape and its evolution. About 20 years ago Landau et al. (1986), studying a sample of LBLs over a very broad fequency range, noticed that the SEDs of BL Lacs appear to be curved and that the best description could be given in terms of a parabolic fit on a double-log plot. This spectral shape, also known by statisticians as log-normal distribution, was after used by other authors with no physical interpretation. More recently, the log-parabolic model was also used to describe the X-ray spectra of HBLs as Mrk 421 and Mrk 501 (Tanihata et al. 2004, Massaro et al. 2004). In particular, Massaro et al. (2004) first attempted an interpretation and showed that this distribution can be understood in terms of statistical acceleration mechanisms. The idea that the log-parabolic spectral shape is not only a good and simple empirical model to fit the SEDs of Blazars, but that can provide important clues to understand the physical conditions and acceleration mechanisms in their jets begins now to be discussed.

On the other hand, the fact that this distribution, in principle, can be obtained as a solution of the diffusion equation for relativistic particles, can be traced back to the early works on the physics of radio sources in the classic paper by Kardashev (1962).

The present PhD. Thesis is essentially devoted to the problem of investigating how the SED modeling can be used to enrich our knowledge on the physics of Blazars. The most important and new tool that I will depelop is the search and the study of relations between the spectral parameters, and specifically the one describing the curvature, of BL Lac objects in different luminosity states. These relations will be interpreted in terms of acceleration mechanisms and of synchrotron and inverse Compton emission in relativistic jets.

I focused my work on the HBL objects detected at TeV energies, for which spectral data on both synchrotron and inverse Compton components are available. I reduced and analysed the X-ray spectra of eleven years of archival and new observations of HBLs performed with *BeppoSAX*, *XMM-Newton* and *Swift*. New procedures have been designed and performed to compare the spectra obtained with different instruments. The observations analysed involve 16 HBLs detected in the TeV band, and 11 HBLs which are good candidates to be detected at these very high energies.

The synchrotron and the inverse Compton emission processes have been studied to establish possible scaling relations between the spectral parameters. In particular, for the synchrotron radiation I found two relations involving the peak energy with the SED peak level and the spectral curvature. These relations were then verified using the data set obtained from my analysis work. In addition, I derived theoretical relations for the inverse Compton emission of both the first and the second order.

I also developed several numerical codes to calculate the SEDs of these sources. In detail, I developed a Synchrotron Self Compton (SSC) code able to reproduce both the synchrotron bump and the first and the second order inverse Compton emission. Another code was written to model the various components that can contribute to the External Compton (EC) emission. It evaluates the inverse Compton scattering between the electron jet population and an external radiation field from an accretion disk. Several energy electron distributions can be used, and in particular, those produced by statistical/stochastical acceleration processes leading to log-parabolic electron distributions. Each code has also a best fitting section to determine spectral parameters of the BL Lac SEDs. Moreover, I studied the conditions and wrote some criteria to take into account of the violation of the so called Compton Catastrophe limit.

I think that the main results of my work reside in the correlations and trends between some spectral parameters that were found in the X-ray data set of the sample of TeV BL Lacs. A detailed and exhaustive statistical analysis was performed for Mrk 421, whose behavior in the plane of spectral parameters appears not to reflect beaming variations, as expected from “internal shock” models of BL Lac jets. It is worth of notice the discovery that similar trends are showed by at least four other sources HBLs detected also at TeV energies indicating, that the basic physical mechanisms should not be different. Numerical simulations provided a good description of the SEDs of all HBLs in the sample and were used to constrain the values of physical input parameters. These constraints were then used to describe a sample of HBLs candidate as TeV emitters.

The last issue presented in this Thesis is a study of the SED of BL Lacertae, the eponymic BL Lac object, that was recently detected at TeV energies by MAGIC (Albert et al. 2007). Thus is the first LBL object observed at these very high energies and, therefore, the interpretation of its emission can be crucial to understand how many sources of this type could be detected in the near future and by AC telescopes of the next generation. I analysed some simultaneous X-ray observations performed with *Swift*, and using the numerical codes quoted above. I computed the SED of this source to understand the origin of the TeV photons.

The organisation of the Thesis and a description of the content of the individual Chapters is presented in detail in the following guidelines. The original scientific results have been published in some international conferences and in the articles in international journals as reported in the following.

Guidelines to the reader:

This thesis is mostly basis on original results. New analysis of unpublished BL Lacs X-ray observations are reported and discussed in the framework of several models. All new results found during these studies are published or submitted to the astronomical international review *Astronomy & Astrophysics* and have been presented in several conferences.

In *Chapter One* an historical introduction combined with main observational properties and interpretations of blazars is reported.

Chapter Two describes general issues on the radiative transport, especially in the case of spherical sources, to introduce several basic equations used to develop numerical codes. Corrections due to relativistic beaming and to cosmology are reported. It was necessary to summarize the main properties of shperical radiation fields and introduce the nomenclature used in all following sections to build numerical codes.

Chapter Three is dedicated to remind general concepts on the acceleration mechanisms, both statistical and stochastical. In detail, the main properties of the log-parabolic electron distribution are described.

In *Chapter Four* the synchrotron and inverse Compton emission mechanism spectral properties are summarized. Synchrotron Self Compton (SSC) and external Compton (EC) radiation are also described, taking into account of the 2^{nd} order inverse Compton emission.

Chapter Five reports relations between observed spectral parameters are derived, to investigate the behaviour of BL Lacs objects emission. These relations are proposed also for the 2^{nd} order inverse Compton emission. Pratical formulae are evaluated to investigate Klein-Nishina regime for emitting electrons and for the Compton Catastrophe in the SSC scenario. In particular, new useful calculations are developed to derive physical parameters of the source from observed variables of the spectral energy distribution (SED) combined with timing variability. The behaviour of SSC and EC sources are described SEDs of BL Lacs, taking into account of changes of the source parameters.

In *Chapter Six*, the main description of *BeppoSAX*, *XMM-Newton*, *Swift* satellites is reported. In detail, the data reduction and data analysis procedures, used to investigate the X-ray spectra of BL Lacs are described.

In *Chapter Seven* a detaild spectral and statistical analyses of the HBL Mrk 421 is presented. These analyses allow me to interpret X-ray spectral evolution of this source in terms of signature of synchrotron emission and acceleration mechanisms. I perform also the same analyses for the complete sample of HBLs detected at TeV energies, concluding that all sources in this class have similar behaviours of Mrk 421. This chapter reports also the X-ray spectral analyses of a sample of HBLs candidate as TeV emitters. With the numerical codes developed, described in *Chapter Five*, the predictions of VHE emission for these sources have been performed.

Chapter Eight is dedicated to the only LBL object detected at TeV energies: BL Lacertae. A multiwavelength campaign was performed during 2005, collecting data from radio to TeV energy range. The analysis of the X-ray *Swift* observations of BL Lac and its spectral energy distribution in terms of SSC multicomponent models are here described.

Finally, in *Chapter Nine*, the summary and the conclusions are presented.

Acknowledgments

This thesis is realized within the Astronomy PhD Course (XX cycle) of the Rome University ”Tor Vergata”, this work was supported by a fellowship of the Italian Space Agency (ASI) and of the ”Istituto di Astrofisica Spaziale e Fisica Cosmica”, IASF-Rome/INAF in the context of the AGILE Space Mission.

I thank first Prof. Alfonso Cavaliere, for giving me the possibility to carry out my research activity during these years, and to whom I am really grateful for many interesting discussions that allowed me to learn the spirit of research and to grow. I thank a lot Dr. Marco Tavani that sustaining me during my PhD studies.

Special thanks go to Dr. Paolo Giommi that allow me to attend the Italian Space Agency Data Center (ASDC) where I improve my knowledge in high energy astrophysics, in particular, for this purpose, I would thank : Dr. Matteo Perri, Prof. Gino Tosti and Dr. Giancarlo Cusumano. I also thank Prof. Roberto Buonanno, my PhD coordinator, and all Professors that followed me during these three years with helpful discussion and courses.

Really special thanks go to Andrea Tramacere, that introduced me in the ”mysteries” of statistics and with me shared all problems in X-ray spectral analysis. I thank a lot Alessandro Paggi, Valerio Vittorini & Andrea Lapi, for helpfu discussions and encouragements in my PhD.

Finally, I would thank Prof. Giorgio Matt & Dr. Stefano Bianchi for introducing me in the astrophysics world encouraging me during my laurea thesis, and Dr. Dan Harris that will allow me to continue in astrophysics research in the future.

The last but certainly not least words are for my family: my mother Vincenza, my sister Luciana, and my father Enrico, for their support, their encouragements and their sustain in my research activity.

List of publications concernig the PhD thesis

Refereed papers

- ”Signatures of synchrotron emission and of electron acceleration in the X-ray spectra of Mrk 421” A. Tramacere, **F. Massaro**, A. Cavaliere, A&A 2007, 466, 521

- ”X-ray spectral evolution of TeV BL Lac objects: Eleven years of observations with BeppoSAX, XMM-Newton and Swift satellites” **F. Massaro**, A. Tramacere, A. Cavaliere, M. Perri, P. Giommi, A&A accepted

- ”The X-ray spectrum and a 26 year-long X-ray light-curve of 1E 1207.9+3945, one of most extreme BL Lac object” A. Maselli, P. Giommi, M. Perri, R. Nesci, A. Tramacere, **F. Massaro**, and M. Capalbi, A&A accepted

- ”Swift observations of IBL and LBL objects” **F. Massaro**, P. Giommi, G. Tosti, A. Cassetti, R. Nesci, M. Perri, D. Burrows, N. Gerehls, A&A preprint

Presentations at Meetings and Conferences

- ”Intrinsic spectral curvature in TeV blazars” **F. Massaro**, A. Tramacere, A. Cavaliere, PROC. AGN7 CONF., May 2006

- ”Acceleration mechanism and Spectral curvature in TeV Blazars” A. Tramacere, **F. Massaro**, A. Cavaliere, PROC. AGN7 CONF., May 2006

- ”25 years X-ray observations of the HBL object 1207.9+3945” A. Maselli, P. Giommi, M. Perri, **F. Massaro**, A. Tramacere, R. Nesci, M. Capalbi, PROC. AGN7 CONF., May 2006

- ”The giant X-ray flare of Mrk 421 in spring-summer 2006”
  A. Tramacere, P. Giommi, A. Maselli, **F. Massaro**, M. Perri, & the SWIFT team, PROC: First GLAST Symposium CONF:, February 2007

- ”Acceleration mechanism and Spectral curvature in TeV Blazars” A. Tramacere, **F. Massaro**, A. Cavaliere, October 2006

- ”Blazars: from precision X-ray spectra to gamma-ray predictions” **F. Massaro**, A. Tramacere, A. Cavaliere, M. Perri, P. Giommi, A. Paggi, PROC. SciNeGHE07 CONF., June 2007

The most great observational evidence
of the dark matter and the dark energy....
is that you cannot observe them
so
when I will start to believe that in the Universe
I can see only a few of everything that exsits...
I will finish to work...

"Passepartout, please, take my suitcases..."

"Dio non gioca a dadi con l'universo"
"...li ha lanciati una volta di troppo ... e ci ha fregato tutti!!"

To my three minutes before sleeping

Contents

1

Historical outline and properties of Blazars

1.1 HISTORICAL INTRODUCTION

The object BL Lacertae had been in the catalogue of variable stars for some time; it was originally discovered by Cuno Hoffmeister in 1929 (Hoffmeister, 1929). To understand the nature of this new source it was necessary to wait sixty years. In 1968, Schmitt noticed that a variable radio source was located at the same position of BL Lacertae (Schmitt, 1968). The radio source VRO 42.22.01 had been detected at the Vermillon River Observatory by MacLeod et al. in 1965. BL Lacertae was not a periodic variable, but rather its intensity varied irregularly with no apparent pattern of its the brightening and dimming. When the spectrum of this ”variable star” was taken, it was discovered that in the optical emission it was featurless; there were no emission lines as from quasars, and no absorption lines as found in most stars. Peter Strittmatter and several others identified four objects closely similar to BL Lac by 1972 (Strittmatter et al., 1972); therefore the class name *BL Lac Objects*.

Later in 1974, James E. Gunn and J. B. Oke, two Caltech astronomers, determined that BL Lacertae was actually located in a normal elliptical galaxy (Oke & Gunn, 1974). By blocking the light from the central region of the source, light from the surrounding area showed absorption lines that permitted an estimate of its redshift $z \simeq 0.07$. This corresponds to a distance at about 420 Mpc ($h_0 = 0.7$), indicating that the core of BL Lacertae shines with a luminosity $L \simeq 10^{46}$ erg/s.

The discovery that some radio-loud quasars show a continuum similar to BL Lac Objects, but with the occurrence of broad spectral lines, was important for a complete definition of the class of new sources; Ed Spiegel jokingly referred to these objects as *blazars* and this nickname seems to have stuck (Blandford & Rees, 1978). The word *blazar* is a combination of the two words: BL Lac and quasar, and today it is also connected with *blazing*.

Moore and Stockman gave an important contribution in 1981 (Moore & Stockman, 1981) when they performed a polarization survey in which they discovered 17 high polarization quasars (HPQs) and discussed their link to BL Lacs. So the division of this new class of Active Galactic Nuclei in two main subgroups, now referred to as BL Lacs and Flat Spectrum Radio Quasars (FSRQ), was firmly established.

1.2 OBSERVATIONAL PROPERTIES AND CLASSIFICATION OF BLAZARS

Blazars are the most enigmatic class of active galactic nuclei (AGNs). They are characterized by high and variable polarization, superluminal motion, and very high luminosities coupled with a flat radio spectrum that steepens in the IR-optical bands and a rapid variability from the radio to X-ray bands with weak or absent emission lines. In short they are the most “active” kind of AGNs. The observational properties of BL Lac objects have been interpreted in terms of a relativistic jet aligned within a small angle to the line of sight (Blandford & Rees 1978). This model led to conclude that these sources appear as a parent population of radio sources, that could be intrinsically identical to BL Lac objects, but with the jets oriented at large angles to the line of sight.

Blazar emission extends from radio to TeV energies and their spectral energy distribution (SED) is double bump: the first component tipically peaks from IR to X-ray band and the second one at high energy gamma-rays. The weak-lined blazars, or BL Lac objects, fall into two categories, defined by Padovani & Giommi (1995) as “Low-frequency peaked BL Lacs” (LBLs) and “High-frequency peaked

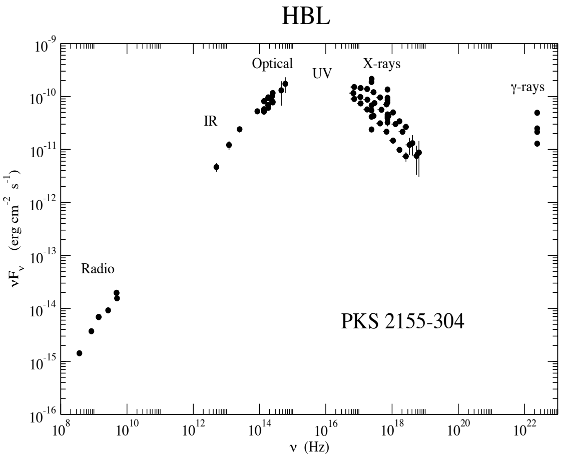

Figure 1.1: The spectral energy distribution of PKS 2155-304, an example of a high frequency peaked BL Lac object. In this source the peak of the first component lies betewwn the UV and the X-ray band.

BL Lacs" (HBLs), depending on whether $\alpha_{rx} = log(F_{5\ GHz}/F_{1\ keV})/7.68$ is greater than or less than 0.75, respectively.

Most HBLs have been found in X-ray surveys, and so have been known previously as XBLs (X-ray-selected BL Lac objects), while most LBLs have been found in radio surveys and so are also known as RBLs. As such surveys go deeper, however, the mix of types in a given survey will change, with increasing numbers of LBL in X-ray surveys and more HBLs in radio surveys, hence the need for a quantitative and clear distinction between the two types.

The spectral energy distributions (SEDs) of these sources include two main components: a low-energy component with power peaking in the range from the IR to the X-ray band, and a substantial high-energy component often dominated by γ rays. It is widely agreed that the low-energy component is produced by synchrotron radiation of ultrarelativistic electrons in the jet. Following the widely entertained synchrotron self-Compton scenario (SSC; e.g. Jones et al., 1974; Ghisellini & Maraschi, 1989) the second component may be interpreted as inverse-Compton scattering of the synchrotron photons by the same electron population.

Usually X-ray observations of HBLs show the peak and the fall of the synchrotron emission and for LBLs the rise of inverse Compton radiation. In particular, there are some BL Lacs, named intermediate BL Lacs (IBLs), that present features of the two components in the 0.5-10 keV range. At this point, it is not clear whether there exist two distinct classes of BL Lac object or whether there is a continuous distribution of spectral shapes between the classically discovered LBLs and HBLs. In Fig. 1.1 and in Fig. 1.2, the SEDs of a HBL and a LBL objects are plotted, while an example of an IBL is reported in Fig. 1.3.

The observed differences in continuum spectral shape, are that the synchrotron power of LBLs peaks at submm to IR wavelengths while that of HBLs peaks at UV to X-ray wavelengths, and the Compton components peak at GeV energies for LBLs and at much higher (TeV) energies for HBLs. HBLs tend to be fainter EGRET sources than LBLs even though they are a lower redshift population; their ratio of peak gamma-ray flux to peak synchrotron flux is around one or less (REF).

The strong-emission-line blazars are denoted by FSRQs (Flat-Spectrum Radio Quasars); the label FSRQ is more or less equivalent to "BL Lac" since essentially all are highly variable and (at least some

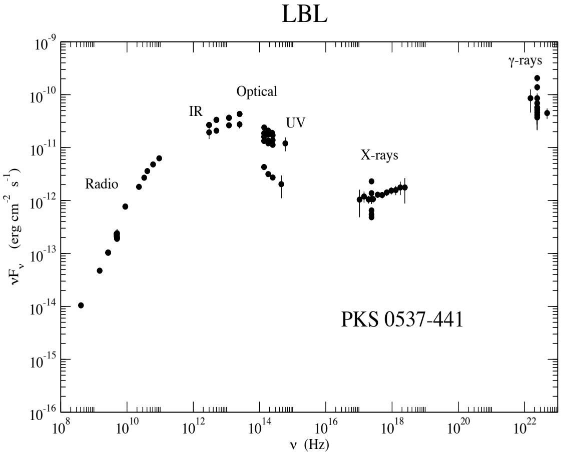

Figure 1.2: The spectral energy distribution of PKS 0537-441, an example of a low frequency peaked BL Lac object.In this source the peak of the first component lies betewwn the IR and the optical band.

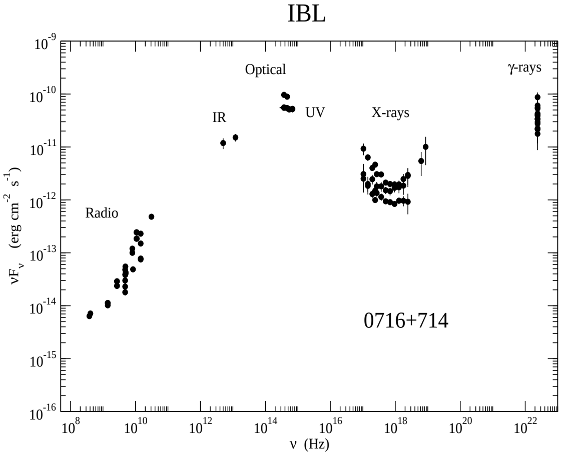

Figure 1.3: The spectral energy distribution of 0716+714, an example of an intermidiate BL Lac object. In this source, in the x-ray band it is possible to see both the fall of the first component and the rise of the second one.

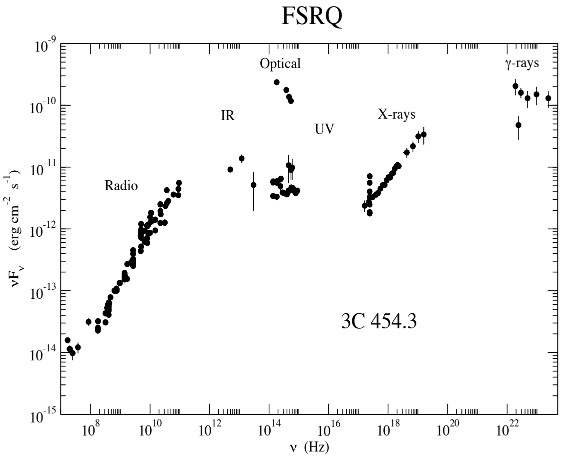

Figure 1.4: The spectral energy distribution of 3C 454.3, an example of a Flat Spectrum Radio Quasar.

of the time) highly polarized, as well as superluminal. The continuum shapes of FSRQs are very similar to those of LBLs (Sambruna et al. 1996), with synchrotron peaks at 10^{13} – 10^{14} Hz and Compton peaks at 10^{22} – 10^{23} Hz. The SED of a FSRQ is shown in Fig. 1.4.

In general, FSRQs are more luminous than BL Lacs. For FSRQs the ratio of Compton to synchrotron power is higher than for LBLs. This is illustrated with real multiwavelength spectra in a paper by Sambruna et al. (1996), who discuss possible physical connections among FSRQs, LBLs, and HBLs.

One popular hypothesis is that LBLs are viewed at smaller angles than HBLs, so that the difference is purely an orientation effect. Sambruna et al. (1996) conclude to the contrary that there must instead be intrinsic differences because for plausible emission models it is not possible to shift the wavelength of the peak emission by as much as four orders of magnitude.

2

Radiative transfer and relativistic effects

The main relations used to describe the radiation field are considered in this chapter. Here, the nomenclature and the formulae used in the following sections are collected, in particular for the case of spherical sources. There are many reviews concerning the radiative transfer in detail, as: Chandrasekhar (1965), Pacholczyk (1970), Tucker (1975), Rybicki & Lightman (1979), Shu (1991), Longair (2000).

2.1 GENERAL DEFINITIONS

Considering an emitting spherical source of radius R, its radiation field can be completely described by the *specific intensity*: the energy radiated per unit of area dA, time interval dt, frequency $d\nu$ in the solid angle $d\Omega = \sin\vartheta d\vartheta d\varphi$ (see Fig. 2.1)

$$I_\nu = \frac{dE}{dAdtd\nu d\Omega} \quad , \tag{2.1}$$

where the energy of the single photon is related to its frequency by: $E = h\nu$. The integral over the frequency will provide the total intensity: $I = \int I_\nu d\nu$. The number of photons N_{ph} per unit of volume

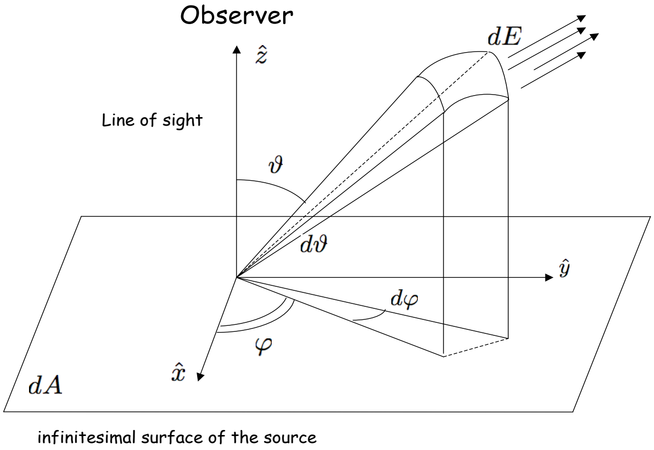

Figure 2.1: Schematic view of the radiation field.

dV, frequency $d\nu$ and radiated in the solid angle $d\Omega$: $n(\nu, \Omega)$, the specific density of emitted photons $n(\nu)$ and the photon density n_{ph} are defined as

$$n(\nu, \Omega) = \frac{dN_{ph}}{dVd\nu d\Omega} \qquad n(\nu) = \frac{dN_{ph}}{dVd\nu} \qquad n_{ph} = \frac{dN_{ph}}{dV} \quad , \tag{2.2}$$

respectively. The relations between these quantities are expressed by the integrals

$$n(\nu) = \int n(\nu, \Omega) d\Omega \qquad n_{ph} = \int \int n(\nu, \Omega) d\Omega d\nu = \int n(\nu) d\nu \quad . \tag{2.3}$$

The energy density of the radiation field is the energy per unit of volume

$$u = \frac{dE}{dV} = h\nu \frac{dN_{ph}}{dV} = h\nu n_{ph} \quad . \tag{2.4}$$

To study the emission processes it is convenient to define the *emissivity* j_ν and the *emission coefficient* ϵ_ν:

$$j_\nu = \frac{dE}{dV dt d\nu} \quad , \qquad \epsilon_\nu = \frac{dE}{dV dt d\nu d\Omega} \quad , \tag{2.5}$$

while the *absorption coefficient*, for the photon scattering with cross section σ_ν, is indicated as $\alpha_\nu = n_{ph}\ \sigma_\nu$. From the following conditions on the emission and absorption coefficients it is possible to describe the assumption of isotropical emission, as

$$\frac{\partial j_\nu}{\partial \vartheta} = \frac{\partial j_\nu}{\partial \varphi} = 0 \quad and \quad \frac{\partial \alpha_\nu}{\partial \vartheta} = \frac{\partial \alpha_\nu}{\partial \varphi} = 0 \tag{2.6}$$

and, under this hypotesis, the emissivity j_ν and the emission coefficient ϵ_ν are related by:

$$\epsilon_\nu = \frac{1}{4\pi} j_\nu \quad . \tag{2.7}$$

In detail, assuming isotropical emission, the photon densities can be written in terms of the emissivity, or of the emission coefficent, as

$$n(\nu) = \frac{R}{h\nu c} j_\nu = \frac{4\pi R}{h\nu c} \epsilon_\nu \qquad and \qquad n(\nu, \Omega) = \frac{R}{4\pi h\nu c} j_\nu = \frac{R}{h\nu c} \epsilon_\nu \quad . \tag{2.8}$$

It is worth to be noted that the expression for $n(\nu)$ can be generalized in the case of spherical sources in the form

$$n(\nu, \Omega) = \frac{t_{cr}}{h\nu} \epsilon_\nu = \frac{R}{h\nu c} \epsilon_\nu \quad , \tag{2.9}$$

with $t_{cr} = R/c$ the *light crossing time*. The integral of the specific intensity, over the solid angle, along the line of sight (characterized by the angle ϑ, see Fig. 2.1) is the *specific flux*

$$F_\nu = \int_0^{4\pi} I_\nu \cos\vartheta \, d\Omega \quad , \tag{2.10}$$

that is the energy emitted per unit of area dA, time dt and frequency $d\nu$

$$F_\nu = \frac{dE}{dA dt d\nu} \qquad \phi_\nu = \frac{dN_{ph}}{dA dt d\nu d\Omega} \quad , \tag{2.11}$$

where $F_\nu = h\nu\ \phi_\nu$. Integrating the eq. 2.11 over the frequency it is possible to obtain the flux:

$$F = \int F_\nu d\nu \quad . \tag{2.12}$$

In the case of a uniformly bright sphere (e.g. isotropic), the flux scales with the inverse square law of the distance (see Ribicky & Lightman, 1979 for details). In fact, considering a sphere of uniform intensity I, the flux measured in P (see Fig. 2.2) will be given by the relation

$$F = \int I \cos\theta d\Omega = 2\pi I \int_0^{\theta_R} \sin\theta \cos\theta d\theta \quad , \tag{2.13}$$

Table 2.1: Radiation field variables

Name	*Symbol*	*units*
Source radius	R	cm
Source volume	V	cm^3
Observer distance	D	cm
Specific intensity	I_ν	$erg\ cm^{-2}\ s^{-1}\ Hz^{-1}\ st^{-1}$
Photon specific density	$N(\nu)$	$ph\ cm^{-3}\ Hz^{-1}$
Photon density	n_{ph}	$ph\ cm^{-3}$
Energy density	u	$erg\ cm^{-3}$
Emissivity	j_ν	$erg\ cm^{-3}\ s^{-1}\ Hz^{-1}$
Emission coefficient	ϵ_ν	$erg\ cm^{-3}\ s^{-1}\ Hz^{-1}\ st^{-1}$
Absorption coefficient	α_ν	cm^{-1}
Optical depth	τ_ν	
Specific flux	F_ν	$erg\ cm^{-2}\ s^{-1}\ Hz^{-1}$
Photon specific flux	ϕ_ν	$ph\ cm^{-2}\ s^{-1}\ Hz^{-1}$
Flux	F	$erg\ cm^{-2}\ s^{-1}$
Specific luminosity	L_ν	$erg\ s^{-1}\ Hz^{-1}$
Luminosity	L	$erg\ s^{-1}$
Spectral Energy Distribution	S_ν	$erg\ cm^{-2}\ s^{-1}$

where $\theta_R = arcsin(R/D)$ is the angle at which the light ray is tangent to the sphere. Noting that the intensity will be equal to I if the light ray intersects the sphere and zero otherwise. It follows that

$$F = \pi I(1 - \cos^2\theta_R) = \pi I \sin^2\theta_R \quad , \tag{2.14}$$

and replacing with the definition of θ_R it can be written as

$$F = \pi I \left(\frac{R}{D}\right) \quad . \tag{2.15}$$

Note that the flux at the surface ($D = R$) is simply πI.

Integrating the specific flux over the area it is possible to define the *specific luminosity* observed at distance D from the source

$$L_\nu = \frac{dE}{dtd\nu} = \int_0^{4\pi D^2} F_\nu \, dA \quad , \tag{2.16}$$

that, under the assumption of isotropic emission, eq. 2.16 can be written as: $L_\nu(D) = 4\pi D^2 F_\nu$ and it follows that, at the source surface ($D = R$), the specific luminoity will be: $L_\nu(R) = 4\pi R^2 F_\nu$. In particular, considering the source surface and neglecting the absorption, the specific luminosity it is related to the emission coefficient as follows

$$L_\nu = 4\pi \int_V \epsilon_\nu dV \quad . \tag{2.17}$$

Finally, the integrated luminosity will be given by the relation:

$$L = \int L_\nu d\nu \tag{2.18}$$

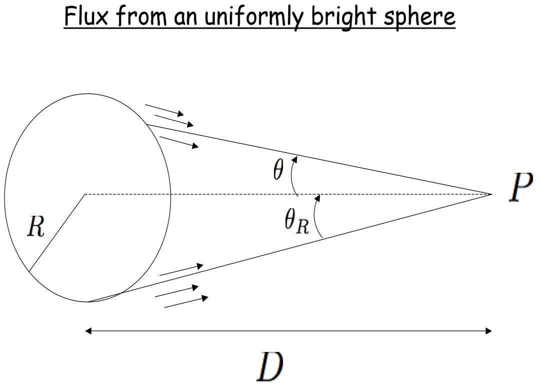

Flux from an uniformly bright sphere

Figure 2.2: Flux from an uniformly bright sphere D is the distance between the centre of the spherical source and the observer.

The link between the luminosity and the energy density can be derived, in the spherical cases, as

$$u = \frac{dE}{dV} = \frac{t_{cr}L}{V} = \frac{3L}{4\pi R^2 c} \quad , \tag{2.19}$$

and can be generally approximated with the equation:

$$u \simeq \frac{L}{4\pi R^2 c} \quad . \tag{2.20}$$

It is convenient define the quantity S_ν, the *Spectral Energy Distribution* (SED):

$$S_\nu = \nu F_\nu \quad , \tag{2.21}$$

This quantity is useful beacause it is possible to demonstrate that the SED evaluated at its peak frequency is proportional to the integrated flux (see App. A for details), so:

$$S_\nu(\nu_p) = S_p \propto F \quad , \tag{2.22}$$

where ν_p is the maximum value of S_ν. The nomenclature for the emission processes, used also in the following sections, is summarized in Tab. 2.1.

2.2 RADIATIVE TRANSFER EQUATION

The equation of radiative transfer describes the radiation travel from the source to the observer. The radiation, during its travel, loses energy by absorption, and gains energy by emission, and redistributes energy by scattering. Neglecting the scattering, the differential form of the equation for the radiative transfer is usually expressed in terms of the specific intensity as

$$\frac{dI_\nu}{dr} = j_\nu - \alpha_\nu I_\nu \quad , \tag{2.23}$$

where j_ν and α_ν are defined in the previous section. Solutions to the equation of radiative transfer form an enormous body of work (Chandrasekhar 1965, Pacholczyk 1970, Tucker & Wallace 1975, Rybicki & Lightman 1979, Band & Grindlay 1985, Shu 1991, Kataoka 1999). The differences however, are essentially due to the various expressions for the emission and absorption coefficients. If scattering is ignored, then a general one-dimensional solution in terms of the emission and absorption coefficients may be written

$$I_\nu(r) = I_\nu(0)e^{-\tau(r)} + \int_0^r 4\pi\epsilon_\nu(r)e^{-\tau(r)}\,dr \quad , \tag{2.24}$$

where $\tau_\nu(r) = \int_0^R \alpha_\nu dr$ is the optical depth along the light travel, and r is the coordinate along the light travel. The first term of eq. 2.24 correspond to the dilution of the radiation that is passing through an absorbing material described by the coefficent α_ν, while the second term is the contribution to the emission due to this material, opportunely corrected for its absorption. Under the assumption that both the emission and absorption coefficients are independent of r, the solution for the observed flux at distance D in the spherical case, will be simply

$$F_\nu = \frac{4\pi R^2}{3D^2}\frac{\epsilon_\nu}{\alpha_\nu}(1 - e^{-\alpha_\nu R}) \quad . \tag{2.25}$$

2.2.1 The solution for the homogenous spherical sources

It is possible also to derive a more complete solution of the radiative transfer equation in the spherical case as described by Band & Grindlay (1985), Shu (1991), Kataoka (1999), and reported in this section. The schematic view of the homogeneus sphere is given in Fig. 2.3.

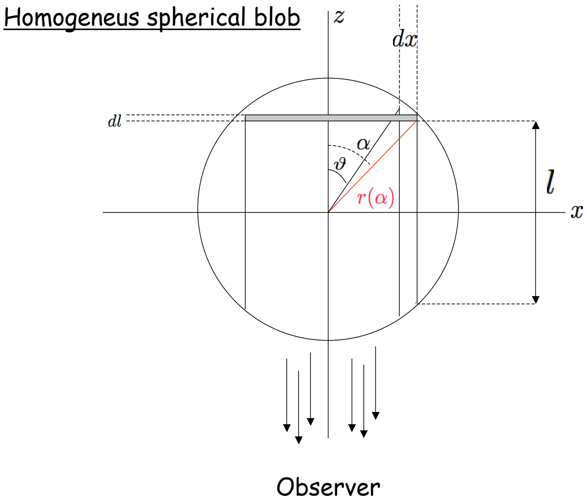

Figure 2.3: Schematic view of the cross section of a homogeneus spherical source. The shaded area in figure correspond to a ”ring”.

Considering the observed flux at distance D, neglecting the first term of eq. 2.24, this can be written

$$F_\nu = \frac{1}{4\pi D^2}\int_V 4\pi\epsilon_\nu\, e^{-\tau_\nu} dV \quad , \tag{2.26}$$

where τ_ν indicates the *optical depth*: $\tau_\nu(2R) = \int_0^{2R} \alpha_\nu dl$, with l the coordinate along the light travel (see Fig. 2.3). The spherical source now, with radius R, can be divided into the sum of cylindrical shells, whose center-lines are aligned to the z axis. Each shell has the thickness dx (see Fig. 2.3)

$$dx = R\cos\vartheta d\vartheta \quad . \tag{2.27}$$

These shells can be further cut into rings, which are aligned in parallel to xy plane. Each ring has an equal width of height dl in the z direction. First, the emission from the each ring is considered; summing up to a single cylinder next, and adding all the contribution from the cylindrical shells it is possible to calculate the emission from the sphere. The infinitesimal element dl is defined (see Fig. 2.3)

$$dl = \frac{R\sin\vartheta}{\sin^2\alpha} d\alpha \quad , \tag{2.28}$$

and the ring volume dV is given by the following relation

$$dV = 2\pi R\sin\vartheta dx dl = 2\pi R^3 \sin^2\vartheta \frac{\cos\vartheta}{\sin^2\alpha} d\vartheta d\alpha \quad , \tag{2.29}$$

The specific flux emitted by each ring will be absorbed by an exponential factor $e^{-\alpha_\nu l}$ before escaping from the entire sphere. The specific luminosity emitted from the ring in the solid angle $d\Omega$ is

$$dL_\nu = \epsilon_\nu e^{-\alpha_\nu l} d\Omega dV = \frac{1}{\sin^2\alpha} G(\vartheta) e^{-\alpha_\nu K(\alpha,\vartheta)} d\alpha d\Omega d\vartheta \quad , \tag{2.30}$$

where the functions $G(\vartheta)$ and $K(\alpha,\vartheta)$ are defined as follows

$$G(\vartheta) = 2\pi R^3 \epsilon_\nu \sin^2\vartheta \cos\vartheta e^{-\alpha_\nu R\cos\vartheta} \quad , \tag{2.31}$$

$$K(\alpha,\vartheta) = \frac{\cos\alpha}{\sin\alpha} R\sin\vartheta \quad . \tag{2.32}$$

Note that

$$\frac{d}{d\alpha}(e^{-\alpha_\nu K(\alpha,\vartheta)}) = \alpha_\nu R \frac{\sin\vartheta}{\sin^2\alpha} e^{-\alpha_\nu K(\alpha,\vartheta)} \quad . \tag{2.33}$$

Next, the emission from a single cylindrical shell is considered. Integral of dL_ν over α yields the solution

$$L_\nu = \int_0^{4\pi} d\Omega \int_0^{\frac{\pi}{2}} d\vartheta \int_\vartheta^{\pi-\vartheta} d\alpha \frac{G(\vartheta)}{\alpha_\nu R\sin\vartheta} \frac{d}{d\alpha} e^{-\alpha_\nu K(\alpha,\vartheta)} \quad . \tag{2.34}$$

Finally, summing up the contribution of each cylindrical shell and integrating over the solid angle $d\Omega$ it is possible to obtain the specific flux, observed at distance D

$$F_\nu = \frac{\pi R^2}{D^2} \frac{\epsilon_\nu}{\alpha_\nu} (1 - \frac{2}{\tau_\nu^2}[1 - e^{-\tau_\nu}(1+\tau_\nu)]) \quad . \tag{2.35}$$

In particular, negleting the absorption

$$F_\nu = \frac{V}{D^2}\epsilon_\nu = \frac{4\pi R^3}{3D^2}\epsilon_\nu \quad , \tag{2.36}$$

where V is the volume of the radiation field. Then the relation between the specific flux and the photon density per unit of solid angle will be

$$F_\nu = \frac{h\nu V}{D^2 t_{cr}} n(\nu,\Omega) \quad . \tag{2.37}$$

In general, the the number of photons per unit of volume dV, frequency $d\nu$ radiated in the solid angle $d\Omega$: $n(\nu,\Omega)$, can be derived from the specific flux with the simple relation

$$n(\nu,\Omega) \simeq \frac{1}{4\pi h\nu c} F_\nu \quad . \tag{2.38}$$

2.2.2 The photon density distribution

The photon density distribution, in the case of spherical sources, was developed by Gould (1979) and the main concepts are reported in this section. Assuming, in the following calculations, spherical symmetry, described in terms of one basic parameter: the radius R of the source, it is useful to introduce two dimensionless quantities

$$\bar{\rho} = \frac{\bar{r}}{R} \qquad \rho = \frac{r}{R} \quad , \tag{2.39}$$

designating the radial distance within the source from its centre. With the definitions in Fig. 2.4, it possible to express the lenght l as:

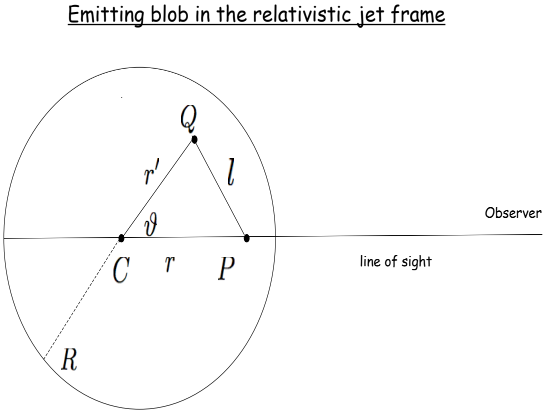

Figure 2.4: Shematic representation of a spherical emitting blob.

$$l^2 = r^2 + \bar{r}^2 - 2r\bar{r}\cos\vartheta = R^2(\bar{\rho}^2 + \rho^2 - 2\bar{\rho}\rho\cos\vartheta) \quad , \tag{2.40}$$

and the infinitesimal volume element $d\bar{V}$

$$d\bar{V} = \bar{r}^2 d\bar{r}\sin\vartheta d\vartheta d\varphi = 2\pi R^3\bar{\rho}^2\sin\vartheta d\vartheta d\bar{\rho} \quad . \tag{2.41}$$

Suppose that photons are emitted isotropically at every point within a spherical-symmetric source. Let dF_ν the differential specific flux at the distance $\bar{r}$ from the centre of the source (see eqs. 2.5 and 2.11)

$$dF_\nu = \frac{1}{4\pi l^2} j_\nu(\bar{r}) d\bar{V} \quad . \tag{2.42}$$

Then, inside or outside the source, if it is optically thin, the specific photon density, expressed by eq. 2.2, will be given by

$$n(\nu) = \frac{1}{h\nu c} F_\nu = \frac{1}{4\pi l^2 h\nu c} j_\nu(\bar{r}) d\bar{V} \quad . \tag{2.43}$$

Including eq. 2.40 and eq. 2.41 it can be written as follows

$$dn(\nu) = \frac{1}{4\pi h\nu c} j_\nu(\bar{r}) \frac{2\pi R^3 \bar{\rho}^2 \sin\vartheta}{R^2(\bar{\rho}^2 + \rho^2 - 2\rho'\rho\cos\vartheta)} d\vartheta d\bar{\rho} \quad , \tag{2.44}$$

Integrating over the angle ϑ, it is possible to obtain

$$n(\nu) = \frac{t_{cr}}{2h\nu}\frac{1}{\rho}\int_0^1 d\bar{\rho}\bar{\rho}\ln\left|\frac{\rho+\bar{\rho}}{\rho-\bar{\rho}}\right| j_\nu(\bar{\rho}) \quad . \tag{2.45}$$

Describing the inhomogeneity of the source in terms of a Taylor series (approximated to the second order) expressed as a function of central values and their derivates, the emissivity can be written

$$j_\nu(\bar{\rho}) = j_\nu(0) + \frac{1}{2} j_\nu''(0)\bar{\rho}^2 = j_\nu(0)(1 - e_p\bar{\rho}^2) \quad , \tag{2.46}$$

where odd terms do not apper for the symmetry of this spherical model. With this assumption the specific photon density becomes

$$n(\nu) = \frac{t_{cr}}{2h\nu}\frac{1}{\rho}\int_0^1 d\bar{\rho}\bar{\rho}\ln\left|\frac{\rho+\bar{\rho}}{\rho-\bar{\rho}}\right| j_\nu(0)(1 - e_p\bar{\rho}^2) \quad . \tag{2.47}$$

Finally, integrating on the dimensionless radius $\bar{\rho}$ it follows:

$$n(\nu) = \frac{t_{cr}}{h\nu} j_\nu(0)[\Phi(\rho) - e_p\Psi(\rho)] \quad , \tag{2.48}$$

where the two functions $\Phi(\rho)$ and $\Psi(\rho)$ (here called *Golud functions*, see Gould 1979) are defined by

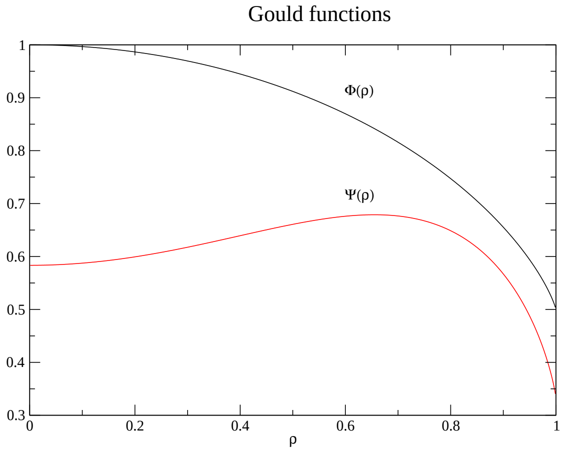

Figure 2.5: Plot of the two radial functions $\Phi(\rho)$ and $\Psi(\rho)$.

$$\begin{cases} \Phi(\rho) = \frac{1}{2\rho}\int_0^1 d\bar{\rho}\bar{\rho}\ln|\frac{\rho+\bar{\rho}}{\rho-\bar{\rho}}| = \frac{1-\rho^2}{4\rho} ln|\frac{1+\rho}{1-\rho}| + \frac{1}{2} \\ \Psi(\rho) = \frac{1}{2\rho}\int_0^1 d\bar{\rho}\bar{\rho}^3\ln|\frac{\rho+\bar{\rho}}{\rho-\bar{\rho}}| = \frac{1-\rho^4}{4\rho} ln|\frac{1+\rho}{1-\rho}| + \frac{\rho^2}{4} + \frac{1}{12} \end{cases} \tag{2.49}$$

with the following asymptotic expressions for $\rho \ll 1$

$$\begin{cases} \Phi(\rho) = 1 - \frac{\rho^2}{3} - \frac{\rho^4}{15} \\ \Psi(\rho) = \frac{1}{3} + \frac{\rho^2}{3} - \frac{\rho^4}{5} \quad , \end{cases} \tag{2.50}$$

and on $\rho \gg 1$

$$\begin{cases} \Phi(\rho) = \frac{1}{3\rho^2}(1 + \frac{1}{5\rho^2} + \frac{3}{35\rho^4}) \\ \Psi(\rho) = \frac{1}{5\rho^2}(1 + \frac{5}{21\rho^2} + \frac{1}{9\rho^4}) \quad . \end{cases} \tag{2.51}$$

In Fig. 2.5 the plot of the two functions: Φ and Ψ in terms of the dimensionless radius ρ is shown, untill $\rho = 1$ at the source surface. Even the value of e_p is negligible the source present an inhomogenity described by the function $\Phi(\rho)$. The total number of emitted photons produced per unit of time and per energy interval is proportional to the integral I of $\Phi(\rho)$ such that

$$\mathcal{I} = 4\int_0^1 d\rho\rho^2\Phi(\rho) = 1 \quad , \tag{2.52}$$

assuming that $\Phi(\rho) \simeq \Phi(0) \simeq 1$, the photon specific density must be corrected out by a factor

$$\mathcal{I}_o = 4\int_0^1 d\rho\rho^2\Phi(0) = \frac{4}{3} \quad , \tag{2.53}$$

so rescaling for $\mathcal{I}_o$ the emission coefficent will be

$$\epsilon_\nu = \frac{h\nu c}{4\pi}\frac{n(\nu)}{\mathcal{I}_o} = \frac{3}{16\pi}h\nu c n(\nu) \quad . \tag{2.54}$$

2.2.3 Light travel time effects

The observed specific flux at distance D from the center of a spherical source (see Fig. 2.6), under the assumption $D >> R$, and neglecting the absorption, is given by

$$F_\nu(D,t) = \frac{1}{4\pi D^2}\int_V j_\nu(r,\widehat{t})dV \quad , \tag{2.55}$$

where t is the observe's time, while $\widehat{t}$, in the following equation, is the emission one, linked to t by the following relation

$$\widehat{t} = t - \frac{D+x}{c} \quad , \tag{2.56}$$

and where the volume dV is

$$dV = z\, dx\, d\varphi\, dz \quad . \tag{2.57}$$

Using the light crossing time t_{cr} of the light it is possible to define the new dimensionless variables τ_o and ξ

$$t_{cr} = \frac{R}{c} \quad \rightarrow \quad \tau_o = \frac{1}{2t_{cr}}(t - \frac{D}{c}) \qquad , \qquad \xi = \frac{x}{2R} \quad ; \tag{2.58}$$

so the emisson time $\widehat{t}$, can be written in terms of these new quantities as follows

$$\widehat{t} = 2t_{cr}(\tau_o - \xi) \quad . \tag{2.59}$$

Integrating over the $d\varphi$ and dz with the following limits

$$0 \leq \varphi \leq 2\pi \qquad 0 \leq z \leq [R^2 - (R-x)^2]^{\frac{1}{2}} \quad , \tag{2.60}$$

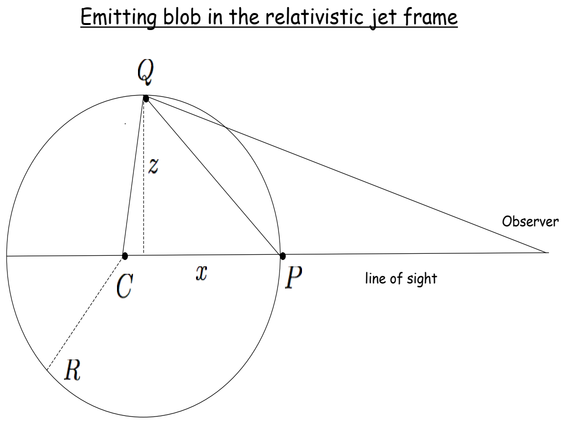

Figure 2.6: Shematic representation of a spherical emitting blob.

and over $d\xi$ one obtains the observed specific flux

$$F_\nu(D,\tau_o) = \frac{2R^3}{cD^2} j_\nu \int_{\xi_1}^{\xi_2} (\xi - \xi^2) d\xi = \frac{2R^3}{cD^2} j_\nu f(\tau_o) \quad . \tag{2.61}$$

To derive the limits of the previous integral and so the timing function $f(\tau_o)$ it is possible to consider the following relations, with $\xi_1 \leq \xi \leq \xi_2$

$$\begin{cases} \tau_o \leq 1 & \rightarrow & 0 \leq \xi \leq \tau_o & \rightarrow & f(\tau_o) & = & \frac{\tau_o^2}{2} - \frac{\tau_o^3}{3} & \tau_o \leq 1 \\ \tau_o > 1 & \rightarrow & 0 \leq \xi \leq 1 & \rightarrow & f(\tau_o) & = & \frac{1}{6} & \tau_o > 1 \end{cases} \tag{2.62}$$

obtaining the correct expression for the observed specific flux, at different time intervals.

2.3 RELATIVISTIC BEAMING IN BLAZAR JETS

2.3.1 Superluminal motion

Suppose that there is an emitting spherical blob (frame K') that moves form points P_1 to P_2 in a time interval Δt (Fig. 2.7a). Because the point P_2 is closer to the observer (frame K) than P_1, the apparent time difference between the received radiation Δt_{app} is

$$\Delta t_{app} = (1 - \beta \cos\theta) \Delta t \quad , \tag{2.63}$$

where $\beta = v/c$. The apparent velocity on the sky is

$$\beta_{app} = \frac{\Delta l}{c \Delta t_{app}} = \frac{\beta \sin\theta}{1 - \beta \cos\theta} \quad . \tag{2.64}$$

Differentiating with respect to θ and setting to zero yields the critic angle θ_c

$$\cos\theta_c = \beta \quad , \quad \sin\theta_c = \sqrt{1 - \beta^2} = \Gamma^{-1} \quad , \tag{2.65}$$

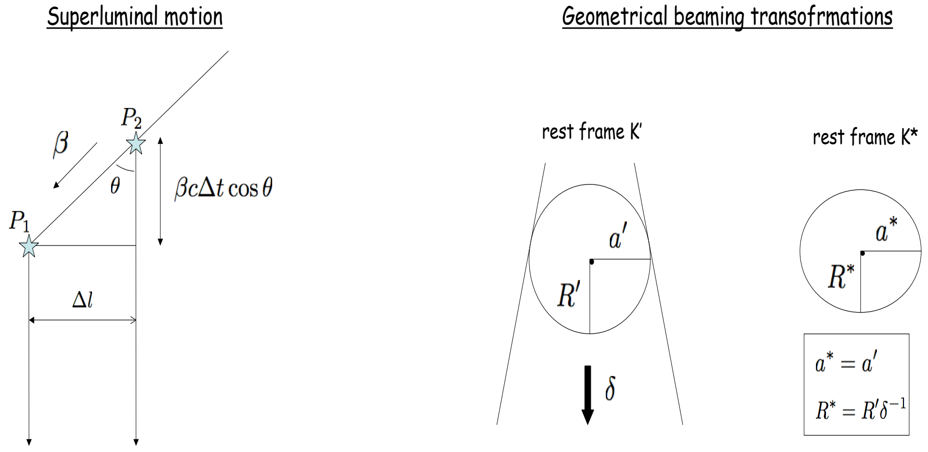

Figure 2.7: a) Schematic view of the interpretations for the superluminal motions of emitting source. b) Geometrical beaming corrections.

Corresponding to the maximum apparent velocity β_{max} is

$$\beta_{max} = \beta_{app}(\theta_c) = \Gamma\beta \quad , \tag{2.66}$$

this clearly exceedes unity when $\Gamma \gg 1$.

From the Lorentz transformations of the time intervals between the two rest frames K' and K: $\Delta t' = \Gamma(1-\beta\cos\theta)\Delta t$, where Γ is the *Lorentz factor*, it is convenient define the quantity

$$\delta = \frac{1}{\Gamma(1-\beta\cos\theta)} \quad , \tag{2.67}$$

so called *beaming factor*. Note that for $\theta \ll 1$

$$\delta \approx \frac{1}{\Gamma(1-\beta)} = \Gamma \quad . \tag{2.68}$$

2.3.2 Aberration of light and beaming effect

Lorentz transformation show how change the directions of the light propagation in the two frames K and K':

$$\sin\theta = \frac{\sin\theta'}{\Gamma(1+\beta\cos\theta')} \qquad \cos\theta = \frac{\cos\theta'+\beta}{(1+\beta\cos\theta')} \quad ; \tag{2.69}$$

these equations represent the *aberration of light*. It is instructive to set $\theta = \pi/2$, that is, a photon is emitted at right angles to v in K':

$$tg\theta = \frac{c}{\Gamma v} \quad , \quad \sin\theta = \frac{1}{\Gamma} \quad , \tag{2.70}$$

For highly relativistic speeds, $\Gamma \gg 1$, θ becomes small

$$\theta \simeq \frac{1}{\Gamma} \quad . \tag{2.71}$$

If photons are emitted isotropically in the frame K', then half of them will have $\theta' < \pi/2$ and the others $\theta' > \pi/2$. Eq. 2.70 shows that in the frame K photons are concentrated in the forward direction, with half of them lying within a cone of half-angle $1/\Gamma$. Very few photons will be emitted having $\theta' \gg 1/\Gamma$. This is called *beaming effect*.

2.3.3 Transformations of radiative quantities

Considering Fig. 2.8, all primed quantities refer to the jet frame K', while quantities marked with (*) are evaluated in the frame K^* that corresponds to an hypothetical observer at the end of the jet, but at the same redshift z of the source. Beaming effects are between the two frame K' and K^*, and cosmological effects, due to the redshift, must be considered between the frame K^* and the real observer in the frame K. Where not differently specificated, this nomenclature will be used in all the thesis.

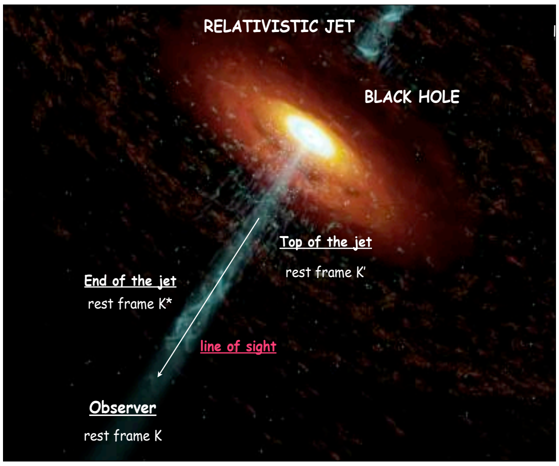

Figure 2.8: Frames considerd for beaming and for cosmological transformations: K' is the jet rest frame, K^* correspond to an hypotetical observer that is at hte end of the jet, at the same redshift of the source. Finally, the frame K is on the Earth.

Since frequencies are the inverse of times, from eq. 2.63, their beaming corrections will be derived as

$$\nu^* = \nu'\delta \qquad t = t'\frac{1}{\delta} \quad , \tag{2.72}$$

the transformations of the infinitesimal solid angle and, consequently, of the infinitesimal surface, derived from eq. 2.69 are

$$d\Omega^* = d\Omega'\frac{1}{\delta^2} \qquad dA^* = dA'\frac{1}{\delta^2} \quad , \tag{2.73}$$

while from Fig. 2.7b it follows that the volume transformation

$$dV* = dV'\frac{1}{\delta} \quad . \tag{2.74}$$

The specific flux, defined by eq. 2.11, in the jet frame is

$$F^*_\nu = \frac{dE^*}{dt^* d\nu^* dA^*} = h\nu^* \frac{dN_{ph}}{dt^* d\nu^* dA^*} \quad , \tag{2.75}$$

and inverting it is possible to obtain the number of photons dN_{ph} that is a relativistic invariant

$$dN_{ph} = \frac{1}{h\nu'} F'_{\nu'}\, dt'\, d\nu'\, dA' \quad . \tag{2.76}$$

From this invariance in the two frames: beamed and unbeamed, it is possible to write

$$dN_{ph} = \frac{1}{h\nu^*} F^*_{\nu^*}\, dt^* d\nu^* dA^* = \frac{1}{\delta^3}\frac{1}{h\nu'} F_\nu\, dt'\, d\nu'\, dA' \quad , \tag{2.77}$$

replacing each Lorentz transformations it is possible to obtain

$$\frac{1}{\delta^3}\frac{1}{h\nu'} F_\nu\, dt'\, d\nu'\, dA' = \frac{1}{h\nu'} F'_{\nu'}\, dt'\, d\nu'\, dA' \quad , \tag{2.78}$$

so the specific flux and the specific intensity corrected for the beaming effect are

$$F^*_{\nu^*} = \delta^3\, F'_{\nu'}, \qquad I^*_{\nu^*} = \delta^3\, I'_{\nu'} \quad . \tag{2.79}$$

Consequently the total flux

$$F^* = \delta^4\, F' \quad , \tag{2.80}$$

and the spectral energy distribution:

$$S'_{\nu'} = \nu' F'_{\nu'} \quad \rightarrow \quad S^*_{\nu^*} = \delta^4\, S'_{\nu'} \quad . \tag{2.81}$$

Finally, the integrated luminosity observed is:

$$L^* = L'\,\delta^2 \quad . \tag{2.82}$$

Tranformations of the radiative quantities due to the beaming factor are summarized in Tab. 2.2.

Table 2.2: Beaming transformations

Quantity	*Beaming correction*	CGS units
Frequency	$\nu^* = \nu'\delta$	Hz
Time	$t^* = t'\delta^{-1}$	s
Solid angle	$d\Omega^* = d\Omega'\delta^{-2}$	st
Surface	$dA^* = dA'\delta^{-2}$	cm^2
Specific intensity	$I^*_{\nu^*} = \delta^3\, I'_{\nu'}$	$erg\ cm^{-2}\ s^{-1}\ Hz^{-1}\ st^{-1}$
Specific flux	$F^*_{\nu^*} = \delta^3\, F'_{\nu'}$	$erg\ cm^{-2}\ s^{-1}\ Hz^{-1}$
Flux	$F^* = \delta^4\, F'$	$erg\ cm^{-2}\ s^{-1}$
Spectral energy distribution	$S^*_{\nu^*} = \delta^4\, S'_{\nu'}$	$erg\ cm^{-2}\ s^{-1}$
Specific luminosity	$L^*_{\nu^*} = L'_{\nu'}\delta$	$erg\ s^{-1}\ Hz^{-1}$
Luminosity	$L^* = L'\,\delta^2$	$erg\ s^{-1}$

2.4 LUMINOSITY DISTANCE AND COSMOLOGICAL CORRECTIONS

As discussed in Sect. 2.3.3 the cosmological corrections must eb introduced between the two frames K' and K^* to derive the real measured quantities (see Fig. 2.8) in the observer frame (see Lucchin 1990, Peebles 1993, Peterson 1997, Kembhavi & Narlikar 1999, Hogg 1999).

The *luminosity distance*, D_L, is a term used in astronomy to describe the distance at which an astronomical source would lie based on its observed luminosity, L, in the absence of any attenuation. The luminosity distance does however take into account the fact that the observed luminosity is attenuated by two factors, cosmological redshift, z, and the Doppler shift of emission, each of which contributes a $(1 + z)$ attenuation

$$L = \frac{L^*}{(1+z)^2} \quad , \tag{2.83}$$

where z is the redshift, and L^* the intrinsic luminosity of the source. The observed flux is therefore given by

$$F = \frac{L}{4\pi D^2} = \frac{L^*}{4\pi D^2 (1+z)^2} \quad , \tag{2.84}$$

where D is the *proper distance* expressed as

$$D = \frac{c}{H_0} \int_0^z \frac{dz}{\sqrt{\Omega_M (1+z)^3 + \Omega_\Lambda}} \quad , \tag{2.85}$$

The relation between the luminosity distance and the D is simply

$$D_L = (1+z)\, D \quad , \tag{2.86}$$

consequently eq. 2.84 can be written in tems of the D_L as:

$$F = \frac{L^*}{4\pi D_L^2} \quad . \tag{2.87}$$

The cosmological transformations of frequencies and time due to the redshift are

$$\nu = \nu^* \frac{1}{(1+z)} \qquad t = t^* \, (1+z) \quad , \tag{2.88}$$

whereas with respect to the beaming corrections, the solid angle and the area are invariant

$$d\Omega = d\Omega^* \qquad dA = dA^* \quad , \tag{2.89}$$

As for the beaming corrections it can be noted that the photon number is cosmological invariant,

$$dN_{ph} = \frac{1}{h\nu} F_\nu \, dt \, d\nu \, dA = \frac{(1+z)^2}{(1+z)} \frac{1}{h\nu^*} F_\nu \, dt^* d\nu^* dA^* \quad , \tag{2.90}$$

and therefore it is possible to obtain the specific and the total flux cosmological corrections

$$F_\nu = \frac{F^*_{\nu^*}}{(1+z)} \qquad F = \frac{F^*}{(1+z)^2} \quad , \tag{2.91}$$

that for the spectral energy distribution correspond to

$$S_\nu = S^*_{\nu^*} \frac{1}{(1+z)^2} \quad . \tag{2.92}$$

Consequently, the specific luminosity will be

$$L_\nu = h\nu \frac{dN_{ph}}{dt d\nu} = \frac{h\nu^*}{(1+z)} \frac{dN_{ph}}{dt^* d\nu^*} = \frac{1}{(1+z)} L^*_{\nu^*} \quad , \tag{2.93}$$

and its integral over the frequencies can be expressed as

$$L = L^* \frac{1}{(1+z)^2} \quad . \tag{2.94}$$

Tranformations of the radiative quantities due to the cosmological correction are summarized in Tab. 2.3.

Table 2.3: Cosmological transformations

Quantity	*Redshift factor*	CGS units
Frequency	$\nu = \nu^{*}(1+z)^{-1}$	Hz
Time	$t = t^{*}(1+z)$	s
Solid angle	$d\Omega = d\Omega^{*}$	st
Surface	$dA = dA^{*}$	cm^{-2}
Specific intensity	$I_{\nu} = I^{*}_{\nu^{*}}(1+z)^{-3}$	$erg\ cm^{-2}\ s^{-1}\ Hz^{-1}\ st^{-1}$
Intensity	$I = I^{*}(1+z)^{-4}$	$erg\ cm^{-2}\ s^{-1}\ st^{-1}$
Specific flux	$F_{\nu} = F^{*}_{\nu^{*}}(1+z)^{-1}$	$erg\ cm^{-2}\ s^{-1}\ Hz^{-1}$
Flux	$F = F^{*}(1+z)^{-2}$	$erg\ cm^{-2}\ s^{-1}$
Spectral energy distribution	$S_{\nu} = S^{*}_{\nu^{*}}(1+z)^{-2}$	$erg\ cm^{-2}\ s^{-1}$
Specific luminosity	$L_{\nu} = L^{*}_{\nu^{*}}(1+z)^{-1}$	$erg\ s^{-1}\ Hz^{-1}$
Luminosity	$L = L^{*}(1+z)^{-2}$	$erg\ s^{-1}$

2.5 THE γ−RAY OPACITY OF THE LOCAL UNIVERSE

High energies photons emitted from a source at redshift z can collide with softer ones to produce $e^{\pm}$ pairs. This *absorption* process occurs when the product of photon energies is at least m^2c^4. In this section, this mechanism will be considered only in the case of the Extragalactic Background Light, due to IR-optical photons emitted by external galaxies (see Kneiske 2004, Dwek & Krennick 2005). Moreover, the $e^{\pm}$ absorption may also occur in the source itself (Gould & Schreder 1967), this process and its implications on the source structure will be discussed in the Chp. 5.

The cross section for the $\gamma + \gamma \to e^{+} + e^{-}$ interaction of a γ-ray photon of energy E_{γ} emitted from a source at redshift z with a background photon of energy ϵ is given by (e.g. Jauch & Rohrlich 1955)

$$\sigma_{\gamma\gamma}(E_{\gamma},\ \epsilon,\ \mu) = \frac{3\sigma_T}{16}\,(1-\beta^2)\left[2\beta(\beta^2-2)+(3-\beta^4)\ln\left(\frac{1+\beta}{1-\beta}\right)\right] \quad , \tag{2.95}$$

where β and the ϵ_{th}, the threshold energy of the interaction are defined as

$$\beta \equiv \sqrt{1-\frac{\epsilon_{th}}{\epsilon}} \quad , \tag{2.96}$$

$$\frac{\epsilon_{th}(E_{\gamma},\ \mu) = 2(m_ec^2)^2}{E_{\gamma}(1-\mu)\quad ,} \tag{2.97}$$

with σ_T is the Thomson cross section and $\mu \equiv \cos\theta$, where θ is the angle between the momenta of photons. The γ-γ cross section for the interaction with an isotropic distribution of background photons has a peak value of $1.70{\times}10^{-25}$ cm^2 for $\beta = 0.70$, which corresponds to energies for which the product $E_{\gamma}\epsilon \approx 4(m_ec^2)^2 \approx 1$ MeV^2, or $\lambda_{\epsilon}(\mu\mathrm{m}) \approx 1.24E_{\gamma}(\mathrm{TeV})$, where λ_{ϵ} is the wavelength of the background photon.

The optical depth traversed by a photon observed at energy E_{γ} that was emitted by a source at redshift z is given by:

$$\tau_{\gamma}(E_{\gamma},\ z) = \int_0^z \left(\frac{\mathrm{d}\ell}{\mathrm{d}z}\right)\mathrm{d}z \int_{-1}^{+1} \mathrm{d}\mu\ \frac{1-\mu}{2} \int_{\epsilon^{*}_{th}}^{\infty} \mathrm{d}\epsilon^{*}\ n_{\epsilon}(\epsilon^{*},\ z)\ \sigma_{\gamma\gamma}(E^{*}_{\gamma},\ \epsilon^{*},\ \mu) \tag{2.98}$$

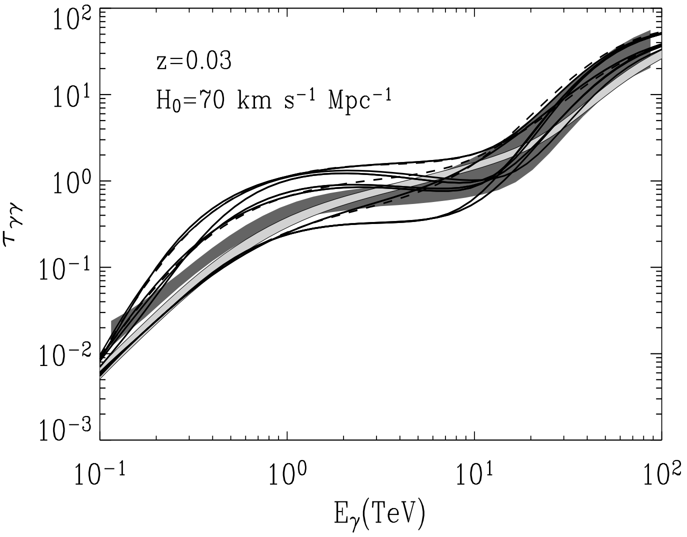

Figure 2.9: The γ-ray opacity for the eight EBL spectra. The lightly shaded area in the figure is bounded by the opacities corresponding to the two EBL spectra adopted by Konopelko et al. (2003), and the darkly shaded one by those adopted by Kneiske et al. (2004).

where $n_\epsilon(\epsilon^*,\ z^*)\mathrm{d}\epsilon^*$ is the comoving number density of EBL photons with energies between ϵ^* and ϵ^*+$\mathrm{d}\epsilon^*$ at redshift z, $\epsilon^*_{th} = \epsilon_{th}(E^*_\gamma,\ \mu)$, $E^*_\gamma = E_\gamma(1+z)$, and where $d\ell/dz$, is given by (e.g. Peacock 1999):

$$\begin{aligned} \left(\frac{\mathrm{d}\ell}{\mathrm{d}z}\right) &= c\left(\frac{\mathrm{d}t}{\mathrm{d}z}\right) = \frac{R_H}{(1+z)E(z)} && (2.99) \\ E(z) &\equiv \left\{(1+z)^2(\Omega_m z + 1) + z(2+z)[(1+z)^2\Omega_r - \Omega_\Lambda]\right\}^{1/2} \quad , \end{aligned}$$

here Ω_m and Ω_r are, respectively, the matter and radiation energy density normalized to the critical density, $\Omega_\Lambda = \Lambda/3H_0^2$ is the dimensionless cosmological constant ($\Omega_m + \Omega_r + \Omega_\Lambda = 1$ in a flat universe), $R_H \equiv c/H_0$ is the Hubble radius, c is the speed of light, and H_0 is the Hubble constant, taken here to be 70 km s^{-1} Mpc^{-1}.

The comoving number density of EBL photons of energy ϵ at redshift z is given by:

$$\begin{aligned} \epsilon^2 n_\epsilon(\epsilon,\ z) &= \left(\frac{4\pi}{c}\right)\nu I_\nu(\nu,\ z) && (2.100) \\ &= \int_z^\infty \nu^* L_\nu(\nu^*,\ z)\left|\frac{\mathrm{d}t}{\mathrm{d}z}\right|\frac{\mathrm{d}z}{1+z} \quad , \end{aligned}$$

where $\epsilon = h\nu$, $\nu^* = \nu(1+z)$, and $L_\nu(\nu^*,\ z)$ is the specific comoving luminosity density at frequency ν' and redshift z. The intrinsic photon spectrum of a source located at redshift z is given by

$$F^*_\nu = \exp[\tau_{\gamma\gamma}(E,\ z)] \times F_\nu \quad , \qquad (2.101)$$

where F_ν is the observed spectrum. Finally, the γ-ray opacity for the eight EBL spectra at redshift $z = 0.3$ is shown in Fig. 2.9.

3

Acceleration mechanisms

The main concepts on the acceleration mechanisms are described in this Chapter. The first order Fermi acceleration (Fermi 1949), originally presented to explain the simple power-law cosmic ray spectrum, is discussed to show how, in more general cases, it yields curved particle distributions in energy, very well approximated by a log-normal function. The problem discussed in this thesis concerns the non-thermal emissions form BL Lacs; in the following only the case of electrons as emitters is considered. Main reviews on these mechanisms are given by Drury 1983, Blandford & Eichler 1987 and Protheroe 1994, 1996, 1999, and this content is reported in this Section.

3.1 FIRST ORDER FERMI ACCELERATION

Fermi's original theory was modified in the 1970's (Axford 1977, Krymsky 1977, Bell 1978, Blandford & Ostriker 1978) to describe more efficient acceleration (1st order in β) taking place at supernova shocks, but is generally applicable to strong shocks in other astrophysical contexts.

Following Protheroe (1996), the velocity of the shock, V_S, depends on the velocity of the ejecta, V_P, and on the ratio of specific heats, γ_{pol}. The theory of shock hydrodynamics shows that for a strong shock, under the hypothesis of monoatomic gas, the ratio between these velocities is:

$$V_S/V_P \simeq 4/3 \quad . \tag{3.1}$$

By considering the rate at which particles cross the shock from downstream to upstream, and upstream to downstream, one finds that the relative energy gain is:

$$\frac{\langle\Delta\gamma\rangle}{\gamma} \simeq \frac{4}{3}\beta \simeq \frac{V_S}{c} \quad , \tag{3.2}$$

where $\beta = V_P/c$. Hereafter, the electron energy is expressed in terms of the electron Lorentz factor $\gamma = E/(mc^2)$. Note this is 1st order in β and is therefore more efficient than Fermi's original theory. This is because of the converging flow – whichever side of the shock you are on, if you are moving with the plasma, or the plasma on the other side of the shock is approaching you at speed V_p. To obtain the energy spectrum it is necessary to derive the probability of a particle encountering the shock once, twice, three times, etc. Looking at the diffusion of a particle as seen in the rest frame of the shock, there is clearly a net flow of the energetic particle population in the downstream direction. Following the description of Protheroe (1996), the net flow rate gives the rate at which particles are lost downstream

$$R_{\text{loss}} = n_{el}V_S/4 \quad , \tag{3.3}$$

since particles with number density n_{el} at the shock are advected downstream with speed $V_S/4$. Upstream of the shock, particles travelling at speed v at angle θ to the shock normal (as seen in the laboratory frame) approach the shock with speed $(V_S + v\cos\theta)$ as seen in the shock frame. Clearly, to cross the shock, $\cos\theta > -V_S/v$ must hold. Then, assuming particles upstream are isotropic, the rate at which they cross from upstream to downstream is

$$R_{\text{cross}} = n_{el}\frac{1}{4\pi}\int_{-V_S/v}^{1}(V_S + v\cos\theta)2\pi d(\cos\theta) = n_{el}v/4 \quad , \tag{3.4}$$

The probability of crossing the shock once and then escaping from the shock (to be lost downstream) is the ratio of these two rates

$$\mathrm{P_{es}} = R_{\mathrm{loss}}/R_{\mathrm{cross}} = V_S/v \quad , \tag{3.5}$$

where the relativistic transformations of the rates are neglected because $V_S \ll c$. The probability of returning to the shock after crossing from upstream to downstream is

$$\mathrm{P_{ret}} = 1 - \mathrm{P_{es}} \quad , \tag{3.6}$$

and so the probability of returning to the shock k times and also of crossing the shock at least k times is

$$\mathrm{P_k} = [1 - \mathrm{P_{es}}]^k \quad . \tag{3.7}$$

Hence, the energy after k shock crossings is

$$\gamma = \gamma_0 \left(1 + \frac{\Delta\gamma}{\gamma}\right)^k \quad , \tag{3.8}$$

where γ_0 is the initial energy.

To derive the distribution, it is worth to note that the its integral over the electron energy (number of particles with energy greater than γ: $N_{el}(>\gamma)$) on acceleration must be given by

$$N_{el}(>\gamma) \propto [1 - \mathrm{P_{es}}]^k \quad , \tag{3.9}$$

where

$$k = \frac{\log(\gamma/\gamma_0)}{\log(1 + \Delta\gamma/\gamma)} \quad . \tag{3.10}$$

Hence,

$$\log N_{el}(>\gamma) = A + \frac{\log(\gamma/\gamma_0)}{\log(1 + \Delta\gamma/\gamma)} \log[1 - \mathrm{Prob.(escape)}] \quad , \tag{3.11}$$

where A is a constant, and so

$$\log N_{el}(>\gamma) = B - \Gamma \log\gamma \quad , \tag{3.12}$$

where B is a constant and

$$\Gamma = -\frac{\log[1 - \mathrm{P_{es}}]}{\log(1 + \Delta\gamma/\gamma)} \approx 1 \quad . \tag{3.13}$$

Hence the distribution of electrons on acceleration will be expressed in the form:

$$n(>\gamma) \propto \gamma^{-1} \qquad \text{(integral form)} \quad , \tag{3.14}$$

$$n(\gamma)d\gamma \propto \gamma^{-2} \qquad \text{(differential form)} \quad . \tag{3.15}$$

3.2 STATISTICAL ACCELERATION: A SIMPLE APPROACH

Assume that the probabiltiy of crossing back the downstream depends on energy in a simple relation given by

$$\mathrm{P_{ret}} \propto \frac{\gamma_0}{\gamma} \quad . \tag{3.16}$$

This assumption may be interpreted, for example, considering that the confinement of a particle in the acceleration region is due the magnetic field. then when the particles increase their energy, their Larmor radius increase, and the probabiity of escape from the acceleration region is higher. So the power-law index of the particle distribution can be written as

$$\Gamma = -\frac{\log(\gamma/\gamma_0)}{\log(1 + \Delta\gamma/\gamma)} \quad . \tag{3.17}$$

Replacing eq. 3.17 in eq. 3.12 it follows that the particle distribution reads

$$\log N_{el} = -r \log^2(\gamma/\gamma_0) \quad , \tag{3.18}$$

correspondent to the *log-parabolic* model (see next Section); this contains the new parameter, relative to the simple power-law, r, the spectral curvature, which depends on the energy gain ε:

$$r = \frac{1}{\log \varepsilon} \quad , \quad \varepsilon = \frac{\gamma_k}{\gamma_{k-1}} \quad . \tag{3.19}$$

3.3 STATISTICAL ACCELERATION: DETAILED CALCULATIONS

The energy spectrum of accelerated particles by some statistical mechanism, like that occurring in a shock wave or in a strong perturbation moving down a jet, is usually written as a power law

$$N(>\gamma) = N_0(\gamma/\gamma_0)^{-s+1} \quad , \tag{3.20}$$

where $N(>\gamma)$ is the number of particles having a Lorentz factor greater than $\gamma = \frac{E}{mc^2}$ and s is the spectral index given by

$$s = -\frac{\log\ p}{\log\ \varepsilon} + 1 \quad , \tag{3.21}$$

here p is the probability that a particle undergoes an acceleration step i in which it has an energy gain equal to ε, generally assumed both independent of energy

$$\gamma_i = \varepsilon\gamma_{i-1} \qquad N_i = pN_{i-1} = N_0\, p^i \quad . \tag{3.22}$$

A *log-parabolic* (i.e. a curve having a parabolic shape in a double log plot) energy spectrum follows when the condition that p is independent of energy is released (Massaro et al. 2004, 2006)and one assumes that it can be described by a power relation as

$$p_i = g/\gamma_i^q \quad , \tag{3.23}$$

where g and q are positive constants; in particular, for $q > 0$ the probability for a particle to be accelerated is lower when its energy increases. Note that eq. 3.23 is the generalization of eq. 3.16. Such a situation can occur, for instance, when particles are confined by a magnetic field with a confinement efficiency decreasing for an increasing gyration radius. After simple calculations one finds:

$$N_i = N_0 \frac{g^i}{\prod_{j=0}^{i-1} \gamma_j^q} \quad . \tag{3.24}$$

Using eq. 3.22 one can write the product on the rhs as

$$\prod_{j=0}^{i-1} \gamma_j^q = \gamma_0^{iq} \prod_{j=1}^{i-1} \varepsilon^{jq} = \gamma_0^{iq}\, (\varepsilon^q)^{i(i-1)/2} \quad , \tag{3.25}$$

where γ_0 is the initial Lorentz factor of the particles; inserting this result into eq. 3.24 it is possible to obtain

$$N_i = N_0 \left(\frac{g}{\gamma_0^q}\right)^i (\varepsilon^q)^{-i(i-1)/2} \quad . \tag{3.26}$$

Finally, combining this equation with eq. 3.22 one can obtain the integral energy distribution of the accelerated particles, which is a *log-parabolic* law

$$N(>\gamma) = N_0(\gamma/\gamma_0)^{-[s-1+r\log(\gamma/\gamma_0)]} \quad , \tag{3.27}$$

with

$$s = -\frac{\log(g/\gamma_0)}{\log\ \varepsilon} - \frac{q-2}{2} \qquad r = \frac{q}{2\ \log\ \varepsilon} \quad . \tag{3.28}$$

The differential spectrum $n(\gamma)$ is

$$\begin{aligned} n(\gamma) &= \frac{n}{\gamma} \frac{d\ \log n}{d\ \log(\gamma/\gamma_0)} \\ &= \frac{n_0}{\gamma_0} |s - 1 + 2r \log(\gamma/\gamma_0)|\ (\gamma/\gamma_0)^{-s-r\log(\gamma/\gamma_0)} \quad . \end{aligned} \tag{3.29}$$

This is not an exact log-parabolic law, but differs from this function very little, due to a factor only logarithmically dependent on the particle energy. Numerical calculations show that the differences between this law and a truly log-parabolic one is smaller than 10% over several decades of energy. Practically, the spectral curvature corresponding to eq. 3.29 cannot be distinguished from a log-parabola in a spectral analysis. In the following it will be assumed, therefore, that the differential energy distribution of accelerated particles is well approximated by a log-parabola as results from approximating the log term with a constant which can be included in the normalisation.

It is important to note that the spectral parameters given by eq. 3.28 are in a linear relationship; in fact, after eliminating log ε one obtains

$$s = -r\left(\frac{2}{q}\log(g/\gamma_0)\right) - \frac{q-2}{2} \quad , \tag{3.30}$$

(Lemoine & Pelletier 2003, Vietri 2006)

Finally, as shown by eq. 3.8 and 3.22, in each acceleration step the energy gain of a single electron is constant, and therefore the energy increases according to a multiplicative process. This implies that the resulting energy distribution is *log − normal* instead gaussian. Thus the so called *log − parabolic* distribution corresponds exactly to the log-normal one. Note also that its integral over the entire energy range can be expressed in terms of the integral of gaussian one (Massaro et al., 2004).

3.4 STOCHASTIC ACCELERATION: THE DIFFUSION EQUATION APPROACH

According to Kardashev (1962) the general kinetic equation, for the time-dependent distribution function of the electrons with respect to the energy $n(\gamma, t)$ is

$$\frac{\partial n(\gamma, t)}{\partial t} = \lambda_1(t)\frac{\partial}{\partial\gamma}\left(\gamma^2\frac{\partial n}{\partial\gamma}\right) - \lambda_2(t)\frac{\partial}{\partial\gamma}(\gamma n) \quad . \tag{3.31}$$

The term comtaining $\lambda_1(t)$ describes the random acceleration by the Fermi mechanism, the term containing $\lambda_2(t)$ takes into account systematic acceleration by the Fermi mechanism and the variation in energy in the adiabatic expansion; while synchrotron losses of relativistic electrons and terms which take into acocunt of the "disappearance" of fast electrons that escape from the acceleration region are neglected for the time being. The first term on the rhs in the eq. 3.31 takes into account energy fluctuations.

Let the energy distribution be specified, at each instant of time t_0, by the δ-function

$$n(\gamma, 0) = n_{el}\delta(\gamma - \gamma_0), \qquad with \quad \int_0^\infty n(\gamma, 0)d\gamma = n_{el} \quad . \tag{3.32}$$

Then utilizing the techniques developed in Kaplan (1955), one finds that

$$n(\gamma, t) = \frac{1}{2\sqrt{\pi}}\frac{n_{el}}{\gamma_0}\frac{1}{\sqrt{\Lambda_1}}e^{-\frac{(\Lambda_1+\Lambda_2)^2}{4\Lambda_1}}\left(\frac{\gamma}{\gamma_0}\right)^{-\frac{1}{2}\left(1-\frac{\Lambda_2}{\Lambda_1}\right)-\frac{\ln 10}{4\Lambda_1}\log(\gamma/\gamma_0)} \quad , \tag{3.33}$$

where

$$\Lambda_1(t) = \int_0^t \lambda_1(t)dt, \qquad \Lambda_2(t) = \int_0^t \lambda_2(t)dt \quad ; \tag{3.34}$$

this obviously leads to

$$\int_0^\infty n(\gamma, t)d\gamma = n_{el} \quad , \tag{3.35}$$

the electron density remaining constant in time.

The maximum of the distribution function is found at the energy corresponding to γ_m

$$\gamma_m = \gamma_0 e^{\Lambda_2 - \Lambda_1} \quad ; \tag{3.36}$$

if $\Lambda_1 = \Lambda_2$, then $\gamma_m = \gamma_0$, i.e., it is time invariant.

Note that the value at the maximum

$$n(\gamma_m, t) = \frac{n_{el} e^{-\Lambda_2}}{2\sqrt{\pi \Lambda_2}\gamma_0} \tag{3.37}$$

falls off with time if Λ_2 0, i.e., an initially monochromatic spectrum of electrons eventually spreads out in energy, and the peak is displaced to a region of lower or higher energy, depending on the sign of $(\Lambda_2 - \Lambda_1)$. The total energy of the electrons

$$E_{tot} = V \int E n(E, t) dE = V n_{el} E_0 e^{2\Lambda_1 + \Lambda_2} \quad , \tag{3.38}$$

with $E = \gamma mc^2$ and $E_0 = \gamma_0 mc^2$, as well as the mean particle energy

$$\langle E \rangle = \frac{E_{tot}}{n_{el}} = E_0 e^{2\Lambda_1 + \Lambda_2} \quad , \tag{3.39}$$

increases or decreases depending on the sign of $(2\Lambda_1 + \Lambda_2)$. The quantity λ_2 incorporates the deceleration due to expansion, and usually it is negative. The quantity λ_1, related to random acceleration, is consistently positive and accordingly the condition of increasing γ_m orresponds to increasing the total energy; conversely, the condition of decreasing total energy corresponds to a drop in γ_m.

In general, the solution of the electron kinetic equation described by eq. 3.31 can be written in the form of a *log – parabolic* formula similar to eq. 3.27

$$n(\gamma) = n_0 \left(\frac{\gamma}{\gamma_0}\right)^{-s - r\log(\gamma/\gamma_0)} \quad , \tag{3.40}$$

where s is the power-law index, r the curvature parameter and n_0 the normalization

$$s = \frac{1}{2}\left(1 - \frac{\Lambda_2}{\Lambda_1}\right) \qquad r = \frac{\ln 10}{4\Lambda_1} \qquad n_0 = \frac{1}{2\sqrt{\pi}} \frac{n_{el}}{\gamma_0} \frac{1}{\sqrt{\Lambda_1}} e^{(\Lambda_1 + \Lambda_2)^2/4\Lambda_1} \quad . \tag{3.41}$$

with n_0 calculated in the range $[-\infty, +\infty]$.

3.5 PROPERTIES OF THE *LOG – PARABOLIC* ELECTRON DISTRIBUTION

The log-parabolic electron distribution is described by the form

$$n(\gamma) = \frac{dN_{el}}{dVd\gamma} = n_0 \left(\frac{\gamma}{\gamma_0}\right)^{-s - r\log(\gamma/\gamma_0)} \quad , \tag{3.42}$$

corresponding to a parabola in the logarithmic coordinates

$$\log\left(\frac{n(\gamma)}{n_0}\right) = -s\log\left(\frac{\gamma}{\gamma_0}\right) - r\log^2\left(\frac{\gamma}{\gamma_0}\right) \quad , \tag{3.43}$$

where the parameter s is the *power-law index* at $\gamma = \gamma_0$, the *curvature* parameter r corresponds to the second order derivate of the log-parabolic distribution

$$\left|\frac{d^2 \log n(\gamma)}{d\gamma^2}\right| = 2r \quad , \tag{3.44}$$

and n_0 is the normalization of the distribution. The case $r = 0$ corresponds to the simple power-law electron distribution

$$n(\gamma) = \frac{dN_{el}}{dVd\gamma} = n_0\left(\frac{\gamma}{\gamma_0}\right)^{-s} \quad . \tag{3.45}$$

The integral of the log-parabolic distribution can be expressed as a gaussian one, obtaining for the electron density n_{el} and for the normalization parameter n_0, respectively

Table 3.1: Log-parabolic electron variables

Quantity	*Symbol*	*units*
Distribution	$N(\gamma)$	cm^{-3}
Density	n_{el}	cm^{-3}
Spectral index	s	
Curvature	r	
Normalization of the distribution	N_0	cm^{-3}
Maximum of the distribution	γ_m	
Moments of the distribution	γ_k	
Mean Lorentz factor	$\langle\gamma\rangle$	
Mean quadratic Lorentz factor	$\langle\gamma^2\rangle$	
γ peak of $\gamma^2 N(\gamma)$	γ_p	
γ peak of $\gamma^3 N(\gamma)$	γ_{3p}	

$$n_{el} = \frac{dN_{el}}{dV} = \int_0^\infty n(\gamma)d\gamma = \sqrt{\ln 10}\, n_0\gamma_0 10^{(s-1)^2/4r}\sqrt{\frac{\pi}{r}} \quad , \tag{3.46}$$

$$n_0 = \frac{n_{el}}{\gamma_0}10^{-(s-1)^2/4r}\sqrt{\frac{r}{\pi}}\frac{1}{\sqrt{\ln 10}} \quad , \tag{3.47}$$

The maximum of this distribution corresponds to:

$$\gamma_m = \gamma_0 10^{-\frac{s}{2r}} \qquad with \qquad n\left(\gamma_m\right) = n_0 10^{\frac{s}{4r}} \quad , \tag{3.48}$$

and its moments are:

$$m_k(\gamma) = \int_0^\infty \gamma^k n(\gamma)d\gamma = n_0{\gamma_0}^{k+1}10^{(s-k-1)^2/4r}\sqrt{\frac{\pi}{r}}\sqrt{\ln 10} \quad , \tag{3.49}$$

while the moments normalized will be given by the expression

$$M_k = \frac{m_k}{m_0} \quad with \quad m_0 =_{el} \tag{3.50}$$

In particular, the peak of $\gamma^2 n(\gamma)$ and of $\gamma^3 n(\gamma)$ correspond to:

$$\gamma_p = \gamma_0 10^{(2-s)/2r} = \gamma_m 10^{1/r} \qquad \gamma_{3p} = \gamma_0 10^{(3-s)/2r} \quad , \tag{3.51}$$

respectively, and it is worth to note that:

$$\gamma_{3p}^2 = \gamma_p^2 10^{1/r} \propto \gamma_0^2 \quad . \tag{3.52}$$

The first and the second normalized momentum of the distribution are given by

$$\langle\gamma\rangle = \gamma_0 10^{(3-2s)/4r} = \gamma_m 10^{3/4r}, \tag{3.53}$$

$$\langle\gamma^2\rangle = {\gamma_0}^2 10^{(2-s)/r} = {\gamma_p}^2 \quad . \tag{3.54}$$

A practical relationship may be derived to describe the log-parabolic distribution in terms of the spectral index s, the curvature b, the normalization n_0 and the value of γ_p instead of γ_0. In fact, noting that

$$\log\left(\frac{\gamma}{\gamma_0}\right) = \log\left(\frac{\gamma}{\gamma_p}\right) + \log\left(\frac{\gamma_p}{\gamma_0}\right) \quad , \tag{3.55}$$

and replacying with eq.3.51, obtains

$$\log\left(\frac{\gamma}{\gamma_0}\right) = \log\left(\frac{\gamma}{\gamma_p}\right) + \left(\frac{2-s}{2r}\right) \quad . \tag{3.56}$$

Introducing the above equation in the eq. 3.43, it follows

$$\log\left(\frac{n}{n_0}\right) = -s\left[\log\left(\frac{\gamma}{\gamma_p}\right) + \left(\frac{2-s}{2r}\right)\right] - r\left[\log\left(\frac{\gamma}{\gamma_p}\right) + \left(\frac{2-s}{2r}\right)\right]^2 \quad . \tag{3.57}$$

Finally, the anticipated relation is given by the following equation

$$n(\gamma) = \frac{dN_{el}}{dVd\gamma} = n_0 10^{(s^2-4)/4r}\left(\frac{\gamma}{\gamma_p}\right)^{2-r\log\left(\gamma/\gamma_p\right)} \quad . \tag{3.58}$$

The simple scenario which the acceleration probability decreases with the electron energy (eq. 3.23) can be modified assuming that for energies smaller than a characteristic break value it is constant. This fact can be explained in terms of size of the acceleration region: for instance, if the acceleration probability is the same for all electrons having a Larmor radius much smaller than the typical scale size of the acceleration region. In general, this picture is described by a power-law up to γ_b combined it with a log-parabolic distribution

$$n(\gamma) = \begin{cases} n_0\left(\frac{\gamma}{\gamma_0}\right)^{-s} & \gamma_{min} \leqslant \gamma \leqslant \gamma_b \\ n_1\left(\frac{\gamma}{\gamma_0}\right)^{-s-r\log(\gamma/\gamma_0)} & \gamma_b \leqslant \gamma \leqslant \gamma_{max} \end{cases} \tag{3.59}$$

where γ_{min} and γ_{max} define the energy range and n_1 is calculated in order to have the electron distribution described by a continue function with its first derivate continue too.

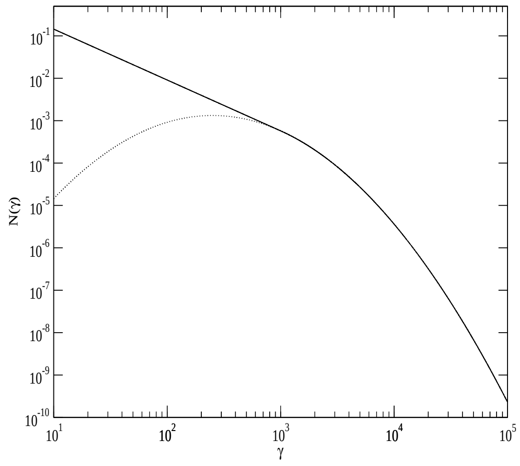

Figure 3.1: Comparison between the simple log-parabolic model decribed by the eq. 3.42 (dotted line) and the log-parabolic model combined with the power-law low energy tail given by eq. 3.60 (solid line).

To reduce the number of free parameter used to describe this spectral shape, it is convenient to assume $\gamma_b = \gamma_0$, so the relation given by eq. 3.59 becomes:

$$n(\gamma) = \begin{cases} n_0 \left(\frac{\gamma}{\gamma_0}\right)^{-s} & \gamma_{min} \leqslant \gamma \leqslant \gamma_0 \\ n_0 \left(\frac{\gamma}{\gamma_0}\right)^{-s-r\log(\gamma/\gamma_0)} & \gamma_0 \leqslant \gamma \leqslant \gamma_{max} \end{cases} \tag{3.60}$$

In this case the normalization of the $n(\gamma)$ cannot be derived analitically but it is defined as

$$n_0 = n_{el} / \int_{\gamma_{min}}^{\gamma_{max}} n(\gamma) d\gamma \quad . \tag{3.61}$$

Fig. 3.1 reports the comparison between the simple log-parabolic model (eq. 3.42) and the log-parabolic model combined with the power-law at low energies (eq. 3.60), some examples of the behaviours of these two models for different values of the spectral parameters: γ_0, s, r are show in Fig. 3.2, respectively.

3.6 OTHER ELECTRON DISTRIBUTIONS

Other electron distributions are often used in the literature to describe the spectra of emitting particles. The most common laws are: the power-law, the broken power-law and the power-law with an high energy exponential cut-off. The log-parabolic distribution, when the curvature parameter r is equal to zero, becomes a simple power-law model, and it can be written as

$$n(\gamma) = n_0 \left(\frac{\gamma}{\gamma_0}\right)^{-s} \quad . \tag{3.62}$$

A similar spectrum can be derived combining two power-laws, in the way

$$n(\gamma) = \begin{cases} n_1 \left(\frac{\gamma}{\gamma_0}\right)^{-s_1} & \gamma_{min} \leqslant \gamma \leqslant \gamma_b \\ n_2 \left(\frac{\gamma}{\gamma_0}\right)^{-s_2} & \gamma_b \leqslant \gamma \leqslant \gamma_{max} \end{cases} \tag{3.63}$$

often named broken power-law; γ_b is the break energy where the model changes the power-law index. In this model, $n_2 = n_1 \left(\frac{\gamma_b}{\gamma_0}\right)^{-s_1+s_2}$ to avoid a discontinuity in number.
Another variant is a power-law with a high energy cut-off γ_c, described by the relation

$$n(\gamma) = n_0 \left(\frac{\gamma}{\gamma_0}\right)^{-s} e^{-\gamma/\gamma_c} \quad . \tag{3.64}$$

The normalizations n_0 for these models can be evaluated with the eq. 3.61.

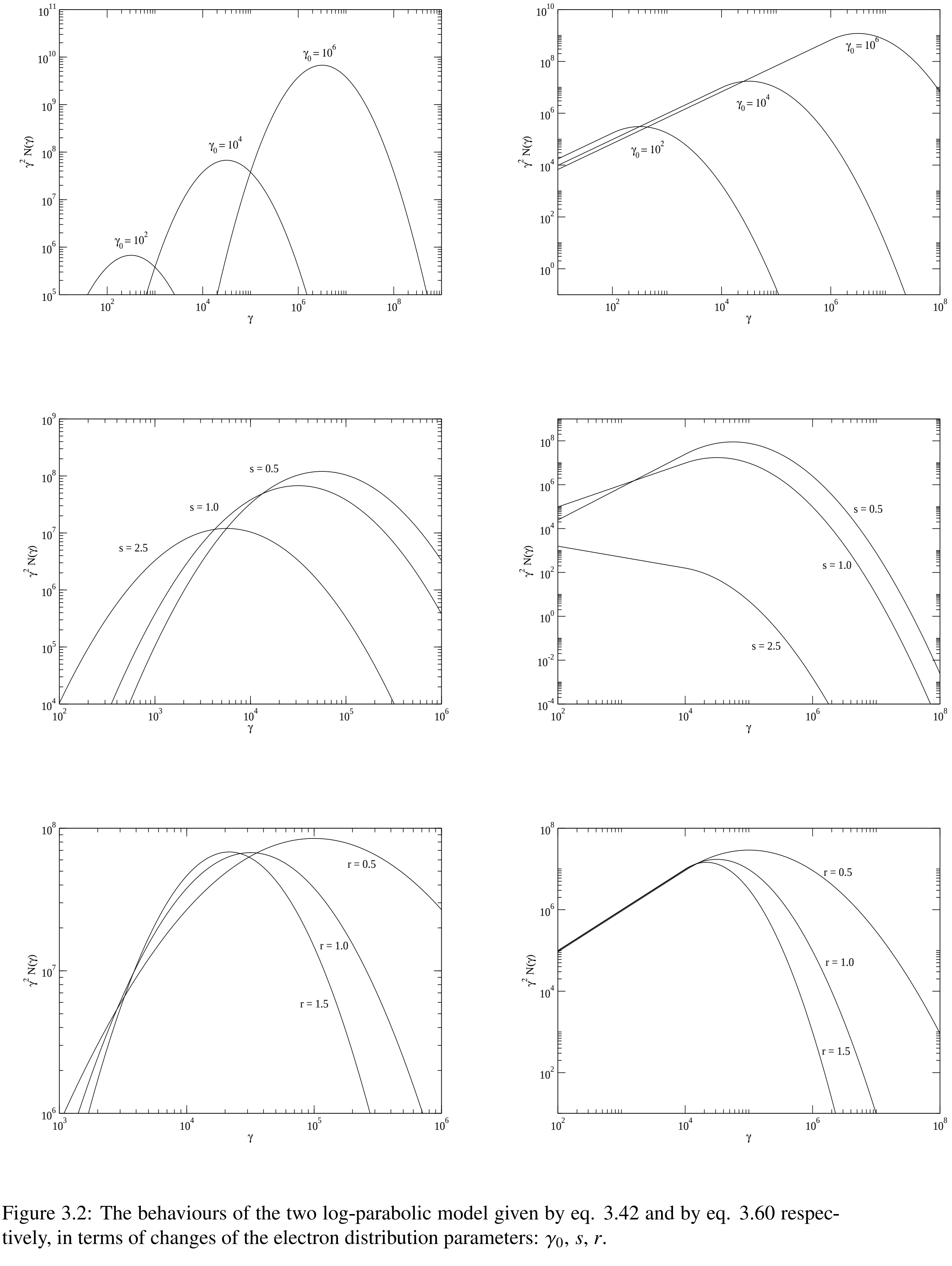

Figure 3.2: The behaviours of the two log-parabolic model given by eq. 3.42 and by eq. 3.60 respectively, in terms of changes of the electron distribution parameters: γ_0, s, r.

4

Radiative processes

4.1 SYNCHROTRON RADIATION

The synchrotron radiation is the emission process of relativistic particles centripetally accelerated in a magnetic field. Many reviews and books treat this emission mechanism in detail, as for example, Blumenthal & Gould (1970), Rybicki & Lightman (1979), Longair (2000) and references therein. Here the basic formulae used are collected; in particular, the case of homogeneus self absorbed source is considered.

4.1.1 Synchrotron emission from a single electron

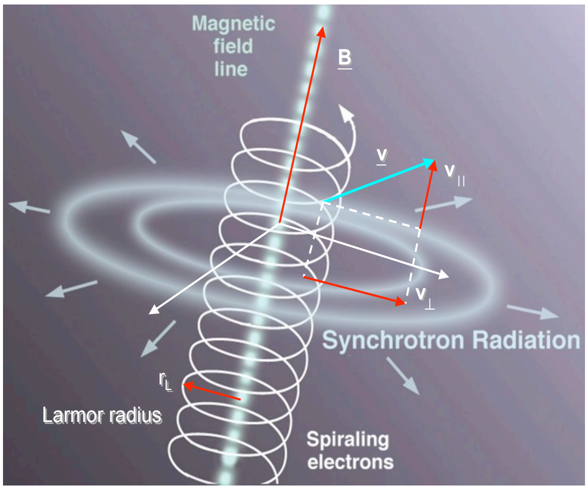

Figure 4.1: Helical motion of an electron in a uniform magnetic field

The motion of an electron of mass m and charge e in a uniform magnetic field B (see Fig. 4.1), is described by the relativistic equations:

$$\begin{cases} \frac{d}{dt}(\gamma m v) = \frac{e}{c}\underline{v} \times \underline{B} \\ \frac{d}{dt}(\gamma m c^2) = e\underline{v} \times \underline{E} \end{cases} \tag{4.1}$$

The last equation implies that, for small radiated power, γ can be considered as a constant: it follows

$$m\gamma\frac{d\underline{v}}{dt} = \frac{e}{c}\underline{v} \times \underline{B} \quad , \tag{4.2}$$

Separating the velocity components along the line of the magnetic field, $\underline{v}_\parallel = \underline{\beta}_\parallel c$, and in a plane ortogonal to the B direction, $\underline{v}_\perp = \underline{\beta}_\perp c$, and indicating with θ_p the *pitch angle* between the velocity direction and the magneic field line, eq. 4.2 can be written as

$$\frac{dv_{\|}}{dt} = 0 \qquad \frac{d\underline{v}_{\perp}}{dt} = \frac{e}{\gamma mc^2}\underline{v}_{\perp} \times \underline{B} \quad . \tag{4.3}$$

It follows that $\underline{v}_{\|}$ is constant, and since γ is constant also $\underline{v}_{\perp} = costant$. The solution to this equation is an *helical* motion of the electron around the field line. The frequency of rotation is

$$\nu_B = \frac{eB}{2\pi\gamma mc} = \frac{\nu_L}{\gamma} \qquad with \qquad \nu_L = \frac{eB}{2\pi mc} \quad , \tag{4.4}$$

where ν_L is the *Larmor frequency*. A practical formula to evaluate the Larmor frequency in CGS units is provided by

$$\nu_L = 2.80 \times 10^6 B(G) \sin\theta_p \quad \mathrm{Hz} \quad . \tag{4.5}$$

The motion in the plane perpendicular to the magnetic field line is circular with the Larmor radius

$$r_L = \frac{mc^2}{eB}\gamma\beta\sin\theta_p = 1.71 \times 10^3 \gamma B^{-1}(G)\sin\theta_p \quad \mathrm{cm} \quad , \tag{4.6}$$

where: $\beta = \frac{v}{c}$ as usual.

The acceleration is perpendicular to the velocity and, from the Larmor formula, the total emitted power is

$$P_S = \frac{dE}{dt} = \frac{2}{3} r_e^2 c\beta^2\gamma^2 B^2 \sin^2\theta_p = 2\sigma_T c\beta^2\gamma^2 \frac{B^2}{8\pi}\sin^2\theta_p \quad , \tag{4.7}$$

that in CGS units reads

$$P_S = 1.59 \times 10^{-15} \beta^2\gamma^2 B^2(G) \sin^2\theta_p \quad erg\ s^{-1} \quad . \tag{4.8}$$

For an isotropic distribution of velocities it is necessary to average this value over all *pitch angles*; then it is obtained

$$\langle P_S \rangle = \frac{4}{3}\sigma_T c\beta^2\gamma^2 u_B = 1.06 \times 10^{-15}\beta^2\gamma^2 B^2(G)\ \mathrm{erg\ s^{-1}} \quad , \tag{4.9}$$

where $u_B = \frac{B^2}{8\pi}$ is the energy density of the magnetic field.

Detailed calculations allow to write the *synchrotron spectrum* for the single ultrarelativistic electron ($\beta \sim 1$), as

$$\frac{dP}{d\nu} = c_0 \mathcal{F}_S\left(\frac{\nu}{\nu_c}\right) \quad , \tag{4.10}$$

with

$$c_0 = \frac{\sqrt{3}e^3 B\sin\theta_p}{mc^2} = 2.34 \times 10^{-22} B(G)\sin\theta_p \quad \mathrm{erg\ s^{-1}\ Hz^{-1}} \quad , \tag{4.11}$$

and

$$\nu_c = \frac{3}{2}\gamma^2\nu_L \sin\theta_p = 4.20 \times 10^6 \gamma^2 B(G)\sin\theta_p \quad \mathrm{Hz} \quad . \tag{4.12}$$

The latter is the *synchrotron critical frequency*, and the *synchrotron kernel* $\mathcal{F}_S(\frac{\nu}{\nu_c})$ (see Fig. 4.2) by the relation

$$\mathcal{F}_S\left(\frac{\nu}{\nu_c}\right) = \mathcal{F}_S(\chi) = \chi\int_{\chi}^{\infty} K_{5/3}(\eta)d\eta \quad , \tag{4.13}$$

with $K_{5/3}$ is the modified Bessel function of 5/3 order

$$K_n(\eta) = \frac{\delta\left(n+\frac{1}{2}\right)(2\eta)^n}{\sqrt{\pi}} \int_0^{\infty} \frac{\cos y}{\left(y^2+\eta^2\right)^{n+\frac{1}{2}}}\mathrm{d}y \quad . \tag{4.14}$$

The maximum of the single electron spectrum correspond to the frequency ν_m, given by the relation

$$\nu_m \simeq 0.29\nu_c = 1.22 \times 10^6 \gamma^2 B(G) \sin\theta_p \quad \mathrm{Hz} \quad . \tag{4.15}$$

Integrating eq. 4.10 over the frequencies, again the total emitted power for a single electron is

$$P_S = \int \frac{dP}{d\nu} d\nu = 2\sigma_T c \beta^2 \gamma^2 u_B \quad . \tag{4.16}$$

Finally, an useful relation to approximate the integral of the Bessel function is

$$\mathcal{F}_S(\chi) = \chi^{\frac{1}{3}} \frac{2.79\chi + 2.13}{2.15\chi^{\frac{5}{6}} e^{\chi} + 0.5\chi + 0.96} \quad . \tag{4.17}$$

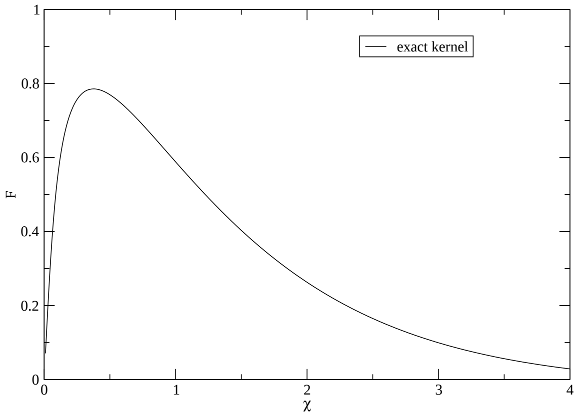

Figure 4.2: The synchrotron kernel $\mathcal{F}_S(\chi)$, solid line corespond to the exact relation given by eq. 4.13.

For each emission process, it is possible to define a *cooling time* as

$$t_{cool} = \frac{\gamma m c^2}{P} \quad , \tag{4.18}$$

and in the case of the synchrotron emission of ultrarelativistic electrons from eq. 4.18 it can be expressed by the relation

$$t_{cool,S} = 5.16 \times 10^8 \gamma^{-1} B^{-2}(G) \sin^{-2}\theta_p \ \mathrm{s} \quad , \tag{4.19}$$

in CGS units.

4.1.2 Synchrotron emission from an electron distribution

For an electron isotropic distribution $n(\gamma)$ the emission coefficient can be expressed as

$$\epsilon_\nu = \frac{1}{4\pi} \int_{\gamma_{min}}^{\gamma_{max}} n(\gamma) \frac{dP}{d\nu}(\gamma) d\gamma = \frac{c_0}{4\pi} \int_{\gamma_{min}}^{\gamma_{max}} n(\gamma) \mathcal{F}_S\left(\frac{\nu}{\nu_c(\gamma)}\right) d\gamma \quad , \tag{4.20}$$

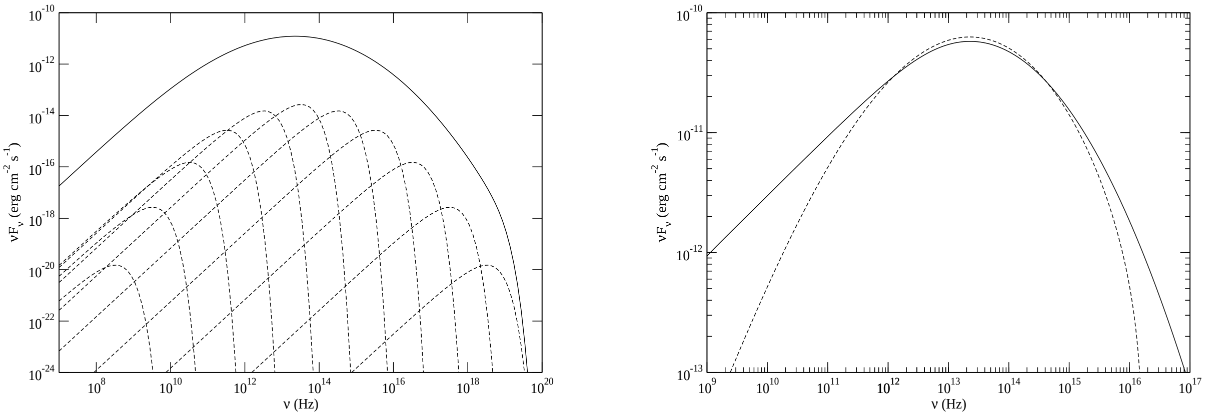

Figure 4.3: a) The superposition of the emitted spectrum $\mathcal{F}(\nu/\nu_c)$ of each electron in a log-parabolic distribution combined with a power-law energy tail at low energies. b)The synchrotron emitted spectrum by a simple log-parabolic electron distribution (dashed line) compared with the log-parabolic model with a low energy power-law tail (solid line).

and it corresponds to the superposition of the emitted spectrum $\mathcal{F}_S(\nu/\nu_c)$ of eah electron over their energy distribution (see Fig. 4.3a in the case of a log-parabolic electron population). The absorption coefficent is given by the relation

$$\alpha_\nu = \frac{c_0}{8\pi m\nu^2}\int_{\gamma_{min}}^{\gamma_{max}} \gamma^2 \frac{\partial}{\partial\gamma}(\frac{n(\gamma)}{\gamma^2})\mathcal{F}_S\left(\frac{\nu}{\nu_c(\gamma)}\right)d\gamma \quad , \tag{4.21}$$

Assuming that each electron can radiate only at the critical frequency ν_c (*synchrotron delta approximation*), the emission coefficient will be

$$j_\nu \approx \frac{4}{3}\sigma_T c\beta^2 u_B \int d\gamma\gamma^2 n(\gamma)\delta(\nu-\nu_c) \quad . \tag{4.22}$$

or in an equivalent formula

$$j_\nu \approx P_S(\gamma(\nu))\, n(\gamma(\nu)) \left|\frac{d\gamma}{d\nu}\right| \quad , \tag{4.23}$$

where P_S is defined by eq. 4.7 and

$$\gamma(\nu) = \left(\frac{2}{3\nu_L}\right)^{\frac{1}{2}} \nu^{\frac{1}{2}} \qquad with \qquad \left|\frac{d\gamma}{d\nu}\right| = \left(\frac{1}{6\nu_L}\right)^{\frac{1}{2}} \nu^{-\frac{1}{2}} \quad . \tag{4.24}$$

Under this assumption, the synchrotron photon spectrum emitted by a log-parabolic electron energy distribution (eq. 3.42) is still log-parabolic, and it can be expressed in the form

$$\phi_\nu = \phi_0 \left(\frac{\nu}{\nu_0}\right)^{-a-b\log(\nu/\nu_0)} \quad , \tag{4.25}$$

with $F_0 = h\nu\phi_0$ (see eq. 2.11) and where the relation between the spectral parameters of the electron distribution (s, r) and those of the synchrotron emitted spectrum (a, b) are

$$a = \frac{s+1}{2} \qquad b = \frac{r}{4} \quad . \tag{4.26}$$

The normalization ϕ_0 is proportional to the electron one n_0. Detailed numerical calculations (Massaro et al. 2006) show that the emitted synchrotron spectrum is well described by a log-parabolic law and, in particular, the relation between the two curvature parameters is

$$b \simeq \frac{r}{5} \quad , \tag{4.27}$$

with an accuracy of about 10%. Fig. 4.3b shows the emitted synchrotron spectrum of the two log-parabolic electron distributions, expressed by eq. 3.42 and eq. 3.60, respectively.

4.2 INVERSE COMPTON RADIATION

The *Compton scattering* is the general interaction between photons and particles, in the following it is treated the electron case, relevant in high energy astrophysical processes. For low photon energies, $h\nu \ll mc^2$, the scattering of radiation from free charges reduced to the classical case of the *Thomson scattering*, in which the incident photons are approximated as a continous electromagnetic wave. In this case, the energy of scattered photons is conserved and the scattering is called *elastic*. Quantum effects of the interaction between electrons and photons appear in two ways: first, through the kinematics of the scattering mechanism and, second, through the change of the cross section. In this case, the process is more generally indicated as *Compton scattering*. In the astrophysical framework, the so called *inverse Compton scattering* occurs when in the scattering, scattered photons gain energy from electrons.

4.2.1 Inverse Compton scattering

Fig.4.4 reports a schematic view of the the *inverse Compton scattering* in the laboratory frame K. The $\widehat{\beta}$ indicates the velocity of the electron while $\widehat{k_0}$ and $\widehat{k}$ refers to the photon momenta before and after the scattering, respectively, as indicated by the corresponding angles in the same figure. In the laboratory frame K the main quantities for the inverse Compton scattering are indicated as

$$\begin{cases} \gamma mc^2 = electron\ energy\ before\ scattering \\ E_0 = h\nu_0 = energy\ of\ the\ incident\ photon \\ E = h\nu = energy\ of\ the\ scattered\ photon \end{cases} \tag{4.28}$$

while in the electron frame K' they are denoted by

$$\begin{cases} mc^2 = electron\ energy\ before\ scattering \\ E'_0 = h\nu'_0 = energy\ of\ the\ incident\ photon \\ E' = h\nu' = energy\ of\ the\ scattered\ photon \end{cases} \tag{4.29}$$

the relations for the aberration of light can be written as follows

$$\cos\alpha' = \frac{\cos\alpha - \beta}{1 - \beta\cos\alpha} \qquad \sin\alpha' = \frac{\sin\alpha}{\gamma(1 - \beta\cos\alpha)} \quad , \tag{4.30}$$

and the Lorentz transformation for the energy

$$\begin{aligned} E'_0 &= \gamma E_0(1 - \beta\cos\alpha) \\ E &= \gamma E'(1 + \beta\cos\psi') \quad , \end{aligned} \tag{4.31}$$

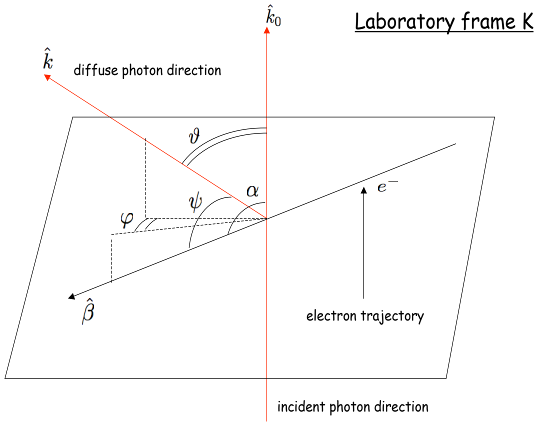

Figure 4.4: Schematic view of the Compton scattering

finally the *Compton formula* (see App. B.2.1) written in the K' frame

$$E' = \frac{E'_0}{1 - \frac{E'_0}{mc^2}(1 - \cos\vartheta')} \quad . \tag{4.32}$$

Combining all these relation it is possible to obtain the energy of the scattered photon in the laboratory frame K

$$E = \gamma^2 E_0 \frac{(1 - \beta\cos\alpha)(1 + \beta\cos\psi')}{1 + \frac{\gamma E_0}{mc^2}(1 - \beta\cos\alpha)(1 - \cos\vartheta')} \quad , \tag{4.33}$$

for the ”head-on” collisons (see App. B.2.2), corresponding to $\alpha = \alpha' = \pi \rightarrow -\cos\vartheta' = \cos\psi'$ it becomes

$$E = \gamma^2 E_0 \frac{(1 + \beta)(1 - \beta\cos\vartheta')}{1 + \frac{\gamma E_0}{mc^2}(1 + \beta)(1 - \cos\vartheta')} \quad , \tag{4.34}$$

two cases can be distinguished

$$\vartheta' = 0 \quad \rightarrow \quad E = \gamma^2 E_0 (1 - \beta^2) = E_0 \quad , \tag{4.35}$$

that occurs when there is no interaction, and

$$\vartheta' = \pi \quad \rightarrow \quad E = \gamma^2 E_0 \frac{(1 + \beta)^2}{1 + \frac{2\gamma E_0}{mc^2}(1 + \beta)} \quad , \tag{4.36}$$

that corresponds to the maximum energy transfer, that in the ultraerlativistic limit ($\beta \sim 1$) follows

$$E_{max} = \frac{4\gamma^2 E_0}{1 + \frac{4\gamma E_0}{mc^2}} \quad . \tag{4.37}$$

It is possible to distinguish the maximum energy gained in the inverse Compton scattering in the Thomson and Klein-Nishina regimes, respectively

$$\begin{cases} E_{max} \simeq 4\gamma^2 E_0 & \gamma E_0 \ll mc^2 \ \ (Thomson\ regime) \\ E_{max} \simeq \gamma mc^2 & \gamma E_0 \sim mc^2 \ \ (Klein - Nishina\ regime) \end{cases} \tag{4.38}$$

Finally, the differential cross section for the Compton scattering for unpolarized incident radiation, is

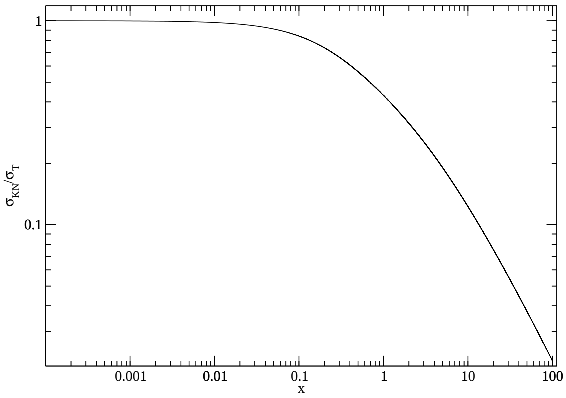

Figure 4.5: The ratio between the Klein-Nishina cross section and the Thomson one, expressed in terms of $x = \frac{E'}{E'_0}$. Note that the decreasing of the Klein-Nishina cross section at high energies ($x > 1$).

known as *Klein – Nishina formula*:

$$\frac{\mathrm{d}\sigma_{KN}}{\mathrm{d}\Omega} = \frac{r_e^2}{2}\left(\frac{E'}{E'_0}\right)^2\left[\left(\frac{E'}{E'_0}\right)^2 + \left(\frac{E'}{E'_0}\right)^2 - \sin^2\theta'\right] \quad . \tag{4.39}$$

note that for $E' \simeq E'_0$ the Klein-Nishina differential cross section reduces to the Thomson one. The main effect is to reduce the cross section from its classical value as the photon energy becomes large. Thus the Compton scattering becomes less efficent at high energies. Integrating over the solid angle yields:

$$\sigma_{KN} = \sigma_T\frac{3}{4}\left\{\frac{1+x}{x^3}\left[\frac{2x(1+x)}{1+2x} - \ln(1+2x)\right] + \frac{1}{2x}\ln(1+2x) - \frac{1+3x}{(1+2x)^2}\right\} \quad , \tag{4.40}$$

where $x = \frac{E'}{E'_0}$ and with the asymptotic expressions at low and high energies, respectively:

$$\sigma_{KN} = \begin{cases} \sigma_T\left[1 - 2x + \frac{26}{5}x^2 + \cdots\right] & x \ll 1, \\ \sigma_T\frac{3}{8}\frac{1}{x}\left[\ln(2x) + \frac{1}{2}\right] & x \gg 1. \end{cases} \tag{4.41}$$

In Fig. 4.5, the Klein-Nishina cross section σ_{KN} is plotted in terms of the Thomson cross section σ_T.

4.2.2 Inverse Compton emission from a single electron

Thomson regime

In the electron frame K' the total emitted power is given by the equation

$$P'_{em} = c\sigma_T\int E'n'(E')dE'_0 \quad , \tag{4.42}$$

where $n'(E')$ is the photon density in the source rest frame (see eq. 2.2). Observing that for the radiation field the quantity $\frac{n(E)}{E}dE$ is a Lorentz-invariant, as the emitted power $P'_{em} = P_{em}$, and in the Thomson limit ($\gamma E_0 = E'_0 \ll mc^2$) $E' = E'_0$ the emitted power can be obtained:

$$P_{em} = c\sigma_T \int (E'_0)^2 \frac{n'(E'_0)}{E_0} dE_0 \quad . \tag{4.43}$$

Combining this equation with the energy transformation it is found

$$P_{em} = c\sigma_T \gamma^2 \int (1 - \beta \cos\vartheta)^2 E_0 n(E_0) dE_0 \quad . \tag{4.44}$$

Under the assumption of an isotropic distribution of the incident photons, it is possible to derive the relation

$$\langle \cos\vartheta \rangle = 0 \qquad \langle \cos^2\vartheta \rangle = \frac{1}{3} \quad , \tag{4.45}$$

and indicating with

$$u = \int E_0 n(E_0) dE_0 \quad , \tag{4.46}$$

the energy density of the radiation field, the following relation it obtained

$$P_{em} = c\sigma_T \gamma^2 (1 + \frac{1}{3}\beta^2) u \quad . \tag{4.47}$$

Reminding that the total incident power is given by

$$P_{in} = c\sigma_T \int E_0 n(E_0) dE_0 = c\sigma_T u \quad , \tag{4.48}$$

and the total power for inverse Compton process in Thomson regime is

$$P_C = P_{em} - P_{in} = \frac{4}{3} c\sigma_T \gamma^2 \beta^2 u \quad . \tag{4.49}$$

Klein-Nishina regime

To evaluate the total power emitted for inverse Compton process in the Klein-Nishina limit it is necessary to integrate over the complete cross-section for the photon-electron scattering σ_{KN}. Indicating the emitted power as

$$P_{em} = c \int_0^{\sigma_{KN}} d\sigma \int \gamma^2 (1 - \beta\cos\vartheta)^2 E_0 n(E_0) dE_0 \quad , \tag{4.50}$$

and the incident power as

$$P_{in} = c \int_0^{\sigma_{KN}} d\sigma \int E_0 n(E_0) dE_0 \quad , \tag{4.51}$$

Approximating the total cross section σ_{KN} with a Taylor series up to the second order

$$\sigma'_{KN} \simeq \sigma'_T \left(1 - \frac{2E'_0}{mc^2}\right) \quad , \tag{4.52}$$

a practical relation to the total power can be derived as

$$P_C = P_{em} - P_{in} \simeq \frac{4}{3} c\sigma_T \gamma^2 \beta^2 u \left(1 - \frac{63}{10} \frac{\gamma}{mc^2} \frac{\langle E_0^2 \rangle}{\langle E_0 \rangle}\right) \quad . \tag{4.53}$$

4.2.3 Inverse Compton emission from an electron distribution

The emissivity can be generally described by the relation

$$j_\nu = \int\int \frac{2\pi r_e^2 c}{\gamma^2 E_0} n(\gamma) n(E_0) \mathcal{F}_C(\nu, \gamma, E_0) dE_0 d\gamma \quad , \tag{4.54}$$

where $\mathcal{F}_C(\nu, \gamma, E_0)$ is the *Compton kernel* (see Fig. 4.6)

$$\mathcal{F}_C(\nu, \gamma, E_0) = 2q \ln q + (1 + 2q)(1 - q) + \frac{1}{2} \frac{(\Gamma_e q)^2}{1 + \Gamma_e q}(1 - q) \quad , \tag{4.55}$$

and the parameters q and Γ_e are defined as

$$q = \frac{h\nu}{4E_0(1 - \frac{h\nu}{\gamma mc^2})} \qquad \textit{with} \qquad \Gamma_e = \frac{4\gamma E_0}{mc^2} \quad , \tag{4.56}$$

with the condition

$$1 \gg 1/4\gamma^2 \leq q \leq 1 \quad . \tag{4.57}$$

The expression for the emission coefficient in the Thomson regime (see App. B.2.3 for details) becomes

$$j_\nu = \int\int \frac{r_e^2 c}{2\gamma^4 E_0^2} n(\gamma) n(E_0) \mathcal{F}_\mathcal{T}(\nu, \gamma, E_0) dE_0 d\gamma \quad , \tag{4.58}$$

with $\mathcal{F}_\mathcal{T}(\nu, \gamma, E_0)$ given by

$$\mathcal{F}_\mathcal{T}(\nu, \gamma, E_0) = 2h\nu \ln \frac{h\nu}{4\gamma^2 E_0} + h\nu + 4\gamma^2 E_0 - \frac{h^2\nu^2}{2\gamma^2 E_0} \quad . \tag{4.59}$$

The function $\mathcal{F}_C$ is plotted in Fig. 4.6, for different values of Γ_e.

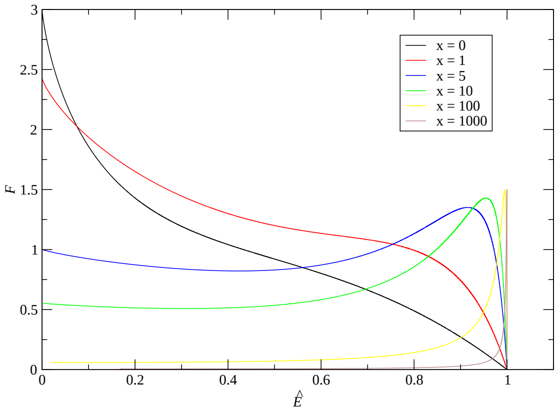

Figure 4.6: The *Compton kernel* $\mathcal{F}_C(\nu, \gamma, \mathcal{E}_r)$ for different values of Γ_e. The quantities reported on axes are defined as: $\widehat{E} = \frac{h\nu}{E_{max}}$ and $x = \frac{2\gamma E_0}{mc^2}$.

4.3 SYNCHROTRON SELF COMPTON EMISSION

The discovery of intense medium-energy gamma radiation from over 60 blazar AGNs with the EGRET instrument on the *Compton Observatory* (Hartman et al. 2001) shows that non-thermal gamma-ray production is an important dissipation mechanism of jet energy generated by black-hole accretion. Gamma rays in leptonic models of broadband blazar emission originate from synchrotron self-Compton (SSC) Reyonlds (1982), Maraschi, Ghisellini, & Celotti(1992), Bloom & Marscher(1996), Tavecchio et al.(1998) or external Compton (EC) (e.g., Melia and Königl (1989), Dermer and Schlickeiser (1993), Inoue & Takahara (1996), Böttcher, Mause, and Schlickeiser (1997), ; see Böttcher (2001)] and Sikora & Madejski (2001) for recent reviews) processes.

If the magnetic field, electron density, and particle energy decrease outward along the jet, the highest energy synchrotron emission comes primarily from the innermost region and progressively longer wavelength emission from more extended regions. The Compton component is presumably produced by scattering of ambient UV or X-ray photons by the same electrons that are radiating the synchrotron photons. Whether the seed photons are the synchrotron photons themselves (the synchrotron self-Compton, or SSC, process), or X-ray or UV light from an accretion disk, or broad-line photons from the BLR has yet to be determined (see next Section).

A significant modeling effort has been devoted to blazar studies. Where the synchrotron and SSC components are the dominant radiation processes, as appears to be the case in some X-ray bright BL Lac objects such as Mrk 421 and Mrk 501, observations of correlated X-ray/TeV loop patterns found in graphs of spectral index versus intensity are explained through combined particle acceleration, injection, and radiative loss effects Kirk, Rieger, and Mastichiadis (1998). The spectral energy distributions of BL Lac objects are successfully modelled with synchrotron and SSC components from broken power-law electron distributions with low energy cutoffs, as in Mrk 501 Mastichiadis and Kirk (1997) , Pian et al. (1998).

In the SSC scenario, the emission coefficient for the synchrotron photons is given by eq. 4.20 and for the IC emission it is expressed by eq. 4.54 , where the photon density is that of synchrotron emission $n_S(E_0)$. A secondary effect can occur in compact sources when the same population of electrons, responsible of the synchrotron and of the inverse Compton emission, radiates via second order inverse Compton scattering with first order IC photons seeds. Using log-parabolic or a similar electron distribution (see Sect. 3.5 and Sect. 3.6), the SED of a SSC source will show a double peaked structure as schematically plotted in Fig. 4.7a and Fig. 4.7b In SSC sources the relations between spectral parameters constitute a relevant tool to investigate the source physics. In the Chp. 5 about these expected relations will be discussed.

4.4 EXTERNAL COMPTON EMISSION

In External Compton models, high energy photons are produced by the inverse Compton scattering between the synchrotron emitting electrons and seed photons originating from regions outside the jet (e.g. the accretion disk, the broad line region BLR or the dust torus, see Fig. 4.8).

The intensities of the external ambient radiation fields, transformed to the comoving jet frame, are generally required to model the production spectra of blazars. External photon fields include the cosmic microwave background radiation (CMBR) field (e.g., Burbidge et al. (1974), Dermer and Schlickeiser (1993), Tavecchio et al. (2000), the accretion-disk radiation field (Dermer et al. (1992), Dermer and Schlickeiser (1993)), the accretion-disk radiation field scattered by surrounding gas and dust Sikora et al. (1994), Dermer, Sturner, and Schlickeiser (1997), infrared emissions from hot dust or a molecular torus Protheroe and Biermann (1997), Blazejowski et al. (2000), Arbeiter, Pohl, and Schlickeiser (2002), reflected synchrotron radiation Ghisellini and Madau (1996), Böttcher and Dermer (1998), broad-line region atomic line radiation Koratkar et al. (1998), Celotti et al. (2007).

Models for the spectral energy distributions of flat spectrum quasars, including external Compton

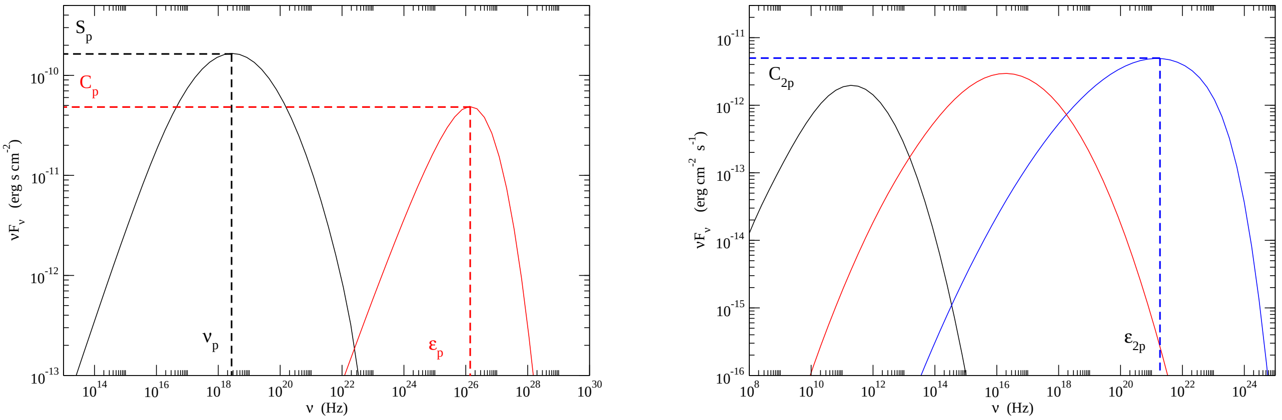

Figure 4.7: a) Schematic view of the spectral energy distribution of the two SSC components. ν_p and S_p corresponds to the peak frequency and to the height of the SED at this frequancy for the synchrotron component, while ϵ_p and C_p are relative to the Compton one and b) $\epsilon_2 p$ and $C_2 p$ to the IC second order.

components, have been presented for different spectral states by Hartman et al. (2001), Mukherjee et al.(1999), and Böttcher (1999), and in papers cited above. More recently, Sikora et al. (2001) have presented a model for blazar variability with time-dependent injection into a relativistically moving blob that contains nonthermal electrons which are subject to radiative and adiabatic losses. The scattered radiation from an external, quasi-isotropic radiation field is treated, and evolving spectral energy distributions and light curves are calculated. No direct accretion disk field is however treated, though the emission sites could be within 0.1-1 pc of the black hole, where such components can make a significant contribution Dermer and Schlickeiser(1994). In Dermer & Schlikheiser (2002) it is shown that the addition of the accretion-disk components produce light curves and correlated multifrequency behaviors that are quite distinct from the behavior calculated by Sikora et al. (2001). These distinct patterns are bright enought to be well detected with the upcoming *Gamma ray Large Area Space Telescope (GLAST)* mission (see http://glast.gsfc.nasa.gov), thus constraining the location of the shocks in gamma-ray blazars and the dominant spectral components.

The photon energy density for the external radiation field, in the case of accretion disk or in the case of the BLR, is derived in the next sections, and applying the eq. 4.54 the IC external radiation is calculated. This contibution to the total spectrum must be added to the first order synchrotron self Compton emission and, when present, also to the second order IC emission.

4.4.1 *Radiation from accretion disk*

The most relevant quantity in the accretion physics is the Eddington luminsity L_{Edd}, correspondent to the maximum luminosity emitted under the assumption of hydrostatic equilibrium, defined as

$$L_{Edd} = \frac{4\pi G M m_p c}{\sigma_T} \simeq 1.26 \times 10^{46} M_8 \text{ erg s}^{-1} \quad . \tag{4.60}$$

It is also possible to define the Eddington accretion rate $\dot{M}_{Edd}$, as that to reach the Eddington luminosity

$$\dot{M}_{Edd} = \frac{L_{Edd}}{c^2} \simeq 0.23 M_8 M_\odot \text{ yr}^{-1} \quad , \tag{4.61}$$

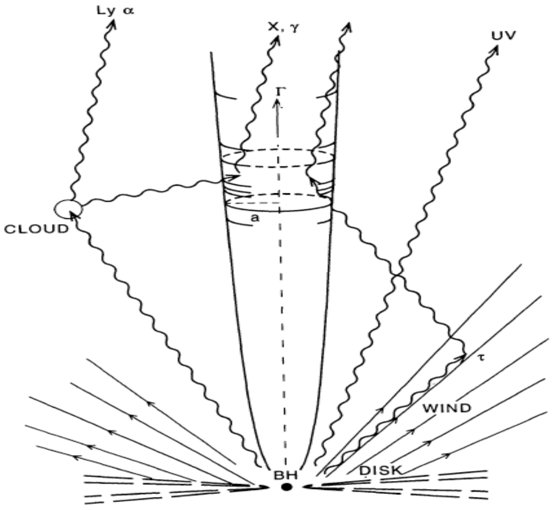

Figure 4.8: Schematic view of the external Compton emission from Sikora et al. (1994)

and the Eddington time t_{Edd}, the time in which the BH can radiate all its mass at the Eddington rate

$$t_{Edd} = \frac{M}{\dot{M}_{Edd}} \quad . \tag{4.62}$$

Reminding that the Schwarzschild radius R_s is given by the relation

$$R_s = 2\frac{GM}{c^2} \simeq 3 \times 10^{13} \frac{M}{M_\odot} \text{ cm} \quad . \tag{4.63}$$

The Eddington temperature T_{Edd}, corresponding to this radius will be given by

$$T_{Edd} = \left(\frac{L_E dd}{4\pi\sigma R_s^2} \right)^{1/4} \quad , \tag{4.64}$$

defined as the temperature of a black body with a radius equal to its R_s.

In the cool, optically-thick blackbody solution by Shakura & Sunyaev (1973), the disk emission is approximated by a surface radiating at the blackbody temperature associated with the local energy dissipation rate per unit surface area, which is derived from considerations on viscous stress of the accreting material Shapiro & Teukolsky(1983).

Considering the accretion disk as a sum of shells of different radius r, the temparature $T(r)$ of each shell is given by the relation

$$T(r) = \left[\frac{3GM\dot{M}}{8\pi r^3 \sigma} \left(1 - \sqrt{\frac{R_{int}}{r}} \right) \right]^{1/4} \quad , \tag{4.65}$$

that for $r \gg R_{int}$ becomes

$$T \simeq T_{int} \left(\frac{r}{R_{int}} \right)^{-3/4} \quad , \tag{4.66}$$

where T_{int} is the temperature at the internal radius R_{int} of the accretion disk

$$T_{int} = \left(\frac{3GM\dot{M}}{8\pi R_{int}^3 \sigma} \right)^{1/4} \quad . \tag{4.67}$$

With the relation $T(r)$, assuming that each shell emits as a black body, its specific intensity will be given by

$$I_\nu(r) = \frac{2h\nu^3}{c^2[exp(\frac{h\nu}{KT(r)}) - 1]} \quad , \tag{4.68}$$

and the correspondent specific flux measured at a distance D_{jet} from the centre of the accretion disk is

$$F_\nu = \frac{2\pi \cos(i)}{D_{jet}^2} \int_{R_{int}}^{R_{ext}} I_\nu(r) r dr \quad , \tag{4.69}$$

and from eq. 4.68 one obtains

$$F_\nu = \frac{4\pi h\nu^3 \cos(i)}{c^2 D_{jet}^2} \int_{R_{int}}^{R_{ext}} \frac{r dr}{[exp(\frac{h\nu}{KT(r)}) - 1]} \quad , \tag{4.70}$$

with the following limits:

$$F_\nu \propto \nu^2 \qquad h\nu \ll KT(R_{ext}) \tag{4.71}$$

$$F_\nu \propto \nu^{1/3} \qquad KT(R_{int}) \gg h\nu \ll KT(R_{ext}) \tag{4.72}$$

$$F_\nu \propto \nu^3 exp\left[-\frac{h\nu}{KT(r)} \right] \qquad h\nu \gg KT(R_{int}) \quad , \tag{4.73}$$

where R_{ext} is the external radius of the accretion disk. Fig. 4.9 shows the spectral energy distribution of the cool, optically-thick accretion disk for different black hole (BH) masses and several accretion rates.

4.4.2 Radiation from the Broad Line Region

In addition to the photons directly originating in the disc, a significant contribution to the soft photon field can come from disc photons reprocessed by the gas permeating the BLR (Sikora, Begelman & Rees 1994, see also Celotti et al. 2007 for a recent review). It is possible to assume that the photon energy distribution follows a blackbody spectrum peaking at the frequency of the Lyman-α hydrogen line, $\nu_{L\alpha} = 2.47 \times 10^{15}$ Hz. This matches the shape of this external radiation component in a restricted energy range around the Lyman–α line, as seen in the comoving frame.

In fact for BLR clouds distributed in two semi–spherical shells (one for each side of the accretion disc), any monochromatic line is seen, in the comoving frame, within a narrow cone of semi-aperture angle $1/\Gamma$ along the jet velocity direction. Accordingly, such photons are blueshifted by a factor ranging from Γ (photons from the border of the cone) to 2Γ (photons head–on). In this (admittedly narrow) frequency range a monochromatic line transforms into a spectrum $\propto {\nu_{\rm obs}}^2$. Although the Lyman–$\alpha$ line represents the most important contribution of the BLR seed photons, the entire spectrum produced by the BLR is more complex. Here, the blackbody assumption is assumed to represent well the more complex SED from the BLR.

Thus, an equivalent temperature of the BLR spectrum is described as:

$$T_{\rm BLR} = \frac{h\nu_{L\alpha}}{2.8k} \sim 4.23 \times 10^4 \,{\rm K} \quad . \tag{4.74}$$

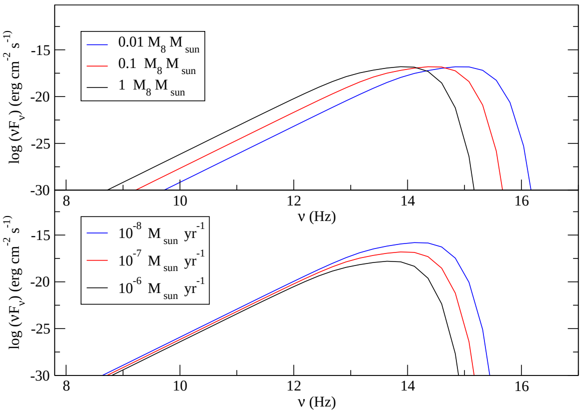

Figure 4.9: The SED of an accretion disk, optically thick, for different values of the Black Hole Mass (upper pannel) and the accretion rate (lower pannel).

In the shell comoving frame this temperature is seen blueshifted by a factor $\sim \Gamma$, while, after scattering, the transformation in the observer frame introduces an additional blueshift, corresponding to a factor δ: therefore $T_{\rm BLR,obs} \sim \Gamma\delta T_{\rm BLR}$.

The bolometric luminosity resulting from the scattering of BLR photons, at a given distance D_{BLR}, is given by

$$L_{\rm BLR,obs}(D_{BLR}) = \sigma_{\rm T} c N u_{\rm BLR} \Gamma^2 \delta^4 \quad , \tag{4.75}$$

where $u_{\rm BLR}$ is the energy density of BLR photons, which is considered constant within the typical distance of the BLR, defined by a radius $R_{\rm BLR}$. For a luminosity $L_{\rm BLR}$ of broad line photons, the observed spectrum will have a blackbody shape, corresponding to the temperature $T_{\rm BLR,obs}$

$$\begin{aligned} L_{\rm BLR,obs}(D_{BLR}, \nu) &= \frac{2h}{c^2} \frac{\nu^3}{\exp\left(h\nu/kT_{\rm BLR,obs}\right) - 1} \cdot \\ & \quad \frac{\sigma_{\rm T} N L_{\rm BLR}}{4\sigma_{\rm SB} R^2_{\rm BLR} T^4_{\rm BLR} \Gamma^2} \quad , \end{aligned} \tag{4.76}$$

which corresponds to the integrated luminosity given by eq. 4.75.

5

Physics of SSC and EC sources

In this chapter, the physical processes that occur in the SSC and EC sources are developed with the aim of obtaining some diagnositc tools for the understanding of the physical structure of sources. In particular, the relations between electron spectral parameters and the observed quantities in the case of log-parabolic SEDs will be discussed. Many results have been obtained by means of numerical calculations. The analysis and the results presented in this chapter are substantially new and still unpublished. A detailed description of the numerical codes used in these calculations is given in App. C.1.

5.1 RELATING THE SYNCHROTRON SPECTRAL PARAMETERS

The synchrotron emission predicts a correlation between the observed SED peak frequency ν_p and its maximum value $S_p = S_\nu(\nu_p)$ which are related to the source parameters as the magnetic field, the size of the emitting region, the number of electrons, their energy and the beaming factor. Studying this correlation it is possible to evaluate what are the main parameters that dominate the spectral evolution of the source. In this section, calculations to derive the expected relation between observable quantities and the physical parameters are described. The nomenclature is defined in Tab. 5.1 and Tab. 5.2.

Table 5.1: Electron and source spectral parameters

Quantity	*Symbol*	*units*
Magnetic field	B'	G
Electron number	N'_{el}	
Electron density	n'_{el}	cm^{-3}
Source radius	R'	cm
Beaming factor	δ	
Redshift	z	

In the following only a scaling analysis will be performed. Consider the source rest frame K' in which the synchrotron SED peak frequency for the log-parabolic spectrum is given by the relation (see App. A.3)

$$\nu'_p = \nu'_0 10^{\frac{2-a}{2b}} \quad , \tag{5.1}$$

where the reference frequency ν'_0 is simply related to the Larmor frequency ν'_L and to the reference electron energy γ'_0 by eq. 4.4

$$\nu'_0 \propto \gamma'^2_0 \nu'_L \quad , \tag{5.2}$$

Using it in eq. 5.1 it is possible to obtain the SED peak frequency of the synchrotron emission in terms of the electron spectral parameters

$$\nu'_p \propto \gamma'^2_0 \nu'_L 10^{\frac{2-a}{2b}} \quad , \tag{5.3}$$

and assuming the δ approximation, the spectral curvature b and the photon index a are related to those of the electron ditribution by eq. 4.26, respectively. It follows that

$$\nu'_p \propto \gamma'^2_0 \nu'_L 10^{\frac{3-s}{2r}} \propto \gamma'^2_{3p} \propto \gamma'^2_p 10^{\frac{1}{r}} \quad . \tag{5.4}$$

The frequency peak of the synchrotron spectral energy distribution ν'_p is directly proportional to

$$\nu'_p \propto \gamma'^2_p B' \quad . \tag{5.5}$$

Under the assumption that there are no relevant variations of the spectral curvature r in the electron distribution, and introducing the beaming factor and the redshift on using eq 2.72 and eq. 2.88, the observed ν_p is related to the physical parameters as follows

$$\nu_p \propto \gamma'^2_p B' \frac{\delta}{(1+z)} \quad . \tag{5.6}$$

Concerning the value of the spectral energy distribution evaluated at its peak frequency, it is directly proportional to the total emitted flux (see App. A.3), that in the synchrotron emission is equal to

Table 5.2: Synchrotron spectral parameters

Quantity	*Symbol*	units
Larmor frequency	ν'_L	Hz
Synchrotron critical frequency	ν'_c	Hz
Single electron luminosity	P'_S	erg s^{-1}
Total flux	F'_S	erg s^{-1} cm^{-2}
SED peak frequency	ν_p	Hz
SED peak height at ν_p	S_p	erg s^{-1} cm^{-2}
Energy density	u'_S	erg cm^{-3}
Photon density	n'_S	ph cm^{-3}

$$S'_p \propto F'_S = N_{el} P'_S \propto n'_{el} R'^3 \gamma'^2_p B'^2 \quad , \tag{5.7}$$

and introducing the beaming factor and the redshift corrections, given by eq. 2.81 and eq. 2.92, it follows

$$S_p \propto n'_{el} R'^3 \gamma'^2_p B'^2 \frac{\delta^4}{(1+z)^2} \quad . \tag{5.8}$$

The dependence of S_p on ν_p (see Tab. 5.2) can be written in a general form of a power-law as

$$S_p \propto \nu_p^\alpha \quad . \tag{5.9}$$

In fact, the synchrotron SED is expected to scale as $S_p \propto N_{el}\ \gamma'^2_p\ B'^2\ \delta^4$ at the frequency $\nu_p \propto \gamma'^2 B'\ \delta$, in terms of total emitter number N_{el}, the magnetic field B', the typical electron energy $\gamma'_p mc^2$, and the beaming factor δ, Thus $\alpha = 1$ applies when the spectral changes are dominated by variations of the electron average energy; $\alpha = 2$ as for changes of the magnetic field; $\alpha = 4$ if changes in the beaming factor dominate; formally, $\alpha = \infty$, applies for changes only in the number of emitting electrons (Tramacere et al. 2007). These cases are reported in Fig. 5.1.

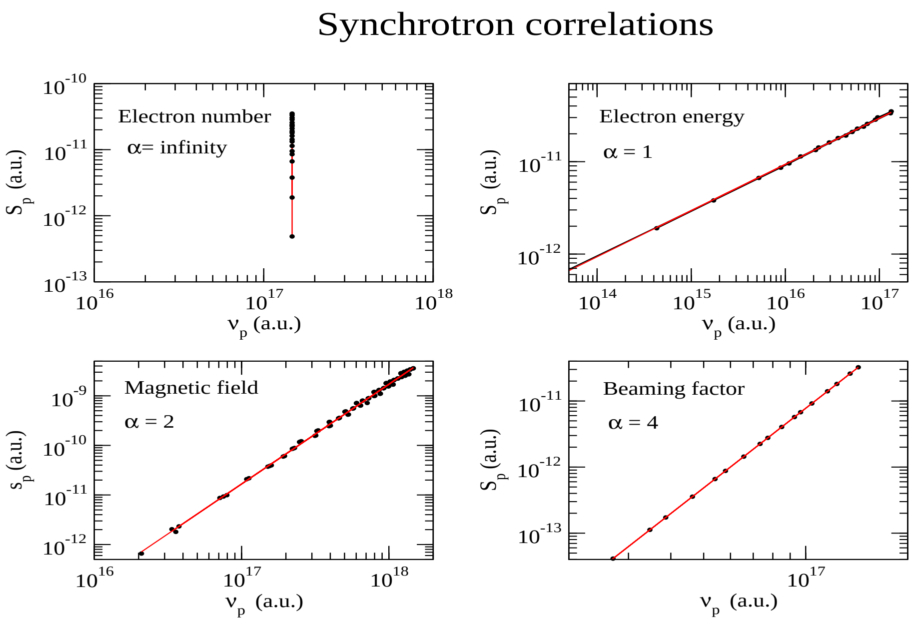

Figure 5.1: Expected synchrotron correlations described by the $S_p \propto \nu_p^\alpha$ relation, expressed in terms of the changes of each synchrotron variable.

5.1.1 Signatures of the statistical acceleration in the synchrotron relations

Under the assumption of a log-parabolic electron distribution, the synchrotron flux (eq. 2.11 and eq. 4.25) can be written

$$F_\nu = F_0 \left(\frac{\nu}{\nu_0}\right)^{-a+1-b\log(\nu/\nu_0)} \quad , \tag{5.10}$$

where the SED peak frequency is given by

$$\nu_p = \nu_0 10^{-(a-2)/2b} \qquad \log\left(\frac{\nu_p}{\nu_0}\right) = -\frac{a-2}{2b} \quad , \tag{5.11}$$

and the Spectral Energy Distribution corresponds to

$$S_\nu = \nu F_\nu = S_p \left(\frac{\nu}{\nu_p}\right)^{-b\log(\nu/\nu_p)} \quad . \tag{5.12}$$

So, evaluating S_ν at the frequency ν_0

$$S_0 = S_\nu(\nu_0) = S_p \left(\frac{\nu_p}{\nu_0}\right)^{-b\log(\nu_p/\nu_0)} \quad , \tag{5.13}$$

one obtains

$$\log\left(\frac{S_p}{S_0}\right) = b\log^2\left(\frac{\nu_p}{\nu_0}\right) \quad , \tag{5.14}$$

and it is possible to derive a practical relation for the maximum of the SED

$$S_p = S_0 10^{(a-2)^2/4b} \quad . \tag{5.15}$$

Replacing the previous relation with eq. 5.11

$$S_p \propto \nu_p^{(2-a)/2} \qquad with \qquad a = \frac{s+1}{2} \quad , \tag{5.16}$$

one concludes

$$S_p \propto \nu_p^{(3-s/)4} \quad . \tag{5.17}$$

So, in this case, the dependence of S_p on ν_p has the power-law index

$$\alpha = \frac{3-s}{4} \quad . \tag{5.18}$$

Some example of the relation, expressed by eq. 5.17, are reported in Fig. 5.2 for several values of s and for r varying in the range 0.5-2.5.

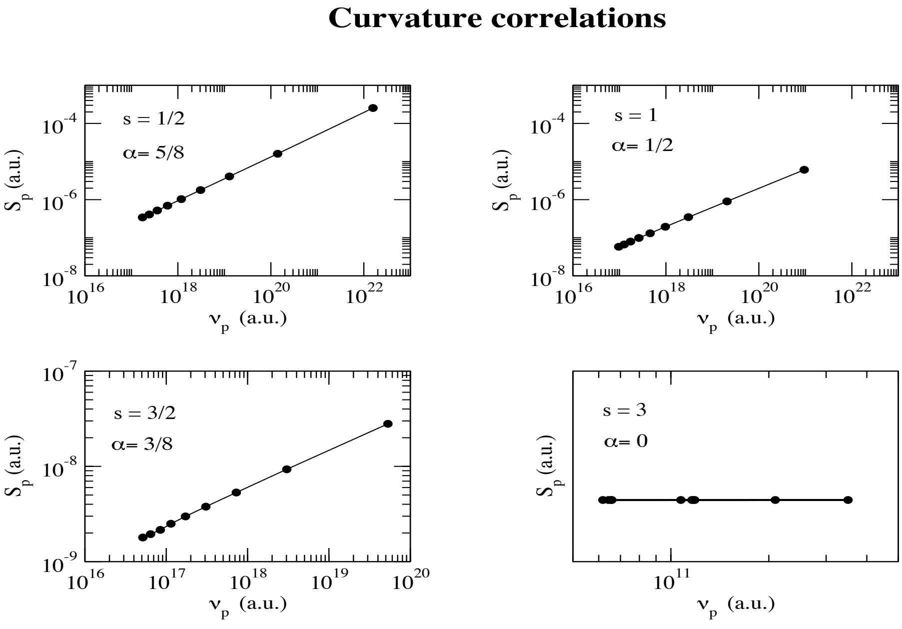

Figure 5.2: The relations given by the log-parabolic expression of the synchrotron emitted spectrum. Each plot represents the relation evaluated changing the curvature r for a fixed electron index s.

5.1.2 Energy constant states

The total electron energy, defined by eq. 3.38, can be approximated in the form $E_{tot} \simeq N_{el}\langle\gamma\rangle mc^2$, where $\langle\gamma\rangle$ is the average Lorentz factor. Assuming that in the jet there is a constant energy available that can be transferred to the high energy electrons, thus $E_{tot} \simeq costant$, then the electron number will scale as $N_{el} \propto \langle\gamma\rangle$. Using this result into eq. 5.8 it is possible to derive the synchrotron scaling relations, given by eq. 5.6 and eq. 5.8, in the form

$$\nu_p \propto \gamma_p'^2 B' \frac{\delta}{(1+z)} \qquad and \qquad S_p \propto \gamma_p' B'^2 \frac{\delta^4}{(1+z)^2} \quad , \tag{5.19}$$

that correspond to an α index equal to $1/2$ in the eq. 5.9.

5.2 RELATING INVERSE COMPTON SPECTRAL PARAMETERS

As for the synchrotron emission it is possible to derive the expected correlations in the IC radiation between the spectral parameters: ϵ_p and C_p (see Tab. 5.3), especially in the case of SSC models. In particular, both the case of the Thomson and the Klein-Nishina regimes are investigated in the following subsections. The nomenclature used in this section is reported in Tab. 5.3. The schematic view of the observed quantities is shown in Fig. 4.7a for the 1^{st} order IC and in Fig. 4.7b for the 2^{nd} order IC, respectively.

Table 5.3: Inverse Compton variables

Quantity	*Symbol*	*units*
Collision frequency	ν'_{coll}	s^{-1}
Mean free path	λ'_e	cm
Klein-Nishina cross-section	σ'_{KN}	cm^2
First order single electron luminosity	P'_C	erg s^{-1}
Second order single electron luminosity	P'_{2C}	erg s^{-1}
First order total flux	F'_C	erg s^{-1} cm^{-2}
Second order total flux	F'_{2C}	erg s^{-1} cm^{-2}
First order SED peak frequency	ϵ_p	Hz
First order SED peak height at ϵ_p	C_p	erg s^{-1} cm^{-2}
Second order SED peak frequency	ϵ_{2p}	Hz
Second order SED peak height at ϵ_{2p}	C_{2p}	erg s^{-1} cm^{-2}
First order energy density	u'_C	erg cm^{-3}
First order photon density	n'_C	erg cm^{-3}

5.2.1 1^{st} order IC in the Thomson regime

In the Thomson regime, for a SSC scenario, the peak frequency of the inverse Compton radiation ϵ'_p is directly proportional to the SED peak frequency of the synchrotron emission. Reminding that the maximun energy transferred is given by eq. 4.38, it is possible to obtain the following relation for the intrinsic IC SED peak frequency

$$\epsilon'_p \propto \gamma_p'^2 \nu'_p \propto \gamma_p'^4 B' \quad , \tag{5.20}$$

and applying the beaming and the cosmological factors (see eq. 2.72 and eq. 2.88)

$$\epsilon_p \propto \gamma_p'^4 B' \frac{\delta}{(1+z)} \quad . \tag{5.21}$$

To derive the relation between the IC SED maximumC'_p and the physical parameters of the source, noting that is proportional to the total emitted flux $F'_C = N_{el} P'_C$ (see App. A.3 for details) and then follows

$$C'_p \propto F'_C = N_{el} P'_C \propto n'_{el} R'^3 \gamma'^2_p u'_S \quad , \tag{5.22}$$

where the energy density of the synchrotron photonscan be derived by the general relation (see eq. 2.19)

$$u'_S \propto \frac{L'_S}{R'^3} t'_{cr} \propto \frac{L'_S}{R'^2} \quad . \tag{5.23}$$

and, from eq. 4.8 one has

$$u'_S \propto \frac{1}{R'^2} N_{el} \gamma'^2_p B'^2 \quad , \tag{5.24}$$

and from the previous equation, it is possible to derive the relation

$$C'_p \propto N_{el} n'_{el} \gamma'^4_p B'^2 R' \propto n'^2_{el} R'^4 \gamma'^4_p B'^2 \quad , \tag{5.25}$$

that, introducing the beaming and the redshift factors (see eq. 2.81 and eq. 2.92), yields

$$C_p \propto n'^2_{el} R'^4 \gamma'^4_p B'^2 \frac{\delta^4}{(1+z)^2} \quad . \tag{5.26}$$

5.2.2 1^{st} *order IC in the Klein-Nishina regime*

In the Klein-Nishina regime, the maximun energy gain in a simple scattering is given by eq. 4.38 and the SED frequancy peak of the IC emission ϵ'_p is so proportional to

$$\epsilon'_p = \gamma'_p mc^2 \quad , \tag{5.27}$$

and, applying the beaming and the redshift factors (see eq. 2.72 and eq. 2.88), it yields

$$\epsilon_p \propto \gamma'_p \frac{\delta}{(1+z)} \tag{5.28}$$

As in the Thomson regime, the relation corresponding to the IC SED maximum C'_p can be obtained using the IC power, in the Klein-Nishina limit, given by the equation

$$P'_C \propto \frac{\gamma' mc^2}{\lambda'_e} \quad , \tag{5.29}$$

where λ'_e is the *mean free path* of electrons, that can be written as

$$\lambda'_e = \frac{1}{c n'_S \sigma'_{KN}} \quad , \tag{5.30}$$

where the n'_S is the photon density of the synchrotron radiation field and σ'_{KN} the Klein-Nishina cross section, that is proportional to γ'^{-1}. After the substitution one finds

$$P'_C \propto \gamma' n'_S \sigma'_{KN} \propto n'_S \quad . \tag{5.31}$$

The IC SED maximum C'_p will be given by

$$C'_p = N_{el} P'_C \propto n'_{el}\, n'_S \quad , \tag{5.32}$$

where the synchrotron photon density is related to the energy density by

$$n'_S \propto \frac{1}{\nu'_p}\, u'_S \quad , \tag{5.33}$$

with u'_S given by the eq. 5.24. Thus the photon density can be written as proportional to

$$n'_S \propto \frac{1}{R'^2} N_{el} B' \propto n'_{el} R' B' \quad . \tag{5.34}$$

Finally, the value of C'_p can be expressed in the form

$$C'_p = n'^2_{el} R'^4 B' \quad , \tag{5.35}$$

and for the beaming-redshift corrected quantity (see eq. 2.81 and eq. 2.92)

$$C_p = n'^2_{el} R'^4 B' \frac{\delta^4}{(1+z)^2} \quad . \tag{5.36}$$

5.2.3 2^{nd} order IC in the Thomson regime

Under the assumption, that both first and second order IC emission are in the Thomson regime, the SED peak frequency ϵ'_{2p} of the 2^{nd} order inverse Compton is related to the physical quantities as follows

$$\epsilon'_{2p} \propto \gamma'^2_p \epsilon'_p \propto \gamma'^4_p \nu'_p \propto \gamma'^6_p B' \quad , \tag{5.37}$$

and, applying the beaming and the cosmological factor (see eq. 2.72 and eq. 2.88)

$$\epsilon_{2p} \propto \gamma'^6_p B' \frac{\delta}{(1+z)} \quad . \tag{5.38}$$

The height of the second order IC SED C'_{2p}, at the peak frequency, is related to the first order inverse Compton energy density u_C by

$$C'_{2p} \propto F'_{2C} = N_{el} P'_{2C} \propto n'_{el} R'^3 \gamma'^2_p u'_C \quad , \tag{5.39}$$

where u'_C, in the SSC scenario, turns out to be proportional to the synchrotron energy density u'_S

$$u'_C \propto \frac{L'_C}{R'^3} t_{cr} \propto \frac{L'_C}{R'^2} \propto \frac{\gamma'^2_p u'_S}{R'^2} \quad . \tag{5.40}$$

Using eq. 5.24 one finds that

$$u'_C \propto \frac{1}{R'^2} N_{el} \gamma'^4_p B'^2 \quad , \tag{5.41}$$

and replacing thus quantity in eq. 5.39, the C'_{2p} can be obtained

$$C'_{2p} \propto N_{el} n'_{el} \gamma'^6_p B'^2 R' \propto n'^2_{el} R'^4 \gamma'^6_p B'^2 \quad . \tag{5.42}$$

Finally, it follows, from eq. 2.81 and eq. 2.92,

$$C_{2p} \propto n'^2_{el} R'^4 \gamma'^6_p B'^2 \frac{\delta^4}{(1+z)^2} \quad . \tag{5.43}$$

5.2.4 2^{nd} order IC in the Klein-Nishina regime

Assuming that the first order IC emission is in the Thomson limit, the expected relation between spectral parameters and the peak frequency ϵ'_{2p} and the height od the SED C'_{2p} of second order IC radiation in Klein-Nishina regime can be derived. For the second order Compton peak frequency ϵ'_{2p} follows

$$\epsilon'_{2p} \propto \gamma'_p mc^2 \quad , \tag{5.44}$$

Table 5.4: Summary of Synchrotron Self Compton correlations

Synchrotron		
SED peak frequency	$\nu_p \propto \gamma_p'^2 B' \frac{\delta}{(1+z)}$	
SED peak height	$S_p \propto n'_{el} R'^3 \gamma_p'^2 B'^2 \frac{\delta^4}{(1+z)^2}$	$\propto N_{el} \gamma_p'^2 B'^2 \frac{\delta^4}{(1+z)^2}$
1^{st} order IC (Thomson regime)		
SED peak frequency	$\epsilon_p \propto \gamma_p'^4 B' \frac{\delta}{(1+z)}$	
SED peak height	$C_p \propto n_{el}'^2 R'^4 \gamma_p'^4 B'^2 \frac{\delta^4}{(1+z)^2}$	$\propto N_{el} R'^{-2} \gamma_p'^4 B'^2 \frac{\delta^4}{(1+z)^2}$
1^{st} order IC (Klein-Nishina regime)		
SED peak frequency	$\epsilon_p \propto \gamma' \frac{\delta}{(1+z)}$	
SED peak height	$C_p \propto n_{el}'^2 R'^4 B' \frac{\delta^4}{(1+z)^2}$	$\propto N_{el} R'^{-2} B' \frac{\delta^4}{(1+z)^2}$
2^{nd} order IC (Thomson regime)		
SED peak frequency	$\epsilon_{2p} \propto \gamma_p'^6 B' \frac{\delta}{(1+z)}$	
SED peak height	$C_{2p} \propto n_{el}'^2 R'^4 \gamma_p'^6 B'^2 \frac{\delta^4}{(1+z)^2}$	$\propto N_{el} R'^{-2} \gamma_p'^6 B'^2 \frac{\delta^4}{(1+z)^2}$
2^{nd} order IC (Klein-Nishina regime)		
SED peak frequency	$\epsilon_{2p} \propto \gamma'_p \frac{\delta}{(1+z)}$	
SED peak height	$C_{2p} \propto n_{el}'^2 R'^2 B' \frac{\delta^4}{(1+z)^2}$	$\propto N_{el} R'^{-4} B' \frac{\delta^4}{(1+z)^2}$

and applying the beaming and the redshift factor yields (see eq. 2.72 and eq. 2.88)

$$\epsilon_{2p} \propto \gamma'_p \frac{\delta}{(1+z)} \tag{5.45}$$

Reminding that the maximum of the SED is proportional to

$$C'_{2p} = F'_{2C} = N_{el} P'_{2C} \quad , \tag{5.46}$$

in the Klein-Nishina regime it follows

$$P'_{2C} \propto n'_C \quad , \tag{5.47}$$

where the first order IC photon density can be written as

$$n'_C \propto \frac{1}{\epsilon'_p} u'_C \propto \frac{1}{\epsilon'_p} \frac{P'_C}{R^2} \quad , \tag{5.48}$$

here, it possible to replace the first order IC luminosity with the relation (Thomson regime assumption)

$$P'_C = \gamma_p'^2 u'_S \quad , \tag{5.49}$$

The photon density will be given thus by the relation

$$n'_C \propto \frac{1}{\gamma_p'^4 B'} \frac{\gamma'^2}{R'^2} u'_S \quad , \tag{5.50}$$

and using eq. 5.24 for the synchrotron energy density

$$n'_C \propto \frac{N_{el} B'}{R'^4} \quad . \tag{5.51}$$

Finally, the maximum of the SED C'_{2p} at the frequency peak ϵ'_{2p} is

$$C'_{2p} \propto \frac{N_{el}^2 B'}{R'^4} \propto n'^2_{el} R'^2 B' \quad , \tag{5.52}$$

and for the observed quantities will be

$$C_{2p} \propto n'^2_{el} R'^2 B' \frac{\delta^4}{(1+z)^2} \quad . \tag{5.53}$$

All functional relations are summarized in Tab. 5.4

5.3 SSC CONSTRAINTS ON THE SOURCE STRUCTURE

In this Section detailed calculations, based on the relations previously derived, are performed to obtain the source parameters in terms of observed quantities. In the following, the calculations are developed only under the Thomson regime assumptions.

It is possible to write the synchrotron relations derived previuosly (eq. 5.6 and eq. 5.8) by introducing some constant factors

$$\begin{aligned} \nu_p &= \xi_1 \, \gamma'^2_p B' \delta & (5.54) \\ S_p &= \xi_2 \, n'_{el} R'^3 \gamma'^2_p B'^2 \delta^4 \quad , & (5.55) \end{aligned}$$

in the spherical geometry. In the Synchrotron Self Compton scenario, in the Thomson regime, the inverse Compton relations given by eq. 5.21 and eq. 5.26 are

$$\begin{aligned} \epsilon_p &= \xi_3 \, \gamma'^4_p B' \delta & (5.56) \\ C_p &= \xi_4 \, n'^2_{el} R'^4 \gamma'^4_p B'^2 \delta^4 \quad , & (5.57) \end{aligned}$$

where all the ξ_i constants that depend on the spectral shape, the redshift, the geometry, and will be derived in the following.

These relations constitute a system of 4 equations with 5 unknown quantities and therefore another equation is necessary to solve completely this system. The final equation can be obtained from the time scale variability t_{var}, assuming that the size of the emitting region is related to t_{var} as

$$R' = c t_{var} \frac{\delta}{(1+z)} \quad \rightarrow \quad \delta = \frac{(1+z)}{c} \frac{R'}{t_{var}} = \xi \frac{R'}{t_{var}} \quad . \tag{5.58}$$

Introducing the new constants c_i defined by the following relations

$$c_1 = \xi \xi_1 \quad , \quad c_2 = \xi^4 \xi_2 \quad , \quad c_3 = \xi \xi_3 \quad , \quad c_1 = \xi \xi_1 \quad , \quad c_4 = \xi^4 \xi_4 \tag{5.59}$$

and combining the SSC eqs. 5.54, 5.55, 5.56 and 5.57, with the above relation (eq. 5.58), it follows

$$\begin{aligned} \nu_p t_{var} &= c_1 \, \gamma'^2_p B' R' & (5.60) \\ S_p t^4_{var} &= c_2 \, n'_{el} \gamma'^2_p B'^2 R'^7 \quad , & (5.61) \end{aligned}$$

and

$$\begin{aligned} \epsilon_p t_{var} &= c_3 \, \gamma'^4_p B' R' & (5.62) \\ C_p t^4_{var} &= c_4 \, n'^2_{el} \gamma'^4_p B'^2 R'^8 \quad , & (5.63) \end{aligned}$$

for the synchrotron and for the inverse Compton emission, respectively. As described in the previuos section, it is possible to derive the electron Lorentz factor γ for the ratio between the peak frequencies of the two components

$$\gamma_p'^2 = \frac{c_1}{c_3}\left(\frac{\epsilon_p}{\nu_p}\right) = A_\gamma\left(\frac{\epsilon_p}{\nu_p}\right) \quad . \tag{5.64}$$

The constant A_γ is introduced to have a simpler notation, a similar constant will be introduced in the following for the other source parameters.

Combining eq. 5.64 with the time variability and the synchrotron peak frequency (see eq. 5.60), it is possible to derive the magnetic field in terms of the radius of the emitting region:

$$B' = \frac{\nu_p t_{var}}{c_1 \gamma_p'^2 R'} = \frac{1}{c_3 R'}\left(\frac{\nu_p^2 t_{var}}{\epsilon_p}\right) \quad , \tag{5.65}$$

that introduced in the eq. 5.61 gives

$$S_p t_{var}^4 = c_2 B'^2 R'^3 (\gamma_p'^2 n_{el}' R'^4) \quad \rightarrow \quad (\gamma_p'^2 n_{el}' R'^4)^2 = \frac{S_p^2 t_{var}^8}{c_2^2 B'^4 R'^6} \quad , \tag{5.66}$$

inserting this in eq. 5.63, concerning the maximum of the Compton SED,

$$C_p t_{var}^4 = \frac{c_4}{c_2^2} \frac{S_p^2 t_{var}^8}{B'^2 R'^6} \quad , \tag{5.67}$$

it is possible to find the first equation that for the radius R in terms of only observable quantities

$$R'^4 = \frac{c_3^2 c_4}{c_2^2} \frac{\epsilon_p^2 S_p^2 t_{var}^2}{\nu_p^4 C_p} = A_R \frac{\epsilon_p^2 S_p^2 t_{var}^2}{\nu_p^4 C_p} \quad . \tag{5.68}$$

Using the relation between the magnetic field and the radius (see eq. 5.58), an equation useful to derive the magnetic field in terms of observable quantities is

$$B'^4 = \left[\frac{1}{R'}\frac{1}{c_3}\left(\frac{\nu_p^2 t_{var}}{\epsilon_p}\right)\right]^4 \qquad \rightarrow \qquad B'^4 = \frac{c_2^2}{c_3^6 c_4} \frac{\nu_p^{12} C_p t_{var}^2}{\epsilon_p^6 S_p^2} = A_B \frac{\nu_p^{12} C_p t_{var}^2}{\epsilon_p^6 S_p^2} \quad , \tag{5.69}$$

and combining the ratio between the height of the SED and the peak frequency of each component in the following way

$$\frac{\epsilon_p S_p}{\nu_p C_p} = \frac{c_2 c_3}{c_1 c_4} \frac{1}{n_{el}' R'} \quad , \tag{5.70}$$

a handy relation to express the electron density can be derived as

$$n_{el}'^4 = \frac{c_2^6 c_3^2}{c_1^4 c_4^5}\left(\frac{\nu_p^8 C_p^5}{\epsilon_p^6 S_p^6 t_{var}^2}\right) = A_n\left(\frac{\nu_p^8 C_p^5}{\epsilon_p^6 S_p^6 t_{var}^2}\right) \quad . \tag{5.71}$$

The equation for the radius and for the time variability (see eq. 5.58), involves the beaming factor

$$\delta^4 = \xi^4 \frac{R'^4}{t_{var}^4} \quad , \tag{5.72}$$

which can be found in terms of observable quantities, as

$$\delta^4 = \frac{\xi c_3^2 c_4}{c_2^2} \frac{\epsilon_p^2 S_p^2}{\nu_p^4 C_p t_{var}^2} = A_\delta \frac{\epsilon_p^2 S_p^2}{\nu_p^4 C_p t_{var}^2} \quad . \tag{5.73}$$

Note that it is possible to derive the numerical constants c_i and their correspondent combination A_i in the case of a log-parabolic shape for the SEDs. For the synchrotron emission the numerical constants c_1 and c_3 can be derived on using the relations given in Sect. 4.1. In detail for the peak frequency ν_p

$$\nu_p = 0.29\nu_c \qquad \rightarrow \qquad c_1 = 4.05\times10^{-5}(1+z) \quad , \tag{5.74}$$

For the constant c_2 note that, under the assumption of a log-parabolic spectral description of the SED, the bolometric flux F and the intrinsic luminosity L^* can be written as

$$F = 2.7\frac{S_p}{\sqrt{b_S}} \qquad \rightarrow \qquad L^* = 4\pi D_L^2\left(\frac{2.7\cdot S_p}{\sqrt{b_S}}\right) \quad , \tag{5.75}$$

and the synchrotron luminosity is given by

$$L^* = N_{el}P'_S\delta^4 = \left(\frac{4\pi}{3}R^3 n_{el}\right)\left(\frac{4}{3}\sigma_T c\gamma^2\frac{B^2}{8\pi}\delta^4\right) \quad . \tag{5.76}$$

Consequently the constant c_2 is

$$c_2 = \frac{5}{243\pi}\frac{\sigma_T}{c^3}\left[\frac{(1+z)^4}{D_L^2}\sqrt{b_S}\right] \quad , \tag{5.77}$$

and in CGS units reads

$$c_2 = 1.61\times10^{-58}\left[\frac{(1+z)^4}{D_L^2}\sqrt{b_S}\right] \quad , \tag{5.78}$$

where b_S is the curvature of the synchrotron spectrum and D_L is the luminosity distance. In the Thomson limit, reminding that the peak frequency of the IC scattering is given by

$$\epsilon_p = \frac{4}{3}\gamma_p'^2\nu_p \quad , \tag{5.79}$$

it is possilbe to derive the constant c_3

$$c_3 = 0.54\times10^{-4}(1+z) \quad . \tag{5.80}$$

Under the log-parabolic hypothesis shape for the SED, the bolometric IC flux will be related with C_p by

$$F = 2.7\frac{C_p}{\sqrt{b_C}} \qquad \rightarrow \qquad L^* = 4\pi D_L^2\left(\frac{2.7\cdot C_p}{\sqrt{b_C}}\right) \quad , \tag{5.81}$$

where the intrinsic luminosity is given by

$$L = L^*\delta^4 = N_{el}P'_C\delta^4 = \left(\frac{4\pi}{3}R^3 n_{el}\right)\left(\frac{4}{3}\sigma_T c\gamma^2 u^S\right) \quad . \tag{5.82}$$

Replacing with eq. 5.24, for the energy density of the synchrotron emission, it is possible to obtain the last constant in the form

$$c_4 = \frac{2}{9\pi}\frac{\sigma_T^2}{c^3}\left[\frac{(1+z)^4}{D_L^2}\sqrt{b_C}\right] \quad , \tag{5.83}$$

that is in CGS units

$$c_4 = 1.16\times10^{-81}\left[\frac{(1+z)^4}{D_L^2}\sqrt{b_C}\right] \quad , \tag{5.84}$$

where b_C is the curvature of the inverse Compton spectrum.

Finally, the numerical constants for the source parameters: the electron energy γ', the source radius R', the magnetic field B', the electron density n'_{el} and the beaming factor δ, in the Thomson regime, are summarized in Tab. 5.5.

These relations can be used only if both the synchrotron and inverse Compton components are observed simultaneously. Unfortunately, this occurs only in very few instances. Other similar calculations have been performed by Sikora et al. (2004).

Table 5.5: Summary of the numerical constants derived in Sect. 5.3

c_1	$= 4.05 \times 10^{-5}(1+z)$	A_γ	$= \frac{c_1}{c_3}$	$= \frac{3}{4}$
c_2	$= 0.54 \times 10^{-58}\left[\frac{(1+z)^4}{D_L^2}\sqrt{b_S}\right]$	A_R	$= \frac{c_3^2 c_4}{c_2^2}$	$= 0.81 \times 10^{23}\frac{D_L^2}{(1+z)^2}\frac{b_C^{1/2}}{b_S}$
c_3	$= 1.62 \times 10^{-4}(1+z)$	A_B	$= \frac{c_2^2}{c_4 c_3^6}$	$= 1.45 \times 10^{-6}\frac{1}{(1+z)^2 D_L^2}\frac{b_S}{b_C^{1/2}}$
c_4	$= 1.16 \times 10^{-81}\left[\frac{(1+z)^4}{D_L^2}\sqrt{b_C}\right]$	A_n	$= \frac{c_2^6 c_3^2}{c_1^4 c_4^5}$	$= 0.25 \times 10^{78}\frac{(1+z)^2}{D_L^2}\frac{b_S^3}{b_C^{5/2}}$
		A_δ	$= \xi^4 A_R$	$= 1.00 \times 10^{-19}(1+z)^2 D_L^2\frac{b_C^{1/2}}{b_S}$

5.4 THOMSON *vs* KLEIN-NISHINA REGIME

The estabilshment of the Klein-Nishina regime, in the inverse Compton emission, depends both on the electron energy $\gamma' mc^2$ and on the seed photon energy E'_0 as expressed in eq. 4.38. In the source rest frame K', the inverse Compton scattering, at peak energies, in the Klein-Nishina regime will occur when

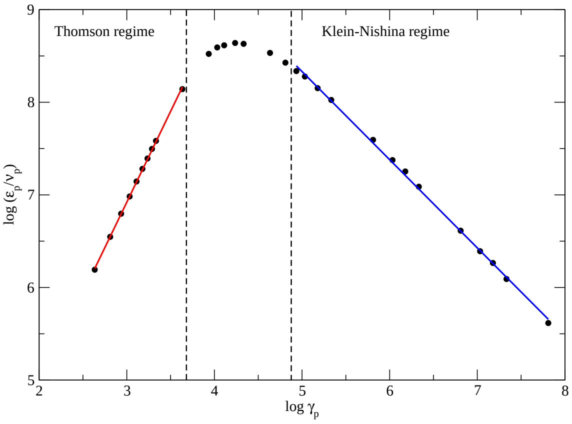

Figure 5.3: Plot of the logarithmic ratio between the IC peak frequency and the synchrotron one versus the electron γ'_p.

$$\gamma' h\nu'_p \simeq mc^2 \quad , \tag{5.85}$$

where ν'_t is the maximum frequency for the synchrotron photon density. Recalling that the observed synchrotron peak frequency ν_p is given by eq. 5.6, one obtains

$$\gamma' \nu_p \simeq \frac{mc^2}{h}\frac{\delta}{(1+z)} = 1.237 \times 10^{19}\frac{\delta}{(1+z)} \quad \text{Hz} \quad , \tag{5.86}$$

and using eq. 4.15 this condition can be written in the form

$$\gamma_p'^3 B' \simeq \frac{40\pi}{87}\frac{m^2c^3}{he}\frac{\delta}{(1+z)} = 1.017\times 10^{15}\frac{\delta}{(1+z)} \quad \mathrm{G} \quad , \tag{5.87}$$

A useful criterion to establish when the Klein-Nishina regime occurs, can be derived from the ratio between the synchrotron peak frequency ν_p and the Compton one ϵ_p. In the Thomson regime this ratio scales as γ^2 as

$$\frac{\epsilon_p}{\nu_p} \propto \gamma_p'^2 \quad (Thomson\ regime) \quad , \tag{5.88}$$

while in the Klein-Nishina regime the dependence upon the source parameters is

$$\frac{\epsilon_p}{\nu_p} \propto \gamma_p'^{-1} B'^{-1} \quad (Klein-Nishina\ regime) \quad . \tag{5.89}$$

From the ratio of these two frequencies and the γ_p' in a log-log plot, it is possible to see when the transition to the Klein-Nishina limit occurs. Fig. 5.3 and Fig. 5.4 show the ratios between the peak frequency and the SED peak maximum in the SSC emission for changing γ_p' with all other source parameter fixed. The main relations are summarized in Tab. 5.6. It is possible to see that the transition between the two regimes occurs in a relatively narrow range of γ_p'.

Table 5.6: Ratio between the peak frequency and the SED peak maximum in the Synchrotron Self Compton models, in Thomson and Klein-Nishina regime.

$\frac{\epsilon_p}{\nu_p} \propto \gamma_p'^2$	$Thomson\ regime$
$\frac{C_p}{S_p} \propto n_{el}' R' \gamma_p'^2$	$Thomson\ regime$
$\frac{\epsilon_p}{\nu_p} \propto \frac{1}{\gamma_p' B'}$	$Klein-Nishina\ regime$
$\frac{C_p}{S_p} \propto \frac{n_{el}' R'}{\gamma_p'^2 B'}$	$Klein-Nishina\ regime$

5.5 PHOTON-PHOTON PAIR PRODUCTION AND SOURCE COMPACTNESS

High energy γ-rays can collide with the softer radiation to produce $e^{\pm}$ pairs. The cross section for the pair production process is maximized for collisions between γ-rays of frequency ν_b' and target photons of frequency ν_t', where

$$h^2\nu_b'\nu_t' \geq m^2c^4 \quad \rightarrow \quad \nu_b'\nu_t' \geq 1.52\times 10^{40} Hz^2 \quad , \tag{5.90}$$

and it equals $\simeq \sigma_T/5$ (Svensson, 1987). For instance, TeV photons ($\nu_b' \sim 10^{25} Hz$) produce $e^{\pm}$ pairs with optical-UV radiation ($\nu_t' \simeq 10^{15}$), while GeV photons ($\nu_b' \simeq 10^{22} Hz$) with the X-rays ($\nu_b' \simeq 10^{18} Hz$). The relevance of this process can be studied in terms of the optical depth

$$\tau_{\gamma\gamma}(\nu_b') = R'\sigma_{\gamma\gamma} n_{ph}'(\nu_t') = R'\frac{\sigma_T}{5} n_{ph}'(\nu_t') \quad , \tag{5.91}$$

where $n_{ph}'(\nu_t')$ is the photon density of the radiation at frequency ν_t', and R' the size of the emitting region. It is possible to derive $n_{ph}'(\nu_t')$ in terms of the luminosity (see eq. 2.20)

$$n_{ph}'(\nu_t') = \frac{L'(\nu_t')}{h\nu_t' c(4\pi R'^2)} \quad , \tag{5.92}$$

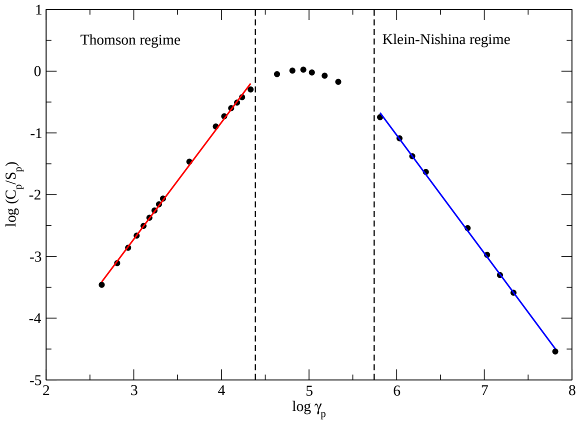

Figure 5.4: Plot of the logarithmic ratio between the IC SED peak and the synchrotron one versus the electron γ'_p.

and inserting for the frequency ν'_t the threshold energy of the pair production process, the optical depth results

$$\tau_{\gamma\gamma}(\nu'_b) = \frac{\sigma_T}{20\pi mc^3}\frac{L'(\nu'_t)}{R'} = 2.703 \times 10^{-29}\frac{L'(\nu'_t)}{R'} \quad . \tag{5.93}$$

The dimensionless parameter l'defined as

$$l'(\nu'_t) = \frac{\sigma_T}{4\pi mc^3}\frac{L'(\nu'_t)}{R'} = 2.152 \times 10^{30}\frac{L'(\nu'_t)}{R'} \simeq \frac{L'_{45}(\nu'_t)}{R'_{15}} \quad , \tag{5.94}$$

is usually named the *source compactness* (Cavaliere & Morrison, 1980, Guilbert, Fabian et al., 1983), where L'_{45} is the source luminosity in units of 10^{45}erg s^{-1} and R'_{15} is the source radius in units of 10^{15}cm. It is interesting consider the previous equation in terms of the observed quantities. The intrinsic luminosity in the source frame K' must be corrected for the beaming factor and for the redshift, to derive the optical depth in terms of the observed flux $F(\nu_t)$ at frequency ν_t (eq. 2.82)

$$L^*(\nu_t) = L'(\nu'_t)\delta^2 \qquad \rightarrow \qquad L'(\nu'_t) = L^*(\nu_t)\delta^{-2} \quad , \tag{5.95}$$

and from eq. 2.87 it follows

$$F(\nu_t) = \frac{1}{4\pi D_L^2}L^*(\nu_t) \quad , \tag{5.96}$$

where the frequency ν_t observed is

$$\nu_t = \nu'_t\frac{\delta}{(1+z)} \quad . \tag{5.97}$$

Combining eq. 5.93 with eq. 5.96 it is possible to write the optical depth for the pair production process as

$$\tau_{\gamma\gamma} = \frac{\sigma_T}{20\pi mc^3}\frac{4\pi D_L^2 F(\nu_t)}{R'}\delta^{-2} \quad . \tag{5.98}$$

If the source is thin to the pair production absorption, the optical depth will be $\tau_{\gamma\gamma} \leq 1$ and one can derive a lower limit on the source radius R'

$$R' \geq \frac{\sigma_T D_L^2}{5mc^3} F(\nu_t)\delta^{-2} \quad , \tag{5.99}$$

that for a beaming factor δ of 10, a source redshift $z = 0.5$ and an observed flux $F(\nu_t)$ of 10^{-11}erg cm^{-2} s^{-1} corresponds to $R' \geq 10^{13} cm$. For a typical time scale variability, one can impose another limit to the source size

$$R' = ct_{var}\frac{\delta}{(1+z)} \quad , \tag{5.100}$$

that for a $t_{var} \sim 10^3 s$ and $\delta \simeq 10$ gives $R' \simeq 10^{14} cm$, consistent with the above lower limit (eq. 5.104) imposed by the source compactness.

The compactness of the source related to the $e^{\pm}$ pair production can be used to constrain the beaming factor δ if it is possible to evaluate t_{var}. Combing eq. 5.98 and eq. 5.100 the optical depth will be given by

$$\tau_{\gamma\gamma}(\nu'_b) = n'_{ph}\sigma_T R' = n'_{ph}\sigma_T ct_{var}\frac{\delta}{(1+z)} \quad , \tag{5.101}$$

and from

$$n'_{ph} \simeq \frac{1}{h\nu'_t}\frac{L'(\nu'_t)}{4\pi R'^2} = \frac{L(\nu_t)\delta^2}{4\pi R'^2 mc^3} \quad , \tag{5.102}$$

it follows

$$\tau_{\gamma\gamma}(\nu'_b) = \frac{L(\nu_t)\sigma_T}{4\pi mc^3}\frac{(1+z)}{ct_{var}\delta^3} \quad , \tag{5.103}$$

with the condition of $\tau_{\gamma\gamma}(\nu'_b) \leq 1$, eq. 5.103 provides the a constraint on the beaming factor in terms of the observed quantities

$$\delta \leq \left[\frac{L(\nu_t)\sigma_T(1+z)}{4\pi mc^3 t_{var}}\right]^{1/3} = 0.129\left[\frac{L(\nu_t)(1+z)}{t_{var}}\right]^{1/3} \quad . \tag{5.104}$$

5.6 COMPTON CATASTROPHE IN THE SSC EMISSION

For both synchrotron and inverse Compton emission, it is possible to define a *cooling time* t_{cool} per a single electron of energy γmc^2 using the relation

$$t'_{cool} = \frac{\gamma' mc^2}{P'} \quad , \tag{5.105}$$

where the power P' is the total energy radiated by each electron per time interval. In the case of synchrotron emission and inverse Compton radiation they are indicated as P'_S and P'_{IC}, respectively, while t'^S_{cool} and t'^C_{cool} are the corrispondent cooling times. In the SSC scenario, when emitting electrons loose energy via inverse Compton radiation faster than for synchrotron emission the source will fall in the *Compton Catastrophe*. It can be summarized introducing the adimensional *Compton Catastrophe parameter* η_c as

$$t'_{cool,S} \;>\; t'_{cool,C} \;\rightarrow\; \eta_c = \frac{t'_{cool,S}}{t'_{cool,C}} > 1 \quad (Compton\ Catastrophe) \tag{5.106}$$

$$t'_{cool,S} \;<\; t'_{cool,C} \;\rightarrow\; \eta_c = \frac{t'_{cool,S}}{t'_{cool,C}} < 1 \quad (No\ Compton\ Catastrophe) \quad , \tag{5.107}$$

It is also possible to derive some constraints on the sources parameters (electron density, magnetic field strenght, etc.) from the condition that our source lies outside the *Compton Catastrophe* limit. To do this it is necessary consider the two different regimes (Thomson - Klein-Nishina) for the inverse Compton luminosity P'_{IC}.

5.6.1 Thomson regime

The synchrotron luminosity emitted by a single electron as derived in Sect. 4.1 is

$$P'_S = \frac{4}{3}\sigma_T c \gamma'^2 u'_B \quad , \tag{5.108}$$

while that for inverse Compton radiation will be (see Sect. 4.2)

$$P'_C = \frac{4}{3}\sigma_T c \gamma'^2 u'_S \quad , \tag{5.109}$$

The energy density of the synchrotron radiation field u'_S can be derived as

$$u'_S = N_{el} t'_{cr} \frac{3P'_S}{4\pi R'^3} \quad , \tag{5.110}$$

where N_{el} is the total number of emitting electrons, t'_{cr} the crossing time and R' the radius in the spherical assumption. So, in Thomson regime, the ratio between cooling times derived from previuos relations is given by

$$\eta_c = \frac{t'_{cool,S}}{t'_{cool,C}} = \frac{P_C}{P_S} = \frac{\sigma_T \gamma'^2 N_{el}}{\pi R'^2} = \frac{8e^4}{3m^2c^4}\frac{\gamma'^2 N_{el}}{R'^2} \quad , \tag{5.111}$$

Following (Tsang & Kirk 2007) it is possible to derive another relation for the occurrance of the Compton Catastrophe, defining the η_c parameter as:

$$\eta_c = \frac{4}{3}\sigma_T R' \gamma'^2 n_{el} = \frac{4}{3}\gamma'^2 \tau_T \quad , \tag{5.112}$$

where τ_T is the *Thomson optical depth* equal to $\sigma_T R' \gamma'^2 n_{el}$. This relation is equivalent to that expressed by eq. 5.111. In particular for an electron distribution eq. 5.112 can be generalized

$$\eta_c = \frac{4}{3}\sigma_T R' \int_{\gamma'_{min}}^{\gamma'_{max}} \gamma'^2 N(\gamma') d\gamma' \quad , \tag{5.113}$$

that, in the case of log-parabolic electron distribution, using eq. 3.54, it can be written as

$$\eta_c \simeq \frac{4}{3}\sigma_T R' \gamma'^2_p n'_{el} \quad , \tag{5.114}$$

Replacying γ'^2_p with eq. 5.64 for the γ'^2_p, and using eq. 5.71 for the electron density, both in terms of the observed quantities, the η_c parameter can be expressed in the form

$$\eta_c = 0.89 \times 10^{-24} A_\gamma \frac{c_2}{c_4}\frac{C_p}{S_p} \quad , \tag{5.115}$$

that in CGS units will be given by

$$\eta_c = 0.123 \frac{C_p}{S_p}\sqrt{\frac{b_S}{b_C}} \quad . \tag{5.116}$$

Note that in Thomson regime, where $b_S \simeq b_C$, the Compton catastrophe occurs when C_p is about one order of magnitude higher than S_p.

5.6.2 Klein-Nishina regime

As derived in the Sect. 4.2 , the inverse Compton power for a single electron is

$$P'_C \propto \gamma' n'_S \sigma_{KN} \propto n'_S \quad , \tag{5.117}$$

where the photon energy density n'_S of the synchrotron emission can be obtained as

$$n'_S \propto \frac{1}{\nu'_p} u'_S = \frac{N_{el} t'_{cr}}{\gamma'^2 \nu_L V'} P'_S \quad . \tag{5.118}$$

The ratio between the cooling times will be

$$\frac{t'_{cool,S}}{t'_{cool,C}} = \frac{P'_{IC}}{P'_S} = \frac{3}{4\pi} m^2 c^3 \sigma_T \frac{N_{el}}{R'^2 \gamma'^2 e B'} \quad , \tag{5.119}$$

that corresponds to:

$$\eta_c = \frac{t'_{cool,S}}{t'_{cool,C}} = 2mc^2 e \frac{N_{el}}{\gamma'^2 R'^2 B'} \quad . \tag{5.120}$$

Relations for the compton catastrophe parameter are summarized in Tab. 5.7. Note that from eqs. 5.116 and 5.120, in Klein-Nishina regime high values of the electron energy and the magnetic field strength reduce the possibility of reaching the Compton catastrophe condition. Moreover, in the Thomson regime η_c does not depend on the magnetic field.

Table 5.7: Compton Catastrophe

$\eta_c = 0.21 \times 10^{-24}\, \gamma^2 N_{el} R^{-2}$	$= 0.89 \times 10^{-24}\, \gamma^2 n_{el} R$	*Thomson regime*
$\eta_c = 0.72 \times 10^{-6}\, \gamma^{-2} N_{el} R^{-2} B^{-1}$	$= 3.01 \times 10^{-6}\, \gamma^{-2} n_{el} R B^{-1}$	*Klein − Nishina regime*

5.7 NUMERICAL CALCULATIONS OF SSC AND EC SOURCE MODELS

To investigate the spectral evolution of SSC models used to interpret the emission from BL Lac objects, several numerical codes have been developed. In this section, the main assumptions adopted in these codes are described and several examples of the resulting SEDs are presented. A detailed description of the numerical codes are reported in App. C.1.

5.7.1 The behavior of synchrotron sources

The following main assumptions are adopted:

1. Radiation is emitted in one zone (single electron population) described as a homogeneus stationary spherical region, with the parameter R' (radius) characterizing all length scales.
2. Energy distribution of electrons, parametrized by a log-parabolic form, is determined self-consistently with the normalization defined by eq. 3.61.
3. The electron energy distribution is assumed isotropic in the source frame; any existing anisotropy is averaged over angles.
4. The source is stationary: the spectral energy distribution of the electrons remains constant.

The source is parametrized by the following quantities: the redshift z, the beaming factor δ, the magnetic field B', the volume of the emitting region V'; in particular, for emitting particles: the electron

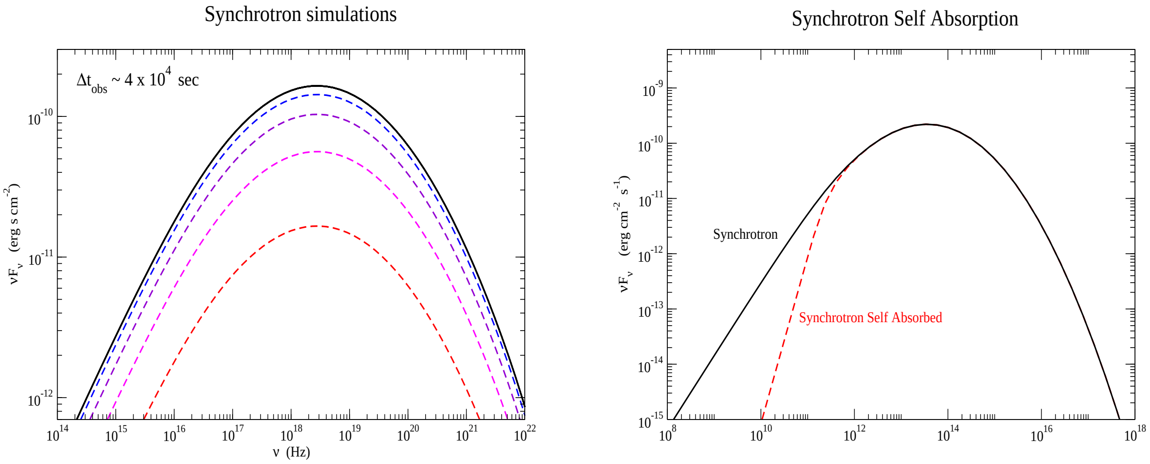

Figure 5.5: a) The SED of a synchrotron source at different observed epochs differing for $\Delta t = t_{cr}/5$. b) The synchrotron SED corrected for the self absorption in comparison with the unabsorbed case. (The input values for these calculations are reported in the *synchrotron* column in tab. 5.8)

density n'_{el}, the electron spectral index s and the curvature parameter r with the γ'_{min} and γ'_{max} the electron energy limits and γ'_0 the reference energy for the electron spectrum.

The output of each simulation provides: the luminosity distance of the source $D_L(Mpc)$, the energy density of the magnetic field u_B, the source radius R, the electron number N_{el} with the normalization of the electron distribution N_0, the peak Lorentz factor γ_p of the $\gamma^2\ N(\gamma)$ and the total electron energy E_{tot} (see eq. 3.38).

The main output of the code is given in three files with the emission coefficient, the intrinsic flux and the spectral energy distribution, as function of the observed frequency, respectively. The total emitted flux and the spectral energy distribution are well described by a log-parabolic function around the peak frequency (see App. A.3,) as expected by simple analytical calculations in synchrotron δ approximation(see Sect. 4.1.2) and from previous works (Massaro et al. 2004). Applying a log-parabolic bestfit to each the file containing the spectral energy distribution, the numerical code calculates: the resulting curvature parameter b_S, the SED peak frequency ν_p, the maximum of the SED S_p.

In detail, the code provides also: the highest frequency reached by the synchrotron radiation ν_{max} (corresponding to γ'_{max}), and the intrinsic luminosity L'.

The synchrotron code is also able to evaluate the SED of the source at different time intervals, taking into account of the light travel effects inside the emitting region as described in Sect. 2.2.3. The observed SED at time intervals Δt_{obs} corresponding to fractions of the crossing time is reported. When $n\Delta t_{obs} = t_{cr}$ the total spectral energy distribution is observed, as shown in Fig. 5.5a.

A basic test for the synchrotron code was performed reproducing, successfully, the expected correlations described in Sect. 5.1. Another test was also provided by the expected curvature values. The synchrotron code reproduces a spectral curvature b about $\frac{r}{5}$ in agreement with the accurate results by (Massaro et al. 2006, Tramacere 2007) simulations. Finally, the synchrotron self absorption has been calculated using the analytical results described in Sect. 2.2 and Sect. 4.1. The absorption coefficient was evaluated on using eq. 4.21 with the electron distribution $n(\gamma)$ given by eq. 3.42 or eq. 3.60, and the emitted flux was calculated on using the solution of radiative transfer expressed by eq. 2.25. The synchrotron SED corrected for the self absorption is shown in Fig. 5.5b in comparison with the unabsorbed one, the input source parameters for this calculations are reported in Tab. 5.8.

Table 5.8: Input values for SSC calculations: SSC$^{(1)}$ indicates calculations using a log-parabolic electron spectrum. $SSC^{(2)}$ indicates calculations using a log-parabolic electron spectrum with a low energy power-law tail. The index 2^{nd} indicates the SSC code with the second order IC emission.

Parameter	*Symbol*	Synchrotron	SSC$^{(1)}$	SSC$^{(1)}$ 2^{nd}	SSC$^{(2)}$	SSC$^{(2)}$ 2^{nd}
Redshift	z	0.0337	0.10	0.10	0.10	0.10
Beaming Factor	δ	15.00	10.00	10.00	10.00	10.00
Magnetic Field	B' (G)	0.10	0.10	0.10	0.10	0.10
Volume	V' (cm^3)	$1.57{\cdot}10^{47}$	$1.00{\cdot}10^{48}$	$1.00{\cdot}10^{48}$	$5.00{\cdot}10^{48}$	$5.00{\cdot}10^{48}$
Density	n' (cm^{-3})	4.25	5.00	$1.00{\cdot}10^{4}$	50.00	$5.00{\cdot}10^{4}$
Electron energy	γ'_0	$4.8 \cdot 10^{4}$	$1.00{\cdot}10^{4}$	$1.00{\cdot}10^{2}$	$5.00{\cdot}10^{4}$	50.00
Spectral index	s	1.12	1.50	1.50	1.50	1.00
Curvature	r	0.81	1.00	1.50	1.00	1.50
Minimum energy	γ'_{min}	10.00	50.00	50.00	5.00	5.00
Maximum energy	γ'_{max}	$5.00 \cdot 10^{7}$	$5.00{\cdot}10^{8}$	$5.00{\cdot}10^{8}$	$5.00{\cdot}10^{8}$	$5.00{\cdot}10^{8}$

It is possible to evaluate the spectral index of the specific emitted flux F_ν within the range of frequencies in which the synchrotron self absorption cannot be neglected, typically below 10^{12} Hz, for the considered source parameters typical for HBLs. Note that in the case of a power-law electron distribution the synchrotron theory predicts a spectral index of the emitted flux corresponding to 2.5 (equal to 3.5 in the SED). Numerical calculations performed with the curvature parameter r equal to zero are in agreement with this fact. However, on using a pure log-parabolic electron distribution, the spectral index found for the numerical calculations is 2 for the emitted flux, corresponding to 3 in the SED representation.

5.7.2 *The behavior of SSC sources*

Under the same assumptions of the synchrotron code, a second numerical code was developed. It is able to evaluate inverse Compton scattering of synchrotron photons by the same population of relativistic electrons that produce the synchrotron emission (SSC). Basic equations to describe this numerical code are reported in Sect. 4.3.

The input parameters are the same of the synchrotron code, described in the previous section. For the electron energy distribution and for the synchrotron emission the numerical code produce the same output of the synchrotron code (see Sect. 5.7.1), adding the parameter ν^{IC}_{max}, that indicates the maximum frequency reached by the inverse Compton emission. The output files produced for the inverse Compton emission contain, for each frequency step: the emission coefficient, the intrinsic flux and the spectral energy distribution, respectively. Applying the bestfit to the SED files (see App. C.2) it is possible to calculate for both synchrotron and inverse Compton components: the curvature parameters b_S and b_C, the observed SED peak frequency ν_p and ϵ_p, the height of the SED S_p and C_p, respectively. Moreover, the code provides also the intrinsic luminosities L'_S and L'_C for both components, respecively, and their ratio.

In order to study the variety of spectral behaviours observed from BL Lacs, it is relevant to investigate how physical quantities in the emitting blob or parameters of the electrons distribution affects the observed spectrum.

To focus the effects caused by variations of each individual parameter, independently of the others, only the value of that parameter was changed with other fixed to values reported in Tab. 5.8. Figs. 5.6, 5.7, 5.8, 5.9 show the changes in the 1^{st} order SSC spectra for different choice of the source parameters,

Table 5.9: Output values for SSC calculations: SSC$^{(1)}$ indicates calculations using a log-parabolic electron spectrum. $SSC^{(2)}$ indicates calculations using a log-parabolic electron spectrum with a low energy power-law tail. The index 2^{nd} indicates the SSC code with the second order IC emission.

Parameter	*Symbol*	Synchrotron	SSC$^{(1)}$	SSC$^{(1)}$ 2^{nd}	SSC$^{(2)}$	SSC$^{(2)}$ 2^{nd}
Luminosity Distance	D_L (Mpc)	$0.15\cdot10^{3}$	$4.60\cdot10^{3}$	$4.60\cdot10^{3}$	$4.60\cdot10^{3}$	$4.60\cdot10^{3}$
Magnetic energy density	u'_B $(erg\ cm^{-3})$	$0.40\cdot10^{-3}$	$0.40\cdot10^{-3}$	$0.40\cdot10^{-3}$	$0.40\cdot10^{-3}$	$0.40\cdot10^{-3}$
Radius	R' (cm)	$0.33\cdot10^{16}$	$0.62\cdot10^{16}$	$0.62\cdot10^{16}$	$1.06\cdot10^{16}$	$1.06\cdot10^{16}$
Electron Number	N_{el}	$0.67\cdot10^{48}$	$0.50\cdot10^{49}$	$0.10\cdot10^{53}$	$0.25\cdot10^{52}$	$0.25\cdot10^{52}$
Normalization	N'_0 cm^{-3}	$0.56\cdot10^{-5}$	$0.16\cdot10^{-3}$	$0.66\cdot10^{2}$	$0.52\cdot10^{-5}$	3.00
Electron peak energy	γ'_p	$0.17\cdot10^{6}$	$0.18\cdot10^{5}$	$0.15\cdot10^{3}$	$0.89\cdot10^{5}$	$0.11\cdot10^{3}$
Total Electron Energy	E'_{tot} (erg)	$0.44\cdot10^{51}$	$0.41\cdot10^{51}$	$0.11\cdot10^{51}$	$0.11\cdot10^{53}$	$0.53\cdot10^{51}$
Synchrotron						
Curvature	b_S	0.17	0.20	0.29	0.29	0.20
Peak Frequency	ν_p (Hz)	$0.27\cdot10^{19}$	$0.11\cdot10^{17}$	$0.39\cdot10^{12}$	$0.87\cdot10^{17}$	$0.19\cdot10^{12}$
SED peak height	S_p $(erg\ cm^{-2}\ s^{-1})$	$0.16\cdot10^{-9}$	$0.15\cdot10^{-11}$	$0.40\cdot10^{-12}$	$0.30\cdot10^{-10}$	$0.21\cdot10^{-11}$
Maximum Frequency	ν^S_{max}	$0.44\cdot10^{22}$	$0.28\cdot10^{24}$	$0.28\cdot10^{24}$	$0.28\cdot10^{24}$	$0.28\cdot10^{16}$
IC Maximum Frequency	ν^{IC}_{max}	———-	$0.56\cdot10^{30}$	$0.56\cdot10^{30}$	$0.56\cdot10^{30}$	$0.56\cdot10^{26}$
Intrinsic Luminosity	L_S	$0.25\cdot10^{45}$	$0.18\cdot10^{46}$	$0.38\cdot10^{45}$	$0.89\cdot10^{41}$	$0.53\cdot10^{40}$
Inverse Compton 1^{st} order						
Curvature	b_C	———-	0.27	0.16	0.38	0.15
Peak Frequency	ϵ_p (Hz)	———-	$0.35\cdot10^{25}$	$0.70\cdot10^{17}$	$0.25\cdot10^{26}$	$0.18\cdot10^{17}$
SED peak height	C_p $(erg\ cm^{-2}\ s^{-1})$	———-	$0.30\cdot10^{-11}$	$0.31\cdot10^{-12}$	$0.45\cdot10^{-10}$	$0.32\cdot10^{-11}$
Luminosity	L_C	———-	$0.30\cdot10^{46}$	$0.41\cdot10^{45}$	$0.10\cdot10^{42}$	$0.11\cdot10^{41}$
Luminosity Ratio	L'_C/L'_S	———-	1.67	1.06	1.14	2.00
Inverse Compton 2^{nd} order						
Curvature	b_{2C}	———-	———-	0.16	———-	0.38
Peak Frequency	ϵ_{2p} (Hz)	———-	———-	$0.62\cdot10^{22}$	———-	$0.13\cdot10^{22}$
SED peak height	C_{2p} $(erg\ cm^{-2}\ s^{-1})$	———-	———-	$0.25\cdot10^{-12}$	———-	$0.54\cdot10^{-11}$
Luminosity	L_{2C}	———-	———-	$0.31\cdot10^{45}$	———-	$0.19\cdot10^{41}$
Luminosity Ratio	L'_{2C}/L'_C	———-	———-	0.77	———-	1.8

both in the cases of a simple log-parabolic electron distribution and the same modified by a low-energy power-law.

Note that in some cases the numerical calculations give energy densities of IC inverse Compton photons higher that of the magnetic field and therefore the source reaches the Compton catastrophe limit (see Sect. 5.6). These states, of course, cannot be stable and can be observed only in occurrence of very faster flares. The states in which the Compton Catastrophe limit is violated are specified in the figure captions.

Simply cosmological changes due to the redshift z are shown in Fig. 5.6a and 5.8a, because the luminosity distance D_L scales as $(1 + z)$ and the observed flux is proportional to D_L^{-2}, the total flux scales as z^{-2} for redshift variations. The spectral changes due to the beaming factor δ are shown in Fig. 5.6b and 5.8b. In this case the total flux scales as δ^4 and the blueshift of the frequencies are proportional to δ. As expected by the SSC correlations, described in Sect. 5.2, the synchrotron emission from the electron distribution, the total luminosity, and the SED peak maximum is proportional to B^2, then the flux becomes higher when B increases, while in these conditions, the ratio between the total flux of the synchrotron and the inverse Compton components does not change.

Also note that the SED peak frequency scales proportionally to the magnetic field. The spectral variations due to changes in the size of the emitting region: V are shown in Fig. 5.6d and 5.8d, while those due to variations in the electron density are plotted in Fig. 5.6e and 5.8e. Note that the synchrotron spectra do not change if the number of emitting electrons remains constant, while the flux of the Compton component increases, when the source becomes more compact, decreasing the volume and increasing the density (see 5.6f and 5.8f.). Finally, the variations due to the electron distribution parameters are reported in Figs. 5.7 and 5.9.

With the same hypotheses of the previous two numerical codes a third one was builded. This code calculates also the second odrder inverse Compton radiation between photons emitted by the first inverse Compton scattering and the same population of electrons. As for the previous SSC code, and with the same input parameters, this new code evaluates the synchrotron emission, the first order inverse Compton radiation with the same output of the previous one, and finally, the second order inverse Compton emission.

Applying the bestfit described in App. C.2 to the second order IC emission, the code evaluates: the curvature parameter b_{2C}, the observed SED peak frequency ϵ_{2p} and the maximum of the SED C_{2p}. It calculates also the intrinsic luminosity L'_{2C} and luminosities ratio between the first order L_C and second orderL_{2C} components. The behaviours of SSC SED code with the second IC component, changing values of input parameters are shown in Figs. 5.10, 5.11, 5.12, 5.13. These behaviors are similar to those of the first order emission, in terms of changes of spectral parameters. The only main difference in the *baseline* parameters regards the electron density: n_{el}.

As shown in Tab. 5.8, the second order IC emission occurs only when the source is highly compact, in the sense that it has a high density value for the emitting electrons for typical radii of $R \sim 10^{16}$ cm. Note that when γ'_0 increases (see Fig. 5.11a and 5.13a) the first order IC emission occurs near the Klein-Nishina regime and the second order IC radiation is negligible. This occurs because the Klein-Nishina cross section descreases with the energy and electron-photon interactions become rare (see eq. 4.41).

5.7.3 The behavior of EC sources

Finally, the external Compton code provides IC emission using seed photons originated from an accretion disk sited at distance D_{jet} from the electrons that radiate via synchrotron emission. The code evaluates the SED and the photon density of an accretion disk (see Sect. 4.4 for details), parametrized with a Black Hole mass M, an accretion rate $\dot{M}$. Later on, it calculates the IC emission from the log-parabolic electron distribution and the accretion disk photon density. Fig. 5.14a and Fig. 5.14b reports several simulations performed with different values of M and $\dot{M}$. In Tab. 5.10 the input parameters for the EC calculations shown in Fig. 5.14 are reported.

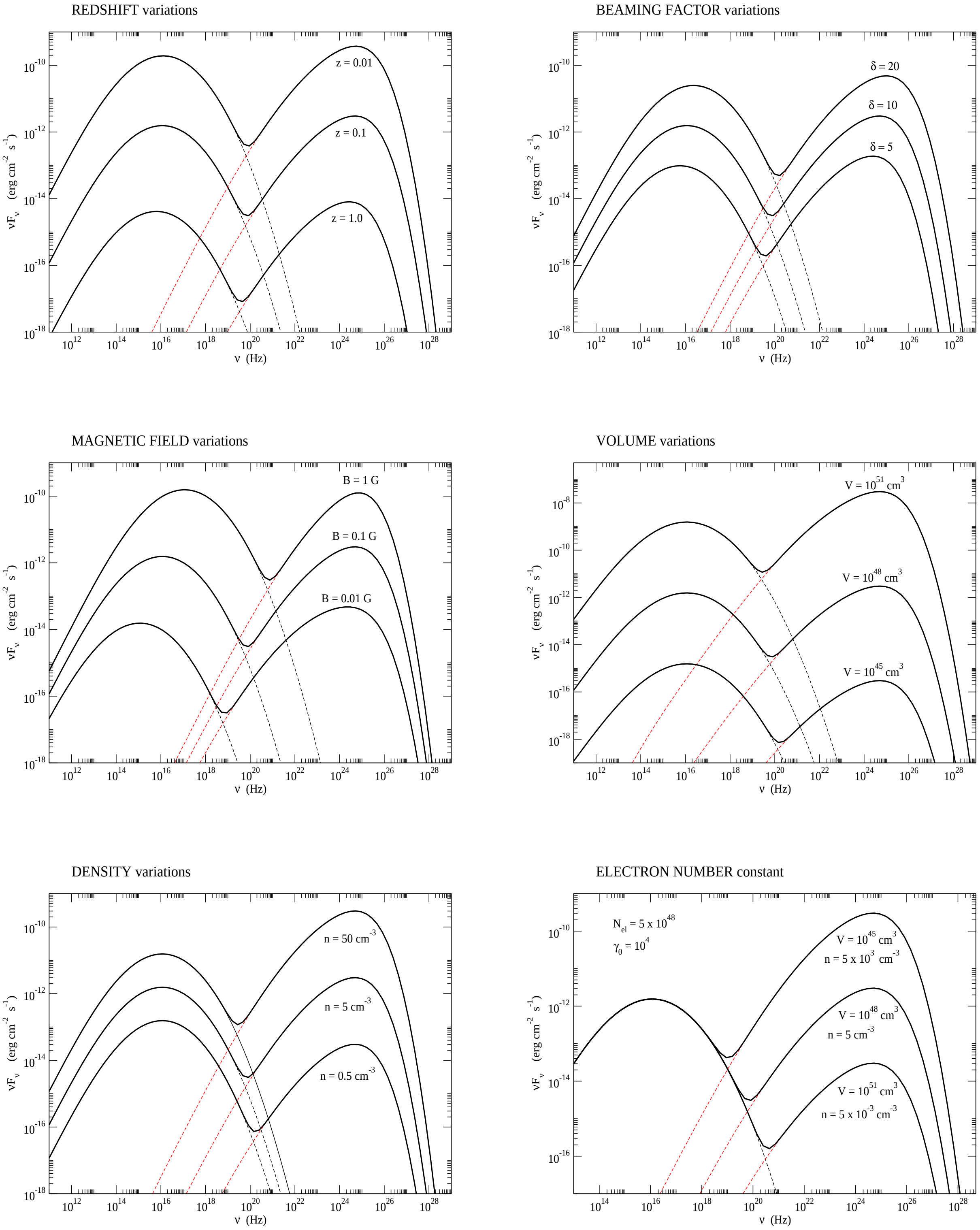

REDSHIFT variations

BEAMING FACTOR variations

MAGNETIC FIELD variations

VOLUME variations

DENSITY variations

ELECTRON NUMBER constant

Figure 5.6: Synchrotron Self Compton simulations performed with a simple log-parabolic electron distribution. The highest SEDs in Fig. 5.6e and Fig. 5.6f violate the Compton Catastrophe limit.

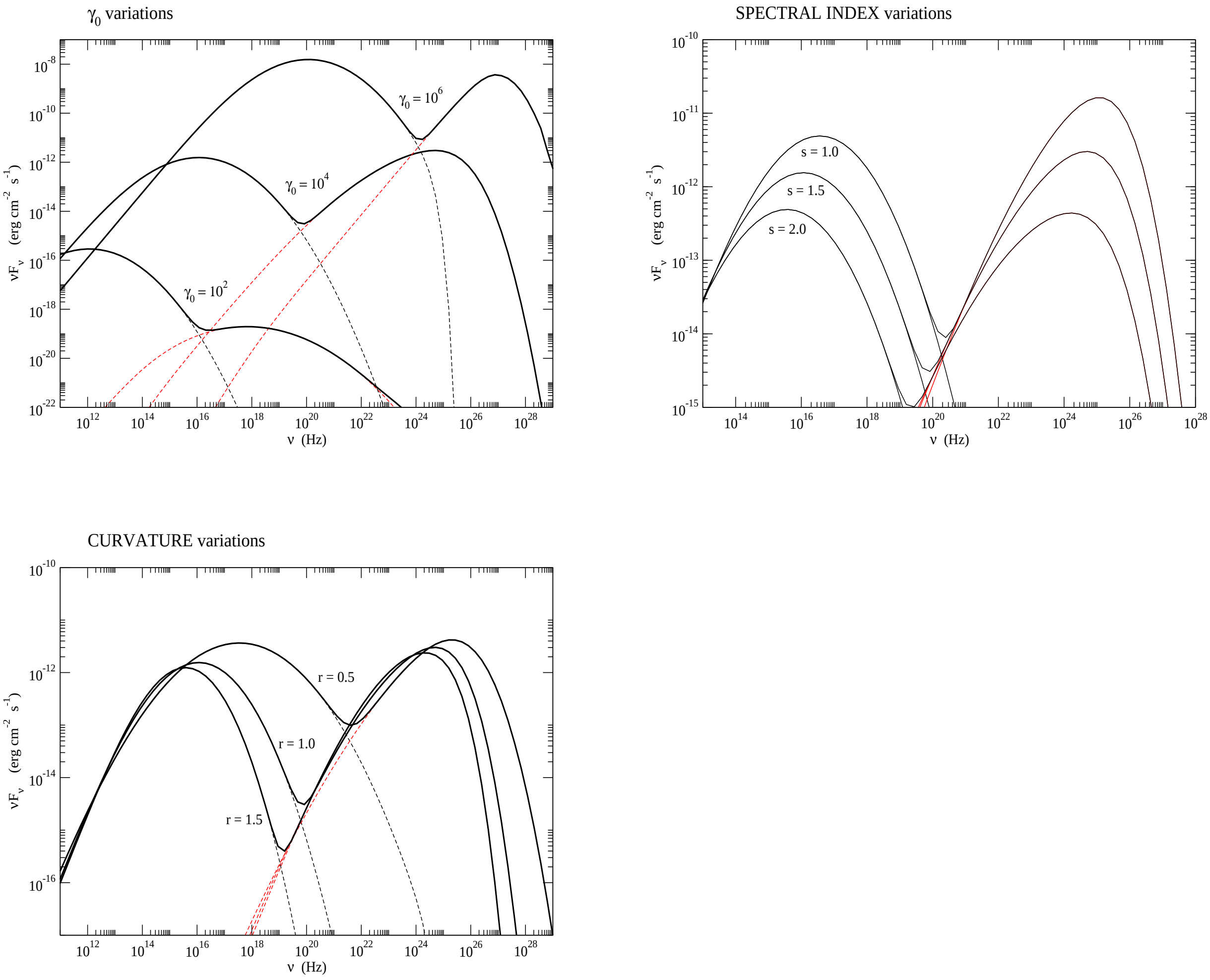

Figure 5.7: Synchrotron Self Compton simulations performed with a simple log-parabolic electron distribution.

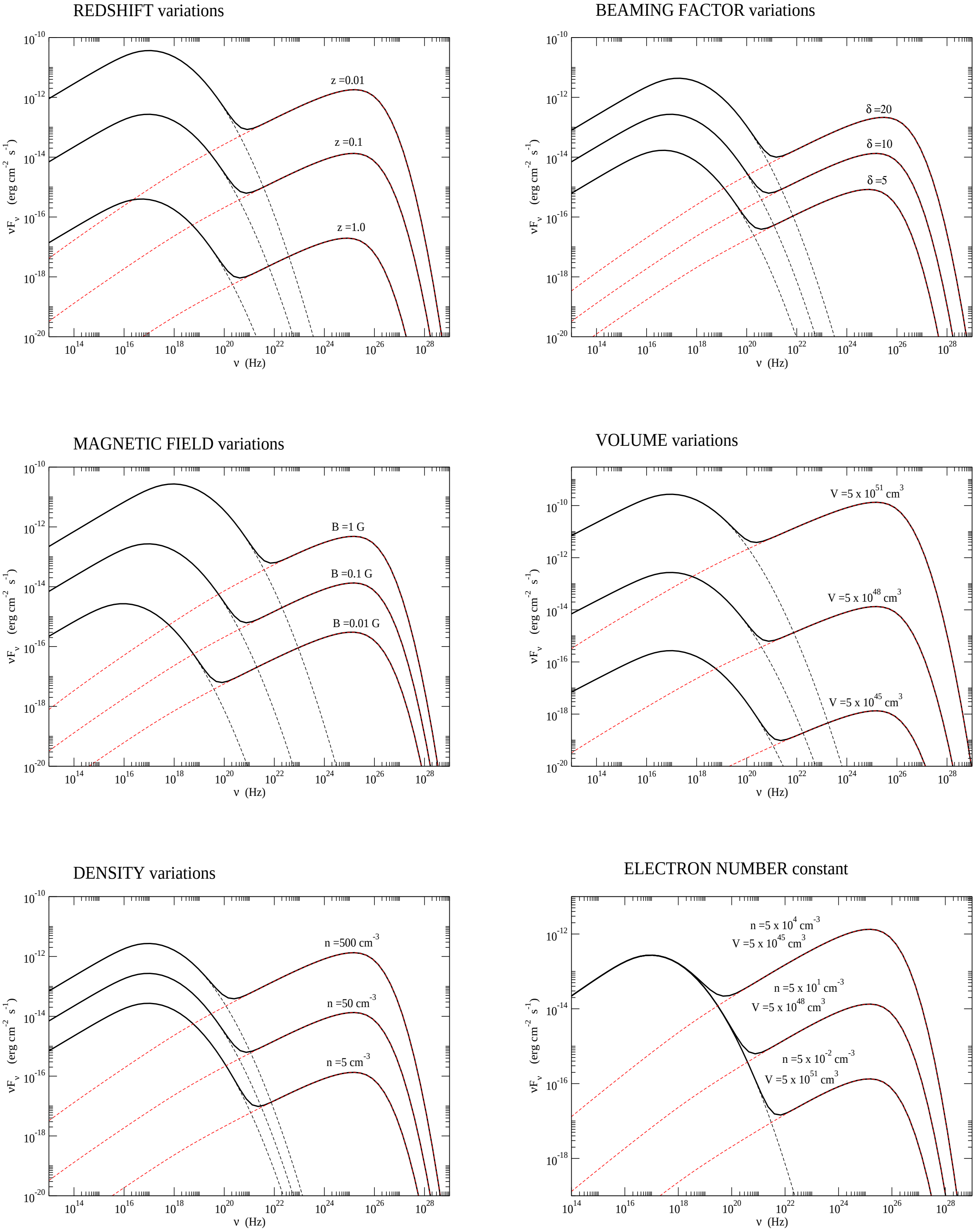

Figure 5.8: Synchrotron Self Compton simulations performed with a log-parabolic electron distribution combined with a power-law model at low energies. The highest SED in Fig. 5.8f violates the Compton Catastrophe limit.

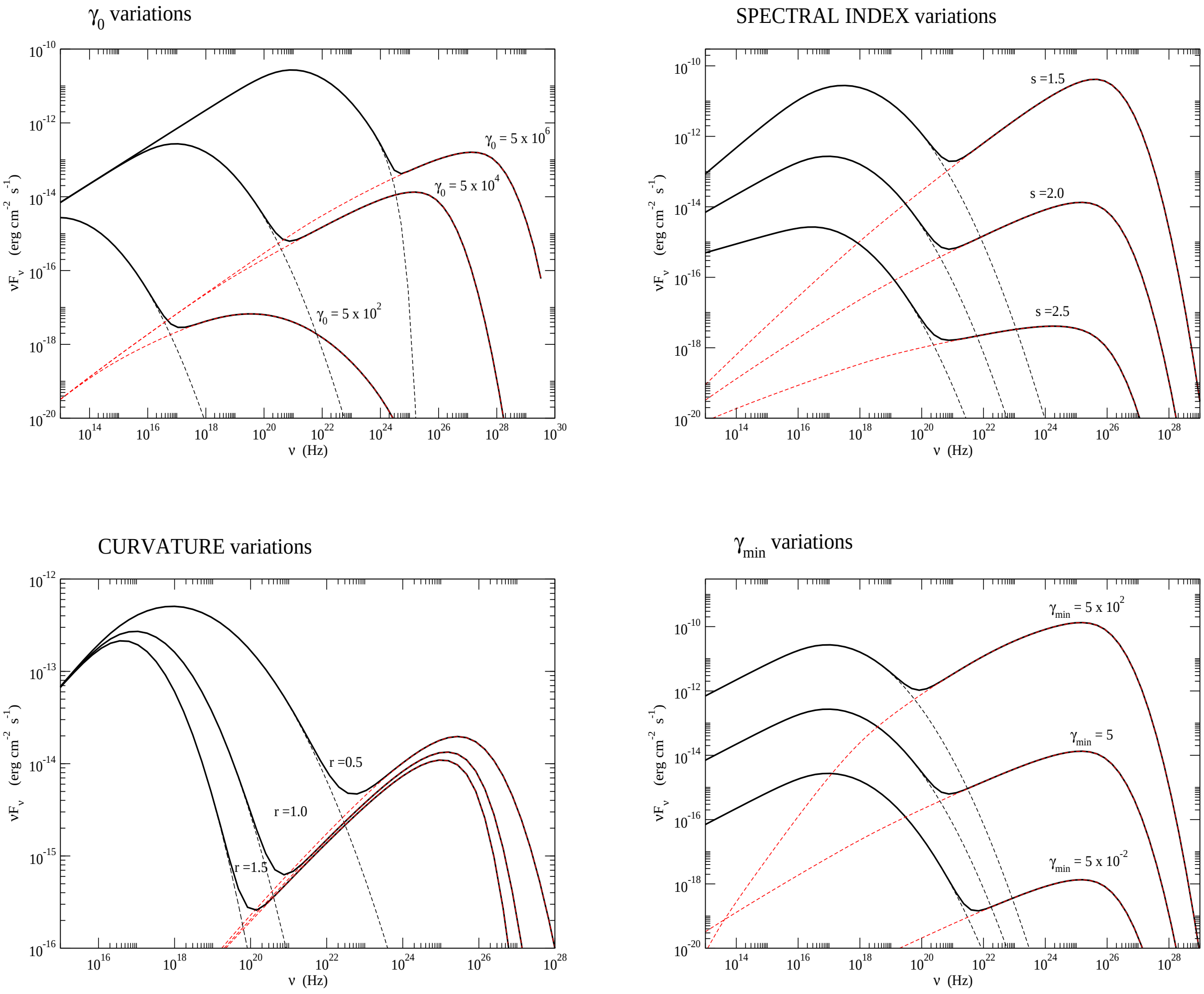

γ_0 variations

SPECTRAL INDEX variations

CURVATURE variations

γ_{min} variations

Figure 5.9: Synchrotron Self Compton simulations performed with a log-parabolic electron distribution combined with a power-law model at low energies.

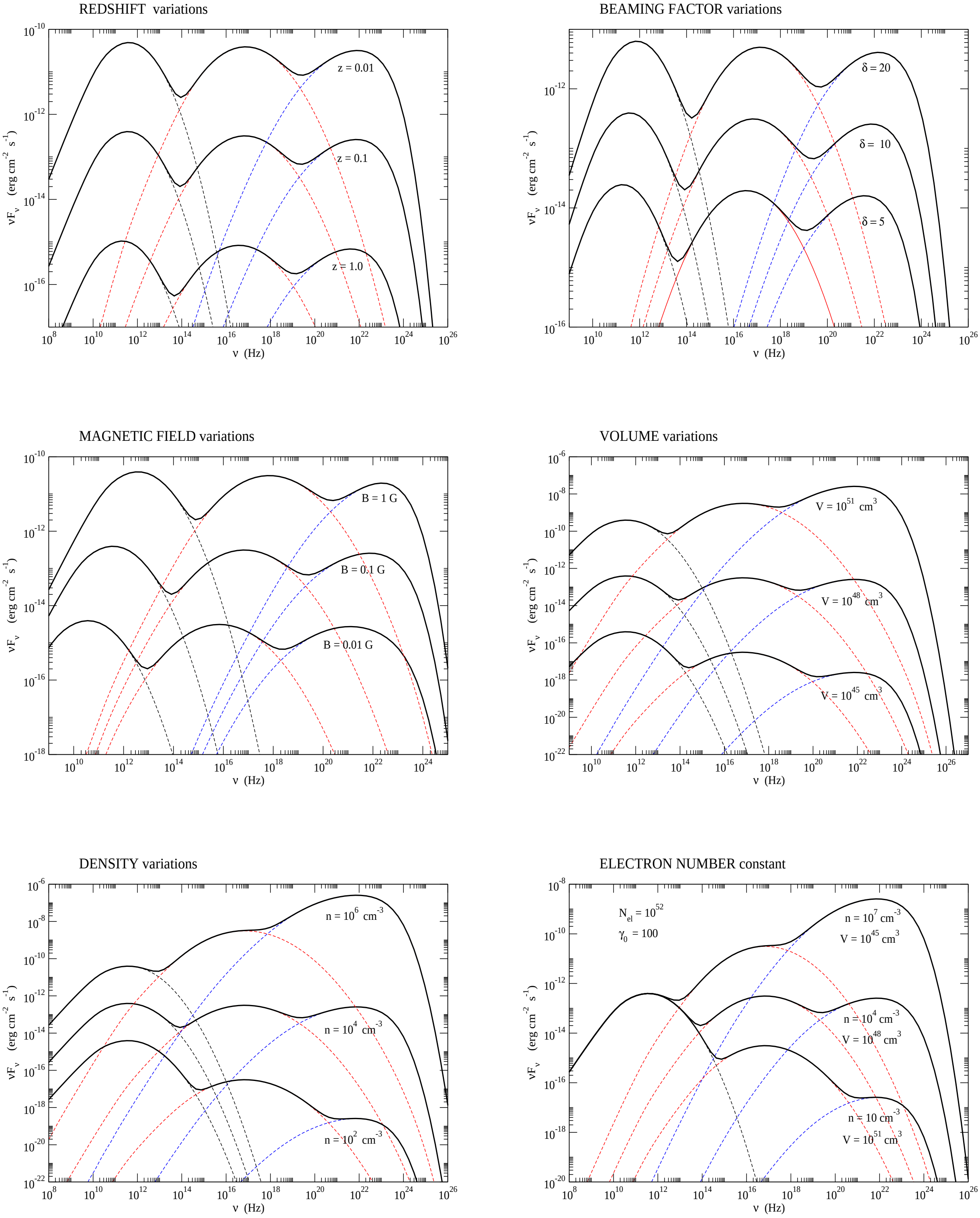

Figure 5.10: Synchrotron Self Compton simulations and 2^{nd} order IC emission, performed with a simple log-parabolic electron distribution. The highest SEDs in Fig. 5.10e and Fig. 5.10f violate the Compton Catastrophe limit.

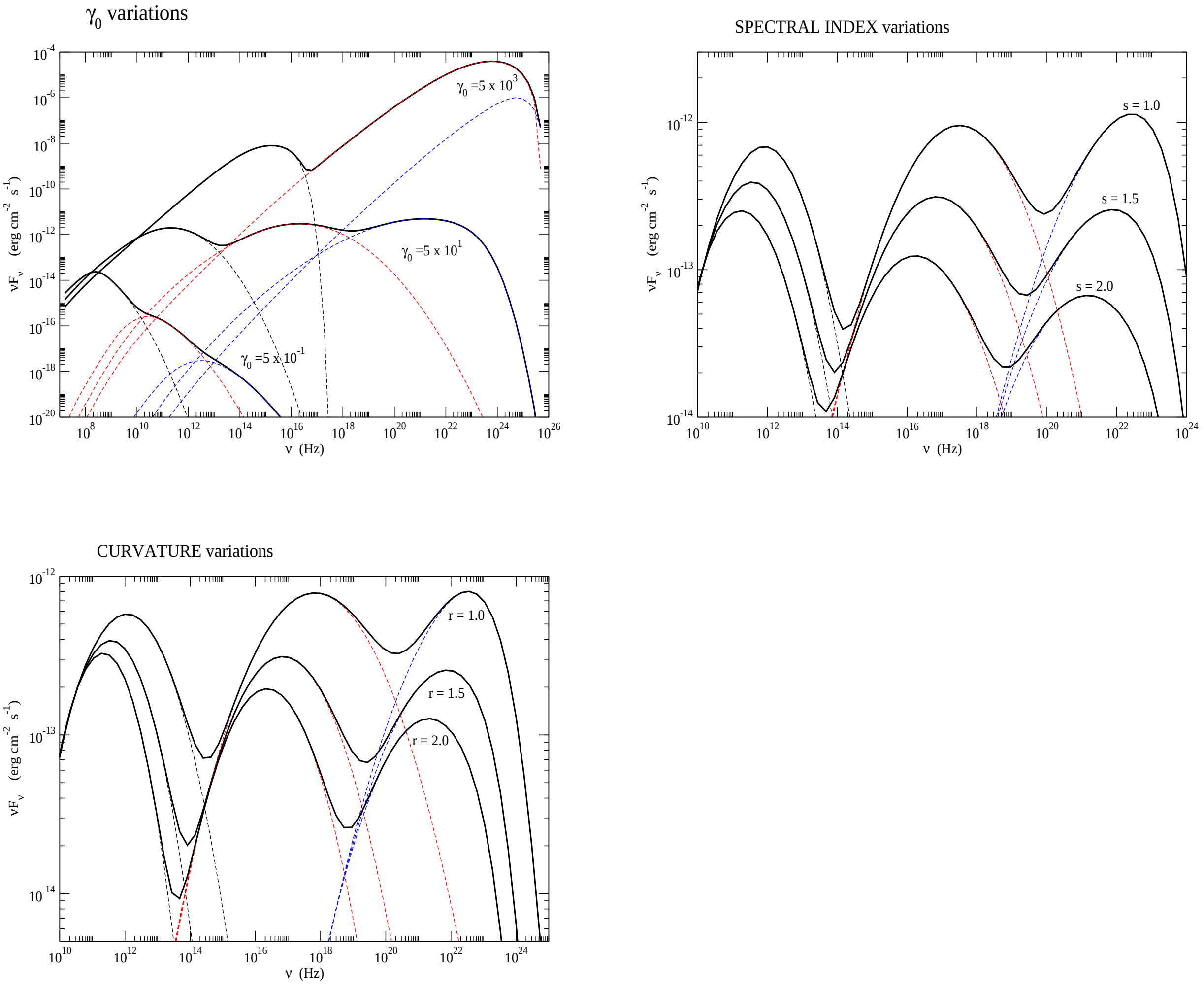

Figure 5.11: Synchrotron Self Compton simulations and 2^{nd} order IC emission, performed with a simple log-parabolic electron distribution. The highest SED in Fig. 5.11a violates the Compton Catastrophe limit.

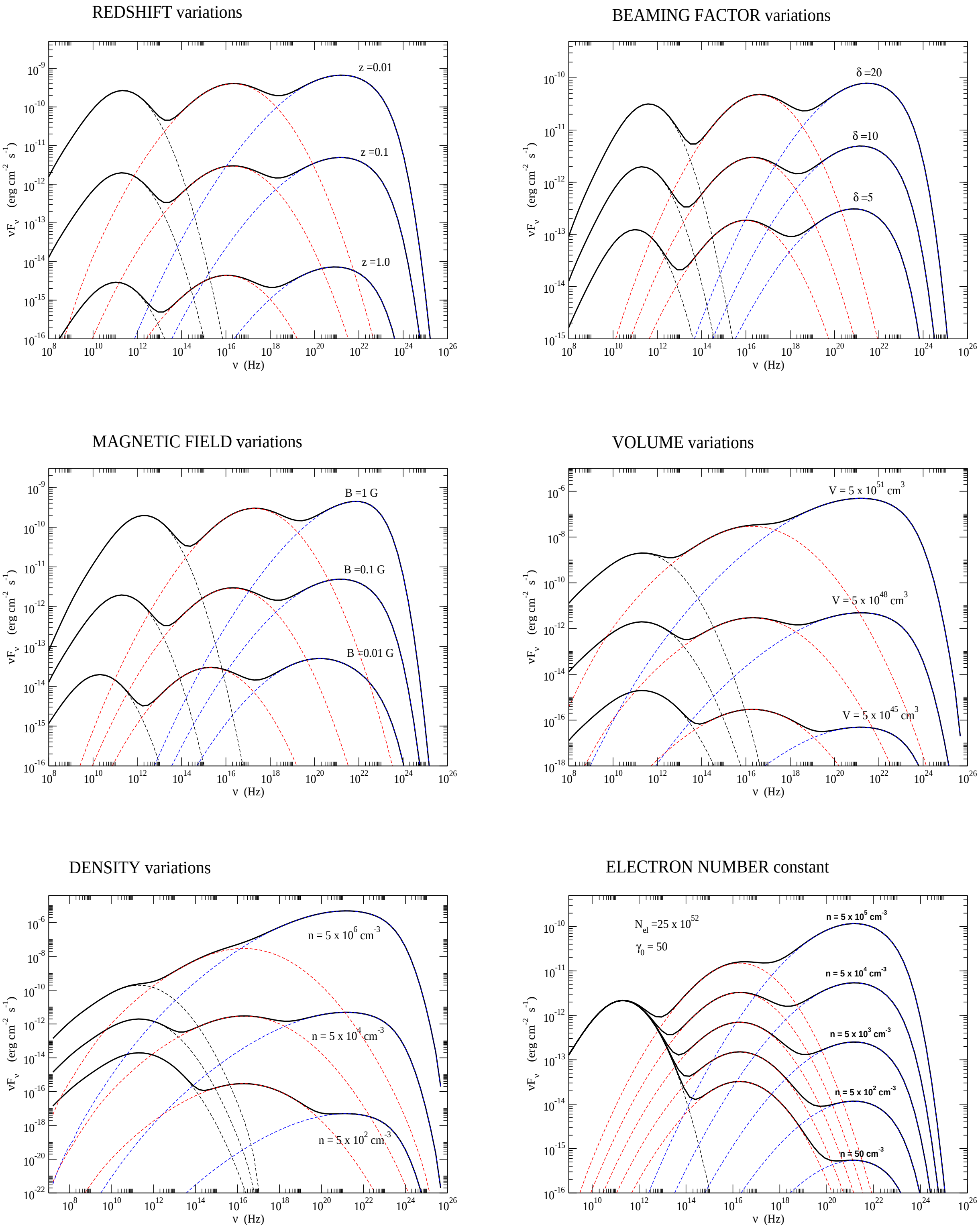

Figure 5.12: Synchrotron Self Compton simulations and 2^{nd} order IC emission, performed with a log-parabolic electron distribution combined with a power-law model at low energies. The highest SEDs in Fig. 5.12d, Fig. 5.12e and Fig. 5.12f violate the Compton Catastrophe limit.

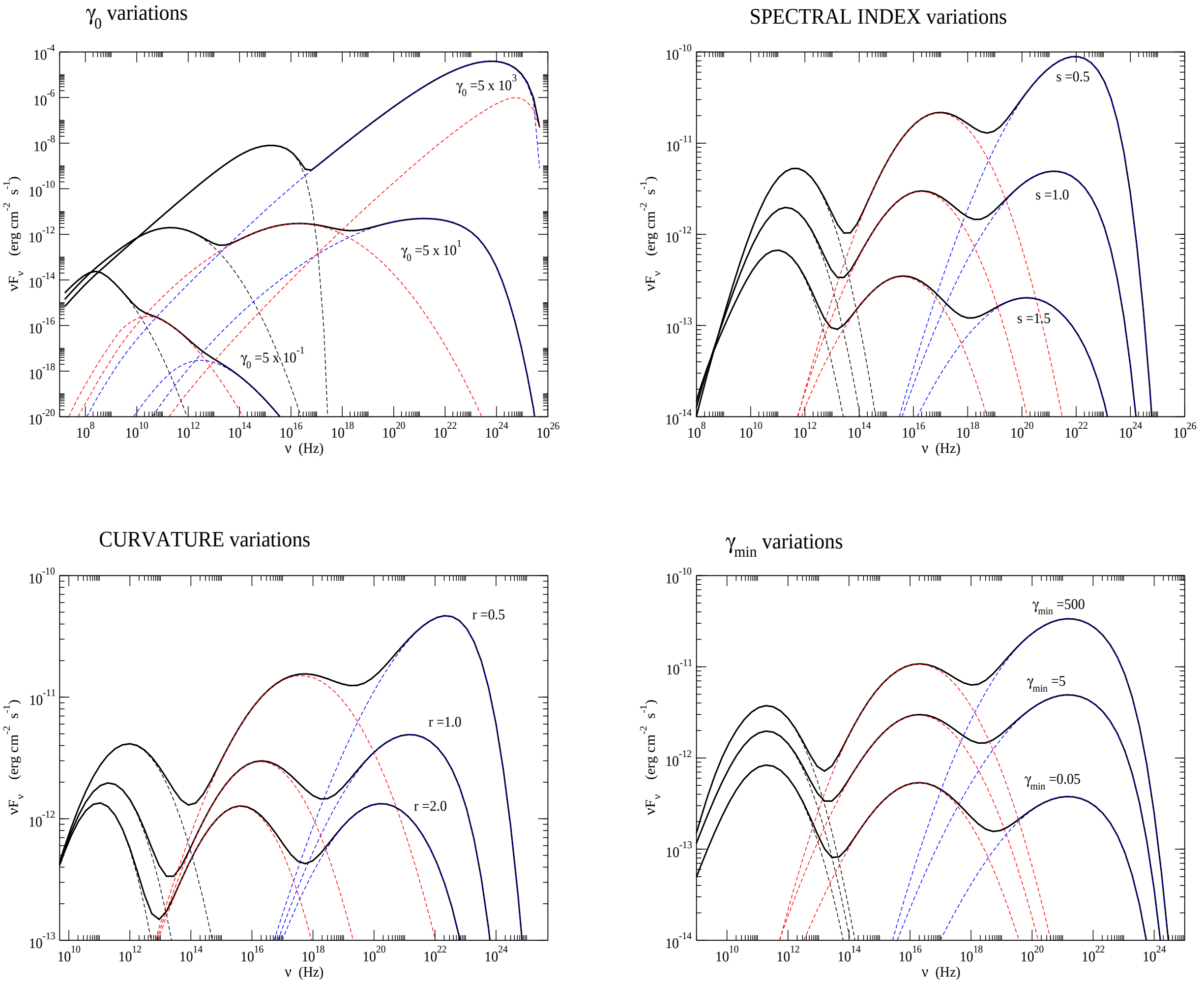

Figure 5.13: Synchrotron Self Compton simulations and 2^{nd} order IC emission, performed with a log-parabolic electron distribution combined with a power-law model at low energies. The highest SEDs in Fig. 5.13b, Fig. 5.13c and Fig. 5.13d violate the Compton Catastrophe limit.

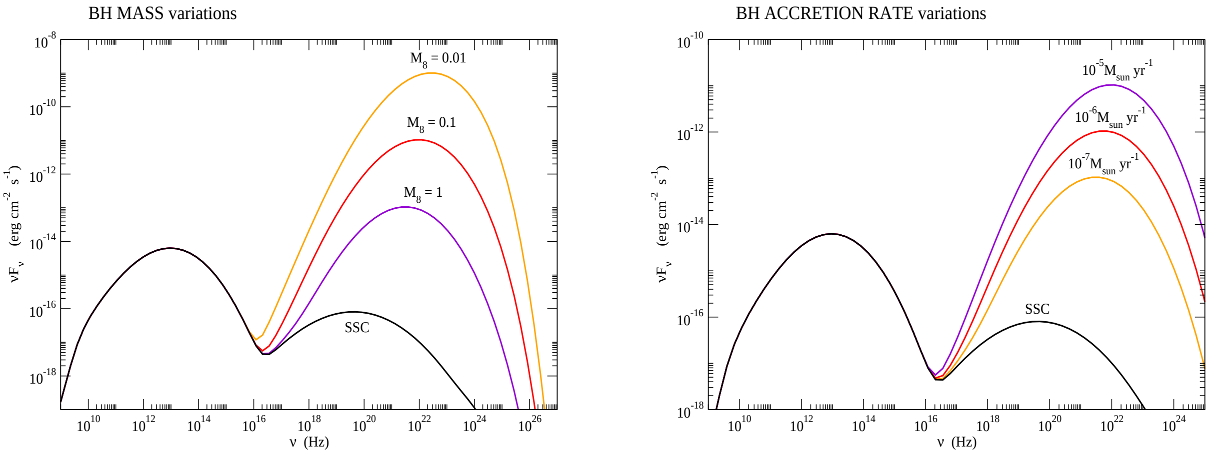

Figure 5.14: External Compton from an accretion disk seed photons simulations in comparison with the single zone SSC model (black line) performed with a log-parabolic electron distribution in Thomson regime. a) Plot of the EC component for different values of the Black Hole masses. b) Plot of the EC component for different values of the accretion rate.

Table 5.10: Input values for EC simulations

Parameter	*Symbol*	Values
Redshift	z	0.01
Beaming Factor	δ	10.00
Magnetic Field	$B\ (G)$	0.10
Volume	$V\ (cm^3)$	$1.00 \cdot 10^{48}$
Density	$n\ (cm^{-3})$	10.00
Electron energy	γ_0	$5.0 \cdot 10^2$
Spectral index	s	1.50
Curvature	r	1.50
Minimum energy	γ_{min}	50.00
Maximum energy	γ_{max}	$5.00 \cdot 10^8$
Disk inclination	$\cos i$	1.00
Disk distance	$D_{jet}\ (pc)$	1.00

6

Instruments, data reduction and analysis

In this thesis, a completely new analysis of X-ray spectra of HBLs rich sample is presented. This work used archival observations of *BeppoSAX* and *XMM-Newton* and more recent data from *Swift* XRT. For this reason a brief description of the instruments on board of these satellites and the data reduction procedures are described in this chapter. In particular, for comparing the results from different instruments an accurate analysis of the intercalibration was performed, as described in detail in Sect. 6.4. More detailed informations can be found on the multimission archive website: www.asdc.asi.it and in particular, for each mission on the: http://www.asdc.asi.it/bepposax/, sci.esa.int/xmm/ and heasarc.gsfc.nasa.gov /docs/swift/swiftsc.html, respectively.

6.1 *BeppoSAX*

6.1.1 Description

The Italian-Dutch X-ray Satellite BeppoSAX will be the first X-ray mission (and, of the coming near-future satellites, the only one) that will have the capability of observing sources over more than tree decades of energy - from 0.1 to 200 keV - with a relatively large area, a good energy resolution, associated with imaging capabilities (resolution of about 1′) in the range of 0.1 – 10 keV.

The configuration of the scientific payload and the energy bands covered by the different instruments are presented in Tab. 6.1 and in the following:

- MECS (Medium Energy Concentrator Spectrometers): a medium energy (1.3-10 keV) set of three identical grazing incidence telescopes with double cone geometry (Citterio et al. 1986, Conti et al. 1994), with position sensitive gas scintillation proportional counters in their focal planes (Boella et. al. 1996 and references therein).

- LECS (Low Energy Concentrator Spectrometer): a low energy (0.1-10 keV) telescope, identical to the other three, but with a thin window position sensitive gas scintillation proportional counter in its focal plane (Parmar et al. 1996 and references therein).

- HPGSPC, a collimated High Pressure Gas Scintillation Proportional Counter (4-120 keV, Manzo et al. 1997 and references therein).

- PDS, a collimated Phoswich Detector System (15-300 keV, Frontera et al. 1996 and references therein) Perpendicular to the axis of the NFI and pointed in opposite directions there are two coded mask proportional counters (Wide Field Cameras, WFC, Jager et al. 1996 and references therein) that provide access to large regions of the sky in the range 2-30 keV. Each WFC has a field of view of 20° x 20° (FWHM) with a resolution of 5′.

Finally, the four lateral active shields of the PDS will be used as a monitor of gamma-ray bursts with a fluence greater than about 10^{-6} erg cm^{-2}s^{-1} in the range 60-600 keV, with a temporal resolution of about 1 ms.

6.1.2 Data reduction procedure

Data set, analysed in this thesis, includes the *BeppoSAX* observations of our sample sources performed with the Narrow Field Instruments (NFIs): LECS (0.1 – 10 keV, Parmar et al. 1997), MECS (1.3 – 10 keV, Boella et al. 1997) and PDS (13 – 300 keV, Frontera et al. 1997). Events for spectral analysis

Table 6.1: *BeppoSAX* Instruments

Instrument	Range (keV)	Field Angul. (¡FWHM)	Res. (arcmin)	Area cm^2 (% FWHM)	Energy Res.
LECS	0.1-10	0.5	3.5 @ 0.25 keV	22 @ 0.25 keV	8 x (E/6) $^{-0.5}$
MECS	1.3-10	0.5	1.2 @ 6 keV	150 6 keV	8 x (E/6) $^{-0.5}$
HPGSPC	4-120 keV	0.5	collimanted	240 @ 30 keV	4 x (E/60) $^{-0.5}$
PDS	15-300 keV	0.5	collimated	60080 keV	15 x (E/60) $^{-0.5}$

were extracted following standard procedures. In particular, LECS and MECS events were selected in circular regions centred at the source position, with radii of 4’ and 8’ depending upon the count rate, as indicated by Fiore et al. (1999). The response matrices and the ancillary response files used in our analysis have been taken from the BeppoSAX SDC ftp server (September 1997 release), and background spectra were taken from the blank field archive. Standard procedures and selection criteria were applied to the data to avoid the South Atlantic Geomagnetic Anomaly, and the solar, bright Earth and particle contaminations using the SAXDAS (v. 2.0.0) package.

6.2 *XMM-Newton*

6.2.1 Description

A project of the European Space Agency XMM-Newton, the X-ray Multi-Mirror Mission, is the second cornerstone of the Horizon 2000 program of the European Space Agency (ESA). XMM-Newton was launched on December 10 1999. The observatory consists of three coaligned high throughput 7.5m focal length telescopes with 6 arc second FWHM ($15''$ HPD) angular resolution.

XMM-Newton provides images over a $30'$ field of view with moderate spectral resolution using the European Photon Imaging Camera (EPIC), which consists of two MOS and one PN CCD arrays. High-resolution spectral information (E/dE$\simeq$300) is provided by the Reflection Grating Spectrometer (RGS) that deflects half of the beam on two of the X-ray telescopes. The observatory also has a coaligned 30 cm optical/UV telescope called the Optical Monitor (OM). Main properties of the instruments on board of *XMM-Newton* are reported in Tab. 6.2.

6.2.2 Data reduction procedure

Extractions of all light curves, source and background spectra were done using the *XMM-Newton* Science Analysis System (SAS) v6.5.0. The Calibration Index File (CIF) and the summary file of the Observation Data File (ODF) were generated using Updated Calibration File (CCF) following the ”User’s Guide to the *XMM-Newton* Science Analysis System” (Issue 3.1) (Loiseau et al. 2004) and ”The *XMM-Newton* ABC Guide” (vers. 2.01) (Snowden et al. 2004). Event files were producted by *XMM-Newton* EMCHAIN pipeline. The standard reduction of the events list for MOS data, was performed involving subtraction of hot and dead pixels, removal of events due to the electronic noise and correction of event energies for charge transfer losses.

To provide the most conservative screening criteria MOS data files were also filtered to include all single to quadruple events (PATTERN $\leq$ 12) with pulse high rate in the range of 500 to 12000 eV and with expression FLAG = 0. Lightcurves for every dataset were extracted and all high-background time intervals, were filtered out by excluding time interval contaminated by solar flare signal. To perform this selection, the count rate in the 10 – 15 keV band for the entire MOS detectors were determined. We first discarded only time intervals with a count rate that exceeds 0.35 counts per second as indicated

Table 6.2: *XMM-Newton* Instruments

Instrument	EPIC MOS	EPIC PN	RGS	OM
Bandpass	0.15-12 keV	0.15 15 keV	0.35-2.5 keV	180-600 nm
Orbital target visibility	5-135 ks	5-135 ks	5-135 ks	5-145 ks
Sensitivity (after 10 ks)	$\sim 10^{-14\ (1)}$	$\sim 10^{-14\ (1)}$	$\sim 8^{-5\ (2)}$	20.7 mag $^{(3)}$
FOV	30’	30’	~ 5’	17’
PSF (FWHM/HEM)	5”/14”	6”/15”	N/A	1.4”-2.0”
Pixel size	40μ m (1.1”)	150 μ m (4.1”)	81 μ m (9 x 10^{-3} A)	0.476513”
Timign resolution	1.5 ms	0.03 ms	0.6 s	0.5 s
Spectral resolution	~ 70 eV	~ 80 eV	0.04/0.025 A	350

(1): erg cm^{-2} s^{-1}.
(2): ph cm^{-2} s^{-1} in 10^4 s.
(3): 5σ detection of an AO star in 1000s.

in the ”User’s Guide to the *XMM-Newton* Science Analysis System” (Issue 3.1) (Loiseau et al. 2004). However applying this criterium, we noticed that a low background state, placed between two high neighboring peaks due to a solar flare, can even include a residual contamination to the source signal which modifies the spectral distribution. A more conservative selection for good time intervals have been adopted to have a high quality signal, excluding time ranges that appeared contaminated by solar flares. Then we selected good time intervals by direct inspection far from solar flare peaks and without count rate variations on time scales shorter than 500 seconds. The TABGTIGEN task of *XMM-Newton* Science Analysis System (SAS) was used to build good time intervals.

Photons were extracted from an annular region using different apertures to minimize pile-up, which affects MOS data. The mean value of external radius for the annular region is 40 ″. To filter out pixels affected by significant pile-up, the internal region was selected by using EPATPLOT task in *XMM-Newton* Science Analysis System (SAS) for each observation.

In FULL WINDOW images, the background spectrum was extracted from a circular region of the size comparable to the source region, in a place where visible sources were not present (typically off axis. For other observations, in PARTIAL WINDOW images, no regions sufficently far from the source for the background extraction were found. In these cases we used background from blank-field event files (www.sr.bham.ac.uk). Anyway we estimated that the average X-rays background flux was always at ~ 1% level of source flux, resulting in a negligible contamination in the spectral parameter determination. The Photon Redistribution Matrix and the Ancillary Region File were created for each observation, by using RMFGEN and ARFGEN tasks of SAS. A more restricted energy range (0.5–10 keV) was used to account for possible residual calibration uncertainties. To insure the validity of Gaussian statistics, data were grouped by combining instrumental channels so that each new bin comprises 40 counts or more.

6.3 *Swift*

6.3.1 Description

Swift is a multiwavelength observatory dedicated to the study of gamma-ray burst (GRB) science. *Swift* , part of a NASA’s medium explorer (MIDEX) program, was developed by an international collaboration and was launched into a low-Earth orbit on a delta 7320 rocket on November 20 2004. It has a complement of three co-aligned instruments: the Burst Alert Telescope (BAT), the X-ray Telescope

Table 6.3: Burst Alert Telescope: BAT

Aperture	Coded Mask
Detecting Area	5200 cm^2
Detector	CdZnTe
Detector Operation	Photon Counting
FOV	2.0 sr (partially coded)
Detection Elements	256 modules of 128 elements
Detector Size	4mm x 4mm x 2mm
Telescope PSF	17 arcminutes
Location Accuracy	1-4 arcminutes
Energy Range	15-150 keV

Table 6.4: X-ray Telescope: XRT

Telescope	Wolter I
Detector	XMM EPIC CCD
Effective Area	135 cm^2 @ 1.5 keV
Detector Operation	Photon Counting & Windowed Timing
FOV	23.6 x 23.6 arcminutes
Detection Elements	600 x 600 elements
Pixel scale	2.36 arcsec/pixel
Telescope PSF	18 arcsec HPD @ 1.5 keV
Location Accuracy	3-5 arcseconds
Energy Range	0.2-10 keV
Sensitivity	2 x 10^{-4} erg cm^{-2} s^{-1} in 10^{-4} sec

(XRT) and the Ultraviolet/Optical Telescope (UVOT). Thecnical description of these three instruments are reported in Tab. 6.3, 6.4 and 6.5 for BAT, XRT and UVOT instruments respectively.

6.3.2 Data reduction procedure

The XRT data analysis is performed with the XRTDAS software (v. 2.1), developed at the ASI Science Data Center (ASDC) and included in the HEAsoft package (v. 6.0.2). Event files were calibrated and cleaned with standard filtering criteria using the XRTPIPELINE task combined with the latest calibration files available in the Swift CALDB distributed by HEASARC. Events in the energy range 0.3–10 keV with grades 0–12 (Photon Counting mode, PC) and 0–2 (Windowed Timing mode, WT) are used in the analyses (see Hill et al. 2004 for a description of readout modes, and Burrows et al., 2005 for a definition of XRT event grades). To avoid artificially high χ^2 values and possible biases in spectral parameter estimations, The advice of the XRT calibration experts were followed, excluding from the analysis the energy channels between 0.4 keV and 0.6 keV (Campana & Cusumano 2006, private communication).

For the WT mode data, events are selected for temporal and spectral analysis using a 40 pixel wide (1 pixel = 2.36 arcs) rectangular region centered on the source, and aligned along the WT one dimensional stream in sky coordinates. Background events are extracted from a nearby source-free rectangular region of 40 pixels width and 20 pixels height.

Table 6.5: Ultraviolet/Optical Telescope: UVOT

Telescope	Modified Ritchey-Chrétien
Aperture	30 cm diameter
F-number	12.7
Detector	Intensified CCD
Detector Operation	Photon Counting
FOV	17 x 17 arcminutes
Detection Elements	2048 x 2048 pixels
Telescope PSF	0.9 arcsec @ 350 nm
Location Accuracy	0.3 arcseconds
Wavelenght Range	170 nm - 650 nm
Colors	6
Spectral Resolution (Grisms)	$\lambda/\Delta\lambda \sim 200$ @ 400 nm
Sensitivity	B = 24 in white light in 1000 sec
Pixel Scale	0.48 arcseconds
Bright Limit	$m_v = 7$ mag

For PC mode data, when the source count rate was above ~ 0.5 counts s^{-1} the data were significantly affected by pile-up in the inner part of the Point Spread Function (PSF). To remove the pile-up contamination only events contained in an annular region centered on the source were extracted. The inner radius of the region was determined comparing the observed PSF profiles with the analytical model derived by Moretti et al. (2005), and tipically has a 4 or 5 pixels size, while the outer radius is 20 pixels for each observations. For *Swift* observations in which the source count rate was below the pile-up limit, events are instead extracted using a 20 pixel radius circle. The background for PC mode is estimated from a nearby source-free circular region of 20 pixel radius.

Ancillary response files are generated with the XRTMKARF task applying corrections for the PSF losses and CCD defects. The latest response matrices (v. 009) available in the Swift CALDB are used.

6.4 Data analysis

6.4.1 Spectral Analysis

The entire spectral analysis was performed with the XSPEC software package, version 11.3.2 (Arnaud, 1996). The X-ray continuum was described with different spectral models: an absorbed power-law with column density either free, or fixed at the Galactic value; a power-law with an exponential cutoff; a log-parabolic model (Landau et al. 1986, Massaro et al., 2004); the latter two models are absorbed by a Galactic column density (see Tab. 7.3).

The log-parabolic model is tested under the form

$$F(E) = K\, E^{-a-b\, log(E)} \quad [photons\ cm^{-2}\ s^{-1}\ keV^{-1}], \tag{6.1}$$

or the alternative SED representation

$$S(E) = S_p\, 10^{-b\, log^2(E/E_p)} \tag{6.2}$$

with $S_p = E_p^2\, F(E_p)$. After eq. 6.2 the values of the parameters E_p (the location of the SED energy peak), S_p (the peak height), and b (the curvature parameter) can be estimated independently in the fitting procedure (Tramacere et al., 2007a). In all models with fixed Galactic column density, we use

N_H values from the LAB survey (Kalberla et al., 2005) or from (Lockman & Savage, 1995), as reported in Tab. 7.3; consistent spectral parameters (within a 1σ interval) from these two column densities are found. Tabs. E1, E.2, E.3 in App. E report the results from the spectral analyses performed with the standard N_H values from Lockman & Savage (1995).

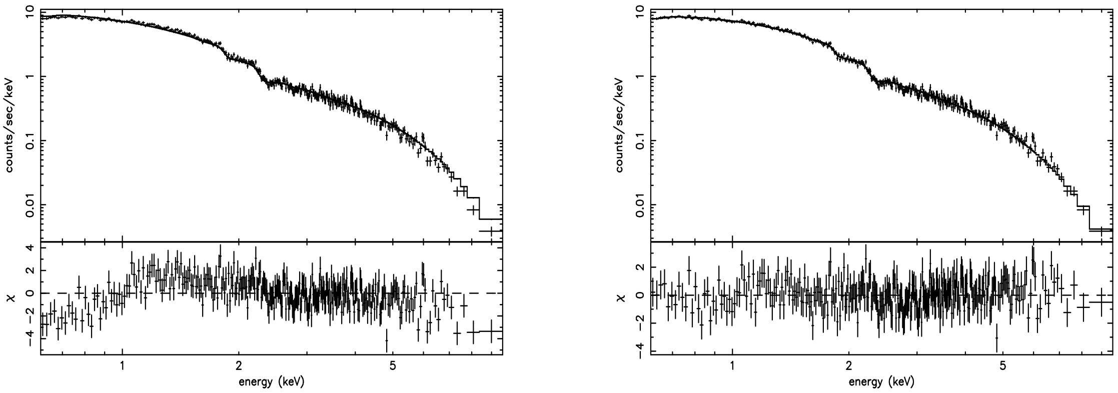

Figure 6.1: *XMM-Newton* EPIC-MOS spectrum from the observation of Mkn 421 performed on 08/05/01. *Left*: the systematic deviations on both sides of the residuals from a best fit power-law with Galactic N_H show the need of intrinsic curvature. *Right*: the deviations disappear with the log-parabolic model with Galactic N_H .

Typically, the X-ray spectra of HBLs appear to be featurless and curved (Giommi et al., 2005, Perri et al., 2007) over a broad energy range. Absence of spectral features related to any absorbing material was also recently confirmed by Blustin et al. (2004) who performed a detailed analysis of *XMM-Newton* RGS spectra of four sources in our sample, namely: 1H 1219+301, 1H 1426+428, Mrk 501 and PKS 0548-322.

With an absorbed power-law model unacceptable values of χ^2_r are usually obtained; even when leaving the low energy absorption as a free parameter, these models are not adequate to describe the high energy end of the X-ray spectra. Fig. 6.1a shows an observation of Mrk 421 performed on 08/05/2001; in this case it is possible to see the systematic deviations on both sides of the residuals from a best fit power-law with Galactic N_H show the need of intrinsic curvature, and their disappearance with the log-parabolic model with Galactic N_H .

Adding to a power-law model a high energy exponential cutoff E_c corrects the residuals at high energies; however, values of E_c beyond the instrumental energy range are often obtained. In a few cases where an exponential cutoff lies within the observed energy range, the χ^2_r values are significantly higher than those found with the log-parabolic model. In some cases, poor statistics (due to short observational exposures) or restricted instrumental energy range (*XMM-Newton* and *Swift* relative to *BeppoSAX*), combine with the location of SED peak outside the observational energy range to make it difficult evaluating a possible spectral curvature; then the single power-law model constitutes an acceptable description of the X-ray spectra.

Analyses of long exposure pointings are performed using time-resolved spectra as described in Tramacere et al., (2007a), to avoid averaging significant spectral variations while still conserving a sufficient number of counts per observation as to evaluate the spectral curvature. Results of the spectral analyses are reported in App. E; the statistical uncertaintes quoted refer to the 68% confidence level (one Gaussian standard deviation). Observations with less than 30 energy bins after the rebinning procedure or with less than 800 seconds of exposure were not considered for these analyses.

In conclusion, in agreement with other previous X-ray analyses (Massaro et al. 2004, Massaro et al. 2006, Tramacere et al. (2007a), Tramacere et al. (2007b), see also Perlman et al. 2005), for about 70% of all observations the best description for synchrotron spectra of HBLs close to their peak energy is provided by a log-parabolic model. The percentage increases to 99% for observations with exposures longer than 2000 seconds.

6.4.2 Intercalibration between different instruments

To study the spectral evolution of the curvature parameter, it is crucial verify the intercalibration between different instruments provide consistent results. It is not possible a direct comparison between *BeppoSAX* and the more recent satellites *XMM-Newton* and *Swift* because there are not simultaneous pointings. It was used a statistical approach comparing, for given sources in similar luminosity states, the range of curvatures measured with *BeppoSAX*, *XMM-Newton* and *Swift*, that resulted in fully satisfactory agreement.

In the case of *XMM-Newton* and *Swift*, there are two simultaneous pointings of 1H 1426+418, performed on the 19/06/05 and 25/06/05. For these observations a detailed analysis was performed and the curvature parameter, the peak frequency and the X-ray flux, evaluated with the log-parabolic model (see eq. 6.1), are in agreement within 1σ interval, for the MOS and XRT instruments. The intercalibration constant evaluated minimizing the distance to the *XMM-Newton* and *Swift* data is k_c = 0.836. Fig. 6.2 reports both the observed SED and the *Swift* corrected one.

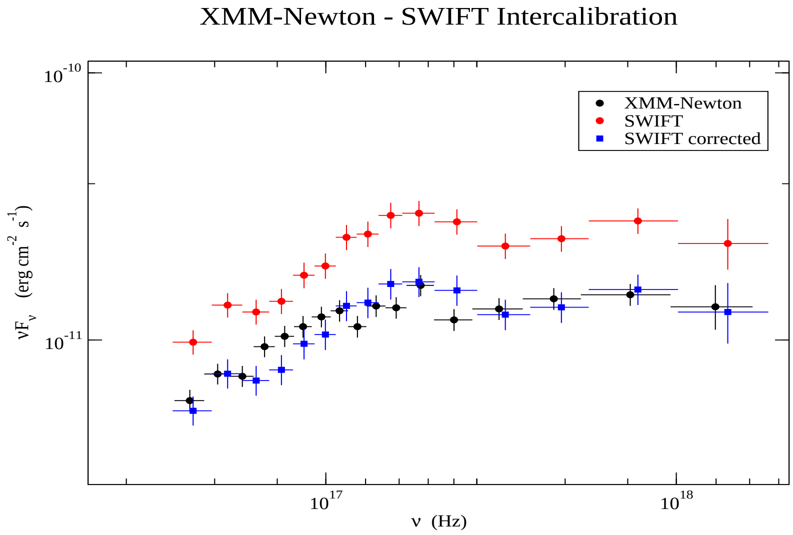

Figure 6.2: SED of the 1H 1426+418 simultaneously observed by *XMM-Newton* (black points) and *Swift* (red points), Blue points represent the *Swift* corrected spectrum for the k_c intercalibration constant.

7

X-ray spectral analysis of HBL objects TeV detected

In this chapter, the results of the X-ray analyses of all HBLs detected at TeV energies up to 01/11/2007 are presented. In the first section, the case of Mrk 421 is considered in details because for these source there is a large number of observations (more than 200) and it is possible perform an exhaustive statistical investigation of the correlations between spectral parameters. This analysis is published in the paper Tramacere, Massaro & Cavaliere (2007). In the second section, the observations of the other 14 TeV detected HBLs are described, and their spectral behavior is compared with that of Mrk 421. All these results are reported in a second paper, Massaro et al. 2007, in Astronomy and Astrophysics inpress. Finally, in the last section, the X-rays analyses of other HBLs, some of them unpublished, that are likely considered good targets for TeV observations.

7.1 THE CASE OF Mrk 421

With its redshift $z = 0.031$, Mrk 421 is among the closest and best studied HBL. In fact, it is one of brightest BL Lac objects in the UV and in the X-ray bands, observed in γ rays by EGRET (Lin et al. 1992); it was also the first extragalactic source detected at TeV energies in the range 0.5-1.5 TeV by the Whipple telescopes (Punch et al. 1992, Petry et al. 1996).

The source is classified as HBL because its synchrotron emission peak ranges from a fraction of a keV to several keVs. In fact, its flux changes go along with strong spectral variations (Fossati et al. 2000a). The spectral shape generally exhibits a marked curvature, well described by a log-parabolic model (Landau et al. 1986).

A new study of the time-variable properties of its SED based on the full collection of *XMM-Newton* data taken with EPIC CCD cameras, sensitive in the energy range 0.3–10 keV is presented here; this work is also performed using previous X-ray observations with *ASCA*, *BeppoSAX*, *RXTE*, *EUVE* to cover an overall time span of nine years. In particular, *XMM-Newton* observed Mrk 421 many times, and a large amount of data has been collected. Some of these observations have been recently analysed by other authors, but a full report of all observations between May 2000 and November 2005 had not been published yet. A new analysis of all *XMM-Newton* observations of Mrk 421was preformed, particularly relevant as its synchrotron emission peaks in the *XMM-Newton* energy range.

Specifically, extending the previous work of Tanihata et al. (2004), the correlations between the position and the height of SED peak have been studied and interpreted in terms of signatures of the synchrotron emission. In addition, a new correlation of the SED peak with the spectral curvature was investigated discussing its implications as to the electron acceleration mechanisms.

The methods and the models used in the spectral analysis are described in Sect. 6.4 and the results for the data set considered is reported in the paper by Tramacere et al. (2007a).

7.1.1 Signatures of the synchrotron emission

Correlations between S_p and E_p provide interesting indications concerning the driver of the spectral changes in X-rays, in terms of the synchrotron emission mechanism from one dominant homogeneous component. The analysis of this correlation is performed on two data sets: the *XMM* set and the *FULL* set . The former corresponds to the results of the spectral analysis reported in Tramacere et al. (2007a) , while the latter is obtained on adding the results from previous analyses as reported in

Tanihata et al. (2004).

Correlations between the spectral parameters are tested on using both a linear correlation coefficient (r_{lin}) and a logarithmic one (r_{log}), and fit the data with a linear and log-linear model following the statistical methods described in D'Agostini (2005) (see also App. D).

Results from this correlation study are given in Tab. 7.1. The correlation coefficient $r_{log} \simeq 0.7$ is significant, specifically with a chance probability value close to zero. The data in the *XMM* set may be described by a power-law function; the value of the exponent α so obtained is $\alpha = 1.4 \pm 0.3$. On fitting the *FULL* set the power-law index found is $\alpha = 1.2 \pm 0.1$, consistent with the above value. Even if we took the range of E_p between $0.5 - 1.0$ keV where the run of the *FULL* data apparently steepens, the values of the best fit would yield $\alpha = 1.2 \pm 0.1$, quite far from 4. This analysis confirms that the cases $\alpha = 1.5$ and $\alpha = 2$ are those most relevant as dominant mechanisms.

A closer analysis and an interpretation of these results are given in the following. A sensitive point in our statistical analysis and its interpretation is the presence of "hidden" parameters contributing to

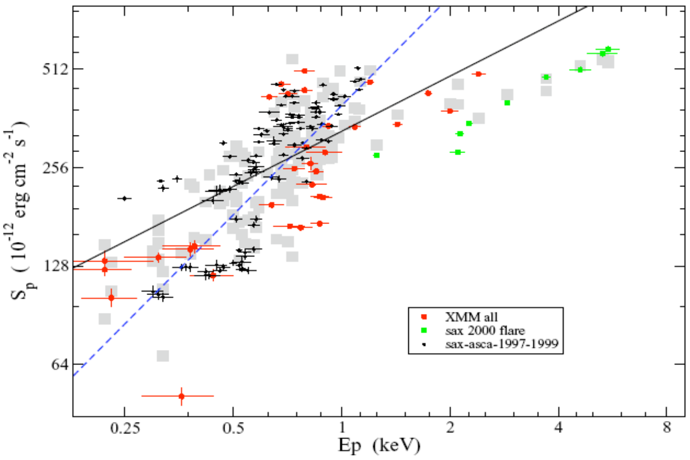

Figure 7.1: The scatter plot of the peak energy E_p and the maximum of the SEDs S_p compared with the results of a Monte Carlo simulation (grey squares). Dashed line represents the power-law best fit without taking into account extravariance for the *FULL* data-set. Solid line represents the power-law best fit taking into account extravariance for the *FULL* data-set.

Table 7.1: Statistical parameters for the correlation between E_p and S_p.

Dataset	r_{lin}	p_{lin}	r_{log}	p_{log}	α	α_v	σ_v
XMM	0.63	< 0.001	0.71	< 0.001	1.4 ± 0.3	0.7 ± 0.1	0.35 ± 0.05
FULL	0.56	< 0.001	0.67	< 0.001	1.2 ± 0.1	0.56 ± 0.05	0.33 ± 0.02
FULL ($E_p < 1.2$)	0.72	< 0.001	0.72	< 0.001	1.7 ± 0.1	0.99 ± 0.07	0.29 ± 0.02
FULL ($E_p > 1.2$)	0.87	0.004	0.84	0.007	0.6 ± 0.1	0.43 ± 0.08	0.13 ± 0.03

variability and/or to correlations. On the basis of the formalism that for reader's convenience is reported in App. D, in the following the possibility that a correlation may be introduced by a parameter that is not directly determined from the data (whence the name "hidden") is discussed.

This issue arises when one estimates two parameters, say x and y, statistically independent but depending physically on a third parameter, k say, that is not directly observed ("hidden"); in other words, it can be observed $x = x(x', k)$ and $y = y(y', k)$. Again, a correlation will arise between x and y due to their dependence on k, and this may add to any physical correlation between x' and y'.

A case in point is provided by the beaming effects. In BL Lacs beaming is a key property; though only rarely measured directly, this can introduce dependence between the observed quantities S_p and E_p. It is convenient to distinguish the variables E'_p, S'_p in the beam reference frame from the observed ones expressed as

$$\begin{aligned} E_p &= E'_p \delta \\ S_p &= S'_p \delta^4. \end{aligned} \tag{7.1}$$

While this corresponds to the case $\alpha = 4$ that our preliminary analysis tended to exclude, it is important to reconsider δ as a hidden parameter introducing a covariance term and contributing to correlation.

Clearly, the actual contribution depends on the probability density functions (PDF) of E_p, S_p and δ. To study this, a sample of uncorrelated pairs of variables was generated with a Monte Carlo code (x', y'). Then these have been transformed according to eq. 7.1, that is, with $x = \delta x'$ and $y = \delta^4 y'$, choosing $\delta = 10$ as a typical value for Mrk 421. The x' variables were generated so that the x variables have the same PDF as E_p; on the other hand, the y' variables were generated from a normal distribution with mean value $\mu' = 1.0$ and $\sigma' = \mu'/3$. The y variables are imposed to have the same dispersion as S_p in the *FULL* data; this dispersion depends not only on σ' but also on the distribution of δ, so we have to derive a constraint on the value of σ_δ. In fact, the standard deviation of the observed values of S_p is about 120 (erg cm^{-2} s^{-1}) to be compared with the average value of about 290 (Fig. 7.1); assuming, as an extreme case, that the dispersion σ_S of S_p is generated only by the variance σ_δ, and applying standard propagation, we obtain $\sigma_\delta/\mu_\delta = \sigma_S/(4\,S_p) \lesssim 10$.

Now generating δ from a normal distribution with $\mu_\delta = 10$ and $\sigma_\delta = 0.75$, and a correlation coefficient $r_{log} = 0.3$ between the logarithms of x and y was found. On decreasing the variance of y' and increasing that of δ, the correlation increases but only slightly; for example, if we take $\sigma' = \mu'/6$ and increase the value of σ_δ to 0.95, we obtain $r_{log} = 0.36$.

In summary, the beaming factor can affect the observed correlation coefficient, but only up to values $r_{log} < 0.3$ which are significantly below the observed value 0.67. Finally, the beaming alone is responsible neither for the values of $\alpha \approx 1$ nor for the correlation observed. Note that the value $\sigma_\delta/\delta \lesssim 0.1$, bounded by the dispersion of the full data, is remarkably low when compared to the average typical value of $\mu_\delta \simeq 10$, and implies the beaming factor to have been closely constant for Mrk 421 during our observational span of about 9 yr.

It follows that both the variations of S_p corresponding to the estimated values of α and their scatter must be importantly contributed by a physical process in the beam rest frame, such as variations of magnetic fields or scaling up or down of all the electron energies.

In fact, a second effect coming from a "hidden" parameter with its fluctuations is to produce scatter of the data. As explained in App. D, it is possible to account for this effect by adding an "extravariance" in the likelihood function. In the case of the *XMM* data set, the extravariance accounting for their scatter is estimated at $\sigma_v = 0.35 \pm 0.05$, and for the corresponding value of the slope we obtain $\alpha_v = 0.7 \pm 0.1$, whilst for the *FULL* data set we obtain $\sigma_v = 0.33 \pm 0.02$ and $\alpha_v = 0.56 \pm 0.05$ (see Tab.7.1). The derived values of the α index are considerably affected by the extravariance; in fact, the extravariance term in the log-likelihood function dominates the term from measurement uncertainties, to the point of providing power-law indices close to those obtained simply from fitting the data with no weights for their precision.

Such different values of α and α_v (Tab. 7.1) lead us to test an actual change in the power-law index *alpha* at about 1 keV. To do this, we split the *FULL* set into two sets, one with $E_p < 1.2$ keV and the other with $E_p > 1.2$ keV; results of fits are reported in the last two lines of Table 3. The values of α found for the two data sets differ significantly, being $\alpha_1 = 1.7 \pm 0.1$ and $\alpha_2 = 0.6 \pm 0.1$, for $E_p < 1.2$ keV and $E_p > 1.2$ keV, respectively. This could be interpreted as a change of α with the state of the source, and the associated likelihood by means of a Monte Carlo simulation was estimated. A set of values for E_p, S_p was generated as follows:

- E_p values are generated as to have the same PDF as observed once transformed by the first of eq. 7.1.
- Beaming factors are generated from a normal distribution with $\mu_\delta = 10$ and $\sigma_\delta = 0.5$.
- The slope of the (unbeamed) power-law is generated from two normal distributions with mean value 0.85 and standard deviation 0.09 for $E_p < 1.2$ keV, and mean value 0.33 and standard deviation 0.07 for $E_p > 1.2$ keV.
- Values of S_p are generated from eq. 5.9 and transformed by the second of eq. 7.1.

The number of events so generated is 150 (similar to the *FULL* data set), and in Fig. 7.1 their scatter plot (grey box) is reported. Interestingly, the simulated and the observed points have similar behaviour and similar statistical properties. Note the correlations, given in the beam reference frame by α_1 and α_2, when subject to beaming with a narrow variance come very close to account for the data with their scatter.

7.1.2 Signatures of the acceleration mechanisms

Finally, a study of correlation between b and E_p is performed, aimed at pinpointing possible signatures of the electron acceleration processes in the spectral evolution of a homogeneous dominant component. The same data set and statistical tools of the previous section are used.

Such a correlation had never been tested previously. An analysis of *XMM* set shows that the correlation coefficients are negative and low, that is, $r_{lin} = -0.29$ and $r_{log} = -0.13$. The former corresponds to a low chance occurrence (0.05), but this is significantly high (0.24) for r_{log}. By direct inspection we see that there are three points (enclosed by the dashed ellipse in Fig. 7.2) corresponding to the same *XMM* pointing on 01/11/00, that maximally deviate from the average sample behaviour. On excising this observation and reanalysing the remaining data (denoted by *XMM* * in Tab.7.2) the substantially higher correlation coefficients $r_{lin} = -0.60$ and $r_{log} = -0.62$ were obtained, corresponding to the high significance, given in Tab. 7.2.

To see whether the 01/11/00 observation constitutes a unique event, we analysed the *FULL* data set with and without (denoted by *FULL* *) this pointing; Tab. 7.2 shows that the values of r_{lin} and r_{log} for *FULL* and *FULL* * are close, indicating that the observation excised has not materially changed the overall statistical behaviour.

These values are sufficiently high to warrant a brief discussion of the importance of the correlation found, along two ways. This pointing may constitute just a rare source state in the sample. On the other hand, this may not constitute a singular event, considering that all *XMM* and *FULL* data (Fig. 7.2) appear to outline an upper limit to the curvature observed at any values of E_p. For example, for E_p around 1 keV, curvatures higher than about $b \approx 0.45$ were never observed. The inverse correlation between b and E_p may be interpreted in the framework of acceleration processes of the emitting electrons.

A first interpretation of the correlation between b and E_p is in the framework of statistical acceleration

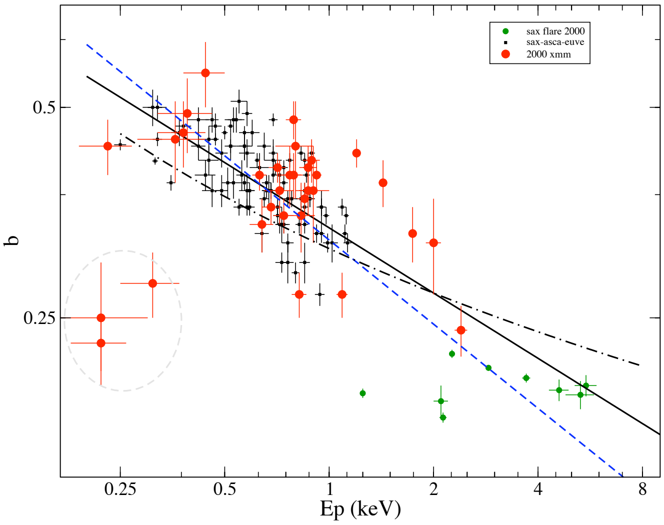

Figure 7.2: The scatter plot of the peak energy E_p and the curvature parameter b. The dashed line represents the power-law best fit without taking into account extravariance for the *FULL* data-set. The solid line represents the power-law best fit on taking into account extravariance for the *FULL* data-set. The dashed-dotted line represents the relation between E_p and b expected from eq. 7.8

Table 7.2: Statistical parameters for the correlation between E_p and b

Dataset	r_{lin}	p_{lin}	r_{log}	p_{log}	α_{pl}	α_{σ_v}	σ_v
XMM	-0.29	0.05	-0.13	0.24	-0.04 ± 0.03	-0.04 ± 0.06	0.18 ± 0.03
XMM *	-0.60	< 0.001	-0.60	< 0.001	-0.20 ± 0.03	-0.22 ± 0.06	0.12 ± 0.02
FULL	-0.63	< 0.001	-0.70	< 0.001	-0.404 ± 0.005	-0.31 ± 0.02	0.13 ± 0.01
FULL *	-0.67	< 0.001	-0.79	< 0.001	-0.404 ± 0.005	-0.34 ± 0.02	0.12 ± 0.02

(Massaro et al. 2006 and references therein). In this scenario the probability for a particle to be further accelerated decreases at high energies, being inversely proportional to the energy itself. For example, this may occur when the particles are confined by a magnetic field, and the confinement efficiency decreases as the gyration radius increases.

In such cases the electron energy distribution is curved into a log-parabolic shape, and its curvature r is related to the fractional acceleration gain ϵ as given by Massaro et. al. (2006):

$$r \propto \frac{1}{\log\,\epsilon}\ . \tag{7.2}$$

Note that r decreases when ϵ increases. The spectrum of the synchrotron emission from these particles is also curved, with

$$b \approx \frac{r}{5}\ . \tag{7.3}$$

On the other hand, E_p scales like ϵ, so a negative correlation between b and E_p is expected. This basically arises from a loss of acceleration efficiency at high energies.

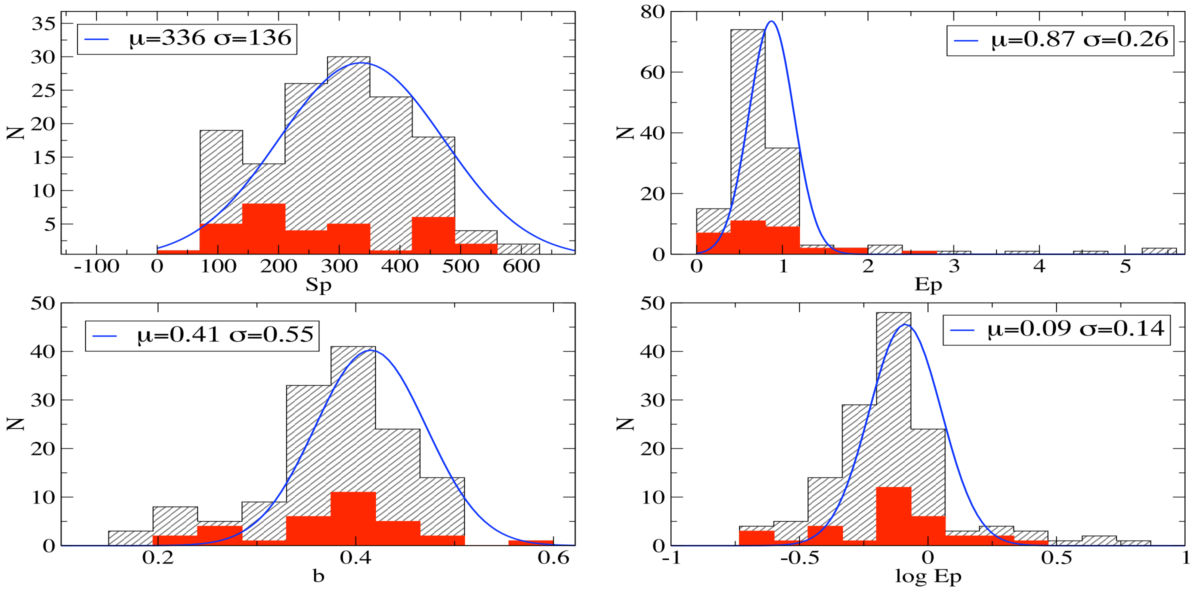

Figure 7.3: Histograms of S_p, b and E_p: filled boxes represent the *XMM* data set, while hatched boxes represent the *FULL* data set. The solid lines show best fits with a Gaussian, with average (μ) and standard deviation (σ) given in the labels.

A connection of log-parabolic spectra with acceleration may be also understood in the framework provided by the Fokker-Planck equation (Kardashev 1962) (see Sect. 3.4). Eq. 3.31 describes the evolution of the distribution function $N(\gamma, t)$ of the electron energies $\gamma\, m\, c^2$ under stochastic and systematic acceleration. The simple solution given by Kardashev (1962) for an initial, monoenergetic injection at the energy $\gamma_0\, mc^2$ is given by eq. 3.33

As previously discussed in Sect. 3.4, eq. 3.33 again describes a log-parabolic distribution (eq. 3.40 and 3.42), with the curvature term inversely proportional to the coefficient of the random acceleration component (see eq. 3.41).

On the other hand, the peak energy of $N(\gamma, t)$ is given by

$$\gamma_m = \gamma_0\, e^{\Lambda_2 - \Lambda_1} = \gamma_0 e^{\Lambda_2 - 1/4r}. \tag{7.4}$$

The logarithm of the peak energy E_p of the SED is closely proportional to the position of the peak of the logarithm of $\gamma^3\, N(\gamma)$. If $N(\gamma)$ has a log-parabolic shape, using again eq. 7.3 that applies to any log-parabolic energy distribution, one can find

$$\ln\, E_p \propto 2 \ln\, \gamma_{max} + \frac{3}{5b}. \tag{7.5}$$

In terms of S_p and E_p we see the logarithm of E_p to be inversely proportional to b; this is consistent with the inverse correlation observed between b and E_p.

In this framework the inverse correlation constitutes the signature of a stochastic acceleration process that broadens $N(\gamma, t)$ as to decrease its curvature while E_p is driven to higher values.

Table 7.3: A list of the HBLs currently detected at TeV energies. Col. (1) reports source names, Col.(2,3) the right ascension and declination respectively, Col.(4) gives the redshift (from NED), Col.(5,6) the galactic column density along the line of sight, Col.(7,8,9) report the observing satellite and number of observations, the final Col.(10) reports the TeV detections.

Name	*RA*	*DEC*	z	$N^{(1)}_{H,Gal}$ $[10^{20} cm^{-2}]$	$N^{(2)}_{H,Gal}$ $[10^{20} cm^{-2}]$	Satellite			TeV detection
1ES 0229+200	02 32 48.6	+20 17 17	0.140	9.21	7.69	*BeppoSAX* (1)			$HESS^{(1)}$
1ES 0347-121	03 49 23.2	-11 59 27	0.185	3.64	3.00	*BeppoSAX* (1)	xmm (1)	swf (1)	$HESS^{(1)}$
PKS 0548-322	05 50 40.6	-32 16 16	0.069	2.21	2.69	*BeppoSAX* (3)	xmm (2)	swf (16)	$HESS^{(1)}$
1ES 1011+496	10 15 04.1	+49 26 01	0.210	0.79	0.82			swf (3)	$MAGIC^{(2)}$
1H 1100-230	11 03 37.6	-23 29 30	0.186	5.76	5.60	*BeppoSAX* (2)	xmm (2)	swf	$HESS^{(3)}$
Mrk 421	11 04 27.3	+38 12 32	0.030	1.61	1.53	*BeppoSAX*	xmm	swf	$Whipple^{(4)}$
Mrk 180	11 36 26.4	+70 09 27	0.045	1.41	1.20	*BeppoSAX* (1)	xmm (1)	swf (2)	$MAGIC^{(5)}$
1ES 1218+304	12 21 21.9	+30 10 37	0.182	1.73	1.81	*BeppoSAX* (1)	xmm (1)	swf (7)	$MAGIC^{(6)}$
1H 1426+428	14 28 32.6	+42 40 21	0.129	1.38	1.10	*BeppoSAX* (1)	xmm (7)	swf (7)	$CAT^{(7)}$
1ES 1553+113	15 55 43.0	+11 11 24	—-	3.67	3.72	*BeppoSAX* (1)	xmm (1)	swf (3)	$HESS^{(8)}$
Mrk 501	16 53 52.2	+39 45 37	0.033	1.71	1.42	*BeppoSAX* (11)	xmm (2)	swf (10)	$Whipple^{(9)}$
1ES 1959+650	19 59 59.8	+65 08 55	0.047	10.0	10.1	*BeppoSAX* (3)	xmm (3)	swf (10)	$Whipple^{(10)}$
PKS 2005-489	20 09 25.4	-48 49 54	0.071	5.08	3.80	*BeppoSAX* (2)	xmm (3)	swf (3)	$HESS^{(11)}$
PKS 2155-304	21 58 52.0	-30 13 32	0.116	1.69	1.42	*BeppoSAX* (3)	xmm (15)	swf (22)	$HESS^{(12)}$
BL Lac	22 02 43.3	+42 16 40	0.069	21.3	17.1	*BeppoSAX*		swf	$MAGIC^{(2)}$
1ES 2344+514	23 47 04.8	+51 42 18	0.044	16.3	14.2	*BeppoSAX* (7)		swf (3)	$Whipple^{(13)}$
1H 2356-309	23 59 07.9	-30 37 41	0.165	1.33	1.36	*BeppoSAX* (1)	xmm (2)		$HESS^{(3)}$

(1) http://www.mpi-hd.mpg.de/hfm/HESS/HESS.html, (2) http://wwwmagic.mppmu.mpg.de/index.en.html, (3) Aharonian et al., 2006a, (4) Punch et al., 1992, (5) Albert et al. 2006a, (6) Albert et al., 2006b, (7) Djannati-Ataj et al., 2002, (8) Aharonian et al., 2006b, (9) Quinn et al., 1996, (10) Nishiyama et al., 1999, (11) Aharonian et al., 2005a, (12) Chadwick et al., 1999, (13) Catanese et al. 1998.

7.2 THE OTHER TeV HBLs

Among the BL Lac objects, several HBLs have been detected at TeV energies as listed in Tab. 7.3. The synchrotron emissions of such HBLs usually peak in the 0.1-10 keV range, and the extensive X-ray observations now available enable precision studies of their spectral shapes. In particular, it is widely known (Landau et al. 1986, Fossati et al., 2000, Massaro et al., 2004) that the spectra and therefore the SEDs of BL Lacs often appear to be intrinsically curved.

A recent analysis of Mrk 421 observations performed by *BeppoSAX*, *XMM-Newton* and ASCA (Tramacere, Massaro, & Cavaliere 2007, hereinafter TMC07) has shown two correlations between spectral parameters: the SED peak energy E_p correlates with the peak flux S_p but anticorrelates with the curvature b (as detailed in Sect. 7.1). These correlations are relevant as signatures of synchrotron emission and of statistical/stochastic acceleration mechanisms for the emitting electrons, respectively.

Using a wide set of archival data the X-ray spectral evolution of other TeV HBLs have been investigated; this includes all *BeppoSAX*, *XMM-Newton* and *Swift* published and unpublished archival observations performed between June 1996 and April 2007.

Two significant correlations between spectral parameters of the log-parabolic model were found by Tramacere et al. (2007a) from studying the X-ray synchrotron emission of Mrk 421, namely, S_p increases with E_p while the curvature b decreases.

Any similar correlations or trends in other TeV HBLs respect to Mrk 421were looked. For effective comparisons it is necessary to make cosmological corrections, even though the redshift range of these sources is rather narrow. In the log-log representation the redshift rescaling corresponds a traslation of the spectral energy distribution to lower energies with a decreased height; but the curvature parameter b, as defined by eq. 6.1 and eq. 6.2, is not afffected while the other parameters, E_p and S_p are.

In particular, the rest frame energy peak E^*_p is given by

$$E^*_p = (1 + z)\, E_p. \tag{7.6}$$

In addition, noting that the value of S_p is proportional to the bolometric emitted flux, the rest frame powers of BL Lacs in terms of the isotropic luminosity peak energy L^*_p are compared:

$$L^*_p \simeq 4\pi D_L^2 S_p. \tag{7.7}$$

Here the luminosity distance D_L of our sources is given by (Peebles, 1993):

$$D_L = \frac{c}{H_0}(1 + z) \int_0^z \frac{dz}{\sqrt{\Omega_M (1 + z)^3 + \Omega_\Lambda}}, \tag{7.8}$$

using a flat cosmology with $H_0 = 72$ km/(s Mpc), $\Omega_M = 0.27$ and $\Omega_\Lambda = 0.73$ (see Spergel et al., 2007).

To search for trends one needs at least 10 observations with E_p, S_p, b well estimated, a requirement satisfied by only 5 of our sources, namely: PKS 0548-322, 1H 1426+418, MRK 501, 1ES 1959+650 and PKS 2155-304. For these sources the spectral analyses was performed to evaluate independently E_p, S_p, b; to these also the redshift corrections discussed above were applied.

The presence of trends was investigated by evaluating the linear correlation coefficient r_{log} between the logarithms of spectral parameters. For Mrk 421 the results are $r_{log} = 0.67$ and $r_{log} = -0.67$ for the $E^*_p - L^*_p$ and $E^*_p - b$ relations, respectively. In Figs. 7.4, 7.5a, 7.6a, 7.7 and 7.8a the values of the spectral parameters are plotted, with their uncertanties, for each of the five sources and include those of Mrk 421 for comparison.

7.2.1 PKS 0548-322

Fig. 7.4 shows the results for PKS 0548-322; it is worth noting that in this source both E^*_p and L^*_p vary in a narrower range compared to Mrk 421. PKS 0548-322 follows the same trend of Mrk 421 on both $E^*_p - L^*_p$ and $E^*_p - b$ planes, with correlation coefficients $r_{log} = 0.61$ and $r_{log} = -0.60$, respectively.

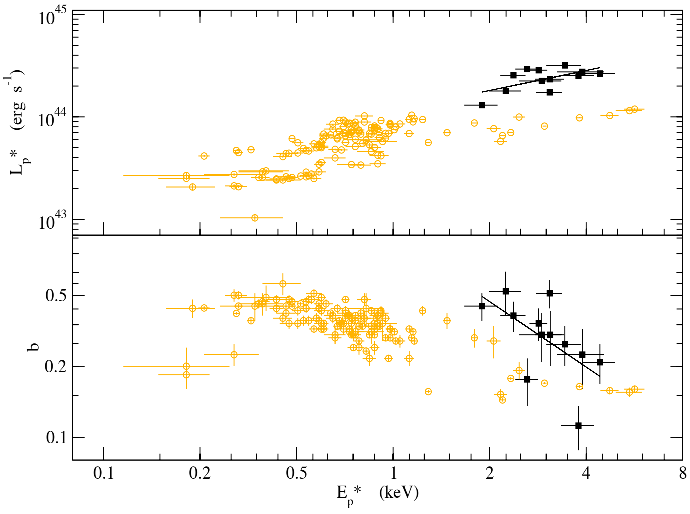

Figure 7.4: $E_p^* - L_p^*$ and $E_p^* - b$ plots for PKS 0548-322 (black filled squares) compared with those of Mrk 421 (orange circles). Black lines indicate the regression underlying the r_{log} correlation coefficient.

7.2.2 1H 1426+428

The source 1H 1426+428 has a similar behaviour to Mrk 421 in the $E_p^* - L_p^*$ and $E_p^* - b$ plots (see Fig. 7.5a), even though if it is an order of magnitude brighter than the latter. In this figure, we also show the *XMM-Newton* observation performed on 16 June 2001 (circled in the Fig. 7.5a), in which the log-parabolic bestfit indicates a value of E_p^* beyond the instrumental energy range; this circumstance makes the formal uncertainty unreliable, and motivates us to exclude this pointing from our statistical analysis. The observation of *XMM-Newton* on 16 June 2001 appears to confirm the statistical trend in the $E_p^* - b$ plane, but in the $E_p^* - L_p^*$ plane it lies in a different position relative to other pointings. As shown in Fig. 7.5b, during this particular pointing 1H 1426+428 shifted its SED peak energy without large variation of L_p^*, at variance with the following ones by *XMM-Newton*. A correlation coefficients $r_{log} = 0.72$ for the $E_p^* - L_p^*$ relation, and $r_{log} = -0.47$ for the $E_p^* - b$ one were found; these confirm the similarity to Mrk 421 and to PKS 0548-322. Note that 1H 1426+428 also covers similar regions on the $E_p^* - L_p^*$ and $E_p^* - b$ to Mrk 421.

7.2.3 Mrk 501

For Mrk 501 the $E_p^* - L_p^*$ and $E_p^* - b$ plots are shown in Fig. 7.6a. Here the range of E_p^* is wider and the luminosities are higher compared to Mrk 421. Fig. 7.6b shows in detail the strong variability of this source. The source has similar trends to Mrk 421, with higher correlation coefficients for the $E_p^* - L_p^*$ and $E_p^* - b$ relations, namely, $r_{log} = 0.89$ and $r_{log} = -0.79$, respectively. Fig. 7.6b shows the SEDs relative to three observations performed with all three satellites to show in detail the variations of E_p, s_p, and curvature b.

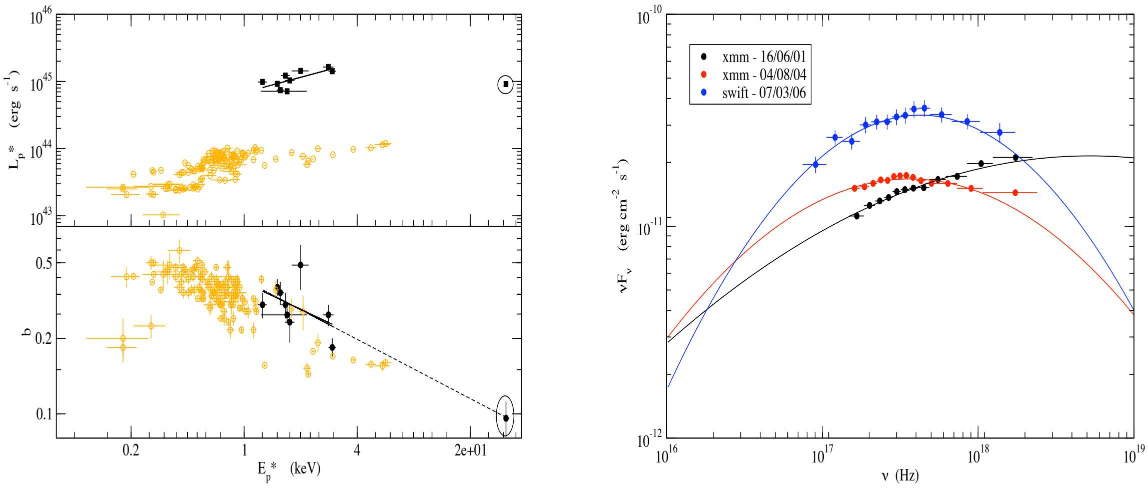

Figure 7.5: a) $E^*_p - L^*_p$ and $E^*_p - b$ plots for 1H 1426+428 (black filled squares) compared with those of Mrk 421 (orange circles). Black lines indicate the regression underlying the r_{log} correlation coefficient. b) The spectral energy distribution for three observations of 1H 1426+428 performed by *XMM-Newton* and *Swift*.

7.2.4 1ES 1959+650

The observations of 1ES 1959+650 cover a narrower subregion of both the $E^*_p - L^*_p$ and the $E^*_p - b$ plane relative to Mrk 421, as shown by Fig 7.7. These observations were mostly performed within ten days during 2006. The observation performed on 29 May 2006 (circled in Fig. 7.7) is peculiar as it yields a very high curvature value. This pointing took place at the end of a set of 6 observations in which the flux was decreasing; this may represent a phase dominated by cooling, when the estimated value of the curvature could well be affected by an exponential cutoff close to the observed energy range.

7.2.5 PKS 2155-304

The source PKS 2155-304 is the truly variant member of our set in a number of respects. In fact, the spectral analysis yields a log-parabolic index $a > 2$, and relatedly E_p is less than 1 keV. It was difficult to evaluate the SED peak location with *BeppoSAX*, *XMM-Newton* and *Swift* because it often falls below the observational X-ray range, as shown in Fig. 7.8b. Such spectra indicate that the X rays constitute the upper end of a synchrotron emission; on the other hand, we never observed a high energy exponential cut-off in our analysis, which confirmes our modelling in terms of a spectral curvature b. The source PKS 2155-304 covers a region in the $E^*_p - b$ plane overlapping that of Mrk 421 in Fig. 7.8a. On the other hand, the same figure shows that the source does not appear to follow a similar trend in the $E^*_p - L^*_p$ plane; a possible explanation is that our X-ray observations may be biased in that you observe the source only with E_p values in the X-rays band, corresponding to higher states relative to its average (Tramacere et al., 2007b).

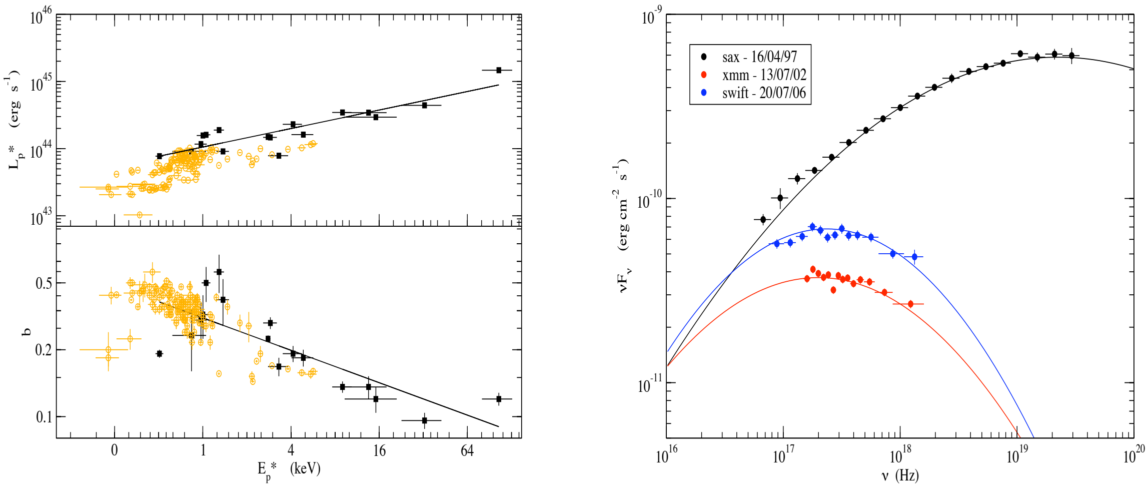

Figure 7.6: a) $E_p^* - L_p^*$ and $E_p^* - b$ plots for Mrk 501 (black filled squares) compared with those of Mrk 421 (orange circles). Black lines indicate the regression underlying the r_{log} correlation coefficient. b) The spectral energy distribution for three observations of Mrk 501 performed by *BeppoSAX*, *XMM-Newton* and *Swift*.

7.3 HBLs TeV CANDIDATES

All HBLs observed by *XMM-Newton* were analysed in order to derive the average spectral properties to verify if there are some TeV candidates among them. The complete list of *XMM-Newton* HBLs is reproted in Tab. 7.4, they are 10 sources pointed plus 1207+392 that is in the same FOV of the bright Seyfert galaxy NGC 4151 (Maselli et al., 2007). All these 10 BL Lacs are in the range of redshift between 0.086 and 0.360, with the only exception of 1207+392 at $z = 0.615$, at the limit of the present TeV detectability considering that the most distant extragalactic source is the FSRQ 3C 279 at $z = 0.5362$ (REF).

To study their detectability, two sources with quasi simultaneous data were analysed and their SEDs were compared with numerical SSC calculations. X-ray spectral analysis of all TeV candidates in this sample were performed as discussed in Sect. 6.4. Finally, SSC calculations were used to evaluate the TeV flux above the thereshold of detectabilty, assumed equal to 10^{-12} erg cm^{-2} s^{-1} above 0.3 TeV. The behaviour of these sources in the $E_p^* - b$ parameter plane is compared with those already known as TeV emitters.

Applying SSC calculations to Mrk 180 and 1ES 1ES 1553+113 it was possible to derive typical source parameters for HBLs that have quasi-simultaneous data in the X-rays and in the TeV band. Fig. 7.9 shows the results for the SED description performed with the numerical SSC code described in Sect. 5.7, using a log-parabolic distribution with a power-law low energy tail (eq. 3.60) for the electron population, for both sources.

As shown in Sect. 5.7.2, the SED of the synchrotron emission depends on the magnetic field, the beaming factor, the electron spectrum, and on the number of emitting particles. Then, it is possible to describe the X-ray emission of HBLs with different combination of radii and electron densities that corresponds to the same particle number. The observations of TeV emission provide a constraint on

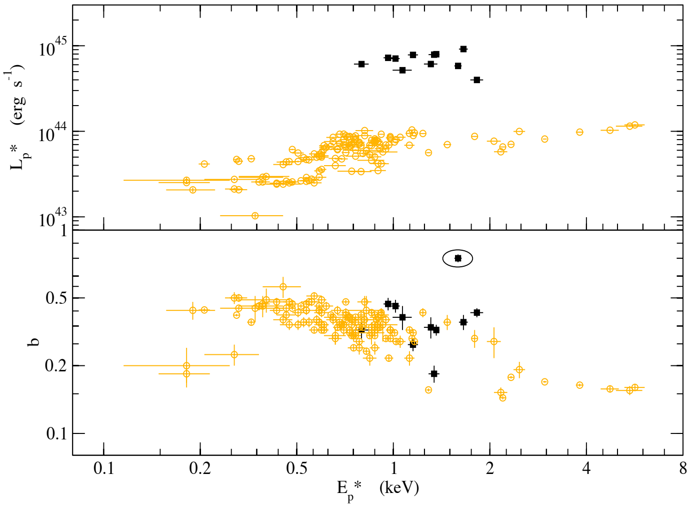

Figure 7.7: $E_p^* - L_p^*$ and $E_p^* - b$ plots for 1ES 1959+650 (black filled squares) compared with those of Mrk 421 (orange circles).

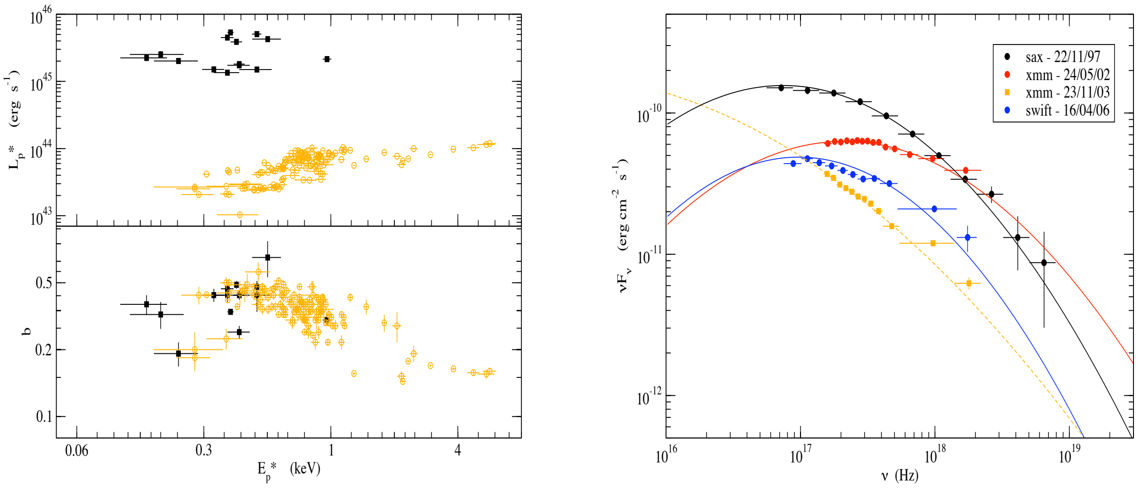

Figure 7.8: a)$E_p^* - L_p^*$ and $E_p^* - b$ plots for PKS 2155-304 (black filled squares) compared with those of Mrk 421 (orange circles). b) The spectral energy distribution for four observations of PKS 2155-304 performed by *BeppoSAX*, *XMM-Newton* and *Swift*.

Table 7.4: *XMM-Newton* HBLs sample

Name	*RA*	*DEC*	z	$N_{H,Gal}$ $10^{22} cm^{-2}$
1ES 0033+595	00 35 52.6	+59 50 05	0.086	4.24×10^{-1}
1ES 0120+340	01 23 08.5	+34 20 47.5	0.272	5.14×10^{-2}
1ES 0145+138	01 48 29.7	+14 02 18	0.125	5.10×10^{-2}
MS 0205.7+3509	02 08 38.2	+35 23 13	0.318	6.28×10^{-2}
1ES 0323+022	03 26 13.9	+02 25 14.7	0.147	8.74×10^{-2}
1ES 0647+250	06 50 46.5	+25 03 00.3	0.203	1.28×10^{-1}
1ES 0737+746	07 44 05.2	+74 33 58	0.315	3.54×10^{-2}
1ES 1028+511	10 31 18.5	+50 53 35.9	0.360	1.16×10^{-2}
1207+392	12 10 26.7	+39 29 09	0.615	2.33×10^{-2}
MS 1229.2+6430	12 31 31.4	+64 14 18	0.163	1.98×10^{-2}
1ES 1255+244	12 57 31.9	+24 12 40.1	0.141	1.26×10^{-2}

these parameters.

However, the solution calculated to descirbe the SED over the wide range of frequencies, from X-rays to TeV energies, is still degenerate. in fact, different combination of all parameters produce the same SED. Nevertheless, one can use other informations, as the variability, to derive unique values of the source physical parameters (see Sect. 5.3 for details).

Solutions for the X-ray emission of TeV HBL candidates were found using the same SSC code as for Mrk 180 and 1ES 1553+113, assuming source parameters value close to those of these two HBLs, given in Tab. 7.5, while Tab. 7.6 shows their output values.

Calculations for all sources, were performed to reproduce the measured spectral parameters within 2 σ range.

Note that to produce the sychrotron peak frequency ν_p, the electron energy required can be derived from eq. 4.12 as:

$$\gamma'_p = 0.91 \times 10^{-3} \nu_t^{1/2} B'^{-1/2} \frac{(1+z)^{1/2}}{\delta^{1/2}} \tag{7.9}$$

For a typical magnetic field $B' = 0.1G$ and a $\delta = 10$, to obtain a ν_p at about 10^{17} Hz, electrons with $\gamma'_p = 10^4$ are required (see Tab. 7.5). Consequently, these sources are near the Klein-Nishina regime (see Sect. 5.4 for details), and the IC peak energy results at $\epsilon_p = \gamma' mc^2 h^{-1} \sim 10^{25}$ Hz.

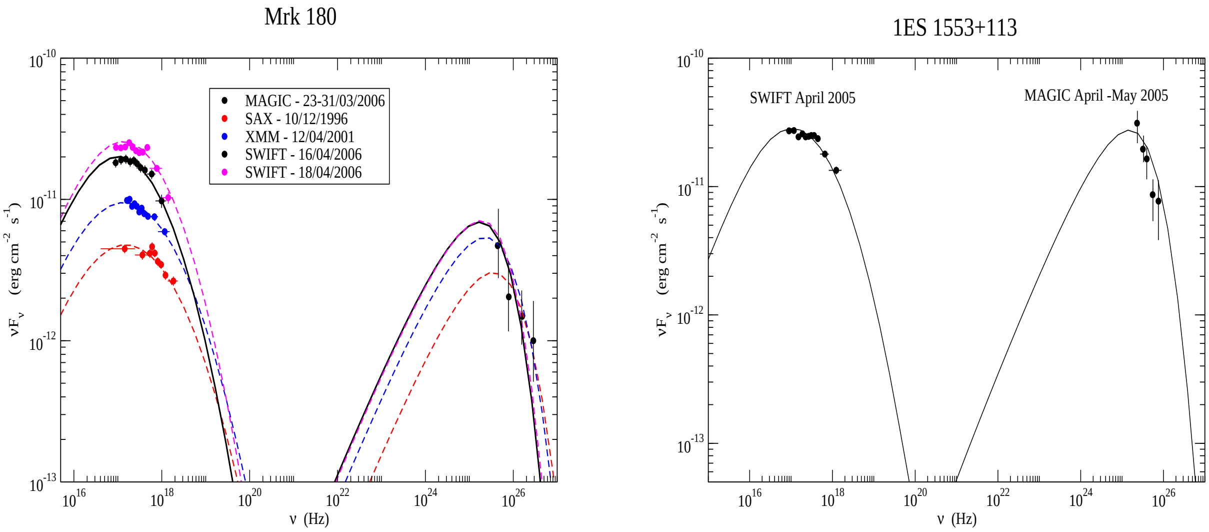

Figure 7.9: The spectral energy distribution of Mrk 180 (a) and 1ES 1553+113 (b) from X-rays to TeV energy range. *XMM-Newton* observations are reported with quasi simultaneous data of their detection at TeV energies. SSC simulations performed with the numerical code described in Sect.() reproduce the same synchrotron parameters: curvature, peak ferquency,and SED peak height within the error ranges, reported in the spectral analysis (see text for details).

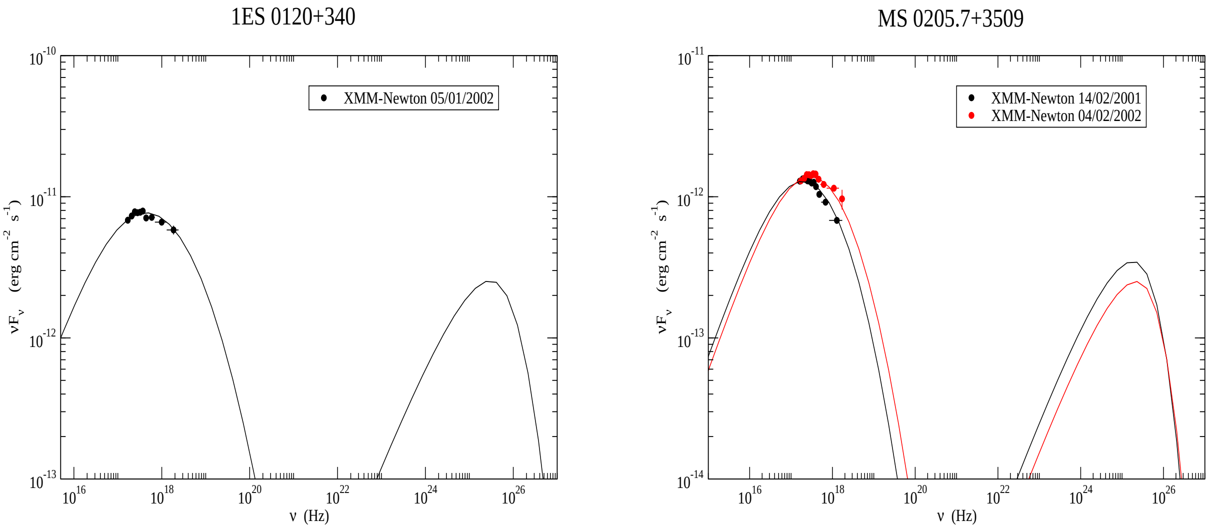

Figure 7.10: The X-rays SED of 1ES 0120+340 (a) and MS 0205.7+3609 (b). SSC simulations reproduce the same synchrotron parameters: curvature, peak ferquency,and SED peak height within the error ranges, reported in the spectral analysis and perform some predisctions of TeV detection (see text for details).

Table 7.5: Input parameters for simulations of TeV detected HBLs

Parameter	*Symbol*	Mrk 180	1ES 1553+113
Redshift	z	0.045	0.250
Date		10/12/1996	20/04/2005
Beaming Factor	δ	10.00	10.00
Magnetic Field	B' (G)	0.10	0.47
Volume	V' (cm^3)	1.40×10^{47}	5.34×10^{48}
Density	n' (cm^{-3})	6.70	4.30
Electron energy	γ'_0	4.00×10^4	2.40×10^4
Spectral index	s	1.30	1.15
Curvature	r	1.23	1.78
Date		12/04/2001	——
Beaming Factor	δ	10.00	——
Magnetic Field	B' (G)	0.20	——
Volume	V' (cm^3)	9.00×10^{46}	——
Density	n' (cm^{-3})	9.95	——
Electron energy	γ'_0	2.70×10^4	——
Spectral index	s	1.30	——
Curvature	r	1.23	——
Date		16/04/2006	——
Beaming Factor	δ	10.00	——
Magnetic Field	B' (G)	0.36	——
Volume	V' (cm^3)	1.25×10^{47}	——
Density	n' (cm^{-3})	7.00	——
Electron energy	γ'_0	2.70×10^4	——
Spectral index	s	1.30	——
Curvature	r	1.70	——
Date		18/04/2006	——
Beaming Factor	δ	10.50	——
Magnetic Field	B' (G)	0.41	——
Volume	V' (cm^3)	1.38×10^{47}	——
Density	n' (cm^{-3})	5.87	——
Electron energy	γ'_0	2.75×10^4	——
Spectral index	s	1.30	——
Curvature	r	1.65	——

Table 7.6: Source output parameters for simulations of TeV detected HBLs

Parameter	*Symbol*	Mrk 180	1ES 1553+113
Luminosity Distance	D_L (Mpc)	0.200 ×10^{3}	0.126 ×10^{4}
Date		10/12/1996	20/04/2005
Magnetic energy density	u'_B $(erg\ cm^{-3})$	0.399 ×10^{-3}	0.879 ×10^{-2}
Radius	R' (cm)	0.322 ×10^{16}	0.108 ×10^{17}
Electron Number	N_{el}	0.938 ×10^{48}	0.230 ×10^{50}
Normalization	N'_0 (cm^{-3})	0.963 ×10^{-5}	0.194 ×10^{-4}
Electron peak energy	γ'_p	0.770 ×10^{5}	0.416 ×10^{5}
Total Electron energy	E'_{tot} (erg)	0.257 ×10^{51}	0.356 ×10^{52}
Date		12/04/2001	——-
Magnetic energy density	u'_B $(erg\ cm^{-3})$	0.159 ×10^{-2}	——-
Radius	R' (cm)	0.278 ×10^{16}	——-
Electron Number	N_{el}	0.895 ×10^{48}	——-
Normalization	N_0 (cm^{-3})	0.242 ×10^{-4}	——-
Electron peak energy	γ_p	0.520 ×10^{5}	——-
Total Electron energy	E_{tot} (erg)	0.128 ×10^{51}	——-
Date		16/04/2006	——-
Magnetic energy density	u_B $(erg\ cm^{-3})$	0.516 ×10^{-2}	——-
Radius	R (cm)	0.310 ×10^{16}	——-
Electron Number	N_{el}	0.875 ×10^{48}	——-
Normalization	N'_0 (cm^{-3})	0.172 ×10^{-4}	——-
Electron peak energy	γ'_p	0.434 ×10^{5}	——-
Total Electron energy	E'_{tot} (erg) 0.107 ×10^{51}	——-	
Date		18/04/2006	——-
Magnetic energy density	u'_B $(erg\ cm^{-3})$	0.669 ×10^{-2}	——-
Radius	R' (cm)	0.321 ×10^{16}	——-
Electron Number	N_{el}	0.810 ×10^{48}	——-
Normalization	N'_0 (cm^{-3})	0.141 ×10^{-4}	——-
Electron peak energy	γ'_p	0.448 ×10^{5}	——-
Total Electron energy	E'_{tot} (erg)	0.104 ×10^{51}	——-

Table 7.7: Synchrotron output parameters for simulations of TeV detected HBLs

Parameter	*Symbol*	Mrk 180	1ES 1553+113
IC Maximum frequency	ν^{IC}_{max} (Hz)	0.59×10^{30}	
Date		10/12/1996	20/04/2005
Curvature	b_S	0.229	0.296
Peak Frequency	ν_p (Hz)	0.147×10^{18}	0.930×10^{17}
SED peak height	S_p $(erg\ s^{-1}\ cm^{-2})$	0.473×10^{-11}	0.269×10^{-10}
Maximum frequency	ν^S_{max} (Hz)	0.291×10^{25}	0.114×10^{25}
Luminosity	L_S $(ergs^{-1})$	0.971×10^{45}	0.195×10^{48}
Date		12/04/2001	——-
Curvature	b_S	0.231	——-
Peak Frequency	ν_p (Hz)	0.133×10^{18}	——-
SED peak height	S_p $(erg\ s^{-1}\ cm^{-2})$	0.942×10^{-11}	——-
Maximum frequency	ν^S_{max} (Hz)	0.582×10^{24}	——-
Luminosity	L_S $(ergs^{-1})$	0.193×10^{46}	——-
Date		16/04/2006	——-
Curvature	b_S	0.289	——-
Peak Frequency	ν_p (Hz)	0.974×10^{17}	——-
SED peak height	S_p $(erg\ s^{-1}\ cm^{-2})$	0.190×10^{-10}	——-
Maximum frequency	ν^S_{max} (Hz)	0.105×10^{25}	——-
Luminosity	L_S $(ergs^{-1})$	0.366×10^{46}	——-
Date		18/04/2006	——-
Curvature	b_S	0.275	——-
Peak Frequency	ν_p (Hz)	0.125×10^{18}	——-
SED peak height	S_p $(erg\ s^{-1}\ cm^{-2})$	0.251×10^{-10}	——-
Maximum frequency	ν^S_{max} (Hz)	0.119×10^{25}	——-
Luminosity	L_S $(ergs^{-1})$	0.473×10^{46}	——-

Table 7.8: Inverse Compton output parameters for simulations of TeV detected HBLs

Parameter	*Symbol*	Mrk 180	1ES 1553+113
Date		10/12/1996	20/04/2005
Curvature	b_C	0.366	0.476
Peak Frequency	ϵ_p (Hz)	0.227×10^{26}	0.834×10^{25}
SED peak height	C_p $(erg\ s^{-1}\ cm^{-2})$	0.285×10^{-11}	0.258×10^{-10}
Luminosity	L_C $(ergs^{-1})$	0.471×10^{45}	0.153×10^{48}
Luminosity Ratio	L_C/L_S	0.485	0.784
Date		12/04/2001	——-
Curvature	b_C	0.438	——-
Peak Frequency	ϵ_p (Hz)	0.144×10^{26}	——-
SED peak height	C_p $(erg\ s^{-1}\ cm^{-2})$	0.539×10^{-11}	——-
Luminosity	L_C $(ergs^{-1})$	0.844×10^{47}	——-
Luminosity Ratio	L_C/L_S	0.437	——-
Date		16/04/2006	——-
Curvature	b_C	0.438	——-
Peak Frequency	ϵ_p (Hz)	0.991×10^{25}	——-
SED peak height	C_p $(erg\ s^{-1}\ cm^{-2})$	0.671×10^{-11}	——-
Luminosity	L_C $(ergs^{-1})$	0.104×10^{46}	——-
Luminosity Ratio	L_C/L_S	0.284	——-
Date		18/04/2006	——-
Curvature	b_C	0.423	——-
Peak Frequency	ϵ_p (Hz)	0.107×10^{26}	——-
SED peak height	C_p $(erg\ s^{-1}\ cm^{-2})$	0.677×10^{-11}	——-
Luminosity	L_C $(ergs^{-1})$	0.106×10^{46}	——-
Luminosity Ratio	L_C/L_S	0.224	——-

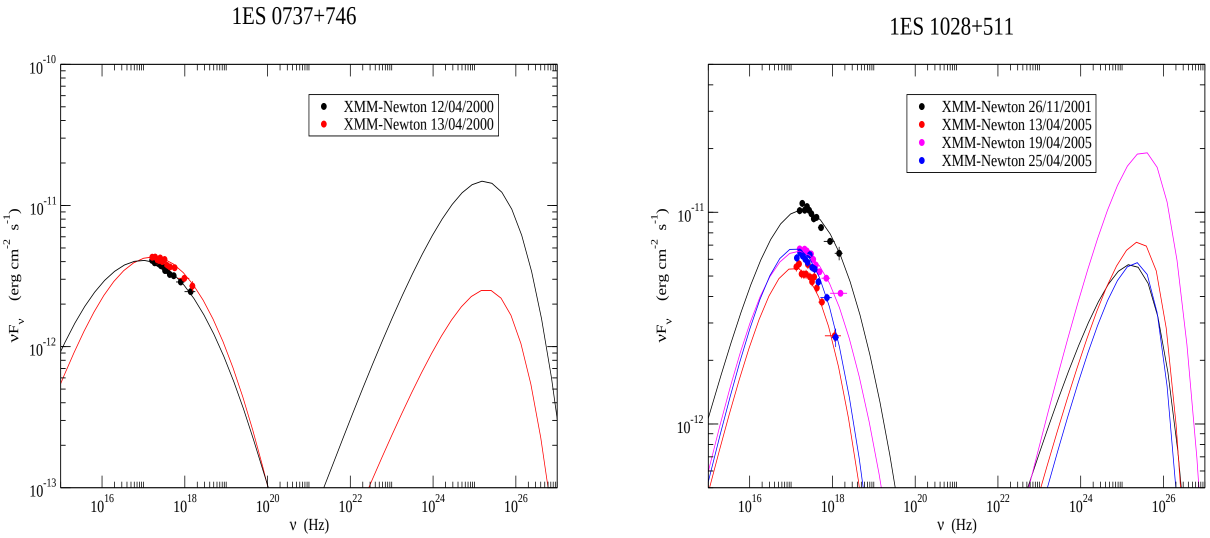

Figure 7.11: The X-rays SED of 1ES 0737+746 (a) and 1ES 1028+511(b). SSC simulations reproduce the same synchrotron parameters: curvature, peak ferquency,and SED peak height within the error ranges, reported in the spectral analysis and perform some predisctions of TeV detection (see text for details).

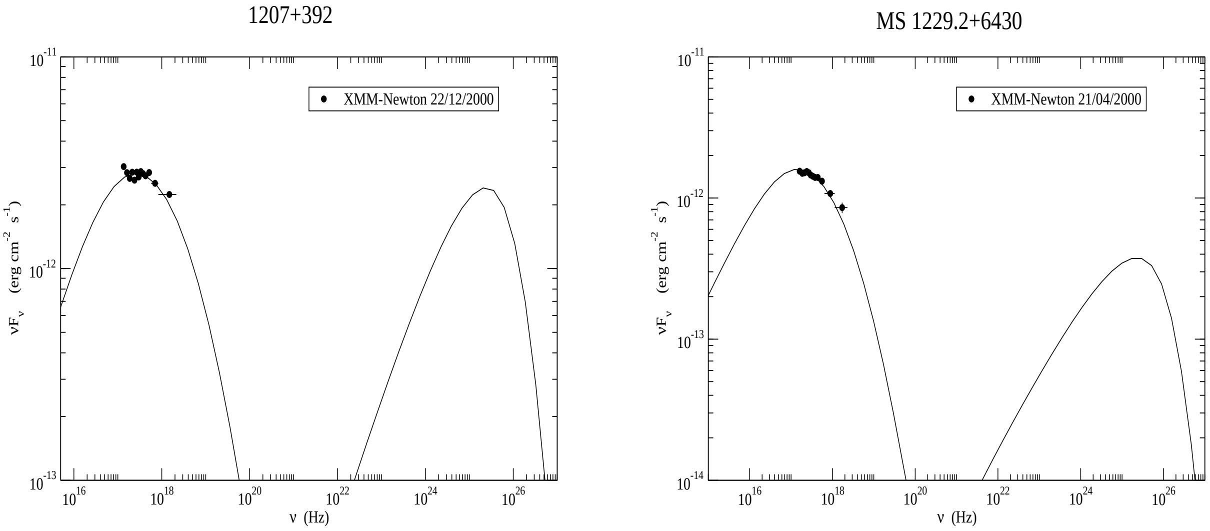

Figure 7.12: The X-rays SED of 1207+392 (a) and MS1229.7+6430 (b). SSC simulations reproduce the same synchrotron parameters: curvature, peak ferquency,and SED peak height within the error ranges, reported in the spectral analysis and perform some predisctions of TeV detection (see text for details).

Table 7.9: Input parameters for simulations

Parameter	*Symbol*	1ES 0120+340	MS 0205.7+3509	1ES 0737+746	1ES 1028+511	1207+392	MS 1229.2+6430
Redshift	z	0.272	0.318	0.315	0.360	0.615	0.163
Date		05/01/2002	14/02/2001	12/04/2000	26/11/2001	22/12/2000	21/04/2000
Beaming Factor	δ	10.00	10.00	11.00	11.00	11.00	11.50
Magnetic Field	B' (G)	0.52	0.72	0.21	0.41	0.25	0.18
Volume	V' (cm^3)	6.28×10^{47}	1.07×10^{47}	9.72×10^{48}	7.57×10^{48}	8.79×10^{48}	9.60×10^{47}
Density	n' (cm^{-3})	4.93	8.01	2.96	7.83	9.79	9.56
Electron energy	γ'_0	4.20×10^4	3.50×10^4	2.27×10^4	3.12×10^4	5.20×10^4	5.73×10^4
Spectral index	s	1.25	1.27	1.37	1.56	1.55	1.75
Curvature	r	1.50	2.08	0.98	1.25	1.27	1.61
Date		——-	04/02/2002	13/04/2000	13/04/2005	——-	——-
Beaming Factor	δ	——-	10.00	11.50	10.00	——-	——-
Magnetic Field	B' (G)	——-	0.78	0.11	0.21	——-	——-
Volume	V' (cm^3)	——-	1.02×10^{47}	6.45×10^{48}	5.97×10^{48}	——-	——-
Density	n' (cm^{-3})	——-	6.02	9.83	6.98	——-	——-
Electron energy	γ'_0	——-	3.95×10^4	1.17×10^4	5.83×10^4	——-	——-
Spectral index	s	——-	1.27	1.17	1.36	——-	——-
Curvature	r	——-	1.98	0.81	2.25	——-	——-
Date		——-	——-	——-	19/04/2005	——-	——-
Beaming Factor	δ	——-	——-	——-	10.50	——-	——-
Magnetic Field	B' (G)	——-	——-	——-	0.12	——-	——-
Volume	V' (cm^3)	——-	——-	——-	8.69×10^{48}	——-	——-
Density	n' (cm^{-3})	——-	——-	——-	5.57	——-	——-
Electron energy	γ'_0	——-	——-	——-	4.13×10^4	——-	——-
Spectral index	s	——-	——-	——-	1.16	——-	——-
Curvature	r	——-	——-	——-	1.35	——-	——-
Date		——-	——-	——-	25/04/2005	——-	——-
Beaming Factor	δ	——-	——-	——-	10.50	——-	——-
Magnetic Field	B' (G)	——-	——-	——-	0.34	——-	——-
Volume	V' (cm^3)	——-	——-	——-	3.39×10^{48}	——-	——-
Density	n' (cm^{-3})	——-	——-	——-	4.97	——-	——-
Electron energy	γ'_0	——-	——-	——-	4.21×10^4	——-	——-
Spectral index	s	——-	——-	——-	1.26	——-	——-
Curvature	r	——-	——-	——-	2.19	——-	——-

Table 7.10: Source output parameters for simulations

Parameter	*Symbol*	1ES 0120+340	0205.7+3509	1ES 0737+746	1ES 1028+511	1207+392	1229.2+6430
Luminosity Distance	$D_L\ (Mpc)$	0.139×10^{4}	0.166×10^{4}	0.164×10^{4}	0.192×10^{4}	0.364×10^{4}	0.782×10^{3}
Date		05/01/2002	14/02/2001	12/04/2000	26/11/2001	22/12/2000	21/04/2000
Magnetic energy density	$u'_B\ (erg\ cm^{-3})$	0.108×10^{-1}	0.206×10^{-1}	0.175×10^{-2}	0.669×10^{-2}	0.247×10^{-2}	0.129×10^{-2}
Radius	$R'\ (cm)$	0.531×10^{16}	0.295×10^{16}	0.132×10^{17}	0.121×10^{17}	0.128×10^{17}	0.612×10^{16}
Electron Number	N_{el}	0.310×10^{49}	0.857×10^{48}	0.288×10^{50}	0.593×10^{50}	0.861×10^{50}	0.918×10^{49}
Normalization	$N'_0\ (cm^{-3})$	0.796×10^{-5}	0.155×10^{-4}	0.723×10^{-5}	0.590×10^{-5}	0.346×10^{-5}	0.110×10^{-5}
Electron peak energy	γ'_p	0.747×10^{5}	0.524×10^{5}	0.476×10^{5}	0.478×10^{5}	0.782×10^{5}	0.685×10^{5}
Total Electron energy	$E'_{tot}\ (erg)$	0.100×10^{52}	0.165×10^{51}	0.273×10^{52}	0.420×10^{52}	0.132×10^{53}	0.713×10^{51}
Date		——-	04/02/2002	13/04/2000	13/04/2005	——-	——-
Magnetic energy density	$u'_B\ (erg\ cm^{-3})$	——-	0.242×10^{-1}	0.481×10^{-3}	0.175×10^{-2}	——-	——-
Radius	$R'\ (cm)$	——-	0.290×10^{16}	0.115×10^{17}	0.112×10^{17}	——-	——-
Electron Number	N_{el}	——-	0.614×10^{48}	0.634×10^{50}	0.417×10^{50}	——-	——-
Normalization	$N'_0\ (cm^{-3})$	——-	0.989×10^{-5}	0.994×10^{-4}	0.480×10^{-5}	——-	——-
Electron peak energy	γ'_p	——-	0.604×10^{5}	0.381×10^{5}	0.809×10^{5}	——-	——-
Total Electron energy	$E'_{tot}\ (erg)$	——-	0.147×10^{51}	0.437×10^{52}	0.132×10^{53}	——-	——-
Date		——-	——-	——-	19/04/2005	——-	——-
Magnetic energy density	$u'_B\ (erg\ cm^{-3})$	——-	——-	——-	0.573×10^{-3}	——-	——-
Radius	$R'\ (cm)$	——-	——-	——-	0.128×10^{17}	——-	——-
Electron Number	N_{el}	——-	——-	——-	0.484×10^{50}	——-	——-
Normalization	$N'_0\ (cm^{-3})$	——-	——-	——-	0.123×10^{-4}	——-	——-
Electron peak energy	γ'_p	——-	——-	——-	0.854×10^{5}	——-	——-
Total Electron energy	$E'_{tot}\ (erg)$	——-	——-	——-	0.220×10^{53}	——-	——-
Date		——-	——-	——-	25/04/2005	——-	——-
Magnetic energy density	$u'_B\ (erg\ cm^{-3})$	——-	——-	——-	0.460×10^{-2}	——-	——-
Radius	$R'\ (cm)$	——-	——-	——-	0.932×10^{16}	——-	——-
Electron Number	N_{el}	——-	——-	——-	0.169×10^{50}	——-	——-
Normalization	$N'_0\ (cm^{-3})$	——-	——-	——-	0.780×10^{-5}	——-	——-
Electron peak energy	γ'_p	——-	——-	——-	0.621×10^{5}	——-	——-
Total Electron energy	$E'_{tot}\ (erg)$	——-	——-	——-	0.447×10^{52}	——-	——-

Table 7.11: Synchrotron output parameters for simulations

Parameter	*Symbol*	1ES 0120+340	0205.7+3509	1ES 0737+746	1ES 1028+511	1207+392	1229.2+6430
IC Maximum frequency	ν_{max}^{IC} (Hz)	0.69×10^{30}					
Date		05/01/2002	14/02/2001	12/04/2000	26/11/2001	22/12/2000	21/04/2000
Curvature	b_S	0.270	0.305	0.198	0.229	0.232	0.243
Peak Frequency	ν_p (Hz)	0.415×10^{18}	0.177×10^{18}	0.164×10^{18}	0.180×10^{18}	0.250×10^{18}	0.132×10^{18}
SED peak height	S_p $(erg\ s^{-1}\ cm^{-2})$	0.763×10^{-11}	0.124×10^{-11}	0.431×10^{-11}	0.101×10^{-10}	0.278×10^{-11}	0.155×10^{-11}
Maximum frequency	ν_{max}^{S} (Hz)	0.124×10^{25}	0.166×10^{25}	0.535×10^{24}	0.101×10^{25}	0.518×10^{24}	0.542×10^{24}
Luminosity	L_S $(ergs^{-1})$	0.706×10^{47}	0.153×10^{47}	0.718×10^{47}	0.215×10^{48}	0.210×10^{48}	0.548×10^{46}
Date		——-	04/02/2002	13/04/2000	13/04/2005	——-	——-
Curvature	b_S	——-	0.306	0.167	0.341	——-	——-
Peak Frequency	ν_p (Hz)	——-	0.267×10^{18}	0.933×10^{17}	0.104×10^{18}	——-	——-
SED peak height	S_p $(erg\ s^{-1}\ cm^{-2})$	——-	0.135×10^{-11}	0.408×10^{-11}	0.536×10^{-11}	——-	——-
Maximum frequency	ν_{max}^{S} (Hz)	——-	0.180×10^{25}	0.293×10^{24}	0.470×10^{24}	——-	——-
Luminosity	L_S $(ergs^{-1})$	——-	0.168×10^{47}	0.762×10^{47}	0.856×10^{47}	——-	——-
Date		——-	——-	——-	19/04/2005	——-	——-
Curvature	b_S	——-	——-	——-	0.252	——-	——-
Peak Frequency	ν_p (Hz)	——-	——-	——-	0.144×10^{18}	——-	——-
SED peak height	S_p $(erg\ s^{-1}\ cm^{-2})$	——-	——-	——-	0.652×10^{-11}	——-	——-
Maximum frequency	ν_{max}^{S} (Hz)	——-	——-	——-	0.282×10^{24}	——-	——-
Luminosity	L_S $(ergs^{-1})$	——-	——-	——-	0.125×10^{48}	——-	——-
Date		——-	——-	——-	25/04/2005	——-	——-
Curvature	b_S	——-	——-	——-	0.342	——-	——-
Peak Frequency	ν_p (Hz)	——-	——-	——-	0.109×10^{18}	——-	——-
SED peak height	S_p $(erg\ s^{-1}\ cm^{-2})$	——-	——-	——-	0.665×10^{-11}	——-	——-
Maximum frequency	ν_{max}^{S} (Hz)	——-	——-	——-	0.799×10^{24}	——-	——-
Luminosity	L_S $(ergs^{-1})$	——-	——-	——-	0.111×10^{48}	——-	——-

Table 7.12: Inverse Compton output parameters for simulations

Parameter	*Symbol*	1ES 0120+340	0205.7+3509	1ES 0737+746	1ES 1028+511	1207+392	1229.2+6430
Date		05/01/2002	14/02/2001	12/04/2000	26/11/2001	22/12/2000	21/04/2000
Curvature	b_C	0.425	0.626	0.386	0.330	0.344	0.280
Peak Frequency	ϵ_p (Hz)	0.174×10^{26}	0.940×10^{25}	0.129×10^{26}	0.982×10^{26}	0.141×10^{26}	0.131×10^{26}
SED peak height	C_p $(erg\ s^{-1}\ cm^{-2})$	0.236×10^{-11}	0.372×10^{-12}	0.252×10^{-11}	0.543×10^{-11}	0.231×10^{-11}	0.360×10^{-12}
Luminosity	L_C $(ergs^{-1})$	0.177×10^{47}	0.342×10^{46}	0.314×10^{47}	0.976×10^{47}	0.147×10^{48}	0.121×10^{46}
Luminosity Ratio	L_C/L_S	0.250	0.223	0.437	0.454	0.697	0.220
Date		——-	04/02/2002	13/04/2000	13/04/2005	——-	——
Curvature	b_C	——-	0.559	0.295	0.482	——-	——
Peak Frequency	ϵ_p (Hz)	——-	0.112×10^{26}	0.124×10^{26}	0.127×10^{26}	——-	——
SED peak height	C_p $(erg\ s^{-1}\ cm^{-2})$	——-	0.253×10^{-12}	0.143×10^{-10}	0.706×10^{-11}	——-	——
Luminosity	L_C $(ergs^{-1})$	——-	0.245×10^{46}	0.203×10^{48}	0.976×10^{47}	——-	——
Luminosity Ratio	L_C/L_S	——-	0.146	2.669	1.141	——-	——
Date		——-	——-	——	19/04/2005	——-	——
Curvature	b_C	——-	——-	——	0.504	——-	——
Peak Frequency	ϵ_p (Hz)	——-	——-	——	0.199×10^{26}	——-	——
SED peak height	C_p $(erg\ s^{-1}\ cm^{-2})$	——-	——-	——	0.193×10^{-10}	——-	——
Luminosity	L_C $(ergs^{-1})$	——-	——-	——	0.273×10^{48}	——-	——
Luminosity Ratio	L_C/L_S	——-	——-	——	2.185	——-	——
Date		——-	——-	——	25/04/2005	——-	——
Curvature	b_C	——-	——-	——	0.581	——-	——
Peak Frequency	ϵ_p (Hz)	——-	——-	——	0.108×10^{26}	——-	——
SED peak height	C_p $(erg\ s^{-1}\ cm^{-2})$	——-	——-	——	0.596×10^{-11}	——-	——
Luminosity	L_C $(ergs^{-1})$	——-	——-	——	0.794×10^{47}	——-	——
Luminosity Ratio	L_C/L_S	——-	——-	——	0.716	——-	——

7.4 DISCUSSION

7.4.1 The case of Mrk 421

Using a large set of X-ray observations of Mrk 421, the results concerning the spectral variations are here presented and discussed. Such correlations exist between the peak values S_p of its SED and the peak positions E_p, and between the spectral curvature b and E_p.

The former may be interpreted in the framework of synchrotron emission. The values of the power-law slopes obtained from the fits in Sect. 7.1.1 are bounded by $\alpha \leq 1.2 \pm 0.1$. As such, they rule out the case $\alpha = 4$ applying if the beaming factor δ were the dominant driver of the spectral evolution; they are instead compatible with a combined effect of variations of B (corresponding to $\alpha = 2$) and of a rescaling of γ ($\alpha = 1$).

In parallel, a secondary role for δ is confirmed by the bound $r < 0.3$ it can contribute to the observed S_p, E_p correlation coefficient value $r \approx 0.7$. On the other hand, an upper limit to the beaming variance is setted; from the analysis in Sect. 7.1.1 a low fractional variation $\sigma_\delta/\mu_\delta \lesssim 10$ even on considering conservative values $\delta \approx 10$ is found. The remarkable implication is that the beaming factor of Mrk 421 remained closely constant during a time span of about 9 years.

This limit is relevant in the framework of the internal shock scenario. This assumes that shells ejected from the central engine with slightly different relativistic velocities and slightly differing angles collide in the jet at sub-parsec scales and produce flares. The temporal behaviour and the radiative efficiency of this process depend on the collision frequency and on the collision energetics, respectively; two versions are found in the literature. Guetta et al. (2004) assume that shells are ejected at a frequency close to 10^{-4} Hz, with Γ values distributed around the average value of about 15 after a random (uniform) distribution with a considerable dispersion, about 3. The dispersion is considerably larger than the values obtained from our analysis. On the other hand, Tanihata et al. (2003) assume values of δ following a normal distribution with $\sigma_\delta/\mu_\delta \ll 0.1$ and ejection intervals around 600 s; whence they obtain a good reproduction of the temporal behaviour, but also a very low radiative efficiency. The upper limit derived from our analysis, much lower than the value assumed by Guetta et al. (2004), emphasizes the efficiency problem reported by Tanihata et al. (2003).

The correlation observed in Mrk 421 between b and E_p is interesting in the framework of the electron acceleration mechanisms. In Mrk 421 A systematically decreasing of the curvature b as the peak energy E_p increasing is observed. To understand this behaviour a Fokker-Planck description of a dominant electron energy distribution were used (see Sect. 3.4). The solution of this equation for an initial mono-energetic injection predicts that with ongoing stochastic acceleration the curvature should decrease while the peak energy moves to higher energies. A more detailed understanding of this dynamics requires a full computation including radiative cooling and fixing the relative weights of the systematic vs. the stochastic acceleration component; this will be studied in a different paper (Tramacere et al. 2007 in prep.). An alternative explanation of this correlation is discussed in Sect. 7.1.2 in terms of statistical, energy-dependent acceleration probability. This leads again to a correlation as observed.

The aim was to stress a common point to both views, that is, the relevance of the curvature parameter to understand the observed spectral evolution of the source. The negative correlation between b and E_p strongly indicates the dynamics of E_p to be related to stochastic or to statistical (and energy dependent) acceleration mechanisms; it would not hold with the beaming as the main driver of spectral variations. So the results from this second correlation are consistent with those from the first, namely, the $S_p - E_p$ correlation.

No significant correlation has been found between S_p and b. This lack may arise from the opposite signs of the correlations between S_p-E_p and E_p-b adding to the considerable dispersion of the data.

Finally, another view on this matter is provided by the analysis given in Sect. 7.1.2 (see Fig. 7.3) concerning the PDF of the spectral parameters S_p, b and E_p. It is seen that S_p and b have enough symmetry in their PDF to be reasonably approximated by a Gaussian distribution with minor deviations in the tail (left panels). The parameter E_p, on the contrary, shows a more skewed distribution (right upper panel), that could be better approximated by a log-normal shape, i.e., by a Gaussian in the variable $\log E_p$ (right bottom panel). Note that a similar distribution has been successfully used also to describe the statistical properties of the GRB peak energy distribution that may depend on broadly similar physics (Ioka & Nakamura 2002).

A point to stress is that the log-normal distribution constitutes the asymptotic limit from the central limit theorem in multiplicative form; in fact, it has been shown by Ioka & Nakamura (2002) that the limiting log-normal form is closely attained already after 3 steps. Stochastic acceleration, for example, may be treated in terms of multiplication of a number of random fractional energy gains ϵ, see Eq. 7.2. The issue will be dealt with in more detail in Tramacere et al. (2007 in prep.); here it provides complementary support to our stress on the relevance of stochastic acceleration to understand the spectral variations of Mrk 421.

7.4.2 The other TeV HBLs

Correlations between L_p^* and E_p^* provide interesting information concerning the driver of the source spectral evolution. For example, using a wide dataset of X-ray observations of Mrk 421 the effects of varing physical parameters in the synchrotron emission, where the dependence of L_p^* on E_p^* may be represented in the form of a power-law, that is, $L_p^* \propto E_p^{*\,\alpha}$ (Tramacere et al., 2007a, and references therein) have been investigated.

In fact, the synchrotron peak is expected to scale as $L_p^* \propto N\,\gamma^2\,B^2\,\delta^4$ while the peak energy scales as $E_p^* \propto \gamma^2 B\,\delta$, in terms of the number N of emitting particles, of the magnetic field B, of the typical electron energy γmc^2, and of the beaming factor δ. Thus $\alpha = 1$ applies; $\alpha = 2$ applies for changes of the magnetic field; $\alpha = 4$ if changes in the beaming factor dominate; formally, $\alpha = \infty$ (i.e., a vertical line in the $E_p^* - L_p^*$ plane) applies for changes only in the number of emitting particles.

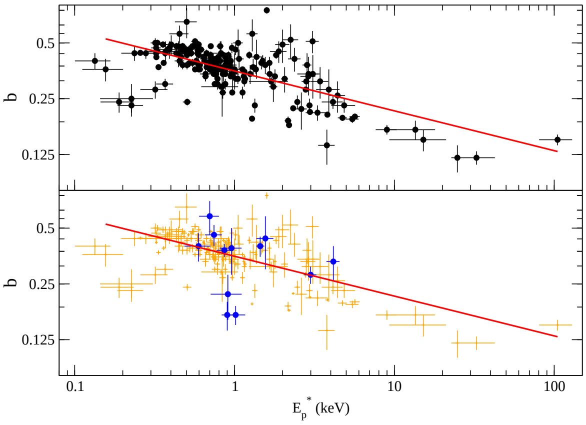

Figure 7.13: Upper panel: The $E_p^* - b$ plot for Mrk 421 and for the five sources analysed in detail in Sect. 7.2. Lower panel: Blue points represents the other TeV HBLs with insufficient data to perform a detailed analysis; the above sources are replotted with orange crosses.

Here an accurate analyses of the X-ray spectra of several TeV HBLs observed over a period 11 years is presented. These spectra are best described with a log-parabolic model, even though in some cases an acceptable fit is also provided by a power-law spectral model absorbed by a Galactic column density.

From these analyses the values of spectral parameters: E_p, S_p and curvature b, have been derived independently. With the cosmological transformations given by eq. 7.6 and eq. 7.7, possible correlations or at least trends among the spectral parameters were searched. Five sources (namely: PKS 0548-322, 1H 1426+428, Mrk 501, 1ES 1959+650, PKS2155-304) have enough data to warrant investigating in some detail the $E_p^* - L_p^*$ and $E_p^* - b$ relations and comparing them with those found for Mrk 421.

On the other hand, the number of observations for each source in our sample does not allow statistical analyses as detailed as in the case of Mrk 421 (Tramacere et al., 2007a); so for these sources it is not yet possible to determine the value of the synchrotron exponent α. Accordingly, only the logarithmic correlation coefficients r_{log} between $E_p^* - L_p^*$ and $E_p^* - b$ for each source have been evaluated.

Comparing these values with those evaluated for Mrk 421, at least three sources (namely: PKS 0548-322, 1H 1426+428 and Mrk 501) follow the same trends as Mrk 421 in the $E_p^* - L_p^*$ plane were found. In the case of 1ES 1959+650, our observed spectral parameters cover a smaller region compared to Mrk 421; nevertheless, the trend so outlined is consistent with that of the latter. Finally, PKS 2155-304 has again a similar behaviour in the $E_p^* - b$ plane but a definitely different one in the $E_p^* - L_p^*$ plane.

An overall comparison of these similarities is given in Fig. 7.13 (upper panel). This portrays the $E_p^* - b$ plane for these five sources plus Mrk 421, to show that the curvature ranges from about 0.12 to about 0.55 (with the exception of only one pointing of 1ES 1959+650 as discussed above); the correlation coefficient for the sample constituted by these sources is $r_{log} = -0.66$. Examination of Tabs. E.1, E.2, E.3 indicates that also the remaining sources in our sample are consistent with the trend estabilished for Mrk 421 and confirmed by the five HBLs discussed above (see also Fig. 7.13 (lower panel)).

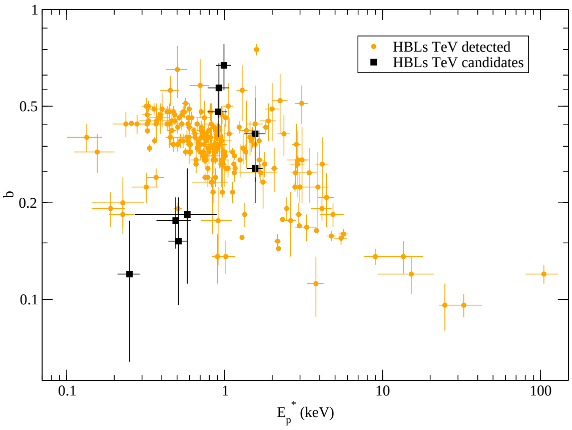

Figure 7.14: The $E_p^* - b$ plot for all TeV HBLs (orange crosses) and the HBLs candidates analysed in detail in Sect. 7.3

Next, two cautionary remarks on biases that may arise in comparing analyses of different sources are pointed out. First, the role of the beaming factor. Although Tramacere et al. (2007a) show that for Mrk 421 the beaming factor is unlikely to be the main driver of the $E_p^* - L_p^*$ relation, it may play subtler role when comparing several sources. In fact, both E_p^* and L_p^* depend on δ; this implies that even though for a single source δ has not a large variation, its value may vary significantly from source to source, affecting the $E_p^* - L_p^*$ plot. The same holds for the magnetic field intensity.

A second effect may be given by a poor temporal sampling. Sources observed sporadically, with observations covering short temporal intervals, may be representative only of flaring or of low emission states, thus producing an uneven coverage of the parameter space.

Finally, a link between the synchrotron peak and the TeV emissions is outlined. In fact, in a SSC scenario the synchrotron signatures derived from X-rays observations are expected to be reflected in the TeV energy range, where the Inverse Compton peak lies, as discussed in details in Chp. 5.

7.4.3 HBLs TeV candidates

As shown by the previous analysis given in Sect. 7.3, the main result for the SSC calculations on the HBLs candidates is that these sources are not in the extreme Klein-Nishina regime (see Tab. 7.9). This fact leads to conclude that these sources can show spectral changes in their TeV flux due to variations of the mean electron energy.

The TeV fluxes predicted with the SSC code are likely higher than the TeV detectability threshold, with the input and output parameters similar to those of TeV detected blazars. Finally, the curvature range evaluated for the TeV candidates is the same of the TeV HBLs, in particular, they cover the same region in the $E_p^* - b$ plane, as shown in Fig. 7.14. An X-ray monitoring of these sources is therefore useful to provide information about the occurrence of high states during the which TeV emission could be easily observed. Otherwise a non-detection would imply a substantial modification of SSC models.

8

The strange case of BL Lacertae

8.1 INTRODUCTION

BL Lacertae was the prototype of the AGN subclass named after it and is one of the best studied blazar in the sky. The source is at the center of a giant elliptical galaxy at a redshift of $z = 0.069$ (Miller, French & Hawley 1978, Stickel & Kuehr 1994 and ref. therein) and due to its low galactic latitude ($b \sim 10.4°$), the field is partially covered by a low surface brightness nebulosity (Penston & Penston 1973). BL Lacertae was identified earlier as a usually featureless low-frequency/intermediate peaked blazar (LBL/IBL, e.g. Fossati et al. 1998), but occasionally the source has shown significant Hα emission lines with equivalent widths > 5Å during periods of very faint optical states in 1995 and 1997 (Vermeulen et al. 1995, Corbett et al. 1996, Corbett et al. 2000). Thus, the source sporadiacally lost its defining characteristics indicating that even in BL Lac objects a broad line region can be observed. Detailed VLBI studies of the source have shown superluminal jet components moving in a bent core-jet structure with apparent speeds β_{app} in the range of 3 to 9 c (e.g. Mutel et al. 1990, Denn et al. 2000, Kellermann et al. 2004, Jorstad et al. 2005).

BL Lacertae is well known for its rapid and strong variability across the whole electromagnetic spectrum. Intra-day to inter-hour variability is usually observed e.g. in the optical together with long-term trends and larger outbursts superimposed. BL Lacertae is well known for its rapid and strong variability across the whole electromagnetic spectrum and the source was target of several intensive multi-frequency investigations over the last decades (e.g. Bregman et al. 1990; Bloom et al. 1997; Madejski et al. 1999; Ravasio et al. 2002; Villata et al. 2002; Böttcher et al. 2003; Böttcher & Reimer 2004; Villata et al. 2004a,b; Bach et al. 2006). Variations on time scales of hours to days are commonly observed in e.g. the radio, optical and X-ray bands (e.g. Kraus et al 2000, Ghosh et al. 2000, Villata et al. 2002, Tanihata et al. 2000, Ravasio et al. 2002), whereas long-term trends and major strong outbursts occur on time scales of weeks to years (e.g. Webb et al. 1988, Fan et al. 1998, Villata et al. 2002, 2004a,b). One of the most prominent example of the latter is the large outburst intensively observed in July 1997 (e.g. Bloom et al. 1997, Böttcher & Bloom 2000), where a dramatic γ-ray flare was reported, accomponied by bright and variable emission in the optical to X-ray bands (Noble et al. 1997, Mattox et al. 1996).

The low-frequency spectral component in the overall SED of BL Lacertae typically peaks in the millimeter to micron range, whereas at high energies the spectral component peaks in the MeV to GeV range. Modeling of the broad band emission observed during the July 1997 outburst appears to require a hybrid SSC/ERC model in which the SSC process is responsible for the X-rays and the ERC process for the γ-ray emission (Madejski et al. 1999, Böttcher & Bloom 2000). However, the previously performed broad band observations of BL Lacertae reveal complex spectral and temporal variability patterns, in particular in the X-ray regime. Here, the source was observed by many satellites and e.g. BeppoSAX detected BL Lacertae up to 100 keV during a multi-frequency campaign performed in 2000 (Ravasio et al. 2003, also for a review of the past campaigns). The *ASCA* and *RXTE* observations of BL Lacertae during the great outburst of 1997 showed flux variations on a timescale of hours together with significant differences between the soft- and hard X-ray spectral as well as variability behaviour. Tanihata et al (2000) interpreted the soft X-ray data as due to the high-energy tail of the synchrotron component and the hard X-ray data as due to the inverse Compton component. Thus, X-ray observations of BL Lacertae are of particular interest since it is in the X-ray regime where the two broad components of its

SED are overlapping and intersecting.

In autumn 2005, BL Lacertae exhibited a new strong optical flare and it was observed as Target of Opportunity (ToO) of a multi-frequency campaign including observations with the *Swift* satallite and a set of three ground-based observatories. Here, the analysis and results of seven pointings with the X-ray Telescope (XRT) instrument onboard *Swift* obtained between July and November 2005 are presented together with (quasi-) simultaneous observations in the radio (1.6, 4.85, 10.5 GHz), IR (J, H, K), optical (I, R, V, B, U) and UV bands providing a total spectral coverage ranging between the radio up to soft (0.7–10 keV) X-ray regime. In addition, an optical spectrum of BL Lacertae was obtained on xxx during the period of the outburst. Furthermore, the strong outburst in autumn 2005 triggered observations with the Cherenkov telescope MAGIC (Major Atmospheric Gamma Imaging Cherenkov telescope, Lorenz et al. 2004) at several occasions to search for multi-GeV emission during October/November 2005.

8.2 OBSERVATIONS

8.2.1 Swift observations

Observations of BL Lacertae were performed with the *Swift* spacecraft (Gehrels et al. 2005) on July 27, 2005 and between October 28 and November 8, 2005 during a total of seven pointings. A summary of these observations is given in Tab. 8.1. Both, the XRT (Burrows et al. 2005) and the Ultraviolet/Optical Telescope (UVOT, Roming et al. 2005) instruments onboard *Swift* were used, whereas the Burst Alert Telescope (BAT, Barthelmy et al. 2005)

XRT observations

Swift–XRT observations of BL Lac were performed simultaneously with the optical and TeV pointings. The log of these observations and the results of the spectral analysis are both reported in Tab. The reduction procedure followed in this analysis is amply discussed in Massaro et al. (2007), here we report a brief description, while the spectral anlysis is described in the next section.

The XRT data analysis is performed with the XRTDAS software (v. 2.1), developed at the ASI Science Data Center (ASDC) included in the HEAsoft package (v. 6.0.2). Event files were calibrated and cleaned with standard filtering criteria using the XRTPIPELINE task combined with the latest calibration files available in the Swift CALDB distributed by HEASARC. Events in the energy range 0.3–10 keV with grades 0–12 (Photon Counting mode) and 0–2 (Windowed Timing mode) were used in the analyses (see Hill et al. for a description of readout modes, and Burrows et al., 2005 for a definition of XRT event grades). Events are extracted using a 20 pixel radius circle. The background for PC mode is estimated from a nearby source-free circular region of 20 pixel radius.

For the WT mode data, events for temporal and spectral analysis are selected using a 40 pixel wide (1 pixel corresponds to 2.36 arcs) rectangular region centered on the source and aligned along the WT one dimensional stream in sky coordinates. Background events are extracted from a nearby source-free rectangular region of 40 pixel width.

Ancillary response files are generated with the XRTMKARF task applying corrections for the PSF losses and CCD defects. The latest response matrices (v. 009) available in the Swift CALDB are used, and source spectra are binned to ensure a minimum of 30 counts per bin in order to utilize the χ^2 minimization fitting technique and insure the validity of Gaussian statistics. The X-ray analysis was performed using an absorbed power-law model with the column density fixed to the Galactic value ($N_H = 2.13 \times 10^{21}\ cm^{-2}$) (Lockman & Savage, 1995):

$$N(E) = N_0 \left(\frac{E}{E_0}\right)^{-\Gamma} \qquad \mathrm{ph\ cm^{-2}\ s^{-1}} \tag{8.1}$$

where Γ is the photon index, and E_0 corresponds to 1keV. It is, typically, less than 2 so, following the SSC scenario, the X-ray emission of BL Lac can be interpreted as the low energy rise of the inverse

Table 8.1: The log of *Swift–XRT* observations and the results of spectral analysis.

Obs ID	*Date*	Expo (s)	Γ	N_0 (10^{-3} $ph\ cm^{-2}\ s^{-1}$)	$F_{(2-10)keV}$ (10^{-11} $erg\ cm^{-2}\ s^{-1}$)	χ^2_r $(d.o.f.)$
00035028001	27/07/2005	563	1.97(0.16)	4.72(0.78)	1.25	0.71 (7)
00035028002	28/10/2005	3434	1.80(0.07)	4.23(0.36)	1.46	1.24 (17)
00035028003$^{(*)}$	29/10/2005	553	1.96(0.15)	4.62(0.66)	1.24	0.92 (5)
00035028004$^{(*)}$	30/10/2005	884	1.98(0.11)	4.40(0.51)	1.15	0.69 (10)
00035028005	31/10/2005	1561	1.92(0.10)	4.40(0.46)	1.26	0.87 (11)
00035028006	01/11/2005	1124	2.02(0.14)	4.58(0.60(	1.13	0.55 (6)
00035028007	02/11/2005	991	2.02(0.16)	4.32(0.59)	1.06	1.27(5)
00035028008	03/11/2005	2692	1.98(0.08)	3.82(0.33)	1.00	0.81(17)
00035028009	08/11/2005	4685	1.76(0.04)	3.25(0.18)	1.19	1.05(42)

(*) observations performed in windowed timing mode (see Sect. 6.3)

Compton component. No features were found in its X-ray spectra and the X-ray power-law description is also in agreement with previous results of historical X-ray observations (BeppoSAX, ASCA 1995 ...). Note that the integrated (2-10 keV) X-ray flux is decreasing from the pointing performed on the 28/10/2005 to the last observation.

UVOT observations

The UVOT instrument onboard the *Swift* satallite is a 30 cm telescope equipped with two grisms and six broadband filters operating at V, B, U, UVW1, UVm2 and UVW2 bands. Simultaneous UVOT data were obtained duing all *Swift* pointings on BL Lacertae with the exception of the first observation on July 25, 2005.

The data were reduced with the SWIFTTOOLS software, included in the standard HEASOFT software package. Photometry was performed using a 6” aperture radius for the V, B and U filters and a 12” radius for the UVW1, UVM2 and UVW2 filters. The raw counts extracted in each aperture after correction for the coincidence loss, were converted into standard magnitutes using the latest UVOT in-orbit zeropoint values (as from 21st July 2005, see eg. Roming et al. 2005a and references therein for a fully discussion about UVOT calibration procedures and photometric accuracy in each filter). The magnitude were de-reddened using the maps of Schlegel, Finkbeiner & Davis (1998) and the extinction curve of Cardelli, Clayton & Mathis (1989) for the optical filters (V, B and U) and those of Seaton (1979) for the UV filters (UVW1, UVM2 and UVW2). The extinction corrected magnitudes were then converted to fluxes using the convertion factors included in the UVOT calibration data. A summary of the UVOT observations and results are given in Tab. 8.2.

8.2.2 Ground-based optical, IR and radio observations

For most of the *Swift* pointings we were able to obtain a contemporaneous, ground-based monitoring of the source in the near-IR and optical regime using the Campo Imperatore and Perugia University observatories. In the radio band, however, flux density measurements with the Effelsberg 100-m telescope at 1.6 GHz were obtained during four pointings between October 29 and November 11, 2005, whereas 4.85 and 10.5 GHz measurments were obtained only during the last *Swift* pointing.

Table 8.2: Summary of the *UVOT* observations and results obtained between October and November 2005. UT date, modified Julian date (MJD) and magnitude plus error are given for each observing band where a measurement was obtained.

UT Date	MJD	V[a]	B	U	UVW1	UVM2	UVW2
2005-10-28	53671.04390	13.70(0.04)	14.72(0.06)	14.29(0.04)	15.02(0.04)	15.92(0.06)	15.87(0.04)
2005-10-28	53671.11060	13.70(0.04)	14.69(0.05)	14.33(0.04)	15.10(0.04)	15.95(0.06)	15.95(0.04)
2005-10-28	53671.17790	13.72(0.04)	14.73(0.06)	14.29(0.04)	15.10(0.04)	15.94(0.06)	16.03(0.04)
2005-10-28	53671.24460	13.64(0.04)	14.72(0.05)	14.30(0.04)	15.14(0.04)	15.93(0.06)	15.93(0.04)
2005-10-28	53671.31200	13.76(0.04)	14.72(0.05)	14.36(0.04)	15.11(0.04)	16.02(0.06)	15.96(0.04)
2005-10-28	53671.37980	–	14.72(0.05)	14.37(0.04)	–	15.99(0.06)	–
2005-10-28	53671.44630	–	–	14.33(0.04)	–	15.95(0.05)	–
2005-10-29	53672.33646	14.07(0.04)	–	14.67(0.05)	15.38(0.04)	16.27(0.06)	16.24(0.04)
2005-10-29	53672.40313	14.09(0.04)	–	14.66(0.05)	15.41(0.04)	16.25(0.06)	16.36(0.05)
2005-10-30	53673.54165	14.21(0.04)	–	14.74(0.05)	15.49(0.05)	16.40(0.07)	16.38(0.05)
2005-10-30	53673.60865	14.26(0.04)	–	14.80(0.05)	15.54(0.05)	16.44(0.07)	16.41(0.05)
2005-10-31	53674.47854	14.46(0.04)	15.36(0.04)	15.02(0.04)	15.84(0.05)	16.67(0.07)	16.72(0.05)
2005-10-31	53674.52772	14.54(0.04)	15.43(0.04)	15.03(0.04)	15.82(0.05)	16.63(0.06)	16.65(0.05)
2005-11-01	53675.26390	14.18(0.06)	15.12(0.10)	14.77(0.06)	15.44(0.07)	16.39(0.09)	16.32(0.07)
2005-11-01	53675.33137	14.21(0.05)	15.15(0.07)	14.81(0.05)	15.44(0.05)	16.23(0.07)	16.37(0.06)
2005-11-01	53675.39800	14.29(0.05)	15.28(0.07)	14.79(0.05)	15.67(0.06)	16.42(0.08)	16.57(0.06)
2005-11-02	53676.33413	14.48(0.04)	15.46(0.06)	14.85(0.04)	15.60(0.05)	16.43(0.07)	16.53(0.05)
2005-11-02	53676.40048	14.43(0.04)	15.33(0.05)	14.83(0.04)	15.53(0.05)	16.60(0.07)	16.38(0.05)
2005-11-03	53677.41580	14.57(0.04)	15.55(0.04)	15.10(0.04)	15.86(0.04)	16.88(0.07)	16.73(0.05)
2005-11-08	53682.37010	14.69(0.02)	15.61(0.02)	15.30(0.02)	15.96(0.03)	16.94(0.04)	16.90(0.03)
2005-11-08	53682.43740	14.68(0.02)	15.58(0.02)	15.24(0.02)	15.95(0.03)	16.88(0.04)	16.87(0.03)

Perugia observatory

Observations at R and I bands were performed between July and November 2005 during a total of xx nights with the Automatic Imaging Telescope (AIT) of the Perugia University Observatory, Italy. The AIT is based on an equatorially mounted 0.4-m Newtonian f/5 reflector having a 0.15-m refractor solidly joined to it. AIT is a robotic telescope equipped with a 192×165 pixels CCD array, thermo-electrically cooled with Peltier elements and Johnson-Cousins BVRI filters are utilised for photometry.

The data were usually taken as a sequence of two or more frames per band and night. After dark-, bias- and flat-field correction, each image was reduced using standard procedures. A combination of the DAOPHOT and Sextractor packages was used to perform standard aperture photometry. The instrumental magnitudes were then further processed to obtain standard magnitudes of BL Lacertae and the relevant errors through differential photometry. Here, an average zero-point correction of each optical frame was applied using the tabulated magnitudes of (please more info here: ref. star sequence, host correction etc.) A summary of the AIT observations at R and I bands is given in Tab. 8.3 including observing date, mean JD and observed magnitudes.

Table 8.3: Summary of the ground-based optical/IR observations and results obtained between July and November 2005. UT date, modified Julian date (MJD) and magnitude plus error are given for each observing band where a measurement was obtained.

UT Date	MJD	K	H	J	I	R	V	B	U
2005-07-05	53556.04236	10.54(0.03)	11.42(.03)	12.42(0.03)	13.46(0.02)	14.29(0.02)	14.96(0.03)	16.11(0.03)	–
2005-07-29	53580.05902	–	–	–	13.35(0.01)	14.17(0.01)	14.81(0.02)	15.86(0.02)	–
2005-10-26	53669.82841	9.27(0.02)	10.15(0.02)	11.02(0.02)	12.29(0.03)	13.06(0.03)	–	–	–
2005-10-27	53670.79355	9.31(0.02)	10.15(0.02)	11.00(0.02)	12.44(0.03)	13.14(0.03)	13.79(0.03)	14.7(0.03)	14.42(0.03)
2005-10-28	53671.84448	9.35(0.02)	10.17(0.02)	11.01(0.02)	12.37(0.03)	13.14(0.03)	–	–	–
2005-10-29	53672.88060	9.34(0.02)	10.18(0.02)	11.06(0.02)	12.48(0.03)	13.28(0.03)	–	–	–
2005-10-30	53673.87192	9.37(0.02)	10.20(0.02)	11.10(0.02)	12.68(0.03)	13.48(0.03)	–	–	–
2005-10-31	53674.97036	9.49(0.02)	10.33(0.02)	11.27(0.02)	–	–	–	–	–
2005-11-02	53676.94018	–	–	–	12.92(0.03)	13.73(0.03)	–	–	–
2005-11-03	53677.87451	–	–	–	–	13.86(0.05)	–	–	–
2005-11-04	53678.82202	–	–	–	12.95(0.03)	13.79(0.05)	–	–	–
2005-11-08	53682.93652	–	–	–	12.92(0.03)	13.78(0.03)	–	–	–

Optical spectrum

Quasi-simultaneous flux density measurements in the radio band were obtained with the Effelsberg 100 m radiotelescope between October 30 and November 01, 2005 at 1.6 GHz and on November 9, 2005 at 4.85 and 10.5 GHz. Here, a single horn receiver mounted in the primary focus (1.6 GHz) and the multi-horn systems installed in the secondary focus (4.85 and 10.5 GHz) were used. The target source BL Lacertae is point-like and sufficiently strong at the observed frequency bands allowing to observe with cross-scans in azimuth and elevation direction. Each cross-scan had an equal number of sub-scans in both directions with the number of sub-scans matching the source brightness at the given frequency. Primary flux density calibrators (e.g. 3C 286) were observed to adjust the focus as well as pointing of the telescope and to finally link the measured fluxes to the standard flux density scale of Baars et al. (1977).

Radio observations

Table 8.4: Summary of the flux density measurements performed with Effelsberg radiotelescope between October and November 2005. Here, the mean flux density $< F >$ is given for each observing day, whereas N_{data} denotes the number of individual scans.

ν [GHz]	UT date	MJD	N_{data}	$< F >$ [Jy]	ΔF [Jy]
1.6					
4.85	2005-11-09	53683.016	1	3.810	0.006
10.5	2005-11-09	53683.013	2	4.103	0.011

The data reduction was done using standard procedures as described in detail by e.g. Kraus et al. (2003). The analysis includes as first step the fitting of gaussian profiles to each individual sub-scan. After correcting the measured amplitudes for small pointing offsets of the order < 5–$10''$ (assuming a Gaussian shape of the telescope beam), the sub-scans were averaged over the full scan. Subsequently, systematic elevation-dependent gain effects were removed using the standard gain-curves of the individual receivers. Finally, the measured antenna temperature for each scan was linked to the absolute flux-density scale using the primary calibrator measurements (Baars et al. 1977, Ott et al. 1994).

The individual flux density errors are composed of the statistical errors from the reduction process including the errors of the Gaussian fits, the weighted average over the sub-scans and the elevation-dependent gain correction and a contribution from the scatter seen in the primary calibrator measurements. The final uncertainties are of the order a few percent. In Tab. 8.4 the results of the flux-density measurments in the radio band are summarized and give the averaged flux density of BL Lacertae for each observing frequency.

8.3 SSC MODELS FOR THE SED DESCRIPTION

8.3.1 Multiwavelenght campaign from July to November 2005

Fig. 8.1b shows the spectral energy distribution of BL Lac obtained from the simultaneous data described in this work. The VHE γ-ray points, taken from Albert et al. (2007), are corrected for the Extragalactic Background Light (EBL) absorption using the ”Low” EBL model of Kneiske et al. (2004). The SED of a single Synchrotron Self Compton (SSC) component is plotted in Fig. 8.2a The electron distribution for the emitting particles is a pure log-parabolic model described in detail in Sect. 3.

When reproducing the IR to X-ray SED of BL Lac with the single zone SSC model, one can observe that the tail in the TeV range is not described by this model, also considering the second order inverse Compton scattering. The X-ray emission in this SSC model is in the Thomson regime and the expected IC peak frequency ϵ_p will be $\simeq \frac{4}{3}\gamma'^2_p \nu_p \simeq 10^{19}$ Hz, where γ'_p is the peak of $\gamma'^2 N(\gamma')$ and ν_p is the synchrotron peak frequency, as reported in Tab. 8.6. An alternative possibility is that of considering a second SSC component able to reproduce the VHE emission without contributing a large additional flux in the low energy bands with respect to the single SSC model. Fig. 8.2b shows the SED of this 2 zones SSC model that is able to fit all the simultaneous data. Similar multicomponent SSC model was successfully used to reproduce the VHE emission in the radio galaxy M87 and to perform TeV predictions of the BL Lac object PKS 0521-36, the radio galaxy Cen A and the FSRQ 3C 273 (Lenain et al., 2007).

Table 8.5: Input values for simulations

Parameter	*Symbol*	1^{st}*component*	2^{nd} component
Redshift	z	0.069	0.069
Beaming Factor	δ	12.00	12.00
Magnetic Field	B' (G)	1.50	0.05
Volume	V' (cm^3)	8.20 $\times 10^{48}$	5.00 $\times 10^{48}$
Density	n' (cm^{-3})	1.80 $\times 10^{2}$	2.00 $\times 10^{1}$
Electron energy	γ'_0	1.80 $\times 10^{3}$	1.5 $\times 10^{4}$
Spectral index	s	4.20	2.50
Curvature	r	1.50	1.00
Minimum energy	γ'_{min}	50.00	50.00
Maximum energy	γ'_{max}	5.00 $\times 10^{8}$	5.00 $\times 10^{8}$

These calculations, the first component is in Thomson regime while the second one, with the synchrotron peak frequency in the near UV, approaches to the Klein-Nishina limit. The second order inverse Compton emission of both components is found to be negligible in comparison to their first order IC radiation. Details of the input and output values for both models are reported in Tab. 8.5.

Note that the second component has an emitting region smaller than the first one, the total electron energy and the γ'_p are one order of magnitude higher with respect to the other, whereas the magnetic field B' is two orders of magnitude lower.

According to the criterion derived in Sect. 5.6, it is possible to evaluate the Compton catastrophe limit for the first component, by means of the η_c parameter, defined by eq. 5.113 and eq. 5.114, that must be lower than unity. For the parameter's values given in Tab. 8.5, $\eta_c \simeq 0.24$, below the Compton catastrophe limit, in agreement with the luminosity ratio L_{IC}/L_S reported in Tab. 8.6.

Note that numerical calculations, when the peak energy of the second component is increased to the X-ray range did not produce acceptable SEDs. In fact, the resulting size of the emitting region R smaller than $10^{13} cm$, a value exceeding the compactness limit of $e^{\pm}$ pair production (Cavaliere & Morrison, 1980, Guilbert et al., 1985) and its IC emission is found to be higher and more energetic than the observed TeV spectrum.

The observed fast optical-UV variability, coupled with the absence of significant changes of the X-ray flux, can be interpreted in terms of the radiative lifetimes. The synchrotron cooling time at the peak frequency ν_p is given by

$$t'_{cool,S} = 5.692 \times 10^{11} \left[\frac{\delta}{\nu_p (1+z)} \right]^{1/2} B'^{-1}(G) \quad \mathrm{s} \quad , \tag{8.2}$$

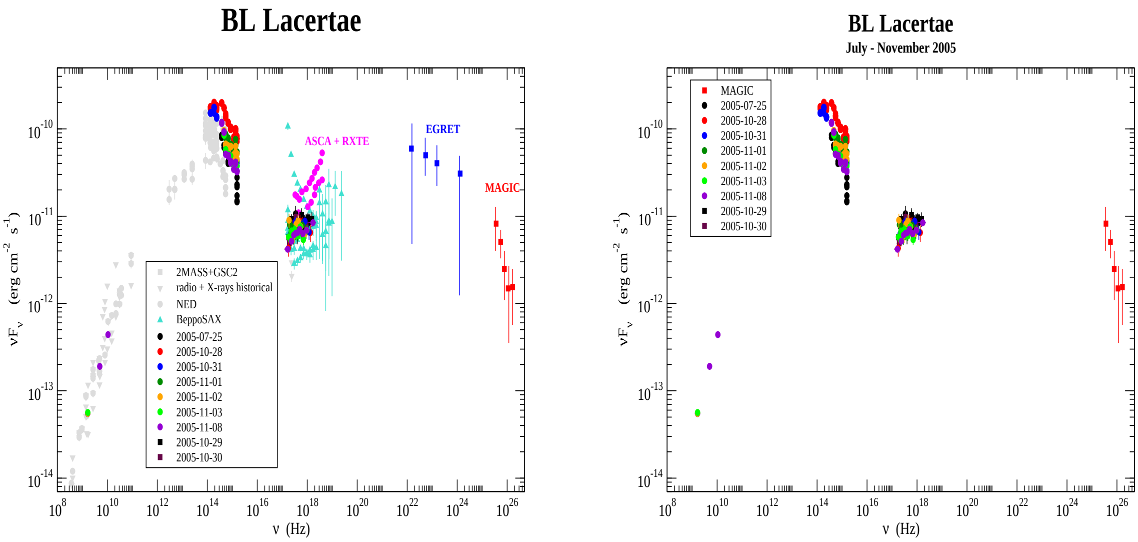

Figure 8.1: a) The SED of BL Lac with historical data (grey points) and observations performed between July and November 2005 (coloured points). b) Only the data set corresponding to the October-November simultaneous pointings.

that, with the input and output parameters in Tab. 8.5 and Tab 8.6, results $\sim 10^3$ s. Noting that the maximum frequency of the synchrotron energy density lies at $\nu_t = \nu_p 10^{-1/2b_S}$, the Lorentz factor of electrons that radiate via inverse Compton scattering at $\epsilon \simeq 10^{17}$Hz, is

$$\gamma' = \sqrt{\frac{3\epsilon}{4\nu_p} 10^{1/2b_S}} \quad , \tag{8.3}$$

which turns out to be smaller than γ'_p. Cooling times scales as the inverse of the electron energy, then the synchrotron $t_{cool,S}$ is grater than that of IC emission. This difference could explain the difference between X-ray and IR-UV time scale variability.

Albert et al. (2007) applied the external Compton (EC) model developed by Ravasio et al. (2002) to reproduce the EGRET and MAGIC data with a single component (see Fig. 8.3). Note however that, when our simultaneous optical, UV and X-ray data are considered this model predicts fluxes significantly lower than the observed ones of at least a factor of about 5. A model with external Compton components introduces more parameters, and an accurate analysis is required to study this scenario.

Finally, note that radio points in Figs. 8.2 lie on the low energy extension of the synchrotron spectrum and are incosistent with the expected synchrotron self absorption. This discrepancy has been already present in the models of other sources (e.g. S5 0716+714, Tsang & Kirk 2007) and it is not clearly explained. A considered possibility is that radio emission is originated in regions at a relatively large distance from the nucleus or it is interpreted as emission by a monoenergetic electron population (Tsang & Kirk, 2007), however the fact that the measured fluxes agree well with the low frequency extrapolation of log-parabolic spectra is an open problem to be investigated.

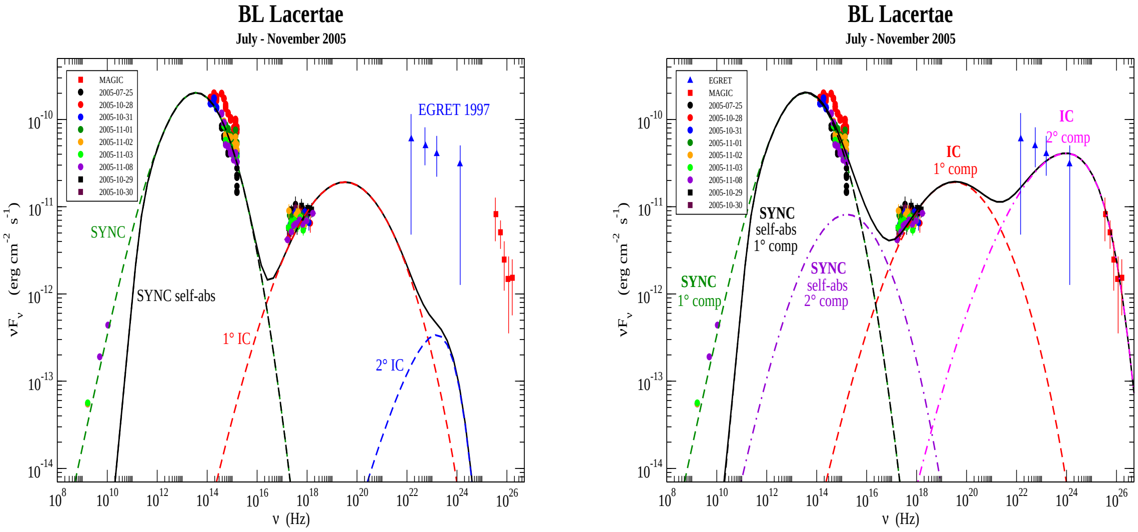

Figure 8.2: a) Single zone SSC model: the synchrotron emission self absorbed(green dashed line) and not self absrobed (black dashed line), the first order inverse Compton component (red dashed line) and the second order one (blue dashed line). b) The SSC two zone model: the synchrotron (violet dashed line) and the inverse Compton (indigo dashed line) emission of the second componet are plotted with the previous zone SSC radiation.

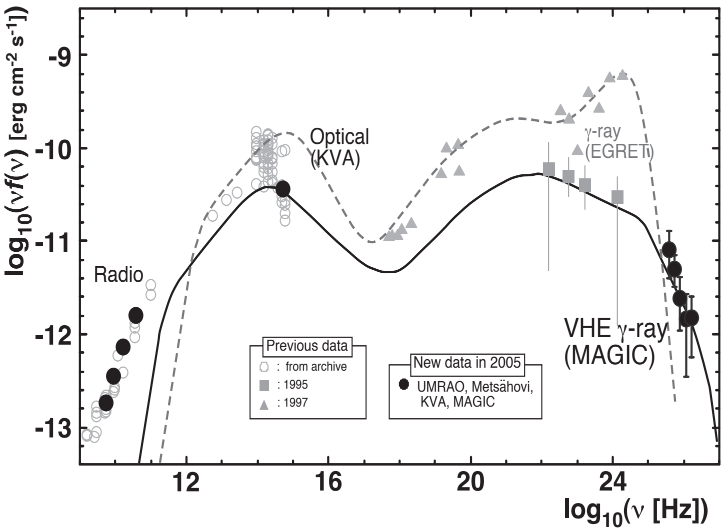

Figure 8.3: The external Compton (EC) model developed by Ravasio et al. (2002) used in Albert et al. (2007) to reproduce the EGRET and MAGIC data with a single component.

Table 8.6: Output values for simulations

Parameter	*Symbol*	1^{st}*component*	2^{nd} component
Source			
Luminosity Distance	$D_L\ (Mpc)$	3.11×10^{2}	3.11×10^{2}
Magnetic energy density	$u'_B\ (erg\ cm^{-3})$	8.95×10^{-2}	0.99×10^{-4}
Radius	$R'\ (cm)$	1.25×10^{16}	1.06×10^{16}
Electron Number	N_{el}	1.48×10^{52}	0.10×10^{51}
Normalization	$N'_0\ (cm^{-3})$	1.01×10^{2}	1.37×10^{-4}
Electron peak energy	γ'_p	0.33×10^{3}	0.84×10^{4}
Total Electron energy	$E'_{tot}\ (erg)$	0.54×10^{51}	0.58×10^{52}
Synchrotron			
Curvature	b_S	0.27	0.20
Peak Frequency	$\nu_p\ (Hz)$	0.34×10^{14}	0.16×10^{16}
SED peak height	$S_p\ (erg\ s^{-1}\ cm^{-2})$	0.22×10^{-9}	0.81×10^{-11}
Maximum frequency	$\nu^S_{max}\ (Hz)$	0.51×10^{25}	0.17×10^{24}
IC Maximum frequency	$\nu^C_{max}\ (Hz)$	0.69×10^{30}	0.69×10^{30}
Luminosity	$L_S\ (ergs^{-1})$	0.12×10^{48}	0.52×10^{46}
Inverse Compton			
Curvature	b_C	0.15	0.17
Peak Frequency	$\epsilon_p\ (Hz)$	0.32×10^{20}	0.76×10^{24}
SED peak height	$C_p\ (erg\ s^{-1}\ cm^{-2})$	0.23×10^{-10}	0.41×10^{-10}
Luminosity	$L_C\ (ergs^{-1})$	0.17×10^{47}	0.28×10^{47}
Luminosity Ratio	L_C/L_S	0.14	5.4

9

Summary and Conclusions

In the light of the aims anticipated in the introduction, I investigated the variability and spectral properties of the high energy emission from BL Lac objects detected also at TeV energies. In the framework of the widely accepted Synchrotron-Self Compton scenario adopted to describe the SEDs of this class of sources, I worked on the interpretation of both the synchrotron and inverse Compton components: the former observed in the X-ray band, and the latter at the highest γ-ray energies.

A first relevant problem is the estimate of the physical parameters. I have shown (Chp. 5) how it is possible to derive these quantities on using spectral relations, based on the position and the height of the SED peaks, of both components together with an additional relation based on the time scale variability. These relations provide an unique solution to constrain the structure of the source. I also derived a new analytical relation to evaluate the occurrence of the Compton catastrophe based on a new definition of the η_C parameter, introduced by Tsang & Kirk (2007), that can directly take into account the observed spectral data for a source in the Thomson regime.

A relevant feature of BL Lacs spectra is the curvature of their SED observed on several decades of frequency. This spectral curvature is very evident around the peak energy, and it was difficult to explain in terms of an extra absorption or with an exponential cut-off. A more straightforward interpretation is that the curvature is a consequence of statistical acceleration mechanisms (Chp. 3 for a brief review), when the fluctuations are properly considered. A second order spectral analysis is then necessary to obtain informations on this issue; in particular an estimate of the spectral curvature, together with the other spectral parameters, the peak and the height of the SEDs, can be derived in the simplest way by means of a log-parabolic law (i.e. a parabola in the log-log plot), that I used throughout all this Thesis.

To complete this work several numerical codes were developed (Chp. 5) to compare the observed SEDs with theoretical expectations. These codes are able to evaluate the SSC emission including the second order IC radiation, and provide also some statistical tools to evaluate directly the spectral parameters of the calculated SED.

The second part of the Thesis is devoted to the observational study of the SEDs of a sample of HBL objects. I used the rich data set of observations performed with *BeppoSAX*, *XMM-Newton* and *Swift* satellites. New data reduction procedures and new data analysis tools were derived (Chp. 6), and the intercalibration between *XMM-Newton* and *Swift* was performed for an accurate comparison of these observations.

I considered first the famous HBL Mrk 421 for which a very wide X-ray data set is available. In this analysis the log-parabolic model was always used (Chp. 4). New results concerning the spectral variations have been presented and discussed (Chp. 7). Correlations exist between the peak values S_p of its SED and the peak positions E_p, and between the spectral curvature b and E_p. The former may be interpreted in the framework of synchrotron emission and, using this correlation, an upper limit to the beaming variance can be set; this limit is relevant in the framework of the internal shock scenario. This assumes that shells ejected from the central engine with slightly different relativistic velocities and slightly differing angles collide in the jet at sub-parsec scales and produce flares. The temporal behaviour and the radiative efficiency of this process depend on the collision frequency and energetics, respectively. Guetta et al. (2004) assume that shells are ejected at a frequency close to 10^{-4} Hz, with Γ values distributed around the average value of about 15 after a random (uniform) distribution with some dispersion, about 3. However, the dispersion is considerably larger than the values obtained from our analysis. On the other hand, Tanihata et al. (2003) assume values of the beaming factor δ following a normal distribution with $\sigma_\delta/\mu_\delta \ll 0.1$ and ejection intervals around 600 s; whence they obtain a good reproduction of the temporal behaviour, but also a very low radiative efficiency. The upper limit derived from our analysis, much lower than the value assumed by Guetta et al. (2004), emphasizes the efficiency problem reported by Tanihata et al. (2003).

The second correlation between b and E_p shows a decrease of the curvature as the peak energy increases. The interpretation of this behavior is in terms of the electron kinetic equation with a diffusion term on the energy axis. The solution of this equation for an initial mono-energetic injection predicts that with ongoing stochastic acceleration the curvature should decrease while the peak energy moves to higher energies. An alternative explanation of this correlation is discussed in terms of statistical, energy-dependent acceleration probability; this leads again to a correlation as observed. The aim was to stress a common point to both views, that is, the relevance of the curvature parameter to understand the observed spectral evolution of the source. This result would not hold with the beaming as the main driver of spectral variations. while it is consistent with those from the first, namely, the $S_p - E_p$ correlation.

For the sake of completeness, the X-ray analysis of the rest of TeV detected HBLs was well performed. I found that also these spectra, as for Mrk 421, are described with a log-parabolic model, even though in some cases an acceptable fit is also provided by a power-law absorbed by the Galactic column density. Five sources (namely: PKS 0548-322, 1H 1426+428, Mrk 501, 1ES 1959+650, PKS2155-304) have enough data to warrant investigating in some detail the $E_p^* - L_p^*$ and $E_p^* - b$ relations. Comparing these values with those evaluated for Mrk 421, at least three sources (namely: PKS 0548-322, 1H 1426+428 and Mrk 501) following the same trends as Mrk 421 in the $E_p^* - L_p^*$ plane were found. In the case of 1ES 1959+650, our observed spectral parameters cover a smaller region compared to Mrk 421; nevertheless, the trend so outlined is consistent with that of the latter. Finally, PKS 2155-304 has again a similar behaviour in the $E_p^* - b$ plane but a definitely different one in the $E_p^* - L_p^*$ plane.

Another interesting line is to search for possible TeV candidates among HBLs that present the same spectral properties of those TeV detected. First of all, a complete X-ray analysis of the *XMM-Newton* observations was performed. Two HBLs in the TeV observed sample, with quasi-simultaneous data in the X-ray and in the TeV band, were selected. Their SEDs were modeled by means of the SSC codes to derive their physical parameters, and these values were used to predict the VHE emission of the complete sample of HBLs observed by *XMM-Newton*. The predicted TeV fluxes are likely higher than the TeV detectability threshold. Finally, the curvature range evaluated for the TeV candidates was found the same of the TeV HBLs; in particular, they cover the same region in the $E_p^* - b$ plane. An X-ray monitoring of these sources is therefore useful to provide information about the occurrence of high states during which TeV emission could be easily observed. Otherwise, a non-detection could need a modification of SSC models.

As shown by the previous analysis, the main result for the SSC calculations on the HBLs candidates is that these sources are not in the extreme Klein-Nishina regime. This fact leads to conclude that these sources can show spectral changes in their TeV flux due to variations of the mean electron energy.

The last chapter is devoted to the study of VHE emission properties of BL Lacertae; thus is a relevant case because it is the first LBL detected at TeV energies. When reproducing the IR to X-ray SED of BL Lac with a single zone SSC model, one can observe that the tail in the TeV range is not described by the model, even considering the second order inverse Compton scattering. An alternative possibility is that a second SSC component is able to reproduce the VHE emission without contributing a large additional flux in the low energy bands relative to the single SSC model. In these calculations, the first component is in Thomson regime while the second one, with the synchrotron peak frequency in the near UV, approaches to the Klein-Nishina limit. The second order inverse Compton emission of both components is found to be negligible in comparison to their first order IC radiation.

According to the criterion derived in Sect. 5.6, it was possible to evaluate that the first component is below the Compton catastrophe limit, in agreement with the luminosity ratio L_{IC}/L_S.

Note that numerical calculations, when the peak energy of the second component is increased to the X-ray range did not produce acceptable SEDs. In fact, the resulting size of the emitting region R smaller than $10^{13} cm$, a value exceeding the compactness limit of $e^{\pm}$ pair production (Cavaliere & Morrison, 1980, Guilbert et al., 1985) and its IC emission is found to be higher and more energetic than the observed TeV spectrum.

The observed fast optical-UV variability, coupled with the absence of significant changes of the X-ray flux, can be interpreted in terms of the radiative lifetimes. Cooling times scales as the inverse of the electron energy, then the synchrotron $t_{cool,S}$ is longer than that of IC emission. This difference could explain the difference between X-ray and IR-UV time scale variability.

Finally, note that radio points on the low energy extension of the synchrotron spectrum are inconsistent with the expected synchrotron self absorption. This discrepancy is already present in the models of other sources (e.g. S5 0716+714, Tsang & Kirk 2007) and it is not clearly explained. Possibilities to be considered are that the radio emission is originated in regions at a relatively large distance from the nucleus, or the emission by a monoenergetic electron population (Tsang & Kirk, 2007); however, the fact that the measured fluxes agree well with the low frequency extrapolation of log-parabolic spectra constitutes an open problem to be investigated.

The work developed in this thesis is mostly devoted to the study of SSC models to describe HBL SEDs, with the only exception of BL Lacertae. A similar analysis could be applied to other LBL objects when the new simultaneous observations of both the synchrotron and the inverse Compton emissions will be avaiable. These will occur in the next year when the new satellites *AGILE*, *GLAST* and *Planck* will provide a large number of data on rich LBL samples. The first period of activity of *AGILE* in which some LBLs and FSRQs have already been detected confirm the relevance of the γ-ray observations for the understanding of the Blazars phenomenon.

Appendix A

Properties of Spectral Energy Distributions

A.1 POWER-LAW MODEL

The photon specific flux ϕ_ν for a simple power-law model can be expressed at fixed frequency ν_0 in terms of two free parameters: the normalization ϕ_0 and the spectral index a

$$\phi_\nu = \phi_0 \left(\frac{\nu}{\nu_0}\right)^{-a} \quad , \tag{A.1}$$

its logarithmic expression will be given by the relation

$$\log\left(\frac{\phi_\nu}{\phi_0}\right) = -a \log\left(\frac{\nu}{\nu_0}\right) \quad ; \tag{A.2}$$

then, multiplying for the photon energy $E = h\nu$ it is possible to derive the specific flux F_ν as

$$F_\nu = (h\nu_0\phi_0)\left(\frac{\nu}{\nu_0}\right)^{-a+1} = F_0\left(\frac{\nu}{\nu_0}\right)^{-a+1} \quad , \tag{A.3}$$

and again the spectral energy distribution S_ν can be derived with another multiplication for the frequency ν

$$S_\nu = (h\nu_0^2\phi_0)\left(\frac{\nu}{\nu_0}\right)^{-a+2} = S_0\left(\frac{\nu}{\nu_0}\right)^{-a+2} \quad . \tag{A.4}$$

Integrating over the frequency it is possible to evaluate the total emitted flux in the range of frequencies between $[0, \nu]$ as follows

$$F = \int_0^\nu F_\nu d\nu = F_0 \int_0^\nu \left(\frac{\nu}{\nu_0}\right)^{-a+1} d\nu = \frac{\nu_0 F_0}{2-a}\left(\frac{\nu}{\nu_0}\right)^{-a+2} \quad . \tag{A.5}$$

It is evident by replacying eq. A.5 in eq. A.4 that the total flux is proportional to the spectral energy distribution.

A.2 POWER-LAW WITH A HIGH ENERGY EXPONENTIAL CUT-OFF MODEL

The most simple emulation of a curved spectrum can be derived combining the power-law model with an high energy exponential cut-off at frequency ν_c. This model will be described in terms of three free parameters: the normalization ϕ_0 and the spectral index a as in the previous case, with the addition of the frequency ν_c to take into account of the exponential cut-off. This spectrum ϕ_ν for this model can be written in the form

$$\phi_\nu = \phi_0\left(\frac{\nu}{\nu_0}\right)^{-a} e^{-\frac{\nu}{\nu_c}} \quad , \tag{A.6}$$

that corresponds in logarithmic expression to

$$\log\left(\frac{\phi_\nu}{\phi_0}\right) = -a\log\left(\frac{\nu}{\nu_0}\right) - \frac{\nu}{\nu_c} \quad . \tag{A.7}$$

It is possible to derive the specific flux from eq. A.6 multiplying for the photon energy, then obtaining

$$F_\nu = (h\nu_0\phi_0)\left(\frac{\nu}{\nu_0}\right)^{-a+1} e^{-\frac{\nu}{\nu_c}} = F_0\left(\frac{\nu}{\nu_0}\right)^{-a+1} e^{-\frac{\nu}{\nu_c}} \quad . \tag{A.8}$$

The correspondent SED for this model will be given by the relation

$$S_\nu = (h\nu_0^2\phi_0)\left(\frac{\nu}{\nu_0}\right)^{-a+2} e^{-\frac{\nu}{\nu_c}} = S_0\left(\frac{\nu}{\nu_0}\right)^{-a+2} e^{-\frac{\nu}{\nu_c}} \quad . \tag{A.9}$$

Integrating over the frequency in the range $[0, \infty]$ it is possible to evaluate the bolmetric flux F_{bol}

$$F_{bol} = \int_0^\infty F_\nu d\nu = F_0 \int_0^\infty \left(\frac{\nu}{\nu_0}\right)^{-a+1} e^{-\frac{\nu}{\nu_c}} d\nu = \nu_0 F_0 \left(\frac{\nu_c}{\nu_0}\right)^{-a+1} \Gamma(a+2) \quad , \tag{A.10}$$

where $\Gamma(a+2)$ is the $Euler's\ function$

$$\Gamma(z) = \int_0^\infty t^{z-1} e^{-t} dt \quad , \tag{A.11}$$

evaluated for the argument $(a+2)$. For this curved model it is possible to derive the peak frequency of the SED: ν_p and the correspondent height at this frequency: S_p.

Evaluating the derivate of the spectral energy distribution it follows that:

$$\left.\frac{dS_\nu}{d\nu}\right|_{\nu_p} = 0 \qquad and \qquad S_p = S_\nu(\nu_p) \tag{A.12}$$

so the peak fequency will be given by the relation

$$\nu_p = (2-a)\nu_c \quad , \tag{A.13}$$

with the correspondnt value of S_p

$$S_p = S_0\left(\frac{\nu_p}{\nu_0}\right)^{(-a+2)} e^{a-2} \quad . \tag{A.14}$$

An useful expression can be derived for this model, describing it in terms of three different parameters: the peak frequency ν_p, the height of the SED at ν_p S_p and the spectral index a. In fact, the the height of the SED at ν_p S_p can be written as

$$S_p = S_\nu(\nu_p) = S_0\left(\frac{\nu_p}{\nu_0}\right)^{a} e^{-\nu_p/\nu_c} \quad , \tag{A.15}$$

then, replacying in the expression of the SED it is possible to obtain

$$S_\nu = S_p\left(\frac{\nu}{\nu_p}\right)^{a} e^{a+2} e^{-\frac{\nu}{\nu_p}(a+2)} \quad , \tag{A.16}$$

and finally, the searched relation will be given by

$$S_\nu = S_p\left(\frac{\nu}{\nu_p}\right)^{a} exp\left[1-\frac{\nu}{\nu_p}\right]^{(a+2)} \quad . \tag{A.17}$$

Using this relation during a fitting procedure the three parameters: ν_p, S_p and a, can be evaluated indipendently.

A.3 LOG-PARABOLIC MODEL

The log-parabolic spectrum ϕ_{nu} can be expressed in terms of three free parameters as in the case of the previous one: the spectral index a, the curvature b and the normalization ϕ_0, all evaluated at fixed frequency ν_0. The simple analytical expression for this model is

$$\phi_\nu = \phi_0 \left(\frac{\nu}{\nu_0}\right)^{-a-b\log\left(\frac{\nu}{\nu_0}\right)} \quad , \tag{A.18}$$

it corresponds to a parabolic spectrum in the logarithminc coordinates, in fact, it can be written in the form

$$\log\left(\frac{\phi_\nu}{\phi_0}\right) = -a\log\left(\frac{\nu}{\nu_0}\right) - b\log^2\left(\frac{\nu}{\nu_0}\right) \quad . \tag{A.19}$$

The specific flux for this spectrum willbe given by the relation

$$F_\nu = (h\nu_0\phi_0)\left(\frac{\nu}{\nu_0}\right)^{-a+1-b\log\left(\frac{\nu}{\nu_0}\right)} = F_0\left(\frac{\nu}{\nu_0}\right)^{-a+1-b\log\left(\frac{\nu}{\nu_0}\right)} \quad , \tag{A.20}$$

and then multiplying for the frequency it is possible to obtain the SED

$$S_\nu = (h\nu_0^2\phi_0)\left(\frac{\nu}{\nu_0}\right)^{-a+2-b\log\left(\frac{\nu}{\nu_0}\right)} = S_0\left(\frac{\nu}{\nu_0}\right)^{-a+2-b\log\left(\frac{\nu}{\nu_0}\right)} \quad . \tag{A.21}$$

Note that the spectral curvature of the specific photon flux is the same of the specific flux and of the SED. Integrating the specific flux over the frequency in the range $[0, \infty]$ it is possible to derive the bolometric flux of the log-parabolic spectrum. The integral of this model can be transformed in to a gaussian one with some substitutions and it yields

$$F_{bol} = \int_0^\infty F_\nu d\nu = F_0 \int_0^\infty \left(\frac{\nu}{\nu_0}\right)^{-a+1-b\log\left(\frac{\nu}{\nu_0}\right)} d\nu = \nu_0 F_0 \sqrt{\frac{\pi}{b}} e^{\frac{(a-2)^2}{4b}} \sqrt{\ln 10} \quad . \tag{A.22}$$

The specific photon flux has a maximum that can be obtained evaluating the derivate of the spectrum as

$$\left.\frac{d\phi_\nu}{d\nu}\right|_{\nu_{max}} = 0 \qquad and \qquad \phi_{max} = \phi_\nu(\nu_{max}) \quad , \tag{A.23}$$

so the maximum frequency ν_{max} correspond to

$$\nu_{max} = \nu_0 10^{-\frac{a}{2b}} \quad , \tag{A.24}$$

and the specific photon flux evaluated at this frequency will be given by the relation

$$\phi_{max} = \phi_0 10^{\frac{a^2}{4b}} \quad . \tag{A.25}$$

Also the SED has a peak frequency ν_p, that can be evaluated by the derivate of $\S_n u$

$$\left.\frac{dS_\nu}{d\nu}\right|_{\nu_p} = 0 \qquad and \qquad S_p = S_\nu(\nu_p) \quad , \tag{A.26}$$

and it is equal to

$$\nu_p = \nu_0 10^{\frac{2-a}{2b}} \quad , \tag{A.27}$$

with the height of the SED calculated at its peak frequency

$$S_p = S_0 10^{\frac{(2-a)^2}{4b}} \quad . \tag{A.28}$$

Note that, combining eq. A.22 and eq. A.28, the bolometric flux is proportional to the SED peak height S_p

$$F_{bol} = \sqrt{\ln 10}\sqrt{\frac{\pi}{b}}S_p = 2.7\frac{S_p}{\sqrt{b}} \quad . \tag{A.29}$$

Also for this spectral model, as for the previous one, a pratical relation that describes the spectrum in terms of three different parameters: the SED peak frequency ν_p, the correspondent SED peak height S_p and the curvature b can be derived as follows. Observing that

$$\log\frac{\nu_p}{\nu_0} = -\frac{a-2}{2b} \quad , \tag{A.30}$$

the SED peak height will be given by the relation

$$S_p = S_\nu(\nu_p) = S_0\left(\frac{\nu_p}{\nu_0}\right)^{-a+2-b\log\left(\frac{\nu_p}{\nu_0}\right)} \quad , \tag{A.31}$$

that in the logarithmic expression, replacying with eq. A.27 it follows

$$\log\frac{S_p}{S_0} = \frac{(a-2)^2}{4b} \quad . \tag{A.32}$$

Noting that for the frequency

$$\log\frac{\nu}{\nu_0} = \log\frac{\nu}{\nu_p} - \frac{a-2}{2b} \quad , \tag{A.33}$$

and observing that for the SED

$$\log\frac{S_\nu}{S_0} = \log\frac{S_{nu}}{S_p} + \frac{(a-2)^2}{4b} \quad , \tag{A.34}$$

combining these two relations it is possible to obtain the following expression in the logarithmic coordinates

$$\log\frac{S_\nu}{S_p} = -b\log^2\frac{\nu}{\nu_p} \quad ; \tag{A.35}$$

it is the searched relation:

$$S_\nu = S_p\left(\frac{\nu}{\nu_p}\right)^{-b\log\left(\frac{\nu}{\nu_p}\right)} \tag{A.36}$$

Also in this case, using this relation during a fitting procedure the three parameters: ν_p, S_p and the curvature b, can be evaluated indipendently.

Appendix B

The Synchrotron and the Inverse Compton radiation

B.1 THE SYNCHROTRON RADIATION

B.1.1 The quantistic limit for the synchrotron emission

The quantistic limit for the synchrotron emission is the value of the magnetic field at which corresponds the transition between the classic theory and the quantistic one. This transition occurs when the Larmor radius of the electron (see Sect. 4.1.1), that is moving in the magnetic field, becomes of the same order of the Compton wavelenght that is

$$\lambda_C = \frac{h}{mc} \quad , \tag{B.1}$$

then comparing these two quantities one finds

$$\rho = \frac{v}{\omega_L} \simeq \frac{c}{\omega_L} = \frac{mc^2}{eB} \quad , \tag{B.2}$$

and it is possible to define the *critical magnetic field* B_{cr} by the relation

$$\frac{mc^2}{eB_{cr}} = \frac{c}{\omega_L} \quad \rightarrow \quad B_{cr} = \frac{m^2c^3}{eh} \simeq 4.414 \times 10^{13}\mathrm{G} \quad . \tag{B.3}$$

Another method to derive B_{cr} is given by the *indetermination principle*: $\Delta x \Delta p \simeq h$. Replacing Δx with the Larmor radius it is possible to obtain

$$\Delta x \Delta p = h \quad \rightarrow \quad \frac{mc^2}{\gamma e B_{cr}} \gamma mc^2 = h \quad . \tag{B.4}$$

It is also possible to derive another expression of the *critical magnetic field* B_{cr} comparing the Larmor frequency ν_L with the condition of the Thomson limit (see Sect. 4.2.1) obtaining

$$h\nu_L = mc^2 \quad \rightarrow \quad \frac{heB_{cr}}{2\pi mc^2} \quad . \tag{B.5}$$

Finally, considering the energy conservation, one electron cannot radiate a single photon of energy grater then γmc^2

$$h\nu_L \leq \gamma mc^2 \quad \rightarrow \quad \frac{3}{2} h \frac{eB}{2\pi mc} \sin\theta_p \gamma^2 \leq \gamma mc^2 \quad , \tag{B.6}$$

and this fact leads to conclude that quantistic limit for the synchrotron emission occurs when

$$\gamma \geq 1 \quad \rightarrow \quad B \leq B_{cr} \quad . \tag{B.7}$$

B.1.2 Energy losses for the synchrotron radiation

The energy variation of a single electron that radiates via synchrotron emission is given by the equation (see Sect. 4.1.1)

$$P_S = -\frac{dE}{dt} = \frac{2}{3} r_e^2 c \gamma^2 B^2 \sin\theta_p \quad , \tag{B.8}$$

that can be writen in terms of the electron energy $E = \gamma mc^2$ as

$$-\frac{dE}{dt} = \frac{2}{3} r_e^2 c \frac{E^2}{m^2c^4} B^2 \sin\theta_p \quad , \tag{B.9}$$

and can be simplified

$$-\frac{dE}{dt} = -\xi_S B_\perp^2 E^2 \quad \rightarrow \quad \xi_S = \frac{2}{3}\frac{e^2}{m^4c^7} \quad . \tag{B.10}$$

Integrating the above relation, under the assumption that the magnetic field is constant one finds

$$\int_{E(t=0)}^{E(t)} -\frac{dE}{E^2} = \xi_S B_\perp^2 \int_0^t dt \quad , \tag{B.11}$$

then the electron energy depends on the time as

$$E(t) = \frac{E_0}{1 + \xi_S B_\perp^2} E_0 t \quad , \tag{B.12}$$

and it is possible to define the *half life time* $t_{1/2}$ by the relation

$$t = t_{1/2} \quad \rightarrow \quad E(t_{1/2}) = \frac{1}{2} E_0 \quad , \tag{B.13}$$

corresponding to the time interval in which the electron has emitted half of its energy

$$t_{1/2} = \frac{1}{\xi_S B_\perp^2 E_0} \quad . \tag{B.14}$$

B.2 THE INVERSE COMPTON RADIATION

B.2.1 The Compton scattering

For the Compton scattering (see Sect. 4.2.1, with references to Fig. 4.4 and with the same nomenclature) the conservation laws of the energy and of the momentum can be written in the form

$$\underline{p} = h(\underline{k} - \underline{k_0}) \tag{B.15}$$

$$mc^2 + h\nu_0 = \gamma mc^2 + h\nu \tag{B.16}$$

where the electron energy is given by

$$\gamma mc^2 = \sqrt{m^2c^4 + p^2c^2} \quad , \tag{B.17}$$

and where $\underline{k}$ and $\underline{k_0}$ are the momenta of the photon scattered and incident, respectively.

From the eq. B.15 it is possible to derive the electron momentum

$$p^2 = h^2(k^2 + k_0^2 - 2kk_0 \cos\theta) \quad , \tag{B.18}$$

then replacing with the above equation one finds

$$\gamma mc^2 = h^2(\nu^2 - \nu_0^2) + 2h(\nu_0 - \nu)mc^2 + m^2c^4 \quad , \tag{B.19}$$

Combing again eq. B.17 with eq. B.19 it yields

$$2h(\nu_0 - \nu)mc^2 = 2h^2\nu\nu_0(1 - \cos\theta) \quad , \tag{B.20}$$

and

$$\frac{\nu_0 - \nu}{\nu_0 \nu} c = \lambda - \lambda_0 = \lambda_e (1 - \cos\theta) \quad , \tag{B.21}$$

where it is possible to define the *Compton wavelenght* for the electron as

$$\lambda_e = \frac{h}{mc} \quad , \tag{B.22}$$

and the *Compton formula* will be given by

$$\Delta\lambda = \lambda_e (1 - \cos\theta) \quad , \tag{B.23}$$

that can be expressed in terms of the electron energy in the form

$$E = \frac{E_0}{1 + \frac{E_0}{mc^2}(1 - \cos\theta)} \quad . \tag{B.24}$$

B.2.2 The "head-on" approximation in Thomson regime

In the case of the inverse Compton scattering the relation between the energy of the photon before E_0 and after the scattering E is given by the following equation (see Sect. 4.2.1, and eq. 4.33)

$$E = \gamma^2 E_0 \frac{(1 - \beta\cos\alpha)(1 + \beta\cos\psi')}{1 + \frac{\gamma E_0}{mc^2}(1 - \beta\cos\alpha)(1 - \cos\theta')} \quad . \tag{B.25}$$

It is useful derive this relation in the case of head-on collisions expressed by the condition

$$\alpha = \alpha' = \pi \quad \rightarrow \quad -\cos\theta' = \cos\psi' \quad , \tag{B.26}$$

then introducing these assumption eq. B.25 becomes

$$E = \gamma^2 E_0 \frac{(1 + \beta)(1 + \beta\cos\theta')}{1 + \frac{\gamma E_0}{mc^2}(1 + \beta)(1 - \cos\theta')} \quad . \tag{B.27}$$

Note that in the case $\theta' = 0$ the photon energy after the scattering is

$$E = \gamma^2 E_0 (1 - \beta^2) = E_0 \quad , \tag{B.28}$$

while in the case $\theta' = \pi$ one finds

$$E = \gamma^2 E_0 \frac{(1 + \beta)^2}{1 + \frac{2\gamma E_0}{mc^2}(1 + \beta)} \quad . \tag{B.29}$$

In this appendix, it will be demonstrated that in the Thomson regime the average photon energy after the IC scattering is the same of that evaluated in head-on approximation. The average photon scattered energy is defined as

$$\langle E \rangle = \int_0^{4\pi} \frac{3}{8\pi r_e^2} E(\theta', \psi') \frac{d\sigma_T}{d\Omega'} d\Omega' \quad , \tag{B.30}$$

and the main relations for the IC scattering in the Thomson regime are given by

$$E'_0 = \gamma E_0 (1 - \beta\cos\alpha) \tag{B.31}$$

$$E'_0 = E' \tag{B.32}$$

$$E = \gamma E' (1 + \beta\cos\psi') \tag{B.33}$$

$$\frac{d\sigma_T}{d\Omega'} = \frac{1}{2} r_e^2 (1 + \cos\theta') \tag{B.34}$$

$$\cos\alpha' = \frac{\cos\alpha - \beta}{1 - \beta\cos\alpha} \quad , \tag{B.35}$$

and these equations are relative to the energy Lorentz transformations (eqs. B.31 and B.33), the Thomson limit (eq. B.32), the Thomson cross section (eq. B.34) and the light aberration relation (eq. B.35). Finally, following the nomenclature in Fig. 4.4, the relation between angles is given by

$$\cos\psi' = \cos\theta' \cos\alpha' - (1 - \cos^2\alpha')^{1/2}(1 - \cos^2\theta')^{1/2}\cos\phi' \quad . \tag{B.36}$$

The function $E(\theta', \psi')$ must be evaluated both in the general case and in the head-on approximation. In the general case it is

$$E(\theta', \psi') = \gamma E'(1 - \beta\cos\psi') = \gamma E_0(1 - \beta\cos\alpha)(1 + \beta\cos\psi') \quad , \tag{B.37}$$

then, replacing with the eq. B.36

$$E(\theta', \psi') = \gamma^2 E_0(1 - \beta\cos\alpha)\{1 + \beta[\cos\theta' \cos\alpha' - (1 - \cos^2\alpha')^{1/2}(1 - \cos^2\theta')^{1/2}\cos\phi']\} \quad , \tag{B.38}$$

and observing that

$$\sin\alpha' = \frac{(1 - \cos^2\alpha)^{1/2}}{\gamma(1 - \beta\cos\alpha)} \quad , \tag{B.39}$$

the average photon scattered energy it is

$$\langle E(\theta', \psi')\rangle = \frac{3}{8\pi r_e^2}\int_0^{2\pi} d\phi' \int_0^{\pi} d\theta' \frac{1}{2} r_e^2 (1 + \cos^2\theta')\sin\theta' E(\theta', \psi') \quad , \tag{B.40}$$

and integrating it yields

$$\langle E(\theta', \psi')\rangle = \gamma E' \quad . \tag{B.41}$$

Now considering the head-on approximation the $E_{app}(\theta', \psi')$ is given by

$$E_{app}(\theta', \psi') = \gamma E'(1 + \beta\cos\psi') = \gamma E_0'(1 + \beta\cos\psi') = \gamma^2 E_0(1 - \beta\cos\alpha)(1 - \beta\cos\theta') \quad , \tag{B.42}$$

and the average photon scattered energy is equal to

$$\langle E_{app}(\theta', \psi')\rangle = \frac{3}{16\pi}\int_0^{2\pi} d\phi' \int_0^{\pi} d\theta' (1 + \cos^2\theta')\sin\theta' E_{app}(\theta', \psi') \quad , \tag{B.43}$$

then again

$$\langle E_{app}(\theta', \psi')\rangle = \gamma^2 E_0(1 - \beta\cos\alpha) = \gamma E' = \langle E(\theta', \psi')\rangle \quad , \tag{B.44}$$

and it is shown that in Thomson regime the average photon scattered energy is the same evaluated in the general case and in with the head-on approximation.

B.2.3 The inverse Compton scattering in Thomson regime

Following the calculations of Reynolds (1982) it is possible to determine the function (see eq. 4.59) for the Compton kernel in Thomson regime. The number of emitted photons per unit of volume, energy and incident solid angle in the laboratory frame is

$$n(E_0, \Omega_i) = \frac{dN_{ph}}{dV dE_0 d\Omega_i} \quad , \tag{B.45}$$

and in the Thomson regime the differential cross section can be written

$$\frac{d\sigma_T}{d\Omega'} = \frac{r_e^2}{2}(1 + \cos^2\psi') = \frac{d\sigma_T}{d\Omega_s'} \quad , \tag{B.46}$$

then the rate of emitted photons per unit of diffusion solid angle in the electron frame will be

$$d\left(\frac{dN_{ph}}{dt'd\Omega'_s}\right) = \frac{d\sigma_T}{d\Omega'_s} cn'(E'_0, \Omega'_i)dE'_0 d\Omega'_i \quad . \tag{B.47}$$

Noting that from the Lorentz invariants follow that

$$n(E_0, \Omega_i)\frac{dE_0}{E_0}d\Omega_i = n'(E'_0, \Omega'_i)\frac{dE'_0}{E'_0}d\Omega'_i \quad . \tag{B.48}$$

introducing into eq. B.47 the above relations one finds

$$d\left(\frac{dN_{ph}}{dt'd\Omega'_s}\right) = E'_0\frac{r_e^2}{2}(1 + \cos^2\psi')cn(E_0, \Omega_i)\frac{dE_0}{E_0}d\Omega_i \quad , \tag{B.49}$$

where assuming the azimutal simmetry it is

$$\frac{dN_{ph}}{dt'd\Omega'_s} = \frac{1}{2\pi}\frac{dN_{ph}}{dt'd\cos\psi'} \quad . \tag{B.50}$$

The number of emitted photons via IC scattering, per unit of energy and time is

$$\frac{dP}{dE} = \frac{dN_{ph}}{dtdE} = 2\pi\frac{dN_{ph}}{dt'd\Omega'_s}\frac{d\cos\psi'}{dE}\frac{dt'}{dt} \quad , \tag{B.51}$$

where one can replace

$$\frac{dt'}{dt} = \frac{1}{\gamma} \quad , \quad \frac{d\cos\psi'}{dE} = \frac{1}{\gamma\beta E'} \quad , \tag{B.52}$$

and introducing the head-on approximation it yields

$$d\left(\frac{dP}{dE}\right) = \pi r_e^2 c(1 + \cos\psi')n(E_0, \Omega_i)\frac{E'_0}{E_0}\frac{1}{\gamma}\frac{1}{\gamma\beta E'}dE_0 d\Omega_i \quad , \tag{B.53}$$

that can be integrated and written as

$$\frac{dP}{dE} = \int d\Omega_i \int dE_0 \frac{\pi r_e^2 c}{\gamma E_0}(1 + \cos^2\psi')n(E_0, \Omega_i) \quad . \tag{B.54}$$

Noting the following angular relation

$$1 + \cos^2\psi' = \frac{E^2}{\gamma^4(1 - \beta\cos\alpha)^2 E_0^2} - \frac{2E}{\gamma^2(1 - \beta\cos\alpha)E_0} + 2 \quad , \tag{B.55}$$

that in the ultrarelativistic case ($\beta \simeq 1$) can be written in the form

$$1 + \cos^2\psi' = \frac{16\widehat{E}^2}{(1 - \cos\alpha)^2} - \frac{8\widehat{E}}{(1 - \cos\alpha)} + 2 \quad , \tag{B.56}$$

while the other relation between the incident angle and the diffusion one is given by

$$\cos\alpha = \frac{1}{\beta}\left[1 - \frac{E}{\gamma^2 E_0(1 - \beta\cos\psi')}\right] \quad , \tag{B.57}$$

with the following limits

$$\cos\alpha_{low} = 1 - \frac{2E_0}{E} \quad \text{(B.58)}$$

$$\cos\alpha_{high} = 1 - \frac{E}{2\gamma^2 E_0} \quad . \quad \text{(B.59)}$$

It is possible to introduce these angular relation and obtaining

$$\frac{dP}{dE} = \frac{2\pi^2 r_e^2 c}{\gamma^2} \int dE_0 E_0 \int_{\cos\alpha_{low}}^{\cos\alpha_{high}} n(e_0, \Omega_i) \left[\frac{16\widehat{E}^2}{(1-\cos\alpha)^2} - \frac{8\widehat{E}}{(1-\cos\alpha)} + 2 \right] d\cos\alpha \quad . \quad \text{(B.60)}$$

Finally, introducing the spherical simmetry

$$n(E_0, \Omega_i) = \frac{n(E_0)}{4\pi} \quad , \quad \text{(B.61)}$$

the photon spectrum of the IC emission in Thomson regime is given by

$$\frac{dP}{dE} = \frac{2\pi^2 r_e^2 c}{\gamma^2} \int \left(1 + \widehat{E} + 2\widehat{E}\ln\widehat{E} - 2\widehat{E}^2\right) \frac{n(E_0)}{E_0} dE_0 \quad . \quad \text{(B.62)}$$

Appendix C

Numerical codes

C.1 CODE DESCRIPTION

The source is parametrized by the following quantities: the redshift z, the beaming factor δ, the magnetic field B', the volume of the emitting region V'; in particular, for emitting particles: the electron density n'_{el}, the electron spectral index s and the curvature parameter r with the γ'_{min} and γ'_{max} the electron energy limits and γ'_0 the reference energy for the electron spectrum.

The output of each simulation provides: the luminosity distance of the source $D_L(Mpc)$, the energy density of the magnetic field u_B, the source radius R, the electron number N_{el} with the normalization of the electron distribution N_0, the peak Lorentz factor γ_p of the $\gamma^2\ N(\gamma)$ and the total electron energy E_{tot} (see eq. 3.38).

The main output of the code is given in three files with the emission coefficient, the intrinsic flux and the spectral energy distribution, as function of the observed frequency of both synchrotron and inverse Compton components, respectively. The emission coefficient for the synchrotron emission was evaluated on using eq. 4.20 while the absorption coefficient with eq. 4.21, and the solution of the radiative transfer is given by the relation eq. 2.25. For the inverse Compton the emission coefficient was calculated with eq. 4.54 for the first and the second order IC scattering, and for the external Compton component, with different incident photon distribution in the case of SSC and EC models, respectively.

The method used to perform integral is with logarithmic steps:

$$dx = 10^{1/N\ \log(x_{max}/x_{min})} \quad with \quad x_i = x_{i-1}dx \tag{C.1}$$

where $N = 10^6$, and the integrals of a generic function $f(x)$ are approximated as

$$I = \Sigma_i f(x_i) x_i (1 - \frac{1}{dx}) \tag{C.2}$$

A test was successfully performed to check the SEDs calculated comparing them with those obtained by the numerical SSC code described in Tramacere (2007). The numerical codes reproduce the same SSC calculations as reported in Fig. C.1 with the same input of Tramacere (2007) for a simultaneous observation of Mrk 501 in the X-ray and in the TeV band.

C.2 CODE STATISTICS

Applying a log-parabolic bestfit to each the file containing the spectral energy distribution, the numerical code calculates: the resulting curvature parameter, the SED peak frequency, the maximum of the SED, of both synchrotron and inverse Compton components. The fitting procedure are described in the following.

The spectral parameters are derived minimizing the following quantity D

$$D = \sum_{i=1}^{N} (y_i - b x_i^2 - a x_i - q)^2. \tag{C.3}$$

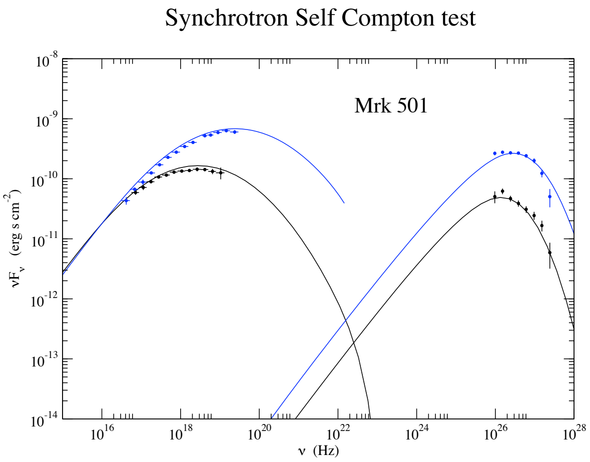

Figure C.1: The SED of Mrk 501 during simultaneous observation performed with *BeppoSAX* in the X-rays and with CAT in the TeV energy range. SSC single zone model can describe the SED with the same input values reported in Massaro et al. (2006).

It is possible to define the quantities involved in the equation system derived to calculate the spectral parameters a, b, q

$$\overline{x^j y^k} = \frac{1}{N} \sum_{i=1}^{N} x^j y^k \qquad \mathit{with}\ j, k = 0, 1, 2, 3, 4, \tag{C.4}$$

and the equation system is given by

$$\frac{\partial D}{\partial b} = \frac{\partial D}{\partial a} = \frac{\partial D}{\partial q} = 0, \tag{C.5}$$

and it can be solved with the Kramer method

$$det = \overline{x^4}(\overline{x^2} - \overline{x}^2) - \overline{x^3}(\overline{x^3} - \overline{x^2}\,\overline{x}) + \overline{x^2}(\overline{x^3}\,\overline{x} - \overline{x^2}^{\,2}) \tag{C.6}$$

in which the spectral parameters are

$$b = \frac{\overline{x^2 y}(\overline{x^2} - \overline{x}^2) - \overline{x^3}(\overline{xy} - \overline{xy}) + \overline{x^2}(\overline{xy}\,\overline{x} - \overline{x^2}\,\overline{y})}{det}, \tag{C.7}$$

$$a = \frac{\overline{x^4}(\overline{xy} - \overline{x}\,\overline{y}) - \overline{x^2 y}(\overline{x^3} - \overline{x^2}\,\overline{x}) + \overline{x^2}(\overline{x^3}\,\overline{y} - \overline{x^2}\,\overline{xy})}{det}, \tag{C.8}$$

$$q = \frac{\overline{x^4}(\overline{x^2}\,\overline{y} - \overline{x}\,\overline{xy}) - \overline{x^3}(\overline{x^3}\,\overline{y} - \overline{x^2}\,\overline{xy}) + \overline{x^2 y}(\overline{x^3}\,\overline{x} - \overline{x^2}^{\,2})}{det}, \tag{C.9}$$

respectively

Appendix D

Correlations and fits in the presence of uncertainties on both axes and of hidden parameters

We first recall the general formalism used to evaluate correlation coefficients for data with uncertainties on both axes.

For two statistical variables defined as:

$$\bar{\mathbf{x}} = \{\bar{x}_i\} = \{x_i + dx_i\} \quad \text{(D.1)}$$

$$\bar{\mathbf{y}} = \{\bar{y}_i\} = \{y_i + dy_i\}\,, \quad \text{(D.2)}$$

the covariance is expressed by

$$\mathrm{cov}(\bar{\mathbf{x}}, \bar{\mathbf{y}}) = \mathrm{cov}(\mathbf{x}, \mathbf{y}) + \mathrm{cov}(\mathbf{x}, \mathbf{dy}) + \mathrm{cov}(\mathbf{y}, \mathbf{dy}) + \mathrm{cov}(\mathbf{dx}, \mathbf{dy})\,, \quad \text{(D.3)}$$

and the correlation coefficient reads

$$r_{\bar{\mathbf{x}},\bar{\mathbf{y}}} = \frac{\mathrm{cov}(\bar{\mathbf{x}}, \bar{\mathbf{y}})}{\sigma_{\bar{\mathbf{x}}}\sigma_{\bar{\mathbf{y}}}}. \quad \text{(D.4)}$$

Here $\sigma_{\bar{\mathbf{x}}}$ is given by

$$\sigma_{\bar{\mathbf{x}}} = \mathrm{cov}(\mathbf{x}, \mathbf{x}) + 2\mathrm{cov}(\mathbf{x}, \mathbf{dx}) + \mathrm{cov}(\mathbf{dx}, \mathbf{dx}), \quad \text{(D.5)}$$

and similarly for $\sigma_{\bar{y}}$.

An issue arising in the analysis of correlations (as anticipated in §4 of the main text), is that "hidden" parameters – adding to the "primary" ones focused by the analysis – can introduce a covariance term, i.e., a correlation. To evaluate its weight we recall the general expression of the covariance term for functions of random variables. When we have M functions $(f_1, ..., f_M)$ of N random variables $x_1...x_N$, the covariance of f_k, f_l is given by Barlow (1989) to read

$$\mathrm{cov(f_k, f_l)} = \sum_{\mathrm{i}} \sum_{\mathrm{j}} \Big(\frac{\partial \mathrm{f_k}}{\partial \mathrm{x_i}}\Big) \Big(\frac{\partial \mathrm{f_l}}{\partial \mathrm{x_j}}\Big)\,\mathrm{cov(x_i, x_j)}\,. \quad \text{(D.6)}$$

Eq. D.6 shows that even when all the variables x_i are mutually uncorrelated (with covariance=0) a finite covariance term arises for the functions f_i which share the same variables.

We then show explicitly the formalism we actually use in fitting our data. We follow the approach of D'Agostini (2005), who discusses a development from the standard formalism (see Kendall & Stuart 1979) basing on Bayesian statistics. This is an unbiased method to perform fits on data, including uncertainties on both axes and a term of extravariance σ_v given by the fluctuations of a"hidden" parameter. The log-likelyhood function discussed by D'Agostini (2005) reads

$$\begin{aligned} L(m, q, \sigma_v; \mathbf{x}, \mathbf{y}) &= \frac{1}{2}\sum_i \log(\sigma_{\mathrm{v}}^2 + \sigma_{\mathrm{y_i}}^2 + \mathrm{m}^2\sigma_{\mathrm{x_i}}^2) + \\ & \frac{1}{2}\sum_i \frac{(y_i - mx_i - q)^2}{\sigma_v^2 + \sigma_{y_i}^2 + m^2\sigma_{x_i}^2}\,, \end{aligned} \quad \text{(D.7)}$$

on having used two models, namely:

$$y_{lin} = x_i\, m + q\ ; \tag{D.8}$$

and a log-linear model $Y = \log y$, $X = \log x$ with uncertainties evaluated on using standard propagation to yield

$$Y = \log x_i\, m + q\ . \tag{D.9}$$

This method was successfully used by Guidorzi et al. (2005).

Appendix E

Spectral analysis of HBLs

Tabs. E1, E2, E3, E4, report the log of HBLs observations and the values of the spectral parameters derived for Tev HBLs and for candidates (see Sects. 7.2 and 7.3).

In Tab. E1, *LECS*, *MECS* and *PDS* columns indicate the exposure time in seconds. In Tab. E2 and in Tab. E4, *Frame* indicates the EPIC camera used (M1=MOS1, and M2=MOS2), the modes (PW=Partial window and FW=Full window) and the filter (Th=Thin, Md=Medium, Tk=Thick) used for each pointing (see Sect. 6.2 for details), and the exposure is reported in the seconds on the column *Exps*. Capital letters near the observation date indicate a different pointing in the same observation, while small letters refer to time resolved spectra (see Sect. 6.4). The BeppoSAX spectral analysis of 1ES 0347-121, 1ES 1011+492, PKS 2344-514 is reported in Giommi et al. (2005, also available at http://www.asdc.asi.it/sedentary/).

The capital letter *F* in *XMM-Newton* Tabs. E2 and E4 indicate that the observation is too much contaminated by solar flares to be used in our spectral analysis.

In *Swift* tables the column *Frame* report on the observation modality (pc=photon counting and wt=windowed timed, see also Sect. 6.3 for details), and the *Exps* is the exposure time in seconds.

All other columns in each table refers to the log-parabolic model or to power-law model (see Sect. 6.4) where the estimate of the spectral parameter is consistent with zero in 3σ interval (continuos lines). Values of E_p are reported in keV, the normalization K in $10^{-4} photons\ cm^{-2}\ s^{-1}\ keV^{-1}$ and S_p in $10^{-13} erg\ cm^{-2}\ s^{-1}$ with F_X denote the $2-10\ keV$ flux measured in $10^{-11} erg\ cm^{-2}\ s^{-1}$. For observations with less than 30 bins only the estimate of the X-ray flux F_X with a Galactic absorbed power-law model is reported.

Table E.1: *BeppoSAX* Results LOGPARABOLIC model

Obs ID	*Date*	*LECS*	*MECS*	*PDS*	a	b	E_p	K	S_p	F_X	χ_r^2
1ES 0229+200											
51472001	16/07/01	17236	68200	33113	1.60(0.10)	0.31(0.08)		43(4)		1.24	0.96(101)
PKS 0548-322											
50493003	20/02/99	5642	12439	9355	1.53(0.07)	0.51(0.07)	2.88(0.27)	75(5)	153.6(3.2)	2.02	1.21(67)
50493004	26/02/99	—-	2025	1003	2.40(0.14)	———	———	12(2)	———-	1.76	1.31(29)
504930042	07/04/99	5251	18943	10164	1.77(0.07)	0.45(0.06)	1.77(0.21)	67(5)	115.2(4.8)	1.36	0.98(67)
1ES 1101-232											
50064017	04/01/97	6146	13868	10676	1.64(0.08)	0.33(0.07)	3.50(0.33)	120(7)	241.6(3.2)	3.71	1.08(184)
50726001	19/06/98	—-	24817	10792	1.97(0.22)	———	———	145(4)	———-	2.55	1.31(80)
Mrk 180											
50064010	10/12/96	5165	18205	7330	2.24(0.08)	0.28(0.08)	0.37(0.16)	36(4)	65.6(14.4)	0.51	0.91(56)
1ES 1218+304											
50863005	12/07/99	10609	42693	20670	2.11(0.03)	0.38(0.03)	0.73(0.08)	98(3)	158.4(6.4)	1.48	0.75(101)
1H 1426+428											
50493006	08/02/99	—-	40657	20432	2.22(0.11)	———	———	103(16)	———-	2.04	0.95(80)
1ES 1553+113											
50064005	05/02/98	4421	10592	4671	2.17(0.07)	0.63(0.08)	0.73(0.11)	115(8)	190.4(1.6)	1.29	1.22(67)
Mrk 501											
50377001*	07/04/97	12387	20571	8936	1.68(0.01)	0.17(0.01)	8.7(1.3)	624(8)	1410(50)	21.5	–
50377002*	11/04/97	12559	20391	8719	1.64(0.01)	0.12(0.01)	31.6(9.6)	609(7)	1800(100)	23.9	–
50377003*	16/04/97	9612	17125	7347	1.41(0.01)	0.15(0.01)	101.6(23.7)	960(10)	6000(500)	52.4	–
50529001*	28/04/98	13552	21892	9873	1.65(0.02)	0.15(0.02)	14.7(5.7)	474(8)	1200(100)	17.6	–
50529002*	29/04/98	14661	21417	9662	1.62(0.02)	0.17(0.02)	13.1(4.3)	543(8)	1400(100)	20.8	–
50529003*	01/05/98	13164	19033	8447	1.71(0.02)	0.24(0.02)	4.0(0.6)	477(8)	940(30)	14.7	–
50666001*	20/06/98	98363	25861	11566	1.79(0.02)	0.21(0.02)	3.2(0.5)	175(4)	320(10)	4.95	–
50666002*	29/06/98	12682	47528	7470	1.69(0.02)	0.23(0.02)	4.7(0.8)	323(6)	660(30)	10.3	–
50666003*	16/07/98	11228	15924	6919	1.70(0.02)	0.33(0.02)	2.8(0.3)	320(7)	600(20)	9.0	–
50666004*	25/07/98	25067	30937	14505	1.76(0.01)	0.28(0.01)	2.7(0.1)	337(5)	610(10)	9.3	–
50944001*	10/06/99	10405	17510	—-	2.15(0.01)	0.24(0.01)	0.49(0.03)	186(2)	315(4)	3.02	–
1ES 1959+650											
50064002	04/05/97	2252	12391	5393	2.02(0.18)	———	———	192(14)	———-	1.77	0.90(56)
51386001	23/09/01										P.
513860011	28/09/01	25255	48037	22416	1.79(0.03)	0.43(0.02)	1.74(0.08)	464(9)	785.6(6.4)	10.35	2.00(125)

(*) refers to Masaro et al. 2004

Table E.2: *BeppoSAX* Results LOGPARABOLIC model

Obs ID	*Date*	*LECS*	*MECS*	*PDS*	a	b	E_p	K	S_p	F_X	χ_r^2
PKS 2005-489											
50046001	29/09/96	—-	9911	7674	2.02(0.19)	———	———	268(12)	——	5.94	1.36(79)
50503002	01/11/98	20067	52467	23437	2.01(0.02)	0.17(0.02)	0.95(0.14)	821(12)	1313.6(19.2)	15.45	1.03(120)
PKS 2155-304											
50016001	20/11/96	35644	10686	—-	2.43(0.01)	0.24(0.01)	0.13(0.01)	504(4)	1240.0(28.8)	5.37	1.22(127)
50160008	22/11/97	22086	59497	28007	2.38(0.01)	0.37(0.01)	0.30(0.01)	780(8)	1569.0(27.2)	8.23	1.75(125)
50880001	04/11/99	45208	10392	49144	2.66(0.01)	0.20(0.01)	———	292(4)	1635.2(118.4)	2.48	1.39(125)
PKs 2354-315											
50493007	21/06/98	15055	40950	18034	1.77(0.03)	0.28(0.03)	2.57(0.22)	90(3)	160.0(1.6)	2.13	1.33(101)

Table E.3: *XMM-Newton* Results LOGPARABOLIC model

Obs ID	*Date*	Exps	Frame	a	b	E_p	K	S_p	F_X	χ_r^2
1ES 0347-121										
0094381101	28/08/02	5362	M1-PW(Th)							F.
PKS 0548-322										
0111830201	03/08/01	47370	M1-PW(Md)	1.84(0.05)	——	——	95(1)	—	3.11	0.95(124)
0205920501	19/10/04	40669	M2-PW(Th)	1.84(0.02)	0.14(0.03)	3.54(0.42)	126(1)	224.0(1.6)	3.54	1.35(307)
1H 1100-230										
0094380601	29/05/01	2926	M1-PW(Md)							F.
0205920601	08/06/04	18267	M2-PW(Th)	2.04(0.02)	0.17(0.03)	0.76(0.06)	202(1)	326.4(1.6)	4.10	1.02(302)
Mrk 180										
0094170101	12/04/01	8294	M1-FW(Th)	2.27(0.03)	——	——	56(1)	—	0.96	0.87(82)
1ES 1218+304										
0111840101	11/06/01	29309	M1-PW(Md)	2.19(0.03)	0.46(0.06)	0.63(0.08)	212(2)	353.6(8.0)	2.68	0.87(147)
1H 1426+428										
0111850201	16/06/01	60496	M1-PW(Md)	1.68(0.02)	0.12(0.02)	21.95(0.60)	82(1)	212.8(6.4)	3.00	0.99(343)
0165770101	04/08/04	65652	M1-PW(Th)	1.89(0.01)	0.31(0.02)	1.50(0.41)	102(1)	166.4(1.6)	2.24	0.96(317)
0165770201	06/08/04	68662	M1-PW(Md)	1.89(0.02)	0.38(0.04)	1.38(0.06)	106(1)	172.8(1.6)	2.16	0.98(202)
0212090201	24/01/05	30163	M1-PW(Md)	1.90(0.02)	0.40(0.03)	1.33(0.04)	132(1)	214.4(1.6)	2.64	1.28(249)
0310190101	19/06/05	46884	M1-PW(Md)	1.81(0.01)	0.23(0.02)	2.61(0.12)	189(1)	331.2(1.6)	5.07	1.23(341)
0310190201	25/06/05	44805	M1-PW(Md)	1.89(0.03)	0.29(0.05)	1.55(0.09)	148(1)	241.6(1.6)	3.33	1.07(184)
0310190501	04/08/05	45480	M1-PW(Md)	1.97(0.02)	0.34(0.04)	1.11(0.06)	143(1)	228.8(1.6)	2.69	1.01(222)
1ES 1553+113										
0094380801	06/09/01	5801	M1-PW(Md)	2.09(0.03)	——	——	22(1)	—	0.50	1.30 (91)
Mrk 501										
0113060201	13/07/02	8740	M2-FW(Tk)	2.05(0.05)	0.29(0.09)	0.81(0.21)	231(4)	371.2(8.0)	4.10	1.13(102)
0113060401	14/07/02	11880	M2-FW(Md)	2.18(0.02)	——	——	242(3)	—	4.73	0.76(119)
1ES 1959+650										
0094380201	23/01/02	306	M1-PW(Md)	1.72(0.02)	——	——	582(11)	—	20.3	0.86(111)
0094383301	16/01/03	2200	M1-PW(Md)							F.
0094383501	09/09/03	7085	M1-PW(Md)							F.
PKS 2005-489										
0205920401	04/09/04	12667	M2-PW(Th)	3.03(0.04)	——	——	19(1)	—	0.12	1.22 (63)
0304080301	26/09/05	21063	M1-PW(Th)	2.27(0.01)	——	——	123(1)	—	2.14	0.96(201)
0304080401	28/09/05	27662	M1-PW(Th)	2.28(0.01)	——	——	116(1)	—	1.96	1.39(214)

Table E.3: *XMM-Newton* Results LOGPARABOLIC model

Obs ID	*Date*	Exps	Frame	a	b	E_p	K	S_p	F_X	χ_r^2
PKS 2155-304										
0124930101	30/05/00a	39301	M1-PW(Md)	2.49(0.02)	0.13(0.04)	——	393(1)	1806.4(592)	4.41	1.16(202)
0124930101	30/05/00b	39301	M1-PW(Md)	2.52(0.01)	——	——	406(3)	—	4.94	0.88(158)
0124930201	31/05/00	56894	M2-PW(Md)	2.55(0.01)	——	——	395(2)	—	4.60	1.16(197)
0080940101	19/11/00a	57650	M2-PW(Th)	2.57(0.01)	0.21(0.02)	——	389(1)	—	3.66	1.04(269)
0080940101	19/11/00b	57650	M2-PW(Th)	2.67(0.01)	0.18(0.03)	——	326(1)	—	2.76	0.94(243)
0080940101	19/11/00c	57650	M2-PW(Th)	2.71(0.02)	0.23(0.04)	——	296(2)	—	2.27	1.03(175)
0080940301	20/11/00a	58549	M2-PW(Th)	2.79(0.02)	——	——	253(2)	—	2.13	0.93(137)
0080940301	20/11/00b	58549	M2-PW(Th)	2.71(0.02)	0.30(0.04)	——	269(2)	—	1.98	1.14(169)
0124930301	30/11/01A	27749	M1-PW(Th)	2.48(0.01)	0.49(0.02)	0.32(0.02)	540(2)	1136.0(22.4)	4.56	1.27(294)
0124930301	30/11/01B	38249	M1-PW(Md)	2.38(0.01)	0.48(0.01)	0.40(0.02)	779(2)	1483.2(16.0)	7.56	1.27(357)
0124930301	30/11/01C	24650	M1-PW(Tk)	2.51(0.01)	0.47(0.02)	0.29(0.02)	601(2)	1316.8(35.2)	4.95	0.97(301)
0124930501	24/05/02a	99165	M1-PW(Md)	2.38(0.01)	0.24(0.03)	0.17(0.04)	262(1)	590.4(35.2)	3.10	1.05(249)
0124930501	24/05/02b	99165	M1-PW(Md)	2.29(0.01)	0.30(0.02)	0.33(0.04)	270(1)	508.8(12.8)	3.41	1.18(286)
0124930501	24/05/02c	99165	M1-PW(Md)	2.04(0.01)	0.34(0.02)	0.86(0.04)	392(2)	628.8(3.2)	6.75	1.23(308)
0124930601	29/11/02Aa	57751	M1-PW(Md)	2.53(0.01)	0.44(0.03)	0.25(0.03)	192(1)	441.6(19.2)	1.58	1.00(219)
0124930601	29/11/02Ab	57751	M1-PW(Md)	2.48(0.02)	0.44(0.03)	0.29(0.04)	184(1)	395.2(16.0)	1.61	1.15(214)
0124930601	29/11/02B	55606	M1-PW(Md)	2.42(0.01)	0.44(0.02)	0.33(0.02)	263(1)	529.6(11.2)	2.50	1.14(298)
0158960101	23/11/03a	26862	M1-PW(Tk)	2.73(0.02)	0.16(0.05)	——	171(1)	—	1.38	1.16(162)
0158960101	23/11/03b	26862	M1-PW(Tk)	2.81(0.02)	——	——	152(1)	—	1.25	0.86(130)
0158960901	22/11/04a	28662	M1-PW(Th)	2.73(0.02)	0.40(0.04)	0.12(0.03)	190(1)	656.0(68.8)	1.24	1.06(177)
0158960901	22/11/04b	28662	M1-PW(Th)	2.68(0.02)	0.36(0.06)	——	168(1)	—	1.22	1.07(144)
0158961001	23/11/04a	40163	M1-PW(Th)	2.61(0.03)	0.33(0.07)	——	241(2)	745.6(137.6)	1.96	1.03(132)
0158961001	23/11/04b	40163	M1-PW(Th)	2.63(0.03)	0.33(0.07)	——	236(2)	—	1.87	0.97(121)
0158961001	23/11/04c	40163	M1-PW(Th)	2.61(0.02)	0.36(0.05)	0.14(0.04)	255(2)	739.2(86.4)	2.02	1.02(165)
0158961101	12/05/05	27838	M1-PW(Th)	2.54(0.02)	——	——	323(3)	—	3.81	1.01(120)
0158961301	30/11/05a	60163	M1-PW(Md)	2.46(0.02)	0.21(0.03)	——	338(2)	—	3.67	1.07(226)
0158961301	30/11/05b	60163	M1-PW(Md)	2.47(0.02)	0.26(0.04)	——	324(2)	854.4(83.2)	3.34	1.08(207)
0158961301	30/11/05c	60163	M1-PW(Md)	2.49(0.01)	0.22(0.02)	——	384(1)	—	3.97	1.34(304)
0158961401	01/05/06	64562	M1-PW(Md)	2.45(0.01)	0.11(0.02)	——	140(1)	—	1.68	1.28(290)
1H 2356-309										
0304080601	15/07/05	18082	M2-FW(Th)	2.05(0.03)	0.22(0.06)	0.78(0.17)	49(1)	8.0(0.2)	9.35	1.11(156)

Table E.4: *Swift* Results LOGPARABOLIC model

Obs ID	*Date*	Frame	Exps	a	b	E_p	K	S_p	F_X	χ_r^2
1ES 0347-121										
00030808001	03/10/06	pc	3187	2.18(0.02)	———	———	102(2)	—-	2.25	0.76(24)
PKS 0548-322										
00044002001	13/12/04	pc	9310	1.68(0.03)	0.26(0.05)	4.13(0.47)	121(2)	234.2(6.4)	3.82	1.06(155)
00044002273	14/01/05	pc	1116	———	———	———	——	——	5.23	———-
00044002005	14/01/05	pc	5704	1.71(0.04)	0.34(0.08)	2.72(0.41)	107(2)	198.4(6.4)	2.98	1.07(87)
00044002008	10/03/05	pc	4248	1.69(0.04)	0.34(0.09)	2.89(0.30)	109(3)	206.4(6.4)	3.12	1.14(65)
00035008001	01/04/05	pc	1256	———	———	———	—-	——	3.63	———-
00035008001	01/04/05	wt	1395	1.85(0.04)	———	———	127(3)	——	3.57	0.82(76)
00035008002	27/04/05	pc	5194	1.69(0.04)	0.28(0.08)	3.64(0.61)	124(3)	243.2(8.0)	3.79	1.19(92)
00035008002	27/04/05	wt	1823	1.81(0.04)	———	———	113(3)	——	4.11	1.16(90)
00035008003	13/05/05	pc	3349	1.69(0.04)	———	———	103(3)	——	3.25	1.07(66)
00035008005	21/05/05	pc	9187	1.68(0.03)	0.38(0.06)	2.66(0.17)	134(2)	252.8(4.8)	3.75	0.95(119)
00044002268	21/05/05	pc	40031	1.83(0.03)	0.22(0.05)	2.45(0.20)	150(2)	259.2(3.2)	3.95	1.02(289)
00035008006	24/05/05	pc	1344	———	———	———	—-	—-	3.95	———-
00035008007	26/05/05	wt	817	1.87(0.05)	———	———	125(4)	—-	4.06	1.05(39)
00035008008	29/05/05	pc	3852	1.72(0.03)	0.41(0.06)	2.22(0.20)	126(2)	225.6(4.8)	3.23	1.31(111)
00044002274	24/06/05	pc	7910	1.69(0.03)	0.31(0.06)	3.21(0.40)	147(3)	281.6(6.4)	4.35	1.26(133)
00066004010	11/01/06	pc	1723	———	———	———	—-	—-	2.85	———-
00030836001	28/11/06	pc	4260	1.67(0.05)	0.52(0.11)	2.10(0.24)	87(3)	158.4(4.8)	2.16	1.26(51)
00044002034	13/03/07	pc	1169	———	———	———	—-	—-	2.18	———-
1ES 1011+496										
00035012002	19/06/05	pc	7966	2.34(0.03)	0.50(0.09)	0.46(0.08)	663(2)	1210(4)	6.67	1.14(75)
00035012003	26/06/05	pc	9123	2.13(0.03)	0.33(0.09)	0.64(0.12)	736(2)	1211(3)	1.14	0.83(80)
00035012003	26/06/05	wt	806	———	———	———	—-	—-	1.02	———
00035012004	20/12/05	pc	7644	2.26(0.03)	0.47(0.10)	———	936(2)	———	1.07	1.23(76)
1H 1100-230										
00035013001	30/06/05	pc	8521	1.93(0.02)	0.40(0.05)	1.22(0.07)	230(3)	369.6(4.8)	4.34	0.92(194)
00035013002	13/07/05	pc	2295	1.99(0.10)	———	———	229(6)	——	4.21	0.94(50)
00035013003	04/11/05	pc	1163	1.95(0.09)	———	———	203(10)	——	4.51	0.81(19)
Mrk 180										
00035015001	16/04/06	pc	2932	2.20(0.04)	0.58(0.12)	0.67(0.10)	116(4)	193.6(6.4)	1.31	1.09(44)
00035015002	18/04/06	pc	6373	2.17(0.03)	0.40(0.07)	0.57(0.11)	142(3)	182.4(4.8)	1.94	1.14(113)

Table E.4: *Swift* Results LOGPARABOLIC model

Obs ID	*Date*	Frame	Exps	a	b	E_p	K	S_p	F_X	χ^2_r
1ES 1218+304										
00035016002	30/10/05	pc	2013	1.97(0.06)	———	———	121(5)	——	2.39	1.18(30)
00035016001	31/10/05	pc	3701	2.07(0.04)	0.39(0.11)	0.81(0.13)	111(3)	179.2(4.8)	1.76	1.11(56)
00030376001	08/03/06	pc	3082	2.15(0.06)	———	———	62(3)	——	0.80	0.89(25)
00030376002	09/03/06	pc	3149	2.25(0.06)	———	———	51(3)	——	0.88	0.96(23)
00030376003	18/05/06	pc	1670	———	———	———	——	——	2.09	——-
00030376004	19/05/06	pc	1448	———	———	———	——	——	1.87	——-
00030376005	20/05/06	pc	1330	———	———	———	——	——	2.22	——-
00030376006	21/05/06	pc	2223	1.89(0.05)	0.44(0.14)	1.32(0.16)	115(4)	187.2(8.0	2.22	0.56(34)
1H 1426+428										
00035020001	30/03/05	pc	1056	———	———	———	——	——	0.55	——-
00035020001	30/03/05	wt	1879	1.99(0.05)	———	———	64(2)	——	1.64	1.19(57)
00035020003	02/04/05	wt	3425	2.03(0.02)	———	———	137(2)	——	3.52	0.90(178)
00051000002	19/06/05	pc	21375	1.75(0.02)	0.31(0.03)	2.49(0.16)	213(2)	382.4(4.8)	5.71	0.92(276)
00051000003	25/06/05	pc	22818	1.89(0.02)	0.34(0.04)	1.47(0.08)	174(2)	284.8(4.8)	3.76	1.37(198)
00030375001	07/03/06	pc	2064	1.76(0.05)	0.49(0.10)	1.77(0.18)	195(6)	334.4(11.2)	4.37	0.57(51)
00030375002	07/03/06	pc	925	———	———	———	——	——	4.13	——-
00030375003	20/03/07	pc	2343	1.86(0.03)	———	———	118(4)	——	2.56	1.28(35)
1ES 1553+113										
00035021001	20/04/05	pc	5167	2.21(0.03)	0.36(0.07)	0.51(0.11)	157(3)	268.8(8.0)	2.10	1.29(95)
00035021002	06/10/05	pc	8528	2.14(0.02)	0.24(0.04)	0.52(0.09)	435(5)	728.0(11.2)	7.16	1.04(221)
00035021002	06/10/05	wt	2236	2.21(0.02)	———	———	432(5)	————-	7.29	0.94(215)
00035021003	07/10/05	pc	9093	2.11(0.02)	0.23(0.04)	0.57(0.09)	387(5)	640.0(9.6)	6.66	1.04(216)
00035021003	07/10/05	wt	1587	2.21(0.02)	———	———	407(6)	————-	6.75	0.92(175)
Mrk 501										
00035023001	21/04/05	pc	544	———	———	———	——	———	4.82	——-
00035023002	18/06/05	pc	1828	1.89(0.05)	0.56(0.11)	1.25(0.10)	476(14)	771.2(24.8)	8.25	0.85(51)
00030793001	18/07/06	pc	4465	2.02(0.03)	0.34(0.07)	0.94(0.09)	298(6)	476.8(4.8)	5.29	1.06(114)
00030793002	19/07/06	pc	993	2.16(0.06)	———	———	412(17)	——	5.66	1.19(28)
00030793003	19/07/06	pc	1024	2.12(0.06)	———	———	316(13)	——	5.37	1.25(30)
00030793004	20/07/06	pc	2954	2.01(0.03)	0.36(0.08)	0.97(0.09)	400(9)	640.0(14.4)	7.12	1.02(88)
00030793005	21/07/06	pc	2278	1.99(0.03)	0.50(0.09)	1.02(0.07)	410(10)	656.0(16.0)	6.53	0.97(79)
00030793006	23/03/07	pc	2027	2.22(0.04)	———	———	239(7)	——	3.67	0.71(47)
00030793007	30/03/07	pc	2281	1.90(0.04)	0.42(0.10)	1.33(0.13)	229(7)	371.2(11.2)	4.49	0.73(55)
00030793008	07/04/07	pc	2038	1.91(0.05)	———	———	191(7)	——	4.32	0.82(51)

Table E.4: *Swift* Results LOGPARABOLIC model

Obs ID	*Date*	Frame	Exps	a	b	E_p	K	S_p	F_X	χ_r^2
1ES 1959+650										
00035025001	19/04/05	wt	4433	2.09(0.01)	0.36(0.03)	0.76(0.04)	744(5)	1203.2(8.0)	11.68	0.95(342)
00035025002	19/05/06	wt	1279	1.99(0.02)	0.41(0.05)	1.02(0.07)	638(8)	1020.8(14.4)	10.90	1.02(205)
00035025003	21/05/06	wt	1990	1.93(0.02)	0.37(0.04)	1.25(0.06)	747(7)	1204.8(12.8)	14.51	0.92(266)
00035025004	23/05/06	wt	5365	1.95(0.01)	0.23(0.02)	1.28(0.05)	964(5)	1552.0(9.6)	20.85	1.04(418)
00035025005	24/05/06	wt	2319	1.85(0.01)	0.39(0.03)	1.58(0.05)	1087(8)	1801.6(14.4)	23.38	0.95(346)
00035025006	25/05/06	wt	4381	1.92(0.01)	0.36(0.02)	1.30(0.03)	970(5)	1569.6(9.6)	19.29	1.04(414)
00035025007	26/05/06	wt	4384	1.97(0.01)	0.31(0.02)	1.10(0.04)	962(5))	1540.8(8.0)	18.69	1.07(411)
00035025008	27/05/06	wt	4273	2.03(0.01)	0.47(0.03)	0.92(0.03)	890(5)	1425.6(8.0)	13.66	1.23(364)
00035025009	28/05/06	wt	4399	2.01(0.01)	0.46(0.03)	0.97(0.03)	872(5)	1395.2(8.0)	13.84	1.02(360)
00035025010	29/05/06	wt	3306	1.72(0.03)	0.75(0.03)	1.52(0.04)	675(6)	1145.6(9.6)	12.41	1.08(273)
PKS 2005-489										
00035026001	31/03/05	wt	2214	2.96(0.03)	———	———	170(3)	——	1.17	1.28(116)
00035026002	05/04/05	wt	5858	3.14(0.05)	———	———	109(2)	——	0.63	0.80(115)
00035026003	06/04/05	pc	15745	3.02(0.02)	———	———	97(2)	——	0.54	1.09(129)
00035026003	06/04/05	wt	2511	3.09(0.09)	———	———	83(2)	——	0.50	1.09(48)

Table E.5: *Swift* Results LOGPARABOLIC model

Obs ID	*Date*	Frame	Exps	a	b	E_p	K	S_p	F_X	χ^2_r
PKS 2155-304										
00035027001	17/11/05	pc	934	———	———	———	——	——	1.51	———
00035027002	11/04/06	pc	2600	2.31(0.04)	———	———	261(8)	——	3.59	1.15(61)
00035027003	16/04/06	pc	5664	2.35(0.03)	0.44(0.07)	0.40(0.07)	235(5)	440.0(16.0)	2.45	0.87(104)
00035027004	20/04/06	pc	2386	2.21(0.12)	———	———	315(10)	——	4.09	0.98(43)
00035027005	30/04/06	pc	8064	2.46(0.03)	———	———	146(3)	——	1.63	0.88(96)
00030795001	29/07/06	wt	4916	2.56(0.01)	0.22(0.02)	———	811(5)	——	7.66	1.12(304)
00030795002	01/08/06	pc	1239	2.45(0.04)	0.65(0.12)	0.45(0.07)	653(18)	1248.0(48.0)	5.06	1.33(60)
00030795003	01/08/06	wt	1843	2.67(0.01)	0.20(0.04)	———	565(6)	——	4.75	1.16(189)
00030795004	03/08/06	wt	1605	2.53(0.01)	0.24(0.04)	———	687(7)	——	6.63	1.19(199)
00030795005	05/08/06	wt	516	2.80(0.03)	———	———	495(12)	——	3.21	0.78(83)
00030795006	06/08/06	pc	648	———	———	———	——	——	2.71	———
00030795008	08/08/06	pc	679	———	———	———	——	——	4.36	———
00030795008	08/08/06	wt	438	2.72(0.03)	———	———	490(12)	——	3.98	0.88(80)
00030795009	10/08/06	pc	709	2.50(0.05)	———	———	493(19)	———	4.75	0.77(35)
00030795010	11/08/06	pc	919	———	———	———	——	——	2.15	———
00030795012	13/08/06	pc	1131	———	———	———	——	——	1.65	———
00030795013	14/08/06	pc	931	———	———	———	——	——	2.44	———
00030795014	15/08/06	pc	899	———	———	———	——	——	1.55	———
00030795015	16/08/06	pc	943	———	———	———	——	———	1.09	———
00030795016	17/08/06	pc	1006	———	———	———	——	———	1.19	———
00030795017	18/08/06	pc	1116	———	———	———	——	———	1.89	———
00030795024	26/08/06	pc	904	———	———	———	——	———	0.74	———
00030795025	27/08/06	pc	943	———	———	———	——	———	1.20	———
1ES 2344+514										
00035031001	19/04/05	pc	4665	1.45(0.14)	1.06(0.24)	———	48(3)	———	0.98	1.09(35)
00035031002	19/05/05	pc	4183	———	———	———	——	———	1.20	———
00035031003	03/12/05	pc	12204	1.72(0.01)	———	———	41(2)	———	1.05	0.98(53)

Table E.6: *XMM-Newton* Results LOGPARABOLIC model

Obs ID	*Date*	Exps	Frame	a	b	E_p	K	S_p	F_X	χ^2_r
1ES 0033+595										
0094381301	01/02/03	1596	M1-PW(Th)							F.
1ES 0120+340										
0094382101	05/01/02	5638	M1-PW(Md)	1.94(0.04)	0.32(0.07)	1.23(0.14)	46.4(0.84)	74.7(1.3)	0.94	1.12(130)
1ES 0145+138										
0094383401	23/01/03	5657	M1-PW(Th)							F.
MS 0205.7+3509										
0084140101	14/02/01	38070	M1-FW(Md)	2.15(0.04)	0.48(0.08)	0.69(0.10)	8.10(0.18)	13.3(0.6)	0.11	0.81(127)
0084140501	04/02/02	11683	M1-FW(Md)	1.94(0.07)	0.41(0.12)	1.18(0.18)	8.56(0.33)	13.8(0.5)	0.16	1.10(65)
1ES 0323+022										
0094382501	05/02/02	4563	M1-PW(Md)	2.49(0.04)			18.0(0.74)		0.22	0.71(45)
1ES 0647+250										
0094380901	25/03/02	2106	M1-PW(Md)	2.66(0.04)			55.9(1.6)		0.56	1.06(53)
1ES 0737+746										
0123100201	12/04/00	19580	M!-FW(Th)	2.21(0.04)	0.15(0.07)	0.19(0.03)	23.5(0.04)	45.0(2.7)	0.38	0.98(134)
0123100101	13/04/00	10622	M1-PW(Th)	2.15(0.04)	0.19(0.07)	0.39(0.05)	25.6(0.5)	44.0(0.2)	0.434	1.01(128)
1ES 1028+511										
0094382701	26/11/01	5629	M1-PW(Md)	2.17(0.04)	0.23(0.09)	0.43(0.23)	63.1(1.1)	108.3(0.9)	1.02	0.86(116)
0303720201	13/04/05	89065	M1-FW(Th)	2.19(0.04)	0.67(0.11)	0.73(0.08)	32.3(0.83)	53.2(1.9)	0.34	1.00(92)
0303720301	13/04/05	89065	M1-FW(Th)	2.19(0.02)	0.22(0.04)	0.36(0.09)	39.8(0.40)	69.9(3.0)	0.63	1.08(191)
0303720601	25/04/05	89065	M1-FW(Th)	2.19(0.04)	0.57(0.11)	0.68(0.10)	36.7(0.89)	61.0(2.1)	0.42	1.25(92)
1207+392										
0112830201	22/12/00	58838	M1-FW(Md)	1.88(0.02)	0.36(0.03)	1.00(0.08)	16.8(0.2)	28.3(0.3)	0.36	0.97(225)
0112830501	22/12/00	21897	M1-FW(Md)	2.00(0.03)	0.28(0.06)	0.99(0.11)	17.4(0.3)	27.8(0.5)	0.33	1.04(147)
MS 1229.2+6430										
0124900101	21/05/00	16222	M1-FW(Th)	2.09(0.05)	0.34(0.09)	0.74(0.18)	0.92(0.27)	15.0(0.7)	0.15	0.98(98)
1ES 1255+244										
0094383001	26/06/02	670	M1-SW(Md)							F.
0094383201	12/12/02	5788	M1-PW(Md)	2.01(0.03)			2.10(0.63)		0.53	1.06(90)

Bibliography

Chapter One

[1] Blandford, R. D., Rees, M. J., 1978, PROC. ”Pittsburgh Conference on BL Lac objects”, 328

[2] Ghisellini, G. & Maraschi, L. 1989, ApJ, 340, 181

[3] Hoffmeister, C., 1929, AN, 236, 233

[4] Jones, T. W., O’Dell, S. L., & Stein, W. A. 1974, ApJ, 188, 353

[5] MacLeod, J. M., Swenson, G. W. Jr., et al., 1965, *Astron. J.*, 70, 756

[6] Moore, R. L., Stockman, H. S., 1981, ApJ, 243, 60

[7] Oke, J. B., Gunn, J. E., 1974, ApJ, 189L, 5

[8] Padovani, P., & Giommi, P., 1995, MNRAS, 277, 1477

[9] Sambruna, R. M., Maraschi, L., Urry, C. M., 1996 ApJ, 463, 444

[10] Schmitt, J. L., 1968, Nat., 218, 663

[11] Strittmatter, P. A., Serkowski, K., Carswell, R., et al., 1972, ApJ, 175L, 7

Chapter Two

[12] Band, D. L., Grindlay, J. E., 1985 ApJ, 298, 128

[13] Chandrasekar, S., 1965, ”Radiative transfer”, New York, Dover Publications Inc.

[14] Dwek, E., Krennrich, F., 2005, ApJ, 618, 657

[15] Gould, R. J., & Schréder, G. 1967, Phys. Rev., 155, 1408

[16] Gould, R. J., 1979, A&A, 76. 306

[17] Hogg, D. W., 1999, arXiv:astro-ph/9905116

[18] Kataoka, J., 1999, PhD Thesis

[19] Kembhavi, A. K., Narlikar, J. V., 1999, *Quasars and Active Galactic Nuclei*, Cambridge, Cambridge University Press

[20] Kneiske, T. M., Bretz, T., Mannheim, K., Hartmann, D. H., 2004, A&A, 413, 807

[21] Konopelko, A. et al. 2003, ApJ, 597, 851

[22] Jauch, J. M., & Rohrlich, F. 1955, ”The Theory of Photons and Electrons”, (Cambridge, MA: Addison-Wesley)

[23] Lucchin, F., 1990, ”Introduzione alla cosmologia”, Bologna, Zanichelli

[24] Pacholczky, A. G., 1970, ”Radio Astrophysics: Nonthermal Processes in Galactic and Extragalactic Sources”, San Francisco, W.H. Freeman

[25] Peacock, J. A. 1999, ”Cosmological Physics” (Cambridge: Cambridge University Press)

[26] Peebles, P. J. E., 1993, ”Principles of Physical Cosmology”, (Princeton University Press)

[27] Peterson B.M., 1997, ”An introduction to active galactic nuclei”, (Cambridge University Press)

[28] Rybicki, G. B., & Lightman, A. P., 1979, ”Radiative Processes in Astrophysics” (New York: Wiley)

[29] Shu, F. H., 1985, ”The Physics of Astrophysics”, University Science Books

[30] Tucker ,W. H., 1975, ”Radiation processes in astrophysics”, Cambridge, The MIT Press

Chapter Three

[31] Axford W.I. Astrophysical Aspects of Cosmic Rays ed. M. Nagano and F. Takahara (World Scientific, Singapore, 1991)

[32] Bell A.R., 1978, MNRAS.182, 443B

[33] Blandford, R. D., Ostriker, J. P. 1978ApJ, 221L, 29B

[34] Blandford, R., Eichler, D. 1987PhR, 154, .1B

[35] Drury L. 1983 SSRv, 36, 57D

[36] Fermi, E., 1954, Phys. Rev., 75, 1169

[37] Kardashev, N. S., 1962, SvA, 6, 317

[38] Krymskii, G. F., 1977, DoSSR, 234, 1306

[39] Lemoine M. & Pelletier G. 2003, ApJ, 589L, 73

[40] Protheroe, R. J., 1996, arXiv:astro-ph/9612212

[41] Protheroe, R. J., Stanev, Todor 1999, APh, 10, 185

[42] Massaro, E., Perri, M., Giommi, P., et al. 2004, A&A, 422, 103

[43] Massaro, E., Tramacere, A., Perri, M., et al. 2006, A&A, 448, 861

[44] Vietri, M., 2006, *Astrofisica delle alte energie*, Torino, Bollati Boringhieri

Chapter Four

[45] Arbeiter, C., Pohl, M., Schlickeiser, R., 2002, A&A, 386, 415

[46] Bednarek, W., and Protheroe, R. J. 1999, MNRAS, 302, 373

[47] Blazejowski, M., Sikora, M., Moderski, R., Madejski, G. M., 2000, ApJ, 545, 107

[48] Bloom, S. D., & Marscher, A. P. 1996, ApJ, 461, 657

[49] Böttcher, M., Mause, H., & Schlickeiser, R. A&A, 1997, 324, 395

[50] Böttcher, M., and Dermer, C. D. 1998, ApJ, 501, L51

[51] Böttcher, M. 1999, ApJ, 515, L21

[52] Böttcher, M. 2001, in "Gamma-Ray Astrophysics through Multiwavelength Experiments 2001", Mt. Abu, India, March 8 - 10, 2001 (Bull. Astron. Soc. India, in press) (astro-ph/0105554)

[53] Blumenthal, G. R., Gould, R. J., 1970, Rev. Mod. Phys., 42, 237

[54] Burbidge, G. R., Jones, T. W., and O'Dell, S. L. 1974, ApJ, 193, 43

[55] Celotti, A., Ghisellini, G., Fabian, A. C., 2007, MNRAS, 375, 417

[56] Dermer, C. D., Schlickeiser, R., and Mastichiadis, A. 1992, A&A, 256, L27

[57] Dermer, C. D., and Schlickeiser, R. 1993, ApJ, 416, 458

[58] Dermer, C. D., Sturner, S. J., and Schlickeiser, R. 1993, ApJS, 109, 103

[59] Dermer, C. D., and Schlickeiser, R. 1994, ApJS, 90, 945

[60] Dermer, C. D., Schlickeiser, R., 2002, ApJ, 575, 667

[61] Ghisellini, G., and Madau, P., 1996, MNRAS, 280, 67

[62] Hartman, R. C., et al. 2001, ApJ, 553, 683

[63] Inoue, S., Takahara F., 1996, ApJ, 463, 555

[64] Koratkar, A., Pian, E., Urry, C. M., & Pesce, J. E. 1998, ApJ, 492, 173

[65] Kirk, J. G., Rieger, F. M., and Mastichiadis, A. 1998, A&A, 333,452

[66] Jones, F. C., 1968, Phys. Rev. 167, 1159

[67] Longair, M. S., 1997, *High Energy Astrophysics*, Cambridge, Cambridge Univ. Press

[68] Maraschi, L., Ghisellini, G., & Celotti, A. 1992, ApJ, 397, L5

[69] Mastichiadis, A., and Kirk, J. G. 1997, A&A, 320, 19

[70] Melia, F., and Königl, A. 1989, ApJ, 340, 162

[71] Mukherjee, R. et al., 1999, ApJ, 527, 132

[72] Pian, E. et al. 1998, ApJ, 492, L17

[73] Protheroe, R. J., Biermann, P. L., 1997, APh, 7, 181

[74] Reynolds, S. P., 1982, ApJ, 256, 13

[75] Rybicki, G. B., & Lightman, A. P., 1979, ”Radiative Processes in Astrophysics” (New York: Wiley)

[76] Shakura, N. I., Syunyaev, R. A., 1973 A&A, 24, 337

[77] Shapiro S. L., & Teukolsky S. A., 1983, ”Black Holes, white dwarfs and Neutron Stars”, (New York: Wiley)

[78] Sikora, M., Begelman, M. C., and Rees, M. J. 1994, ApJ, 421, 153

[79] Sikora, M., and Madejski, G., in Proc 2nd KIAS Astrophysics Workshop ”Current High Energy Emission Around Black Holes,” Seoul, Korea (Sep. 3 - 8, 2001) (astro-ph/0112231)

[80] Tavecchio, F., Maraschi, L., & Ghisellini, G. 1998, ApJ, 509, 608

[81] Tavecchio, F., Maraschi, L., Sambruna, R. M., Urry, C. M., 2000, ApJ, 544, L23

Chapter Five

[82] Cavaliere A., & Morrison, P., 1980, ApJ, 238L,63

[83] Guilbert, P. W., Fabian, A. C., Rees, M. J., 1983, MNRAS, 205, 593

[84] Massaro, E., Perri, M., Giommi, P., et al. 2004, A&A, 422, 103

[85] Massaro, E., Tramacere, A., Perri, M., et al. 2006, A&A, 448, 861

[86] Sikora, M., Begelman, M. C., and Rees, M. J. 1994, ApJ, 421, 153

[87] Svensson, R., 1987, MNRAS, 227, 403

[88] Tramacere, A., Massaro, F., Cavaliere, A., 2007, A&A, 466, 521

[89] Tsang, O., Kirk, J., 2007, A&A, 463, 145

Chapter Six

[90] Arnaud, K.A., 1996, ”Astronomical Data Analysis Software and Systems V”, eds. Jacoby G. and Barnes J., p17, ASP Conf. Series volume 101

[91] Blustin, A. J., Page, M. J., Branduardi-Raymont, G., 2004, A&A, 417, 61

[92] Boella G., Chiappetti L., Conti G. et al. 1997, A&AS 122, 327

[93] Burrows, D., Hill, J. E., Nousek, J. A., et al. 2005, SSRv., 120, 165

[94] Citterio, O., Conti, G., Mattaini, E., Santambrogio, E., Sacco, B., 1986, SPIE, 597, 102

[95] Conti, G., Mattaini, E., Santambrogio, E., Sacco, B., Cusumano, G., Citterio, O., Braeuninger, H. W., Burkert, W., 1994, SPIE, 2279, 101

[96] Fiore F., Guainazzi M., Grandi P. 1999, Cookbook for *Beppo*SAX NFI Spectral Analysis (http://www.sdc.asi.it/
software)

[97] Frontera, F., Costa, E., Dal Fiume, D., et al., 1997 A&AS 122, 375

[98] Giommi, P., Piranomonte, S., Perri, M., Padovani, P., 2005, A&A, 434, 385

[99] Hill, J.E., Burrows, D.N., Nousek, J.A. et al., 2004, SPIE, 5165, 217

[100] Kalberla, P.M.W., Burton, W.B., Hartmann, D., 2005, A&A, 440, 775

[101] Jager, R., Mels, W. A., Brinkman, A. C., Galama, M. Y., Goulooze, H., Heise, J., Lowes, P., Muller, J. M., Naber, A., Rook, A., et al., 1997, A&AS, 125, 557

[102] Landau, R., Golish, B., Jones, T. J., et al., 1986, ApJ, 308, L78

[103] Lockman, F. J., & Savage, B. D., 1995, ApJS, 97, 1

[104] Loiseau, N., et al., 2004, ”User’s guide to the *XMM-Newton* Science Analysis System” (issue 3.1)

[105] Manzo, G., Giarrusso, S., Santangelo, A., Ciralli, F., Fazio, G., Piraino, S., Segreto, A., 1997, A&AS, 122, 341

[106] Massaro, E., Perri, M., Giommi, P., et al. 2004, A&A, 422, 103

[107] Massaro, E., Tramacere, A., Perri, M., et al. 2006, A&A, 448, 861

[108] Moretti, A., Campana, S., Mineo, T. et al. 2005, Proc SPIE vol 5898, 360

[109] Parmar, A. N., Kahabka, P., Hartmann, H. W., Heise, J., Martin, D. D. E., Bavdaz, M., Mineo, T., 1997, A&A, 323, 33

[110] Perlman, E. S., Madejski, G., Georganopoulos, M., et al., 2005, ApJ, 625, 727P

[111] Snowden, S., et al., 2004, ”The *XMM-Newton* ABC Guide” (version 2.01)

[112] Perri, M., Maselli, A., Giommi, P., et al., 2007, A&A, 462,889

[113] Tramacere, A., Massaro, F., Cavaliere, A., 2007a, A&A, 466, 521

[114] Tramacere, A., Giommi, P., Massaro, E., et al., 2007b, A&A, 467, 501

Chapter Seven

[115] Aharonian, F., Akhperjanian, A.G., Aye, K.-M. et al. 2005a, A&A, 436, L17

[116] Aharonian, F., Akhperjanian, A.G., Bazer-Bachi, A.R. et al., 2006a, Nature, 440, 1018

[117] Aharonian, F., Akhperjanian, A.G., Bazer-Bachi, A.R., et al. 2006b, A&A, 448,L19

[118] Albert, J., Aliu, E., Anderhub, H. et al., 2006a ApJ 648, L105

[119] Albert, J., Aliu, E., Anderhub, H. et al., 2006b ApJ 642, L119

[120] Antonucci R., 1993, ARA&A 31, 473

[121] Arnaud, K.A., 1996, ”Astronomical Data Analysis Software and Systems V”, eds. Jacoby G. and Barnes J., p17, ASP Conf. Series volume 101

[122] Barlow, R.J., 1989, “Statistics: a guide to the use of statistical methods in the physical sciences” Ed. J. Wiley & Sons

[123] Catanese, M., et al., 1998, ApJ, 501, 616

[124] Chadwick, P. M., Lyons, K., McComb, T. J. L., et al. 1999, ApJ, 513, 161

[125] D'Agostini, G., 2005, arXiv:physics/0511182

[126] Djannati-Ataj, A. et al., 2002, A&A, 391, L25

[127] Fossati, G., Celotti, A., Chiaberge, M., et al., 2000a, ApJ, 541, 153

[128] Fossati, G., Celotti, A., Chiaberge, M., et al., 2000b, ApJ, 541, 166

[129] Fuhrmann, L., Tosti, G., et al, 2007 in preparation

[130] Ghisellini, G. & Maraschi, L. 1989, Apj, 340, 181

[131] Giommi, P., Piranomonte, S., Perri, M., Padovani, P., 2005, A&A, 434, 385

[132] Guetta, D., Ghisellini G., Lazzati D., Celotti A., 2004, A&A 421, 877

[133] Guidorzi, C. et al., 2005, MNRAS, 371, 843

[134] Kardashev, N. S., 1962, SvA, 6, 317

[135] Kendall M., & Stuart, A., 1979, "The Advanced Theory of Statistics", Mac Millan, New York

[136] Jones, T. W., O'Dell, S. L., & Stein, W. A. 1974, ApJ, 188, 353

[137] Ioka, K., Nakamura, T., 2002, ApJ, 570, 21

[138] Landau, R., Golish, B., Jones, T. J., et al., 1986, ApJ, 308, L78

[139] Lin, Y. C., et al. 1992, ApJ, 401, L61

[140] Lockman, F. J., & Savage, B. D., 1995, ApJS, 97, 1

[141] Loiseau, N., et al., 2004, "User's guide to the *XMM-Newton* Science Analysis System" (issue 3.1)

[142] Maraschi, L., Fossati, G., Tavecchio, F., et al., 1999, ApJ, 526, 81

[143] Maselli, A., Giommi, P., Perri, M., Nesci, R., Tramacere, A., Massaro, F., Capalbi, M., 2007,arXiv:astro-ph/0710.2464

[144] Massaro, E., Perri, M., Giommi, P., et al. 2004, A&A, 422, 103

[145] Massaro, E., Tramacere, A., Perri, M., et al. 2006, A&A, 448, 861

[146] Nishiyama, T. 1999, Proceedings of the 26th International Cosmic Ray Conference, ICRC 3, 370.

[147] Padovani, P., & Giommi, P., 1995, MNRAS, 277, 1477

[148] Peebles, P. J. E.,, 1993, "Principles of Physical Cosmology", Princeton University Press

[149] Perri, M., Maselli, A., Giommi, P., et al., 2007, A&A, 462,889

[150] Punch, M., et al. 1992, Nature, 358, 477

[151] Petry D., et al. 1996, A&A, 311, L13

[152] Quinn, J., 1996, ApJ, 456L, 83

[153] Ravasio, M., Tagliaferri, G., Ghisellini, G., et al., 2004, A&A, 424, 841.

[154] Rybicki, G. B., & Lightman, A. P., 1979, ”Radiative Processes in Astrophysics” (New York: Wiley)

[155] Sembay, S., Edelson, R., Markowitz, A., et al., 2002, ApJ, 574, 634

[156] Snowden, S., et al., 2004, ”The *XMM-Newton* ABC Guide” (version 2.01)

[157] Spergel, D. N., et al., 2007, ApJS, 170, 377

[158] Struder, L., et al., 2001, A&A, 365, L18

[159] Tanihata, C., Urry, C. M., Takahashi, T., et al., 2001, ApJ, 563, 569

[160] Tanihata C., Takahashi T., Kataoka J., 2003, ApJ, 584, 153

[161] Tanihata, C., Kataoka, J., Takahashi, T., et al. 2004, ApJ, 601, 759,

[162] Turner, M. L. J., et al. 2001, A&A, 365, L27

[163] Urry, C. M., & Padovani, P. 1995, PASP, 107, 803

[164] Urry, C. M., Scarpa, R., O’Dowd, M., et al., 2000, ApJ, 532, 816

[165] Tramacere, A., Massaro, F., Cavaliere, A., 2007a, A&A, 466, 521

[166] Tramacere, A., Giommi, P., Massaro, E., et al., 2007b, A&A, 467, 501

[167] Urry, C. M., & Padovani, P. 1995, PASP, 107, 803

Chapter Eight

[168] Albert, J., Aliu, E., et al., 2007, ApJ letters accepted, astro-ph: 0703084v2

[169] Aller, M. F., Marscher, A. P., Hartman, R. C., et al. 1997, AIP Conf. Proc. 410, 1423

[170] Altschuler, D. R., Broderick J. J., Dennison, B., et al. 1984, AJ, 89, 1784

[171] Angel, J. R. P., & Stockman, H. S. 1980, ARA&A, 18, 321

[172] Angione, R. J. 1971, AJ, 76, 25

[173] Angione, R. J. 1968, PASP, 80, 339

[174] Balonek, T. J. 2005a, vsnet-alert 8383

[175] Balonek, T. J. 2005b, vsnet-alert 8405

[176] Balonek, T. J. 1982, Ph.D. Dissertation

[177] Begelman, M. C., Blandford, R. D., & Rees, M. J. 1980, Nature, 287, 307

[178] Bertin, E., & Arnouts, S. 1996, A&AS, 117, 393

[179] Blom, J. J., Bloemen, H., Bennett, K., et al. 1995, A&A, 295, 330

[180] Burrows, D., Hill, J. E., Nousek, J. A., et al. 2005, SSRv., 120, 165

[181] Cavaliere, A., Morrison, P., 1980, ApJ, 238, 63

[182] Ciaramella, A., Bongardo, C., Aller, H. D., et al. 2004, A&A, 419, 485

[183] Conconi, P., Cunniffe, R., D'Alessio, F., et al. 2004, Proc. SPIE, 5492, 1602

[184] Fiorucci, M., Tosti, G., & Rizzi, N. 1998, PASP, 110, 105

[185] Foschini, L., Cocco, G. Di, Malaguti, G., et al. 2005, The Astronomer's Telegram, 497, 1

[186] Fuhrmann et al. 2005, A&A, in preparation

[187] Giommi et al. 2005, A&A, in preparation

[188] González-Pérez, J. N., Kidger, M. R., & Martín-Luis, F. 2001, AJ, 122, 2055

[189] Guetta, D., Ghisellini, G., Lazzati, D., & Celotti, A. 2004, A&A, 421, 877

[190] Guilbert, P. W., Fabian, A. C., Rees, M., 1983, MNRAS, 205, 593

[191] Hill, J.E., Burrows, D.N., Nousek, J.A. et al., 2004, SPIE, 5165, 217

[192] Kardashev, N. S., 1962, SvA, 6, 317

[193] Kneiske, T. M. et al., 2004, A&A, 413, 807

[194] Krichbaum, T. P., Britzen, S., Standke, K. J., Witzel, A., Schalinski, C. J., & Zensus, J. A. 1995, Proceedings of the National Academy of Science, 92, 11377

[195] Leanin, J.-P., Boisson, Sol., C. et al., 2007, A&A accepted, astro-ph: 07102847

[196] Lin, Y. C., Bertsch, D. L., Dingus, B. L., et al. 1996, ApJS, 105, 331

[197] Lockman, F. J., & Savage, B. D., 1995, ApJS, 97, 1

[198] Marscher, A. P. 1996, ASP Conf. Ser. 100: Energy Transport in Radio Galaxies and Quasars, 100, 45

[199] Massaro, E., Perri, M., Giommi, P., et al. 2004, A&A, 422, 103

[200] Massaro, E., Tramacere, A., Perri, M., et al. 2006, A&A, 448, 861

[201] Massaro, F., Tramacere, A., Cavaliere, A., 2007, A&A, submitted

[202] Pagels, A., Krichbaum, T. P., Graham, D. A., et al. 2004, European VLBI Network on New Developments in VLBI Science and Technology, 7

[203] Pauliny-Toth, I. I. K. 1998, ASP Conf. Ser. 144: IAU Colloq. 164: Radio Emission from Galactic and Extragalactic Compact Sources, 144, 75

[204] Pian et al. 2005, A&A, in preparation

[205] Pomphrey, R. B., Smith, A. G., Leacock, R. J., et al. 1976, AJ, 81, 489

[206] Raiteri, C. M., Villata, M., Lanteri, L., Cavallone, M., & Sobrito, G. 1998, A&AS, 130, 495

[207] Raiteri, C. M., Ghisellini, G., Villata, M., et al. 1998, A&AS, 127, 445

[208] Ravasio, M., et al., 2002, A&A, 383, 763

[209] Schlegel, D. J., Finkbeiner, D. P., & Davis, M. 1998, ApJ, 500, 525

[210] Stetson, P. B. 1988, PASP, 99, 191

[211] Teraesranta, H., Tornikoski, M., Mujunen, A., et al. 1998, A&AS, 132, 305

[212] Tornikoski, M., Valtaoja, E., Terasranta, H., et al. 1994, A&A, 289, 673

[213] Tosti, G., Bagaglia, M., Campeggi, C., et al. 2004, Proc. SPIE, 5492, 689

[214] Tosti, G., Pascolini, S., & Fiorucci, M. 1996, PASP, 108, 706

[215] Tsang, O., Kirk, J., 2007, A&A, 463, 145

[216] Tsang, O., Kirk, J., 2007, A&A accepted, astro-ph: 0710.1564

[217] Urry, C. M. 1999, Astroparticle Physics, 11, 159

[218] Villata, M., Raiteri, C. M., Ghisellini, G., et al. 1997, A&AS, 121, 119

[219] Villata, M., & Raiteri, C. M. 1999, A&A, 347, 30

[220] Zerbi, F. M., Chincarini, G., Ghisellini, G., et al., 2004, Proc. SPIE, 5492, 1590

For the use of LATEX:

[221] Oetiker T. et al., 2000, *Una (mica tanto) breve introduzione a LATEX 2ϵ*, Free Software Foundation.